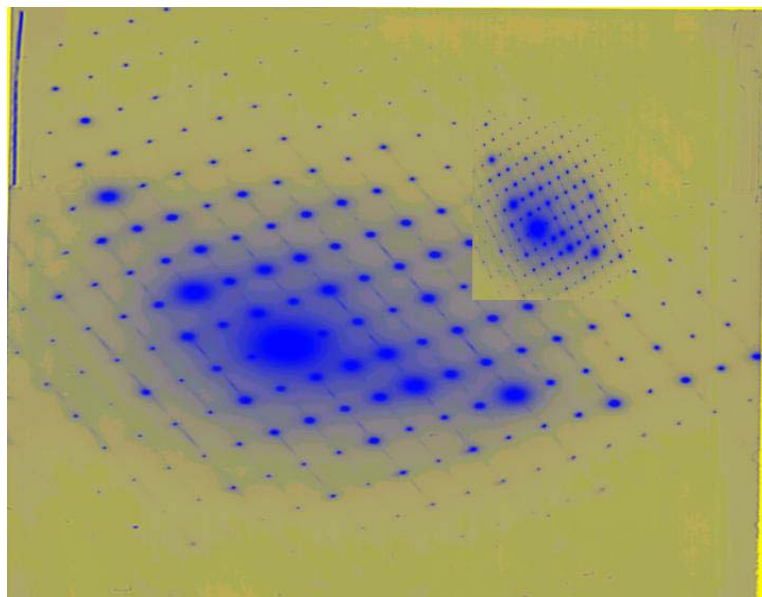


Structural phase transitions in synthetic analogues
of the titanite structure type

INAUGURAL – DISSERTATION

Zur
Erlangung der Doktorwürde
Der
Naturwissenschaftlich-Mathematischen Gesamtfakultät
der
Ruprecht-Karls-Universität
Heidelberg



Vorgelegt von

M.Sc. Geologist Rikke Ellemann-Olesen
Aus: Kalundborg, Dänemark
Tag der mündlichen Prüfung 18/2-05

Structural phase transitions in synthetic analogues
of the titanite structure type

Gutachter,

Prof. Dr. Ronald Miletich
Universität Heidelberg
Mineralogisches Institut
Im Neuenheimer Feld 236
69120 Heidelberg

Prof. Dr. U. Bismayer
Universität Hamburg
Mineralogisch-Petrographisches Institut
Grindelallee 48
20146 Hamburg

Table of contents

Summary.....	<i>i</i>
Zusammenfassung.....	<i>ii</i>
Preface.....	<i>iii</i>
Acknowledgements.....	<i>iii</i>
1. Introduction.....	1
1.1 Titanite and related phases.....	3
1.2 Spontaneous strain.....	13
1.3 Phase transitions and Landau theory.....	20
1.4 Coupling between the spontaneous strain and the order parameter.....	23
1.5 X-ray powder diffraction.....	28
1.6 Profile fitting of powder diffraction patterns.....	35
1.7 Transmission electron microscopy.....	42
1.8 Single crystal diffraction measurement.....	49
2. Samples.....	57
3. High temperature X-ray diffraction study of the solid solution $\text{CaTiO}(\text{Ge}_x\text{Si}_{1-x})\text{O}_4$	59
4. The structure of SrTiOGeO_4 and its solid solution with CaTiOGeO_4	95
5. Temperature- and composition dependence of the phase transitions in $\text{Ca}(\text{Ti}_x\text{Zr}_{1-x})\text{OGeO}_4$	127
6. Concluding remarks.....	153
7. References.....	158
8. Erklärung.....	167

Summary

The aim of the work presented here is to contribute to the understanding of the driving forces behind displacive phase transitions in transition metal oxides. Towards this aim, synthetic derivatives of the mineral titanite, CaTiOSiO_4 , are used as model compounds. The study is focusing on the occurrence of displacive phase transitions in compounds with the 2:4:4 cation charge combination: SrTiOGeO_4 , CaTiOGeO_4 , CaZrOGeO_4 and the binary solid solutions $\text{CaTiO}(\text{Ge}_x\text{Si}_{1-x})\text{O}_4$, $(\text{Ca}_x\text{Sr}_{1-x})\text{TiOGeO}_4$ and $\text{Ca}(\text{Ti}_x\text{Zr}_{1-x})\text{OGeO}_4$. All experiments have been performed on synthetic materials obtained by solid state synthesis from the respective oxides. In the case of the end-member composition CaTiOGeO_4 single crystals have been grown from the melt.

As the phase transitions encountered in these compounds are of a displacive nature and therefore non-quenchable their observation requires *in situ* measurements at elevated temperatures. This applies to electron microscopy as well as to X-ray diffraction. In the case of CaTiOGeO_4 , single crystals have been studied in order to examine the distribution and temperature dependence of diffuse scattering associated with the displacive phase transitions in this material. X-ray powder diffraction measurements at ambient and at elevated temperatures have been used to characterize the temperature evolution of the crystal lattices in the solid solutions as well as in the endmembers.

The observed structural phase transitions occur both as a function of temperature and of composition and are identified based on the determination of spontaneous strain. CaTiOGeO_4 and SrTiOGeO_4 behave in analogy to the well known $\text{P2}_1/a - \text{A2}/a$ transition observed in titanite, CaTiOSiO_4 . While the transition temperature across $(\text{Ca}_x\text{Sr}_{1-x})\text{TiOGeO}_4$ stays constant near $T_c = 590$ K, it increases linearly from $T_c = 487$ K in titanite, to $T_c = 588$ K in CaTiOGeO_4 . Phase transitions across the solid solution $\text{Ca}(\text{Ti}_x\text{Zr}_{1-x})\text{OGeO}_4$ additionally occur as a function of composition. The transition $\text{P2}_1/a - \text{A2}/a$ is not observable above ambient temperature in samples with extrapolated Zr concentration in excess of 18 %. The aristotype structure of titanite (space group symmetry $\text{A2}/a$) is observed for intermediate compounds. CaZrOGeO_4 and compounds with high Zr content exhibit a distorted titanite structure of space group symmetry $\text{A}\bar{1}$. This triclinic form transforms to the monoclinic titanite aristotype structure at elevated temperature and with increasing Ti content. The critical temperature is

488 K for the Zr-endmember and the critical composition at ambient temperature is at about 30% Ti-concentration.

Zusammenfassung

Ziel der vorgestellten Arbeit ist es, einen Beitrag zum Verständnis der Antriebskräfte displaziver Phasenumwandlungen in Übergangsmetalloxiden zu leisten. Dazu werden synthetische Derivate des Minerals Titanit, CaTiOSiO_4 , als Modellsubstanzen herangezogen. Die Studie konzentriert sich auf das Auftreten displaziver Phasenumwandlungen in Verbindungen mit 2:4:4 Kationenladungsverhältnis: SrTiOGeO_4 , CaTiOGeO_4 , CaZrOGeO_4 , sowie die binären Mischkristallreihen $\text{CaTiO}(\text{Ge}_x\text{Si}_{1-x})\text{O}_4$, $(\text{Ca}_x\text{Sr}_{1-x})\text{TiOGeO}_4$ und $\text{Ca}(\text{Ti}_x\text{Zr}_{1-x})\text{OGeO}_4$. Die dargestellten Experimente wurden an synthetischen Proben durchgeführt, die über die Festkörpersynthese aus den entsprechenden Oxiden gewonnen wurden. Für das Endglied CaTiOGeO_4 konnten Einkristalle aus der Schmelze gezüchtet werden.

Weil ausnahmslos displazive Phasenumwandlungen untersucht werden, so dass keine abgeschreckten Proben erhältlich sind, sind zu ihrer Beobachtung in-situ Messungen bei erhöhten Temperaturen erforderlich. Dies gilt sowohl für die durchgeführten Röntgenbeugungsmessungen als auch für die elektronenmikroskopischen Untersuchungen. Im Falle der Verbindung CaTiOGeO_4 wurde die Verteilung und die Temperaturabhängigkeit diffuser Streuung im Zusammenhang mit der displaziven Phasenumwandlung an Einkristallproben untersucht. Pulverdiffraktometrische Röntgenbeugungsmessungen bei Raumtemperatur und bei erhöhten Temperaturen dienen zur Beobachtung der Änderung der Gitterparameter als Funktion der Temperatur in den Endgliedern und den Mischkristallreihen. Strukturelle Phasenumwandlungen werden sowohl als Funktion der Temperatur, als auch als Funktion der Zusammensetzung beobachtet und über die auftretende spontane Gitterverzerrung identifiziert. CaTiOGeO_4 und SrTiOGeO_4 ähneln dabei in ihrem Verhalten dem Titanit (CaTiOSiO_4) und seiner bekannten $P2_1/a - A2/a$ Umwandlung. Während die entsprechende Umwandlungstemperatur in der Reihe $(\text{Ca}_x\text{Sr}_{1-x})\text{TiOGeO}_4$ nahezu konstant bei $T_c = 590$ K liegt, steigt die kritische Temperatur linear von $T_c = 487$ K im Titanit auf $T_c = 588$ K im CaTiOGeO_4 an. Phasenumwandlungen in $\text{Ca}(\text{Ti}_x\text{Zr}_{1-x})\text{OGeO}_4$ erfolgen zusätzlich in Abhängigkeit von der Zusammensetzung. Hier ist die Umwandlung $P2_1/a - A2/a$ in Proben mit einem extrapolierten Zr-Gehalt von 18% oberhalb Raumtemperatur nicht mehr zu beobachten. Die Struktur des Titanit-Aristotyps (Raumgruppensymmetrie $A2/a$) ist für den intermediären Bereich der Mischkristallreihe zu beobachten. CaZrOGeO_4 und Verbindungen

mit hohem Zr-Gehalt zeigen dagegen eine verzerrte Titanit-Struktur der Raumgruppe $A\bar{1}$. Diese triklin Form transformiert sowohl bei erhöhten Temperaturen als auch bei steigendem Ti-Gehalt zurück in den monoklinen Titanit-Aristotyp. Die kritische Temperatur beträgt 488 K für das Zr-Endglied und die kritische Zusammensetzung ist bei ca. 30% Ti-Gehalt erreicht.

Preface

This thesis is written as an accumulative thesis composed of a comprehensive introductory chapter that enlarge on the applied methods and examine the subjects employed in the following chapters. Three submitted scientific papers constitute the succeeding chapters.

Chapter 1 therefore gives a brief overview of the widespread studies on titanite presented in the literature with emphasis on structure and phase transitions as a function of temperature and pressure. Furthermore the stability of the titanite framework with respect to substitution on the different crystallographic sites will be discussed, as various studies comprise the ability of the titanite structure to obtain larger cations. A thorough examination of the types of phase transformations occurring in the studied solid solutions is given along with the fundamental concept of spontaneous strain. The remaining part of the chapter concerns the methods used with emphasis on the elementary theory as well as factors influencing the sampling of data. The methods described are X-ray powder diffraction, single crystal X-ray diffraction and transmission electron microscopy. Chapter 3, 4 and 5 are scientific manuscripts. The papers give a thorough and detailed examination of each of the three studied solid solutions $\text{CaTiO}(\text{Ge}_x\text{Si}_{1-x})\text{O}_4$, $(\text{Ca}_x\text{Sr}_{1-x})\text{TiOGeO}_4$ and $\text{Ca}(\text{Ti}_x\text{Zr}_{1-x})\text{OGeO}_4$, which form the basis of this Phd project. A final chapter gives a summary of the main conclusions to be drawn from the presented work.

I certify that I am first author to the manuscripts and that the results presented are exclusively based on my own research and results. Dr. Thomas Malcherek is in the manuscripts listed as second author due to his role as supervisor.

And I certify that the work presented in this thesis is my own and that work performed by others is appropriately cited.

Acknowledgements

Firstly, thanks to Dr. Thomas Malcherek for his patience, guidance and advice throughout my PhD research. First at Westfälische-Wilhelms-Universität Münster and last during my final year at Ruprecht-Karls-Universität Heidelberg. I am deeply grateful. For his willingness in the first place to accept me as his PhD student I will forever be thankful. Likewise the support of Prof. Dr. Ronald Miletich has been invaluable over the duration of my stay at the Mineralogische Institut in Heidelberg. Thanks for making my stay possible.

A thank to Ilse Glass at Mineralogische Institut, Heidelberg and to Angelika Breit at Institut für Mineralogie, Münster for helping me out and getting me started in the X-ray lab.

I am also very grateful for the financial support through the Deutsche Forschungsgemeinschaft (DFG).

Thanks also to Athanasios Godelitsas, Ingo Sethmann and Josema Astilleros for being such great friends and support, for our numerous nights out, coffee breaks at 3 o'clock, for simply just being my very trusted and good friends at the Institut für Mineralogie in Münster.

A special and great thank to my parents and to my sisters, Mette and Sisse for always being there and for supporting my plan to do my PhD research in Germany. For all their visits and phone calls – they were indispensable. Thanks.

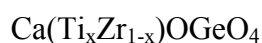
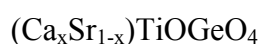
Last, but by no means least, a special mention of my boyfriend Villy who have provided the love and support required for such a work as this to be completed.

Thank you to everyone for all the help, support and encouragement.

1. Introduction

The PhD project is concerned with displacive phase transformations in transition metal oxides and with synthetic titanite-type structures in particular. The titanite structure has attracted substantial interest because of its phase transitions, its occurrence as a metamict mineral (Hawthorne *et al.*, 1991) and its crystal chemical relation to the non-linear optical material KTiOPO_4 (KTP) (Kunz *et al.*, 2000). Titanite is a common accessory rock-forming mineral and is found in a variety of metamorphic and igneous rocks (Xirouchakis and Lindsley, 1998; Xirouchakis *et al.*, 2001ab). In addition, because of the ability of titanite to retain certain radionuclides (*e.g.* uranium, thorium and radium), titanite based ceramics and glass-ceramics have been proposed as hosts for nuclear fuel waste (Hayward and Cechetto, 1982; Gascoyne, 1986). Thus knowledge of the physical and chemical properties of the endmember titanite and solid solutions having the titanite structure can help us to better understand the potential of this material in basic and applied research. The aim therefore is to use the titanite structure as a model structure for displacive phase transitions in transition metal oxides in general, in order to explore the driving forces behind such transitions.

The titanite structure type can accommodate a wide range of different chemical compositions: $\text{A}^{2+}\text{M}^{4+}\text{OX}^{4+}\text{O}_4$ (*e.g.* titanite; CaTiOSiO_4 and malayaite; CaSnOSiO_4), $\text{A}^{2+}\text{M}^{5+}\text{OX}^{3+}\text{O}_4$ (CaTaOAlO_4), $\text{A}^{+}\text{M}^{5+}\text{OX}^{4+}\text{O}_4$ (*e.g.* NaTaOGeO_4 , LiTaOSiO_4) (Higgins and Ribbe, 1976; Speer and Gibbs, 1976; Groat *et al.*, 1996; Malcherek, 2002; Malcherek *et al.*, 2004). The present study is focusing on the occurrence of displacive phase transitions in compounds with the 2:4:4 cation charge combination. Apart from titanite and malayaite so far three such titanite-compounds, SrTiOGeO_4 , CaTiOGeO_4 and CaZrOGeO_4 are known to be stable. The three compounds form the basis of the research project along with the solid solutions they form. In the light of the below listed individual solid solutions the project will offer interesting insights into the structural evolution of compounds having the titanite structure as the effects of substitution on different crystallographic sites.



No literature regarding the above solid solutions has been published. The research presented here will therefore add an important information on compounds with the titanite structure, especially because most work presented in the literature concern endmember compositions and are not including possible solid solutions. Exceptions are the subsolidus relations of the CaTiOSiO_4 - CaSnOSiO_4 join that show complete solid solution at 700°C (Kunz *et al.*, 1997) and the structural changes in titanite along the join TiO-AlF (Troitzsch *et al.*, 1999). Finally, Angel *et al.*, 1999b examined the effect of isovalent Si,Ti substitution on the bulk moduli of $\text{Ca}(\text{Ti}_{1-x}\text{Si}_x)\text{SiO}_5$ titanites.

The structures of the examined solid solutions are topologically identical to that of titanite. Titanite is formed by parallel chains of corner-sharing $[\text{TiO}_6]$ -octahedra running along the *a*-direction. The parallel strings of tilted octahedra are interconnected by $[\text{SiO}_4]$ -tetrahedra sharing corners with the $[\text{TiO}_6]$ -octahedra and by calcium ions in sevenfold coordination. An interesting aspect of this structure type evolves from the off centre distortion of Ti atoms in the titanite low-temperature structure. The off centring of the octahedrally coordinated cation occurs during changes in temperature, composition and pressure. Minerals where off centring plays an important role are perovskites and hollandite (Salje, 1989 and Cheary, 1986).

The detailed and systematic investigation of a series of compounds along the individual solid solutions will as a result offer insights into the structural evolution of a framework structure in response to chemical substitution on a single site within the framework, complementing previous detailed studies on the antiferroelectric to paraelectric $P2_1/a - A2/a$ phase transition of titanite. The research will focus on the various solid solutions in order to track the behaviour of structural phase transitions as a function of composition and temperature in these compounds. The results enable to analyse the crystal chemical driving forces behind the observable structural instabilities. As the phase transitions encountered in these compounds are of a displacive nature and therefore non-quenchable their observation requires *in-situ* measurements at elevated temperatures. This applies to electron microscopy as well as to X-ray diffraction.

In the case of the endmember composition CaTiOGeO_4 , single crystals will be studied in order to examine the spatial distribution and temperature dependence of diffuse scattering in this compound, to correlate these properties with the occurrence of displacive phase transitions and with microstructures generated by them, and to point out similarities or differences to the known behaviour of titanite, CaTiOSiO_4 . Diffuse scattering effects and antiphase domains textures in CaTiOGeO_4 have been investigated by electron diffraction and

X-ray radiation at variable temperature. In addition the study is based on powder diffraction at ambient and at elevated temperatures that has been used to characterize the solid solutions. The synthesis of the compounds studied forms another important part of the work. All experiments are performed on synthetic materials. This involves the growth and structure analysis and composition analysis of single crystals in the case of the end-member composition CaTiOGeO_4 . In order to study the behaviour of the solid solutions, powder samples with several compositions along the different joins have been synthesized by solid state reaction.

1.1 Titanite and related phases

Titanite is a common accessory mineral, probably the most common titanium-bearing mineral besides rutile and ilmenite, in igneous, metamorphic and sedimentary rocks. Interest in its stability and crystal chemistry has been virtually constant among geologists and materials scientists since the late 1920s. (*e.g.* Zachariassen, 1930, De Vries *et al.*, 1955; Robbins, 1968; Hayward *et al.*, 1990). Several studies have demonstrated its significance in petrology and in the glass/ceramics industry (Hunt and Kerrick, 1977; Hayward and Cechetto, 1982).

The structural framework of titanite is formed by parallel chains of corner-sharing $[\text{TiO}_6]$ -octahedra running along the a -direction (Fig. 1.1). The octahedra are twisted in such a way that the equatorial O atoms do not overlap when projected parallel to the chain axis. These parallel strings of octahedra are interconnected by $[\text{SiO}_4]$ -tetrahedra sharing corners with the $[\text{TiO}_6]$ -octahedra and by calcium ions in sevenfold coordination (Speer and Gibbs 1976; Taylor and Brown, 1976). The tilted octahedra in the chain share a common oxygen atom designated O1. A common feature of titanites containing d_0 transition metal cations is the distinctive distortion of the $[\text{TiO}_6]$ -octahedra as the Ti atoms are displaced from the geometrical centres of the octahedra, resulting in alternating long and short Ti-O1 bonds (Ribbe, 1982). The distortion is caused by an electronic second order Jahn-Teller effect and thus occurs around most octahedrally coordinated d_0 transition metals (Kunz and Brown, 1994). In titanite these distortion vectors are parallel within a $[\text{TiO}_6]$ chain, but correlate in an antiferroelectric way between adjacent chains. This antiferrodistortive interaction between adjacent $[\text{TiO}_6]$ chains in titanite cancels the locally induced hyperpolarizabilities and therefore inhibits any interesting non-linear optical effects (Kunz *et al.*, 2000). The $[\text{TiO}_6]$

chains are cross-linked by silicate tetrahedra sharing the remaining four oxygens (3-coordinated O2A and O2B and four coordinated O3A and O3B). The $[\text{SiO}_4]$ -tetrahedra share oxygen atoms with four separate $[\text{TiO}_6]$ -octahedral groups in three separate chains. The oxygen atoms O3A and O3B belong to the same chain while O2A and O2B are shared by two chains. Figure 1.1 displays the titanite structure showing the kinked chain of $[\text{TiO}_6]$ -octahedra cross linked by isolated $[\text{SiO}_4]$ -tetrahedra.

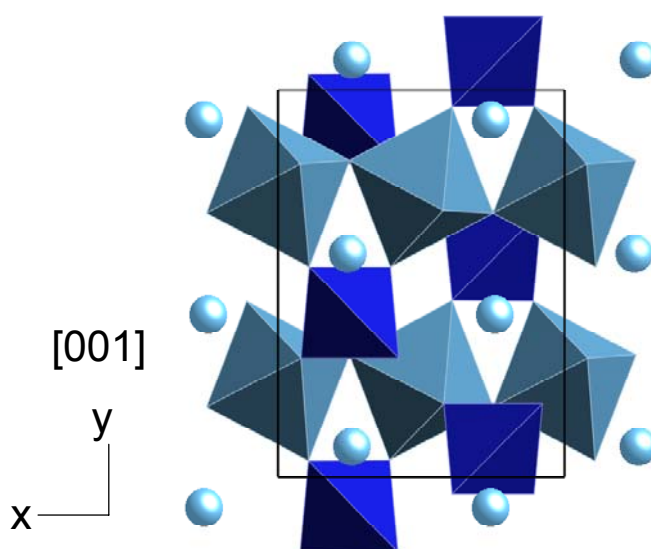


Fig. 1.1 The titanite structure viewed down the z -axis.

Robbins, 1968 was the first to synthesize titanite by crystallizing melts of high-purity oxides in an iridium wire loop in a platinum crucible. Examination of these substances by the X-ray precession method showed that synthetic titanite crystallized in space group $P2_1/a$ instead of $A2/a$, the presumed space group for natural titanite. Robbins, 1968 postulated that the synthetic titanite crystals might contain “two symmetrically inequivalent formula units” related by face centering translation, and that if a disorder amounting to a random succession of the two types of units were introduced the resulting average structure would be face-centered. Contrary Mongiorgi and Di Sanseverino, 1968 refined natural titanites in space group $A2/a$, which is legitimate for most (impure) natural titanites. Speer and Gibbs, 1976 revisited the crystal structure of synthetic titanite. From precession X-ray photographs they determined the crystal structure to have SG-symmetry $P2_1/a$ in agreement with the earlier results of Robbins, 1968. Furthermore Speer and Gibbs, 1976 examined the diffuse reflections ($k + l = \text{odd}$) exhibited by certain natural specimens. They suggest that natural titanites consist

of numerous domains of $P2_1/a$ titanite related by a half turn parallel to the b -axis. This would bring all atoms into coincidence except the titanium atoms due to their off centring. The additions of a half turn to the $P2_1/a$ space group would give the apparent $A2/a$ space group of natural titanites. Their refinement therefore indicated that the primary difference between the primitive synthetic material and the A -centered titanites is the position of the titanium atom in the $[\text{TiO}_6]$ -octahedron.

At a temperature of about 487 K, titanite undergoes a phase transition associated with a characteristic displacement of the titanium atom from the centre of the $[\text{TiO}_6]$ -octahedron (Ghose *et al.*, 1991; Bismayer *et al.*, 1992). Above the transition temperature the space group is A -centered $A2/a$ ($C2/c$) whereas below, the space group is primitive, $P2_1/a$ ($P2_1/c$) (Taylor and Brown, 1976; Ghose *et al.*, 1991). The ordered low temperature phase is characterized by alternating short and long Ti-O bonds along $[100]$, with reversed sense of Ti displacement among adjacent octahedral chains. In the macroscopically disordered form ($A2/a$), Ti is nominally found at the centre of the $[\text{TiO}_6]$ -octahedra. The transition is accompanied by the disappearance of superlattice diffraction maxima with $k + l = 2n + 1$. It is believed that the phase transition at 487 K involves merely a 2-dimensional loss of long-range coherence between the off-centre dipoles, while the structure remains ordered with respect to the Ti-displacement along individual octahedral chains (Malcherek, 1999).

On the basis of high temperature X-ray diffraction studies, Taylor and Brown, 1976 clarified the basic microscopic mechanism of the phase transition in titanite in terms of the Ti-displacements from the centre of the $[\text{TiO}_6]$ -octahedra in the low temperature phase. However they could not distinguish between two possible models for the high temperature phase, namely a single configuration with Ti strictly at the centre of the octahedron *vs.* an average of two configurations with small Ti-displacements parallel and antiparallel to the a -axis. Ghose *et al.*, 1991 similarly determined Ti-displacement as a function of temperature, which they took as the primary order parameter driving the phase transition. They found that the Ti-displacement is small but non-zero above the critical temperature. Furthermore they observed a strong hysteresis effect, where T_c decreased 50 K to 445 K after heating and cooling through the first cycle. However, on further heating and cooling, the hysteresis effect disappeared and super structure reflections ($k + l = \text{odd}$) showed diffuse residual intensities above T_c .

Zhang *et al.*, 1997 reported the direct experimental observation of a structural anomaly near $T_i = 825$ K in synthetic and natural titanite samples by high temperature, hard mode spectroscopy. The question answered by Zhang *et al.*, 1997 is whether the structure observed

immediately above T_c is the correct paraphrase of titanite or, alternatively, whether this phase is an intermediate phase and the true high symmetry phase exists only at much higher temperatures. Previous studies suggest a second anomaly in titanite. First Bismayer *et al.*, 1992 and Meyer *et al.*, 1996 recorded non-zero excess birefringence at temperatures up to 850 K, which is compatible with the assumption that an intermediate phase exists. Second, Sajle *et al.*, 1993a observed that the excess intensities of the Raman signals decrease gradually at temperatures above 500 K with increasing temperature. These observations rule out the idea that the phase transition at $T_c = 487$ K occurs between a paraelectric high symmetry phase and its antiferroelectric low symmetry phase by a simple shift of Ti positions in the $[\text{TiO}_6]$ -octahedra. Zhang *et al.*, 1997 show that IR spectroscopy provides a sufficiently sensitive tool to detect the additional high temperature phase in titanite and suggested that true $A2/a$ symmetry is to be attained at a second phase anomaly around $T_i = 825$ K. Malcherek *et al.*, 1999, confirmed this observation as studies from high temperature X-ray diffraction single crystal experiments are in agreement with the observation of Zhang *et al.*, 1997. They observed a break in thermal expansion near 825 K, which correlates with an effective volume contraction of the Ti octahedron. No symmetry change is involved and the structural changes at this temperature amount to small changes in the interatomic distances and angles. Mainly a reorientation of the Ca-displacement vector and a slight tilting of the $[\text{TiO}_6]$ -octahedra occur (Zhang *et al.*, 1997; Malcherek *et al.*, 1999).

The well-described phase change at 487 K has also been observed at high pressure. Kunz *et al.*, 1996 described this pressure induced phase transition using powder diffraction collected with synchrotron radiation and found that the $P2_1/a - A2/a$ symmetry change occurs between 21 kbar and 69.5 kbar. The mechanism however is proposed to differ from the temperature induced phase transition. The high-pressure phase transition is a response to increasing overbonding of the Ti atoms, which forces individual Ti atoms to shift to the centre of the coordination octahedron unlike the apparently identical phase transition at high temperature, where the observed disappearance of the out of centre distortion is due to a loss of long range order between individual off centre dipoles. Thus the $A2/a$ high-pressure phase, unlike the $A2/a$ high-temperature phase, has both local and long range $A2/a$ symmetry.

To better understand the structural relationships between the pressure dependent phase transition and the two temperature driven phase changes at T_c and T_i , Kunz *et al.*, 2000 collected powder diffraction data at simultaneously high pressure and temperature. This does not only provide more structural information but also yields further thermodynamic

constraints on the intermediate phase between 500 K and 825 K. With these data it is possible to relate the $A2/a$ high-pressure phase at $P > 3.5$ GPa (room temperature) to the $A2/a$ high temperature phase observed above 825 K (room pressure). Kunz *et al.*, 2000 found that the phase boundary extrapolates to around 3.5 GPa at room temperature, consistent with previous experiments at 300 K (Angel *et al.*, 1999a; Kunz *et al.*, 1996). Extrapolating the phase boundary linearly to ambient pressure yields a temperature of about 880 K. As a result Kunz *et al.*, 2000 suggested that the high-pressure $A2/a$ phase corresponds to the high symmetry phase above 825 K rather than to the disordered intermediate $A2/a$ phase between 487 K and 825 K. This result confirms the crystal chemical interpretation of the high-pressure structure as the structure is characterized by a truly symmetric Ti-coordination rather than by a disorder of the out of centre distortion vector (Kunz *et al.*, 1996). The structural analysis based on Rietveld refinements reveals that the polymerized $[\text{CaO}_7]$ -polyhedra dominantly affect the structural response to changing pressure and temperature. The $[\text{TiO}_6]$ -octahedra rotate almost rigidly in response to the compression of the $[\text{CaO}_7]$ -polyhedra. The $[\text{SiO}_4]$ -tetrahedra show a strong angular distortion with only little change in bond lengths.

Based on single crystal XRD data Ghose *et al.*, 1991 measured the spontaneous strain generated by the 487 K transition. In order to extend the strain measurements towards the isosymmetric transition at $T_i = 825$ K and to improve the accuracy of the derived strain tensor Malcherek, 2001 applied the spontaneous strain analysis to titanite. Lattice constants of synthetic titanite powder between room temperature and 1023 K were determined using high temperature X-ray powder diffraction. Only the e_{11} and e_{13} strain components contribute significantly to the strain tensor in the $A2/a$ setting associated with the antiferroelectric – paraelectric phase transition at $T_c = 487$ K. Indications for the additional occurrence of an isosymmetric anomaly at $T_i = 825$ K is observed as the strain component e_{13} does not disappear at T_c but remains finite up to T_i . Hence this shearing characterizes the intermediate phase. Malcherek, 2001 found that the volume strain occurring below T_c correlates with the tricritical character of the phase transition, while the microscopic properties above T_c are likely to be dominated by the pseudo-spin behaviour of the linearly correlated Ti displacements within individual chains.

Silicates and oxides are quite extraordinary in their ability to incorporate many different elements and, at the same time, in having extremely large pressure and temperature stabilities. Titanite is no exception. Substitution and the resulting structural effects have shown to be an intriguing feature of the titanite structure (*e.g.* Higgins and Ribbe, 1976; Angel *et al.*, 1999b;

Malcherek and Bosenick, 2004). The titanite structure type therefore has been extensively studied as a function of temperature and pressure as the ability of the structure to incorporate different atoms (Oberti *et al.*, 1991; Kunz *et al.*, 1997; Knoche *et al.*, 1998).

The chemical substitutions of primary importance in natural titanites are $(\text{Al}, \text{Fe})^{3+} + (\text{F}, \text{OH})^{-} \leftrightarrow \text{Ti}^{4+} + \text{O}^{2-}$, where total Al + Fe is not greater than 30 mol% and Al generally dominates. From quantitative microprobe analyses of the major elements in natural titanites, powder diffraction and X-ray precession methods, Higgins and Ribbe, 1976 discussed how substitution of Al + Fe for Ti in natural specimens influences the symmetry. Natural specimens with less than 3-4 mol% substitution of Fe and Al for Ti have the space group $P2_1/a$ whereas those with more than 4 mol % (Al + Fe) have diffuse reflections $k + l$ odd, which become unobservable above 20 mol% substitution as the average structure approaches $A2/a$ symmetry (Higgins and Ribbe, 1976, Oberti *et al.*, 1991).

Higgins and Ribbe, 1976 solved the structure of the Sn-analogue of titanite known as malayaite, CaSnOSiO_4 in space group $A2/a$. Investigations of malayaite at high temperatures using synchrotron radiation, HRTEM, X-ray powder diffraction and Raman spectroscopy by Groat *et al.*, 1996 revealed a structural anomaly at 500 K, but no deviations from $A2/a$ symmetry were observed, nor any antiphase domains boundaries indicative of reduced symmetry. Most probably the transition in malayaite is similar to the isosymmetric transition at T_i in titanite. Kunz *et al.*, 1997, studied the solid solution between malayaite and titanite in detail. The refinements at room temperature reveal a high sensitivity of the crystal symmetry on the amount of octahedral Sn present. To distinguish between the $P2_1/a$ and the $A2/a$ structures the disappearance of the $k + l = \text{odd}$ reflections characteristic for the $P2_1/a$ space group was used. The measurements were carried out using synchrotron X-radiation and TEM. The series of experiments reveal that already at a Sn concentration of 10 % no $k + l = \text{odd}$ reflections can be observed anymore, thus the addition of 10 % Sn apparently destabilises the ordered $P2_1/a$ phase.

Angel *et al.*, 1996 discovered the titanite structured phase CaSiSiO_5 and showed, based on high-pressure single crystal diffraction, that CaSi_2O_5 is the first example of a displacive transition between the monoclinic and triclinic phases of CaSi_2O_5 involving a coordination change of Si to be observed directly. This material contains fourfold -, fivefold -, and sixfold-coordinated silicon and thus is distinctly different from the triclinic high-pressure phase of malayaite even though its structure type is very similar to the aristotype of malayaite. This

relationship is confirmed by a high-pressure phase transition from triclinic to monoclinic CaSi_2O_5 where the $A2/a$ structure of malayaite is adopted (Angel, 1997).

An important mechanism for phase transitions in the silicates of the Earth's mantle is the change of the coordination of Si by oxygen from four (tetrahedral) to six (octahedral) with increasing pressure. A mechanism for the development of mixed coordination phases is the continuous substitution of Si for other octahedral cations in silicates containing SiO_4 tetrahedra. In the light of the discovery of the titanite structured phase of $\text{CaSi}^{\text{VI}}\text{OSi}^{\text{IV}}\text{O}_4$ (Angel, 1997) and the wide stability field in pressure and temperature of titanite, Knoche *et al.*, 1998 suggested the possibility of a solid solution between the two endmembers titanite and $\text{CaSi}^{\text{VI}}\text{OSi}^{\text{IV}}\text{O}_4$ in which mixed-coordination of Si would evolve as a result of isovalent substitution of Si for Ti. Knoche *et al.*, 1998 examined the phase relations of the $\text{CaTiSiO}_5 - \text{CaSi}_2\text{O}_5$ solid solution and characterized the structural state using a combination of synthesis and reversal experiments in a piston cylinder and a multi-anvil press. The results show that at sufficiently high pressures (8.5 GPa) and temperatures (1350°C) a complete solid solution exists between titanite and CaSi_2O_5 , based upon the exchange of Si for Ti in the octahedral site. This substitution appears to occur without ordering of the octahedral cations and the continuous nature of the solid solution allows the amount of octahedral silicon in the titanite structure to increase continuously with increasing pressure. It is suggested that already by 10 mol% substitution of $\text{Si}^{[6]}$ for Ti is sufficient to completely suppress the long range ordering of the displacements of the Ti cations, the same level as required when Sn is substituted for Ti in malayaite (Kunz *et al.*, 1997). Because the ionic radius of $\text{Si}^{[4]}$ is smaller than Ti, whereas Sn is larger (Shannon, 1976), these results imply that, as originally suggested by Higgins and Ribbe, 1976, the suppression of the $A2/a$ to $P2_1/a$ transition is purely a dilution effect rather than a steric one.

A large number of compounds of general composition AMOXO_4 crystallize with the topology of the titanite structure. Examples are MnSi_2O_5 (Arlt *et al.*, 1998) and CaAlFSiO_4 (Troitzsch and Ellis, 1999). Titanite and the Sn analogue, malayaite are of the type $\text{A}^{2+}\text{M}^{4+}\text{OX}^{4+}\text{O}_4$. Mill *et al.*, 1990 first described one of these compounds LiTaOGeO_4 of the type $\text{A}^+\text{M}^{5+}\text{OX}^{4+}\text{O}_4$. As part of a larger investigation into phase transitions in compounds of the titanite structure type, Malcherek, 2002 determined the low temperature phase of LiTaOGeO_4 and its transition to the disordered $C2/c$ structure. The structure of LiTaOGeO_4 has been refined using X-ray diffraction data collected at room temperature and at 173 K. The low temperature phase is

isostructural with LiTaOSiO_4 (Genkina and Mill, 1992). The transition from the ordered $\text{P2}_1/c$ to the disordered $\text{C2}/c$ structure occurs at $T_c = 231$ K. The low-temperature structure is characterized by the off centre displacement of Ta and an ordered Li configuration. For $T > T_c$ the Li atom flips back and forth between two equivalent tetrahedral positions on a curved pathway.

An example of a compound of the type $\text{A}^{2+}\text{M}^{5+}\text{OX}^{3+}\text{O}_4$ is CaTaOAlO_4 . This compound was reported to be isotypic with the monoclinic structure of the titanite paraphrase with space group symmetry $\text{C2}/c$ (Sales *et al.*, 1999). Malcherek *et al.*, 2004 from Rietveld analysis and based on X-ray powder diffraction and density functional methods in combination with ^{27}Al MAS NMR found that a structural phase transition occurs near room temperature but the diffraction data does not indicate deviation from monoclinic symmetry $\text{C2}/c$. The low-temperature phase is characterized by two distinct Ta environments, distinguished by their nearest neighbour Ca coordination. Compared to the low-temperature structure of titanite the structure of CaTaOAlO_4 is distinguished by the absence of the characteristic off centre displacement of the transition metal cation.

Angel *et al.*, 1996 discovered the titanite structured phase CaSi_2O_5 and showed, based on high-pressure single crystal diffraction, that CaSi_2O_5 is the first example of a displacive transition between the monoclinic and triclinic phases of CaSi_2O_5 involving a coordination change of Si to be observed directly. This material contains fourfold -, fivefold -, and sixfold-coordinated silicon and thus is distinctly different from the triclinic high-pressure phase of malayaite even though its structure type is very similar to the aristotype of malayaite. This relationship is confirmed by a high-pressure phase transition from triclinic to monoclinic CaSi_2O_5 where the $\text{A2}/a$ structure of malayaite is adopted (Angel, 1997).

Compounds exhibiting the typical titanite structure type do not need to have space group symmetry $\text{P2}_1/a$ at low temperatures in analogy with titanite, but can exhibit a triclinically distorted titanite structure. Rath *et al.*, 2003 carried out a single crystal high-pressure diffraction study that showed that monoclinic malayaite (CaSnOSiO_4) transforms into a triclinic high-pressure polymorph, SG-symmetry $\text{A}\bar{1}$ at $P_c = 4.95(1)$ GPa. The monoclinic to triclinic phase transition reveals itself by significant deviations of the α - and γ -angles from 90° . No discontinuity was observed in the pressure dependence of axes and volume. The phase transition was shown to be fully reversible. Structural refinements at four different pressures reveal the structural details of the monoclinic $\text{A2}/a$ and triclinic $\text{A}\bar{1}$ phases. Below

and at the transition temperature the $[\text{SiO}_4]$ -polyhedra show some non-rigid distortion and angular twisting. The SnO_6 chains shift parallel to $[-101]$, inducing a reduction in symmetry above the transition temperature. The structural differences between the triclinic and monoclinic phases are most clearly recognized when looking at cation – cation distances. In the monoclinic structure the $[\text{SnO}_6]$ -octahedra form linear chains parallel to $[100]$. Above the phase transition the distance between adjacent SnO_6 chains is compressed more strongly to $[011]$ than parallel to $[01-1]$, violating both the twofold screw axis and the glide plane. As a consequence, the Sn site splits into two symmetrically distinct sites occupying alternate positions along the octahedral chains. Along with the asymmetric relative shift of the $[\text{SnO}_6]$ -octahedra the chain linking SiO_4 is twisted. Rath *et al.*, 2003 found that the distortion of the $\text{SnO}_6 - \text{SiO}_4$ framework also affects the coordination of the Ca atom. The CaO_7 -polyhedra move closer together. This brings an eighth O atom, which is part of the neighbouring CaO_7 -polyhedra, into the coordination sphere of the Ca atom. Hence the originally linear CaO_7 chains change into CaO_8 sheets parallel to (-111) in the triclinic phase.

The montebrasite-amblygonite series $\text{Li}[\text{Al}(\text{PO}_4)\text{OH}]-\text{Li}[\text{Al}(\text{PO}_4)\text{F}]$ reported by Groat *et al.*, 1990, is topologically identical to the malayaite structure at high-pressure (Rath *et al.*, 2003). These are the only known naturally occurring minerals with a triclinically distorted titanite structure. Groat *et al.*, 1990 reported them as triclinic $C\bar{1}$. As in triclinic malayaite the distances between the octahedral chains are different in different directions. These differences become more pronounced with increasing OH-content. This seems to indicate that chemically imposed structural strain has a similar effect on this structure as pressure induced strain in malayaite.

The structure of CaGe_2O_5 is of the titanite aristotype in its high temperature phase (Aust *et al.*, 1976; Malcherek and Bosenick, 2004). In CaGe_2O_5 a continuous phase transition from triclinic $C\bar{1}$ to monoclinic $C2/c$ symmetry at $T_c^* = 714 \pm 3$ K is observed (Malcherek and Bosenick, 2004). The transition is accompanied by a weak heat capacity anomaly. The strain analysis based on measured lattice constants implies a classical second order phase transition, where the order parameter as measured by the strain component e_{23} is associated with the displacement of the Ca cation.

The displacive phase transitions occurring in the studied solid solutions are characterized by primary bonds, which are not broken but merely distorted due to changes in temperature and composition. Therefore a clear structural relationship exists between the high-temperature

form, which is usually more open and has higher symmetry than the low-temperature form. A tendency for disorder exists at high temperatures, giving way to order at low temperatures. Contrary to reconstructive transitions displacive transitions only involve small changes in energy and are usually fast and unquenchable. However, they provide a range of phenomena relevant to understanding the response of a mineral structure to changes in temperature and pressure, and to development of domain structures in minerals. Most importantly, displacive phase transitions may interact with other aspects of the structure, such as the distribution of cations and their state of order (Nord, 1992).

Structural phase transitions are the result of changes in crystal structure. Phase transitions are grouped according to the type of symmetry reduction where the only criterion is a group-subgroup relationship (Nord, 1992). According to Ghose *et al.*, 1991 the reduction of symmetry operations from the high symmetry phase ($A2/a$) to the low symmetry phase ($P2_1/a$) in titanite involves a loss of the centering translational symmetry $[0, \frac{1}{2}, \frac{1}{2}]$. The size of the unit cell remains the same. The subgroup $P2_1/a$ therefore results from lost symmetry elements of the $A2/a$ space group, which is mainly related to the position of the Ti atoms. In $A2/a$ the Ti position in the centre of the octahedron is fixed by symmetry, whereas in $P2_1/a$ the Ti atoms are displaced off centre in the octahedron closer to one of the apical oxygens (O1). The titanium displacements in adjacent octahedral chains are parallel and antiparallel to the a -axis, thus giving rise to an antiferroelectric arrangement of the polarization vectors in $P2_1/a$ (Taylor and Brown, 1976). In the low-temperature phase the Ca-displacements are also essentially off centre along the octahedral chain at low temperatures as the Ti-atoms. The nearest Ca and Ti atoms are displaced in the same sense. The Ca-displacements therefore are coupled linearly to the Ti-displacements. As in the case of Ti-displacements, the Ca-displacements related by the A -centering are equal and opposite each other. The Ca-displacements are considerably smaller than the Ti-displacements (Ghose *et al.*, 1991).

Microscopically, phase transitions are driven by the creation of order. Since the change in symmetry from $A2/a - P2_1/a$ is a non-ferroic transition and the transition is characterized as a zone boundary transition no strain components can serve as the primary order parameter (Ghose *et al.*, 1991). In titanite the Ti-displacements are taken as the primary order parameter since they are the largest displacements observed experimentally.

1.2 The spontaneous strain

To detail the character and mechanism of the phase transitions occurring in the studied solid solutions the spontaneous strain analysis has been applied and compared. One of the most significant physical effects that accompany structural phase transitions is spontaneous strain (Aizu, 1970). It arises because crystal structures almost invariably undergo some distortion or lattice relaxation on a macroscopic scale as a consequence of cooperative changes that occur on a microscopic scale. The strain is additional to the background effects of thermal expansion and must be separated from the normal response of a crystal to changing temperature or pressure. Originally the concept of spontaneous strain was only applied to ferroelastic transitions (Aizu, 1970; Newnham, 1974). However it has been found useful to expand this definition to all structural phase transitions, which involve a variation of the shape of the crystallographic unit cell in particular for co-elastic materials. In co-elastic transitions both the high- and low-symmetry phases may belong to the same crystal system and yet still display large lattice relaxations (Carpenter *et al.*, 1998).

Spontaneous strain consists of up to six independent components forming a symmetric second rank tensor and is subject to the constraints of symmetry. The magnitudes of its components are hence not uniquely definable because they depend on the crystallographic setting. For any given setting the tensor components can be determined directly from the measured lattice parameters of the low symmetry phase. Any spontaneous strain must conform to Neumann's principle according to which the symmetry elements of any physical property of a crystal must include all the symmetry elements of the point group of the crystal (Nye, 1985). In order to evaluate the spontaneous strain the lattice parameters of the high symmetry phase are extrapolated into the temperature regime of the low symmetry phase. The extrapolation represents that part of the deformation of the unit cell, which is not related to the structural phase transition and therefore does not contribute to the excess spontaneous strain. The numerical values of the spontaneous strain are now defined by the strain tensor, which relates the low symmetry unit cell to the high symmetry unit cell when extrapolated to the same temperature. By constructing the spontaneous strain the total thermal expansion of the crystal is reduced to that part which is true excess quantity, *i.e.*, the excess quantity defines the spontaneous strain and the thermal expansion is completely removed. The non-relevant background thermal expansion has been absorbed in the

baseline. Given that strains as little as 1 ‰ can be detected in lattice parameter data collected using quite routine diffraction techniques, strain measurements can provide particularly valuable and detailed insights into the nature and mechanisms of most phase transitions (Salje, 1993).

The principles of strain analysis have been widely applied to phase transitions in minerals and related compounds. Examples include anorthite (Redfern and Salje, 1987; Redfern *et al.*, 1988), quartz (Hatch and Ghose, 1991), perovskites (*e.g.* Carpenter *et al.*, 2001), $\text{Pb}_3(\text{PO}_4)_2$ (Salje *et al.*, 1993b), lawsonite (Carpenter *et al.*, 2003) and others.

Malcherek, 2001 and Ghose *et al.*, 1991 both described the spontaneous strain in synthetic titanite. Using high-temperature X-ray powder diffraction data Malcherek, 2001 determined the spontaneous strain associated with the antiferroelectric-paraelectric phase transition at $T_c = 487$ K. The strain associated with the phase transition is relatively small. Only the e_{11} and e_{13} spontaneous strain components contribute significantly to the strain tensor. The e_{11} component is related to the Ti- and Ca-displacements parallel and anti-parallel to the a -axis and the relative inflexibility of the structure along this direction. The e_{13} component is finite at temperatures above T_c and it vanishes only at $T_i = 825$ K. The disappearance of this shear strain marks the isosymmetric transition near 825 K. The shearing therefore characterizes the intermediate phase. The e_{22} is zero within the limits of the measurement accuracy and e_{33} is very small and negative for $T < T_c$. The temperature evolution of the squared order parameters correlates with the spontaneous strain e_{11} . Similar agreement is seen in the volume strain that is associated with the transition at $T_c = 487$ K.

Figure 1.2 illustrates the definition of strain. According to Carpenter *et al.*, 1998 the linear strain will be defined as $\Delta l/l$ when a length l , of some material is changed by a small amount Δl . In Figure 1.2 two linear tensile strains define the lattice distortion. First $(a-a_0)/a_0$ parallel to the x -axis and second $(b-b_0)/b_0$ parallel to the y -axis, where a and b are the lattice parameters after deformation and a_0 and b_0 are the lattice parameters prior to deformation. When negative it implies contraction while when positive it implies elongation. Second when the distortion is defined by a shear through the angle θ , the shear strain is defined as $\tan \theta$ but can, according to Figure 1.2, be rewritten as $(b-b_0)/\cos \gamma$. These definitions are extended to three dimensions. From a fixed coordinate system a single set of equations can be used to determine the spontaneous strain from measured lattice constants for phase transitions involving any change of symmetry.

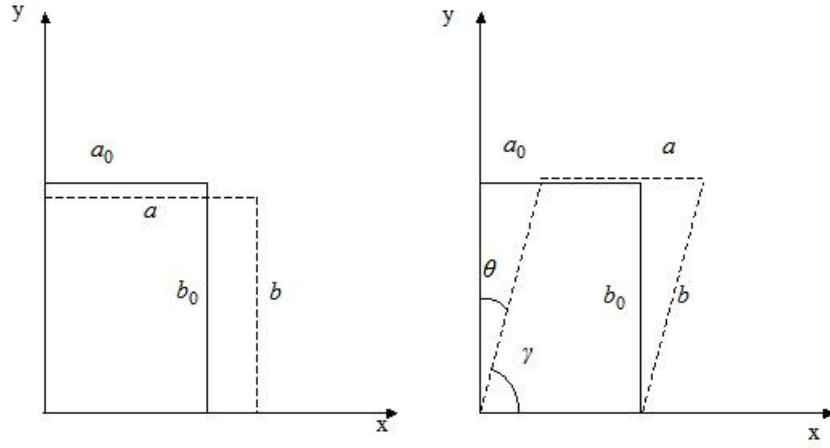


Fig. 1.2 Illustration of the geometry of shear. After Carpenter *et al.*, 1998.

To define the general equations an underlying Cartesian coordinate system, with axes X , Y and Z is selected, such that Y is parallel to the crystallographic y -axis, Z is parallel to the normal to the (001) plane, *i.e.* parallel to c^* . X is perpendicular to both. Therefore the strain component e_{11} is a tensile strain parallel to X , e_{22} is a tensile strain parallel to Y etc. Based on the coordinate system presented and according to Carpenter *et al.*, 1998 the general equations give the components of the spontaneous strain tensor as

$$e_1 = e_{11} = \frac{a \sin \gamma}{a_0 \sin \gamma_0} - 1 \quad (1)$$

$$e_2 = e_{22} = \frac{b}{b_0} - 1 \quad (2)$$

$$e_3 = e_{33} = \frac{c \sin \alpha \sin \beta^*}{c_0 \sin \alpha_0 \sin \beta_0^*} - 1 \quad (3)$$

$$\frac{1}{2} e_4 = e_{23} = \frac{1}{2} \left[\frac{c \cos \alpha}{c_0 \sin \alpha_0 \sin \beta_0^*} - \frac{b \cos \alpha_0}{b_0 \sin \alpha_0 \sin \beta_0^*} + \frac{\cos \beta_0^*}{\sin \beta_0^* \sin \gamma_0} \left(\frac{a \cos \gamma}{a_0} - \frac{b \cos \gamma_0}{b_0} \right) \right] \quad (4)$$

$$\frac{1}{2} e_5 = e_{13} = \frac{1}{2} \left(\frac{a \sin \gamma \cos \beta_0^*}{a_0 \sin \gamma_0 \sin \beta_0^*} - \frac{c \sin \alpha \cos \beta^*}{c_0 \sin \alpha_0 \sin \beta_0^*} \right) \quad (5)$$

$$\frac{1}{2}e_6 = e_{12} = \frac{1}{2} \left(\frac{a \cos \gamma}{a_0 \sin \gamma_0} - \frac{b \cos \gamma_0}{b_0 \cos \gamma_0} \right) \quad (6)$$

If the high-symmetry phase is monoclinic and the low symmetry phase is triclinic equations (1) – (6) simplify to

$$e_{11} = \frac{a}{a_0} \sin \gamma - 1 \quad (7)$$

$$e_{23} = \frac{1}{2} \left(\frac{c \cos \alpha}{c_0 \sin \beta_0^*} + \frac{a \cos \beta_0^* \cos \gamma}{a_0 \sin \beta_0^*} \right) \quad (10)$$

$$e_{22} = \frac{b}{b_0} - 1 \quad (8)$$

$$e_{13} = \frac{1}{2} \left(\frac{a \sin \gamma \cos \beta_0^*}{a_0 \sin \beta_0^*} - \frac{c \sin \alpha \cos \beta^*}{c_0 \sin \beta_0^*} \right) \quad (11)$$

$$e_{33} = \frac{c \sin \alpha \sin \beta^*}{c_0 \sin \beta_0^*} - 1 \quad (9)$$

$$e_{12} = \frac{1}{2} \left(\frac{a}{a_0} \cos \gamma \right) \quad (12)$$

$\alpha_0 = \gamma_0 = 90^\circ$ and β^* is the reciprocal lattice angle and given by

$$\cos \beta^* = \frac{\cos \gamma \cos \alpha - \cos \beta}{\sin \gamma \sin \alpha} \quad (13)$$

In the above equations a , b , c , α , β^* and γ refer to the low symmetry form at a given temperature (and pressure), and a_0 , b_0 , c_0 , α_0 , β_0^* and γ_0 are the cell parameters that the high symmetry form would possess at the same temperature (and pressure) had the transition not taken place. The spontaneous strain components e_{12} and e_{23} are symmetry breaking components for a monoclinic to triclinic transition, while the other components are non-symmetry breaking. Equations (7) to (12) are applicable to strain analysis of monoclinic-triclinic transitions observed in $\text{Ca}(\text{Ti}_x\text{Zr}_{1-x})\text{OGeO}_4$. In the remaining compounds studied both the high- and low-symmetry forms are monoclinic, $\alpha = \gamma = 90^\circ$ and $\beta^* = 180 - \beta$ and the strain components become

$$e_{11} = \frac{a}{a_0} - 1 \quad (14)$$

$$e_{13} = \frac{1}{2} \left(\frac{c \cos \beta}{c_0 \sin \beta_0} - \frac{a \cos \beta_0}{a_0 \sin \beta_0} \right) \quad (16)$$

$$e_{33} = \frac{c \sin \beta}{c_0 \sin \beta_0} - 1 \quad (15)$$

$$e_{22} = \frac{b}{b_0} - 1 \quad (17)$$

$$e_{23} = 0$$

(18)

$$e_{12} = 0$$

(19)

A symmetry breaking strain is a strain, which transforms as any irreducible representation of the point group of the high-symmetry phase, other than the identity representation. Also the symmetry breaking strain is a shearing deformation, which by symmetry cannot include a change in molar volume contrary to the non-symmetry breaking spontaneous strain paragraph. The spontaneous strain associated with the triclinic to monoclinic phase transition in the titanite structure is relatively large and is dominated by the symmetry breaking strain components e_{12} and e_{23} (Malcherek and Bosenick, 2004; Malcherek and Ellemann-Olesen, 2004). This is in agreement with the triclinic compounds across $\text{Ca}(\text{Ti}_x\text{Zr}_{1-x})\text{OGeO}_4$, where the strain components e_{12} and e_{23} are an order of magnitude larger than the non-symmetry breaking strains. However increasing Ti content across $\text{Ca}(\text{Ti}_x\text{Zr}_{1-x})\text{OGeO}_4$ leads to a decrease in symmetry breaking spontaneous strain. The spontaneous strain due to the $\text{P2}_1/a - \text{A2}/a$ phase transition in compounds across the solid solutions $\text{CaTiO}(\text{Ge}_x\text{Si}_{1-x})\text{O}_4$ and $(\text{Ca}_x\text{Sr}_{1-x})\text{TiOGeO}_4$ and in monoclinic compounds across $\text{Ca}(\text{Ti}_x\text{Zr}_{1-x})\text{OGeO}_4$ is relatively small and is dominated by the components e_{11} and e_{13} . This behaviour is in perfect analogy with the behaviour of titanite (Malcherek, 2001). The evolution of strain in the compound CaTaOAlO_4 , which is topologically similar to the titanite structure (Malcherek *et al.*, 2004), is identical to the observed spontaneous strain in the here studied compounds. The non-symmetry breaking strain is nearly identical to CaZrOGeO_4 , while there is no symmetry breaking strain, because there is no triclinic distortion associated with the phase transition in CaTaOAlO_4 . In analogy to titanite CaTaOAlO_4 is characterized by a monoclinic – monoclinic phase transition. However the behaviour of the non-symmetry breaking strain components is nearly identical to the triclinic – monoclinic transition in compounds belonging to the $\text{Ca}(\text{Ti}_x\text{Zr}_{1-x})\text{OGeO}_4$ solid solution. It is convenient for a comparison of the degree of spontaneous lattice distortion due to phase transitions in different materials to define a total (scalar) spontaneous strain. In the following Aizu's definition of scalar strain is used (Aizu 1970).

$$e_s = \left(\sum e_{ij}^2 \right)^{1/2} \quad (20)$$

The magnitude of e_s represents a measure of the spontaneous strain.

Error estimation in the strain analysis

In calculation the uncertainties related to the strain analysis the Gaussian error propagation law has been applied (Muscat, 2000). The method allows a propagation of the uncertainties on the data through the calculation of the strain components. To estimate the errors involved in the strain calculations the error propagation analysis was employed based on the equations for spontaneous strain given by Carpenter *et al.*, 1998. First step is to calculate the error of the individual line fits of the thermal expansion calculated for each lattice constant. Second the actually error on each of the individual spontaneous strain components are estimated.

It is presumed that the errors involved in the calculated strain components are of the same order of magnitude irrespective of composition. As a result the calculations were carried out only for one compound, $\text{CaTiO}(\text{Ge}_{70}\text{Si}_{30})\text{O}_4$ and transferred to the remaining compounds.

The equations used are:

$$\sigma(e_{11}) = \sqrt{a_0^{-2} \sigma^2(a) + a^2 a_0^{-4} \sigma^2(a_0)} \quad (21)$$

$$\sigma(e_{22}) = \sqrt{b_0^{-2} \sigma^2(b) + b^2 b_0^{-4} \sigma^2(b_0)} \quad (22)$$

For e_{33} the variance is

$$\sigma^2(e_{33}) = \frac{\sin^2 \beta}{c_0^2 \sin^2 \beta_0} \sigma^2(c) + \frac{c^2 \cos^2 \beta}{c_0^2 \sin^2 \beta_0} \sigma^2(\beta) + \frac{-c^2 \sin^2 \beta}{c_0^4 \sin^4 \beta_0} c_0^2 \cos^2 \beta_0 \sigma^2(\beta_0) + \frac{-c^2 \sin^2 \beta}{c_0^4 \sin^2 \beta_0} \sigma^2(c_0) \quad (23)$$

and the error

$$\sigma(e_{33}) = \sqrt{\sigma^2(e_{33})} \quad (24)$$

For e_{13} the variance is

$$\sigma^2(e_{13}) = \frac{\partial^2 e_{13}}{\partial a} \sigma^2(a) + \frac{\partial^2 e_{13}}{\partial a_0} \sigma^2(a_0) + \frac{\partial^2 e_{13}}{\partial c} \sigma^2(c) + \frac{\partial^2 e_{13}}{\partial c_0} \sigma^2(c_0) + \frac{\partial^2 e_{13}}{\partial \beta} \sigma^2(\beta) + \frac{\partial^2 e_{13}}{\partial \beta_0} \sigma^2(\beta_0)$$

(25)

and the error is then the square root of the variance

$$\sigma(e_{13}) = \sqrt{\sigma^2(e_{13})} \quad (26)$$

The error of the scalar strain

$$\sigma(\varepsilon_s) = \sqrt{(2e_{11})^2 \sigma^2(e_{11}) + (2e_{22})^2 \sigma^2(e_{22}) + (2e_{33})^2 \sigma^2(e_{33}) + (4e_{13})^2 \sigma^2(e_{13})} \quad (27)$$

The calculations have been carried out for all temperatures and are displayed in Figure 1.3.

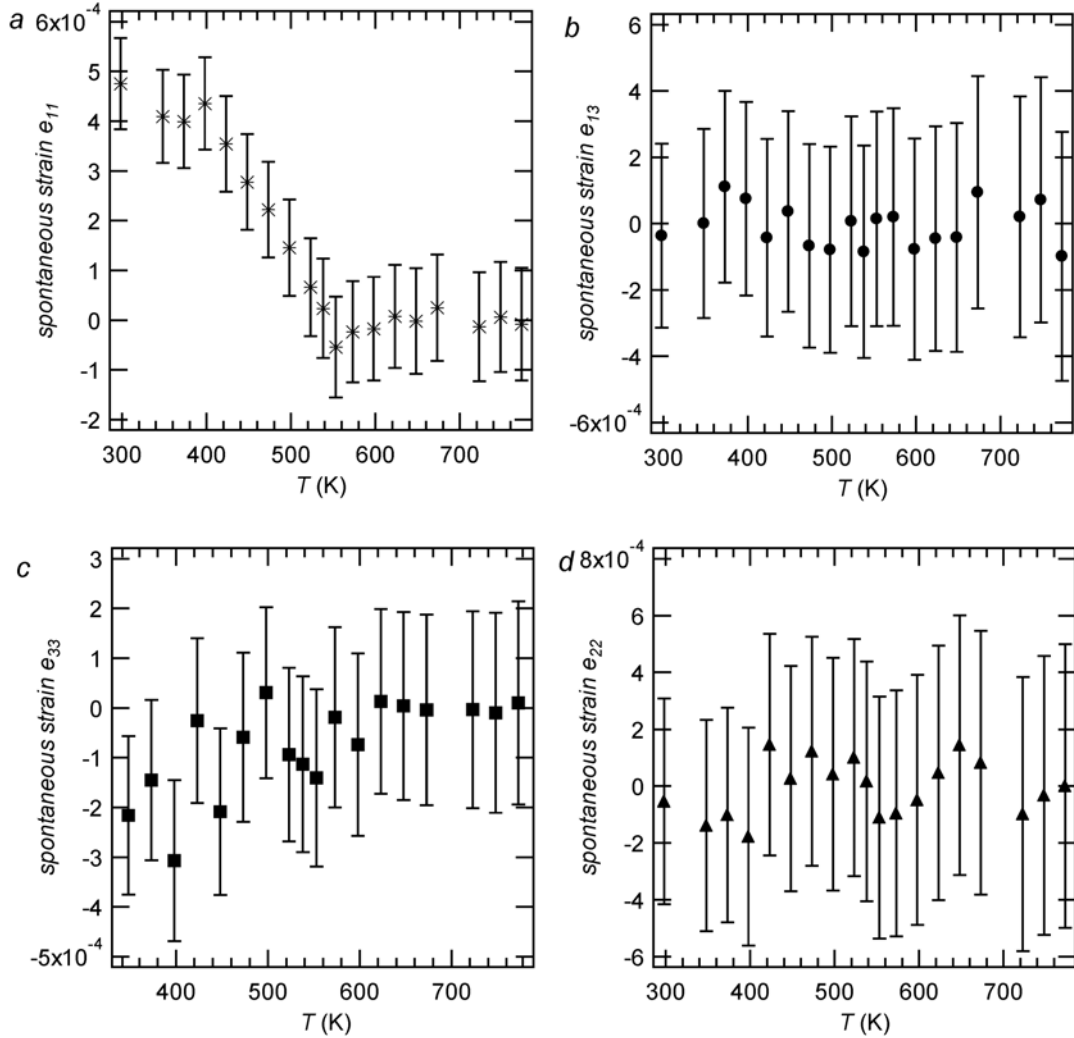


Fig. 1.3 $\text{CaTiO}(\text{Ge}_{70}\text{Si}_{30})\text{O}_4$. The spontaneous strain components and the estimated errors applied.

1.3 Phase transitions and Landau theory

One of the important criteria describing the symmetry change in a phase transition is whether the transition changes the translational symmetry of the crystal structure. If there is no change in translational symmetry of the lattice and the unit cell merely changes its shape, no extra spots will appear in the reciprocal lattice. Transitions of this type are termed zone centre transitions. If there is a change in the reciprocal due to changes in the translational symmetry (*e.g.* change in the lattice type), the boundaries of the Brillouin zone will be affected and new reciprocal lattice points may appear there. The volume of the first Brillouin zone is the deciding factor. This type of transition is termed zone boundary transition (Salje, 1993). The first Brillouin zone defines the short wavelength limits of all wave vectors in the crystal and is the smallest volume of reciprocal space entirely enclosed by planes that are perpendicular bisectors of the reciprocal lattice vectors drawn from the origin (Putnis, 1992). The first Brillouin zone is identical with the Wigner-Seitz Cell of the reciprocal lattice. Both types of transitions are present in the studied materials. Triclinic compounds across the solid solution $\text{Ca}(\text{Ti}_x\text{Zr}_{1-x})\text{OGeO}_4$ exhibit a zone centre transition, while all remaining compounds display a zone boundary transition in analogy with titanite (Ghose *et al.*, 1991; Bismayer *et al.*, 1992). For thermodynamic purposes, the extent of transformation is usually specified in terms of an order parameter Q , which is scaled to vary between zero in the high symmetry phase and unity in the fully transformed low symmetry phase at 0 K. The spontaneous strain often provides an indirect measure of this order parameter, and the interaction between e_s and Q is denoted as strain/order parameter coupling. Apart from being coupled to the order parameter, the spontaneous strain can act as the order parameter itself in certain types of structural phase transitions.

In the case of a zone centre transition the spontaneous strain is proportional to the order parameter Q of the transition, whereas it is proportional to Q^2 in the case of a zone boundary transition as for titanite (Ghose *et al.*, 1991; Malcherek, 2001). This coupling between strain and order parameter has been extensively discussed and applied to various materials (Salje, 1993 and Carpenter *et al.*, 1998).

Landau theory describes the excess free energy of a phase transition about T_c as a function of the order parameter. Based on this free energy derivatives can be obtained, that then describe various

thermodynamic quantities, like the order parameter, entropy, heat capacity, etc. The purpose of Landau theory is to model the thermodynamics of a phase transition. Central to Landau theory is the concept of an order parameter, which describes the course of a phase transition *i.e.* the order parameter is related to the change in some macroscopic property through the phase transition and therefore describes the deviation of the low temperature phase from that of the high temperature phase. Formally for the transition to be continuous the symmetry of the low temperature form must be a subgroup of the high temperature form. It is this underlying symmetry relationship that allows the order parameter Q to be mathematically defined (Salje, 1993).

The following discussion is based on reviews by Salje, 1993; Carpenter and Salje, 1998; Carpenter *et al.*, 1998.

The excess free energy can be expressed in the form of a polynomial expansion of the order parameter Q . When odd-order terms are absent the excess free energy reduces to

$$G = \frac{1}{2}A(T - T_c)Q^2 + \frac{1}{4}BQ^4 + \frac{1}{6}CQ^6 + \dots \quad (28)$$

The odd order terms are neglected by assuming that the free energy is symmetrical about $Q = 0$, *i.e.* it is irrelevant whether Q is positive or negative. This is called a degenerate order parameter, because of the possible presence of two equivalent ordered states, for example realized in antiphase domains which are either ordered or anti-ordered.

The above expression allows the order parameter to change continuously between 0 and 1. However a discontinuity in Q is possible depending on the value of B . When B is negative, both A and C must be positive. The sixth order term is required to obtain a free energy minimum in the low temperature phase when $Q > 0$. This will lead to a discontinuity in Q with temperature and hence the transition is thermodynamically first order. When B is positive and the sixth order term is negligibly small, the expansion describes a thermodynamically second order phase transition. The final case is the special case when $B = 0$ and $C > 0$. This transition is called tricritical and represents the intermediate stage between continuous phase transitions ($B > 0$) and discontinuous

phase transitions ($B < 0$). By definition $Q = 1$ at $T = 0$. Therefore for a second order phase transition $\frac{A}{B} = \frac{1}{T_c}$ in equation (28) and Q can be written as

$$Q = [(T_c - T)/T_c]^{1/2} \quad (29)$$

for a tricritical phase transition this relationship becomes

$$Q = [(T_c - T)/T_c]^{1/4} \quad (30)$$

1.4 Coupling between the spontaneous strain and the order parameter

Materials, which undergo phase transitions can show large variations in their elastic properties and the influence of a transition can extend over a wide P , T range on either side of the transition point. Landau theory provides a basis for predicting the variations of elastic constants associated with phase transitions in minerals. One has to distinguish between zone centre and zone boundary transitions. Whether the critical point is at the zone centre or at the zone boundary is decided purely by symmetry. If the strain is the driving order parameter, as in proper ferroelastic materials, the transition has to be a zone centre transition, as the crystal class has to change. However, there may be other types of zone centre transitions, with other driving order parameters.

First, when the driving order parameter for the transition is a symmetry breaking spontaneous strain, the total excess energy for the transition is purely elastic and is given by

$$G_{elastic} = \frac{1}{2} \sum_{i,k} C_{ik} e_i e_k + \frac{1}{3!} \sum_{i,k,l} C_{ikl} e_i e_k e_l + \frac{1}{4!} \sum_{i,k,l,m} C_{iklm} e_i e_k e_l e_m + \dots \quad (31)$$

Equation (31) has the same form as a Landau expansion in which $G_{excess} = G_{elastic}$. The second-order elastic constant C_{ik} softens as a linear function of temperature with a slope in the low-symmetry phase that depends on the thermodynamic character of the transition. Thus strain is the driving order parameter and the material would be truly ferroelastic. In the limiting case of proper ferroelastic behaviour, individual elastic constants, or some symmetry-adapted combination of them, can become very small if not going to zero.

Second, if the driving order parameter, Q , is some structural feature other than strain, the excess energy is given by

$$G = \frac{1}{2} a(T - T_c) Q^2 + \frac{1}{4} b Q^4 + \sum_{i,m,n} \lambda_{i,m,n} e_i^m Q^n + \frac{1}{2} \sum_{i,k} C_{ik}^0 e_i e_k \quad (32)$$

Equation (32) describes a transition where a structural feature described by Q (bond weakening or a rotation of a polyhedron *etc.*) drives the phase transition. Strain only arises due to the coupling energies in the second term of equation (32) and is referred to as the quadratic coupling term. The order parameter couples with the elastic strain via a coupling energy that is linear in the strain and quadratic in the order parameter. The elastic energy contains only the bare (*i.e.* more or less constant) elastic constants. In contrast the C_{ik} 's in equation (31) vary strongly with temperature and some of them might approach zero values. The coefficients λ describes the coupling between Q and e and the last term describes the elastic energy, where C_{ik} are elastic constants in Voigt notation. a and b determine the Landau free energy in this example without coupling to the strain.

The effect of coupling, described by the term $\lambda e^m Q^n$, is to cause a great diversity of elastic variations depending on the values of m and n , the thermodynamic character of the transition and the magnitudes of any non-symmetry-breaking strains. The values of m and n cannot be deliberately chosen but are constrained by symmetry.

Therefore alternative patterns of elastic - constant variations emerge from the different transition mechanisms represented by equation (31) and (32).

Zone centre and zone boundary transitions are both present in the studied solid solutions. For a zone centre transition (*i.e.* no change in the translational symmetry of the lattice), it is generally assumed that the linear coupling term between the strain and the order parameter is sufficient ($e \propto Q$), and hence the quadratic coupling term in equation (33) is negligible. If a zone centre transition is allowed by symmetry, it follows that all higher order couplings are also symmetry allowed. No bilinear coupling can occur if the symmetry properties of Q and e are different.

The triclinic compounds within the solid solution $\text{Ca}(\text{Ti}_x\text{Zr}_{1-x})\text{OGeO}_4$ exhibit a zone centre transition. The triclinic distortion gives rises to symmetry breaking spontaneous strain components e_{12} and e_{23} in the low temperature phase. It is presumed that the symmetry-adapted spontaneous strain tensor is only required to contain the strain elements e_{12} and e_{23} (e_6 and e_4 in Voigt notation) in the standard crystallographic setting, giving $e_{23} \propto e_{12} \propto Q$ as the expected strain/order parameter relationship. A linear variation of e_{23}^2 is consistent with the expected $e_4^2 \propto Q^2 \propto T$ relationship. The symmetry-breaking strain component $e_4 = 2e_{23}$ is taken to be the driving order parameter with $e_6 = 2e_{12}$ as being linearly coupled to it.

Therefore for a transition with second-order character and with e_4 as the order parameter, the elastic energy can be written in the form of a Landau expansion ($G_{\text{excess}} = G_{\text{elastic}}$) as

$$G = \frac{1}{2}a(T - T_c)e_4^2 + \frac{1}{4}be_4^4 + \frac{1}{2}C_{66}^0e_6^2 + C_{46}^0e_4e_6 \quad (33)$$

In equilibrium there must be no residual stresses in the crystal, and therefore the free energy must be at a minimum with respect to the strain.

$$\frac{\partial G}{\partial e_6} = 0 = C_{66}^0e_6 + C_{46}^0e_4 \quad (34)$$

Solving for e_6 yields

$$e_6 = -\frac{C_{46}^0}{C_{66}^0}e_4 \quad (35)$$

Substituting for e_6 in equation (33) gives

$$G = \frac{1}{2}a(T - T_c)e_4^2 + \frac{1}{4}be_4^4 + \frac{1}{2}C_{66}^0\left(-\frac{C_{46}^0}{C_{66}^0}e_4\right)^2 + C_{46}^0e_4\left(-\frac{C_{46}^0}{C_{66}^0}e_4\right) \quad (34)$$

⇕

$$G = \frac{1}{2}a\left(T - T_c - \frac{C_{46}^0{}^2}{aC_{66}^0}\right)e_4^2 + \frac{1}{4}be_4^4 \quad (35)$$

⇕

$$G = \frac{1}{2}a(T - T_c^*)e_4^2 + \frac{1}{4}be_4^4 \quad (36)$$

where the renormalized critical temperature is given as

$$T_c^* = T_c + \frac{C_{46}^0{}^2}{aC_{66}^0} \quad (37)$$

Equation (37) is equivalent to the standard Landau polynomial for a second order phase transition. Thus the temperature evolution of the squared order parameter follows as

$$e_4^2 = (e_4^0)^2 \left(1 - \frac{T}{T_c^*} \right) \quad (38)$$

$(e_4^0)^2$ is the saturation value of the squared order parameter at low temperatures. The strain therefore has the effect of changing the transition temperature to a renormalized transition temperature T_c^* .

Malcherek and Bosenick, 2004 described this coupling between the order parameter and the spontaneous strain using CaGe_2O_5 and concluded that the same formalism may also be applied to CaZrOGeO_4 (Malcherek and Ellemann-Olesen, 2004). The order parameter can be measured by the strain component e_{23} and demonstrates a linearity of the square of the scalar strain $\sum e_{ij}^2$ with temperature. The formalism used to describe CaGe_2O_5 is such that the strain itself is taken as the driving order parameter with strain only coupled to it, but the data do not allow such distinction to be made. Therefore the model with strain as the order parameter was just the simplest model that fit the data. This is true also in the case of CaZrOGeO_4 .

When a transition does involve a change in the translational symmetry it is termed a zone boundary transition. Ghose *et al.*, 1991 presented an order parameter treatment of the transition in titanite with the Ti-displacement as the primary order parameter. In this case only the quadratic coupling term is affected. The order parameter couples with the elastic strain via a coupling energy that is linear in the strain and quadratic in the order parameter ($e \propto Q^2$). The critical point is the zone boundary point $(0-\frac{1}{2}\frac{1}{2})$ on the surface of the Brillouin zone of the high temperature phase. The volume of the Brillouin zone of the A -centered high-temperature phase is twice the volume of the low-temperature Brillouin zone. The geometrical relation of the Brillouin zones of both phases is shown in Figure 1.4.

During the breaking of the translational symmetry the critical Z-point of the high-temperature Brillouin zone transforms to the origin (Γ -point) of the low-temperature Brillouin zone.

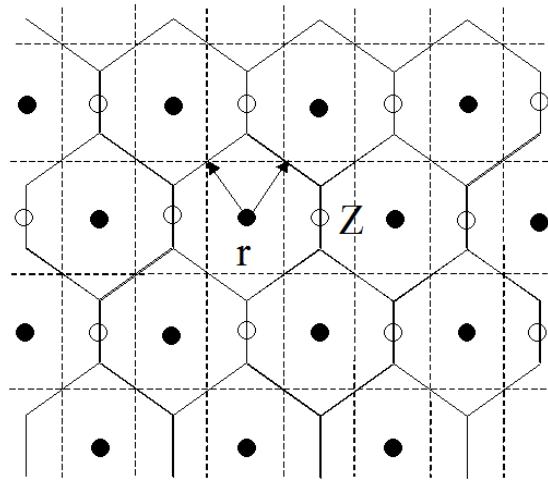


Fig. 1.4 First Brillouin zone and reciprocal lattice points on the $(0kl)$ plane. Full circles represent the $A2/a$ lattice with corresponding Brillouin zones indicated by the solid lines. Open circles show new reciprocal lattice points for the $P2_1/a$ structure with corresponding Brillouin zones as drawn by the broken lines (After Bismayer *et al.*, 1992).

Compounds along the solid solutions $(Ca_xSr_{1-x})TiOGeO_4$ and $CaTiO(Ge_xSi_{1-x})O_4$ exhibit a zone boundary transition as the symmetry changes from $P2_1/a$ to $A2/a$. This is true also for the monoclinic compounds across $Ca(Ti_xZr_{1-x})OGeO_4$.

1.5 X-ray powder diffraction

X-ray powder diffraction is a powerful tool for identification and characterization of minerals and other crystalline materials as well as crystal analysis. The application of the Rietveld refinement method (Rietveld, 1967; 1969), which at least in part circumvents the peak overlap problem, has yielded successful refinements for an increasing number of crystal structures using powder XRD data. The present work is based on powder diffraction both at ambient and elevated temperatures in order to characterize the studied solid solutions. Rietveld and LeBail methods for the analysis of lattice strain and structural studies have been extensively employed. The Rietveld method has been applied only for data collected under ambient conditions, while the LeBail method was used for all measurements at elevated temperatures in order to extract accurate lattice constants.

There are many ways of detecting and recording X-ray powder diffraction patterns, but the geometric set-up is the same in each case. The X-rays diverge from the tube and in order to only strike the specimen they are collimated and directed onto the sample using a divergence slit. When the diffraction angle θ is a correct Bragg angle for reflection for a particular set of (hkl) planes, reflections occur from all those crystals in the specimen, which are in the right orientation. A detector detects the X-ray signal. The function of the detector is to convert the individual X-ray photons into voltage pulses that are counted and/or integrated by the counting equipment, allowing visual indication of X-ray intensity to be obtained (Langford and Louër, 1996). The schematic set-up is displayed in Figure 1.5.

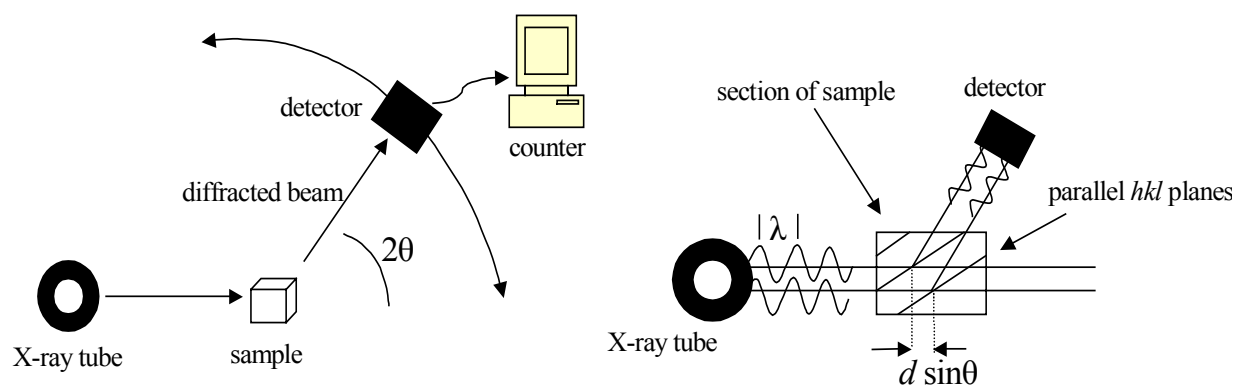


Fig. 1.5 Schematic representation of the X-ray powder method (After Gottstein, 2001).

The diffraction principle developed by Bragg is the most general and powerful diffraction theory (Fig. 1.6) (Ladd and Palmer, 1978; Putnis, 1992). The most common application of the Bragg equation is in the interpretation of X-ray diffraction patterns from powdered crystals. Bragg realized that X-rays scattered by all the lattice points in a plane (hkl) must be in phase for the Laue equations to be satisfied, and further, that scattering from successive (hkl) planes must also be be in phase. In other words, Bragg found that the diffraction pattern could be explained as if they were produced by reflection of X-rays from (hkl) planes, but only when the Bragg equation is satisfied. The condition for diffraction maxima is that

$$2d_{hkl} \sin \theta = n\lambda \quad (39)$$

The integer n refers to the order of the diffracted beam λ is the wavelength of the incident X-ray beam d is the distance between adjacent planes of atoms (the d -spacings) and θ is the angle of incidence of the X-ray beam.

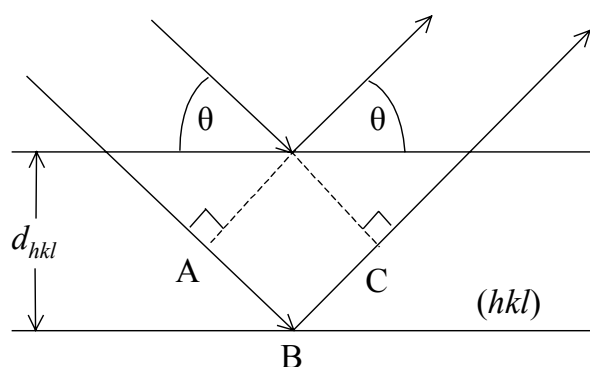


Fig. 1.6 The condition for Bragg reflection from planes hkl with spacing d_{hkl} (After Putnis, 1992).

Therefore by measuring the angles at which a specific characteristic X-ray wavelength λ is diffracted the interplanar spacing d can be related to the diffraction angle θ by the Bragg law (Reynolds, 1989). The characteristic set of d -spacings generated in a typical X-ray scan therefore provides a unique "fingerprint" of the mineral or minerals present in a sample. For each set of planes (hkl) in the sample there will be sufficient at a Bragg angle θ to satisfy the Bragg equation. In a random sample these planes will be present in every angular orientation around the incident beam axis (Giacovazzo, 1992; Jenkins, 1989a).

Each diffracted beam can be viewed as a wave with a characteristic amplitude and phase called the structure factor $F(hkl)$. The structure factor is derived by summing the waves

diffracted by each of the atoms in the unit cell for each hkl reflection. The general expression is given according to Langford and Louër, 1996

$$F_{hkl} = \sum_{r=1}^N f_r \exp 2\pi i(hx_r + ky_r + lz_r) \quad (40)$$

The structure factor for the set of planes concerned is thus obtained by summing the waves diffracted by each of the N atoms in the cell. Its amplitude is given by f_r , the scattering factor for the r th atom and its relative phase by the rest of the term in which x_r etc., are the fractional coordinates. The value of f_r depends on the scattering angle at which the reflection occurs (Langford and Louër, 1996).

A diffraction pattern is made up of diffraction peaks superimposed upon background. The desired peaks arise from diffraction of the assumed experimental wavelength. The background arises from coherent and incoherent scattering from the specimen, air scatter, and (especially at low values of 2θ) scatter from the sample support. That is, if the divergence slit is set too large and the sample support is irradiated as well. According to Reynolds, 1989 and Jenkins, 1989a essentially three types of information can be derived from powder diffraction patterns:

- a) Angular position depending on geometry and contents of unit cell.
- b) Intensities depending mainly on atom type, arrangement and particle orientation.
- c) Shape, depending on instrument broadening, particle dimension and strain.

The major sources of error encountered in powder diffractometer experiments are (Jenkins, 1989ab and Reynolds, 1989):

- a) Systematic errors in the experimental positions of the diffraction lines due to inherent aberrations, including axial divergence. The errors are angle dependent and are observed as an increasing relative error in d -spacing as the diffraction angle is decreased.
- b) Systematic errors in the experimental 2θ maxima due to displacement of the specimen surface from the goniometer-focusing circle and due to specimen transparency.

- c) Line profile shapes may be asymmetrically distorted at lower 2θ angles. The amount of distortion increases as the axial divergence of the collimator increase.
- d) The relative intensities are dependent on particle orientation.
- e) Intensities differ depending upon the selection of the divergence slit aperture.

For indexing purposes, the intensities of the peaks are irrelevant, but for identification or for structure analysis, accurate relative intensities are essential. There are three commonly ignored factors, which can severely affect the relative peak intensities: 1) sample thickness, 2) preferred orientation, and 3) divergence slit(s). However, for routine use of the powder diffractometer, probably the biggest source of experimental error is that due to the specimen preparation (Jenkins, 1989a; Gonzalez, 1987). The ideal specimen for X-ray powder diffraction analysis is completely homogeneous over the distance diameter of less than $10\ \mu\text{m}$, has constant particle size of between $1 - 10\ \mu\text{m}$, and shows no preferred orientation or strain. Ideally oriented specimens may be difficult to obtain in practice thus it is important to realize what problems are likely to arise if the specimen deviates from this ideal state. Problems encountered with coarse grain size include extinction, particle statistics and micro absorption. If crystals are finely ground so that a very large number of them are randomly oriented, then somewhere in the powder many crystal fragments are suitably aligned to produce diffraction peaks as the diffractometer detector scans over the appropriate angles of 2θ .

Bish and Reynolds, 1989 discuss the ideal powder sample. The X-ray powder diffraction method generally assumes that one has an infinitely thick powder sample. This means that the sample must be thick enough so that essentially all of the incident X-ray beam interacts with the sample and does not pass through it. Due to the variable angle of incidence of the X-ray beam in the sample, the minimum required thickness varies with diffraction angle. In addition the minimum thickness is dependent on packing density of the sample. Attention to sample packing is important because diffraction occurs from a volume of sample, not just the surface. Ideally in Bragg-Brentano geometry diffraction should stem only from the surface, as only this is located on the focusing circle, but due to sample transparency this condition may be violated. Loose sample packing can give rise to transparency effects in addition to those related intrinsically to the sample. The surface of the sample should be flat, with no roughness or curvature and not tilted in any direction. Any roughness or curvature has the potential to produce systematic deviations in the positions and breadths of observed reflections related to sample-height-displacement and flat specimen errors. Sample tilting should be avoided

because it changes the angular relationship between the receiving slit and the sample surface and can give rise to systematic errors in intensity and peak breadth (Bish and Reynolds, 1989). Preparation of the powder samples used in this study was carried out with care and was standardized to avoid large differences between individual samples and to achieve a satisfying sample packing and a finely ground sample with a smooth surface.

The function of the divergence slit is to limit the lateral divergence of the X-ray beam so that as much of the sample surface is irradiated as possible, but at the same time avoiding irradiation of the sample support (Langford and Louër, 1996; Jenkins, 1989a). At low angles, the X-ray beam is spread over a larger surface of the specimen than it is at high angles. To ensure that the X-rays interact only with the sample (and not the edges of the specimen holder) a slit is inserted between the X-ray source and the sample to confine the beam to the sample (divergence slit). In many laboratories, data are recorded using a relatively wide single slit that is appropriate for higher angle data, but not for the lower 2θ values. In such a measurement, the relative intensities of the low angle peaks will appear to be too low, because only a part of the X-ray beam interacts with the sample. The divergence slit on the Philips Xpert diffractometer used at the Institute of Mineralogy, Münster was constant.

Absorption is an error inherent in the crystal and affects the measured intensity (McKie and McKie, 1986). It arises when an X-ray beam travels through a sample. Its intensity decreases with the distance traveled through the substance. The fractional decrease in intensity I of an X-ray beam as it passes through a substance is proportional to the distance traversed by the beam, x

$$-\frac{\partial I}{I} = \mu dx \quad (41)$$

where μ is the linear absorption coefficient. This constant is dependent on the material properties, its density and the wavelength of x-rays. Integrating this equation gives

$$I_x = I_0 \exp(-\mu x) \quad (42)$$

where I_0 = intensity of incident beam, and I_x = intensity of transmitted beam after passing through distance x .

For specimens with high surface roughness, an angle-dependent decrease of the intensities is observed, which is caused by micro-absorption of the X-rays due to the microstructure of the

powder sample. Surface roughness can strongly reduce the intensity of Bragg reflections at low scattering angles and is caused by a gradient in the sample packing density as a function of depth. Samples with high absorption are more susceptible to surface roughness effects and if not corrected can yield negative temperature factors in the crystal structure results. In a Rietveld analysis, the thermal parameters are strongly influenced and correlated by this effect and may tend to negative values. Therefore the surface roughness can be one very important source to negative thermal parameters. Due to the occasional negative values of atom displacement parameters a surface roughness correction was therefore applied for Rietveld refinements at ambient temperatures. A normalized form of the function described by Pitschke *et al.*, 1993a has been used with success for refined samples with moderate surface roughness. Pitschke *et al.*, 1993b presented a model for surface roughness corrections and tests in Rietveld refinements. A significant sample displacement, s observed in all refinements (Fig. 1.7), is mainly caused by temperature expansion of the Al_2O_3 sample stage. The absolute value of this displacement is given by $S_v = -s\pi R/36000$, with the diffractometer radius $R = 230$ mm. The sample displacement exhibits a near linear behaviour as a function of temperature.

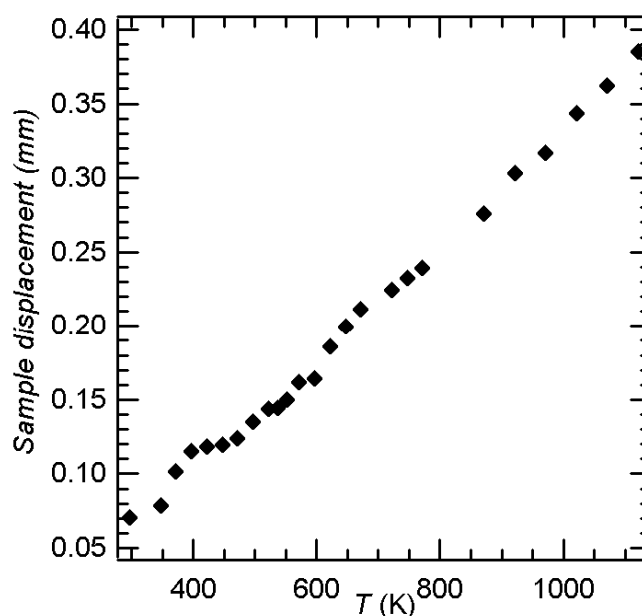


Fig. 1.7 Sample displacement of SrTiOGeO_4 as a function of annealing temperature.

Analysis of a crystal structure using the Rietveld profile technique requires a suitable description of the shape of the peaks. The functions used for peak asymmetry, however, are semi-empirical and take very little account of diffraction optics. Axial divergence of the

incident beam is a non-spectral contribution to the instrumental profile, depending on the instrumental arrangement and causes a substantial asymmetry in the profile, particularly at the lowest angles.

The intersection of the diffraction cone with the detector cylinder is an ellipse. The curvature is forms leads to a peak asymmetry, because intensity from the ends of the intercepted piece of the diffraction cone will intersect the detector slit on the side of the peak closer to the centre of the ellipse but not the other side.

The function most commonly used to correct for axial divergence is the empirical split-Pearson-VII function. This approach is successful for describing modest asymmetry but cannot explain the long low-angle tails for the case of significant asymmetry. Finger *et al.*, 1994 describe a more physical realistic model based on the a modification of the implementation of powder diffraction profile formulations devised by van Laar and Yelon, 1984. Finger *et al.*, 1994 extended the treatment of van Laar and Yelon, 1984 to the case where the sample length is larger than that of the detector slit. Their resulting profile function has been incorporated into the GSAS program.

Diffraction line broadening is a common feature in diffraction profiles. There are two categories of structural imperfections, which give rise to broadening of reflection profiles. In general, sample induced line broadening includes contributions, which are independent of d^* , known as size effects, and which depend on d^* , known as strain effects. Size effects can relate to a sub-domain structure or to the mean thickness of individual crystallites. The second category is based on the distortion of the crystal lattice, which amounts to a variation of d -spacing within domains. This can arise from microstrain, due to an applied or residual stress, or from a compositional gradient in the sample. It is not possible to distinguish between these effects from diffraction data, but the distinction is usually evident from the nature of the sample. An anisotropic apparent strain-like diffraction line broadening occurs in the studied solid solutions. Especially samples with mixed composition show a pronounced line broadening. Thompson *et al.*, 1987 expressed microstrain as a function of hkl . The hkl dependent nature of the strain broadening was modelled by means of ellipsoids and Fourier series and employed to represent line profiles. The number of microstructural parameters to be refined is restricted by adopting a Lorentzian function of size contributions and an intermediate Lorentz-Gauss function for strain broadening. The contribution a given reflection makes to the total profile intensity depends on the shape function for that reflection profile, its width coefficients and the displacement of the peak from the profile position.

1.6 Profile fitting of powder diffraction patterns

There are two approaches to the modelling of a complete diffraction pattern. In one, pattern decomposition, the superposition of analytical line profile functions and a suitable background model are fitted to the observed data and in the other, the Rietveld method, information on crystal structure is included. The Rietveld method employs the entire powder diffraction pattern, thereby overcoming the problem of peak overlap and allowing the maximum amount of information to be extracted from the pattern (Rietveld, 1967, 1969). In the Rietveld method, each data point (2θ step) is an observation, and during the refinement procedure, structural parameters (such as atom positions, temperature- and occupancy factors), background coefficients, and profile parameters are varied in a least-squares procedure until the calculated powder profile, based on the structure model best matches the observed pattern. One of the important strengths of the Rietveld method is the capability of refining precise and accurate unit cell parameters. However, a limitation of the Rietveld method is that one must start with a model that is a reasonable approximation of the actual structure.

Many applications of powder diffraction do not require knowledge of the crystal structure and in such case a diffraction pattern can be characterized adequately by pattern decomposition where the aim is to obtain quantities, which describe each individual Bragg reflection (LeBail *et al.*, 1988; Toraya, 1986). The LeBail method extracts structure factors from powder diffraction data by iterating full pattern profile fitting. The LeBail method involves only a rough estimate of the cell parameters, valid space group symmetry, background coefficients and an approximation of the peak shape profile, which are varied along with the lattice parameters. Therefore the LeBail method is an intensity extraction method employing an iterative fitting procedure. This is a rapid and efficient approach to total pattern decomposition by using space group constraints on Bragg reflection positions. It is based on a simple modification to the approximate procedure used by Rietveld, 1969 for the extraction of integrated intensities. The method can be described as extracting F_{obs} 's by iterating the Rietveld decomposition formula starting from a set of arbitrarily identical F 's. An arbitrary set of structure factors is used, as input to obtain an initial set of F_{obs} 's, while only the lattice and profile parameters are being refined. On subsequent least-squares cycles the set of F_{obs} 's extracted from one cycle are used as the F_{calc} 's for the next. The refinement is repeated until the best fit between observed and calculated patterns is achieved. In this way a set of F_{obs}

magnitudes can be obtained even in the absence of a structural model (Langford and Louër, 1996).

In the presented work lattice parameters and structural parameters were determined using the Rietveld and LeBail methods as implemented in the GSAS program package (Larson and Von Dreele, 1994; Toby, 2001). Rietveld refinements were applied at room temperature only. The isotropic thermal parameters of the oxygen atoms had to be constrained to the same value in order to obtain positive definite thermal parameters for all atoms. The unit cell parameters at elevated temperatures were determined using the LeBail method.

A major advantage of modern powder diffraction is the possibility to fit the entire observed diffraction pattern in order to overcome the problem of line overlap and to obtain parameters, which define each reflection (Will *et al.*, 1983). Parameters defining the model are refined using a least squares minimization procedure. The quantity that is minimized by the least squares procedure is

$$R = \sum_i w_i (Y_{i0} - Y_{ic})^2 \quad (43)$$

where Y_{i0} is the observed intensity and Y_{ic} the calculated intensity at step i and w_i is the weight assigned to each step intensity. The minimization is performed over all of the data points in the diffraction pattern. The observed intensity at each step in a diffraction pattern consists of a contribution from Bragg reflections at that step plus background. Therefore it is essential in any Rietveld refinement to describe the background accurately. GSAS offers approximately 10 different background functions (not all are implemented in EXPGUI). For each of these functions, the number of terms to be used is adjustable. The more terms the more complex the shape that can be fit. Each of these background functions has different shapes, and in theory, each function will have advantages under different circumstances. However the Shifted Chebyshev function (type #1) is preferable to the others for the vast majority of Rietveld refinements. The Bragg reflections are superimposed on a slowly varying background due to incoherent scattering, which mainly arises from thermal diffuse scattering, Compton scattering and, if the energy of the incident radiation is sufficiently high, fluorescence from the sample (Howard and Preston, 1989). One of the major background contributions is scattering from air, unless the diffractometer is run under vacuum conditions.

The Bragg reflections are spread out over a finite range of scattering angles. The intensity of the Bragg peaks varies as a function of crystal structure and preferred orientation. Therefore the intensities are determined by the atom positions and other structure parameters but can be affected by other factors such as absorption, extinction and preferred orientation of particles in the sample. During a Rietveld refinement, the calculated intensity Y_{ic} at point i in the diffraction pattern is determined according to

$$Y_{ic} = Y_{ib} + \sum_{k=k1}^{k2} G_{ik} I_k \quad (44)$$

Y_{ib} is the background intensity, G_{ik} is the normalized peak profile function, I_k is the integrated Bragg intensity, and $k1 \dots k2$ are the reflections contributing intensity to point i (Hill and Madsen, 1987). The integrated Bragg intensity I_k , is given by

$$I_k = sm_k (LP)_k F_{hkl}^2 \quad (45)$$

where s is the scale factor, m_k is the multiplicity and $(LP)_k$ is the Lorentz-polarization factor and F_{hkl} is the structure factor.

The shape of the Bragg peaks in powder XRD patterns deviate significantly from Gaussian and therefore a more complex function is required to accurately describe their profiles. The peak shape is a function of the divergence of the incident beam, various aberrations of the diffractometer, sample displacement, axial divergence, microstructure of the sample (*e.g.* microstrain, crystallite size). Therefore the peak shape is a complex convolution of several sample and instrumental effects and can vary significantly depending on the data collection geometry and type of sample (Langford and Louër, 1996). Young and Wiles, 1982 concluded that pseudo-Voigt and Pearson VII profile functions were best suited. In a Rietveld refinement the widths of the Bragg maxima in powder XRD patterns are typically modelled as a function that is quadratic in $\tan \theta$ and gives the full width at one half of the maximum peak height (FWHM) as a function of the diffraction angle.

$$H^2 = U \tan^2 \theta + V \tan \theta + W \quad (46)$$

This function is termed a Caglioti function. H is the FWHM and U , V and W are refineable parameters. The values of U , V and W depend on the instrumental configuration and choice of profile shape function. The peak width expression, however, does not readily accommodate broadening that is a function of crystallographic direction (Young, 1993). The Rietveld package GSAS (Larson and Von Dreele, 1994) uses a modification of the pseudo-Voigt described by Thompson *et al.*, 1987 to accommodate anisotropic Lorentzian strain and crystallite size broadening. The primary objective of profile fitting is to fit a numerical function, specially referred to as a profile shape function to a measured diffraction line. Profile shape functions are described by three parameters (Will *et al.*, 1983):

- a) The line position $2\theta_k$
- b) A peak or integrated line intensity I_0
- c) The line width expressed as the full-width at half maximum intensity FWHM or H_k

Most of the commonly used profile shape functions are symmetrical about the nominal Bragg peak positions. A variety of instrumental and sample effects, as axial divergence of the X-ray beam and structure disorder in the sample, give rise to pronounced asymmetry in the observed peak shape, especially at low diffraction angles. As a consequence most Rietveld refinement programs include as a variable a semi empirical asymmetry correction term (Klug and Alexander, 1974). This factor corrects primarily asymmetry at low angles caused by the axial divergence in the X-ray beam and does not affect the integrated intensity but will shift the apparent peak position.

For the triclinic compounds $\text{Ca}(\text{Ti}_{10}\text{Zr}_{90})\text{OGeO}_4$ and $\text{Ca}(\text{Ti}_{20}\text{Zr}_{80})\text{OGeO}_4$ and at ambient temperatures peak profiles were modelled using profile function #2, which employs a multi-term Simpson's rule integration (Howard, 1982) of the pseudo-Voigt function described by Thompson *et al.*, 1987. This function gives a better fit to asymmetric profiles than profile function #1 and shows less correlation with the lattice parameters. However it is less qualified when treating the reflection asymmetry at low angles ($2\theta < 10^\circ$) due to axial divergence. Profile function #2 was only used for the data collected with the Philips diffractometer in Heidelberg.

The profile function #3 has been applied to all remaining compounds at ambient and elevated temperatures. The third CW (constant wavelength) profile function is a similar variation of

the pseudo-Voigt function used in the second function. However, it uses a much more successful description of the peak asymmetry due to axial divergence described by Finger *et al.*, 1994. The functional form of the pseudo-Voigt used in this function is exactly the same as used in the second CW function, but this function gives a far better fit to asymmetric profiles than either of the first two functions. This CW profile function is described only by the two ratios, H/L and S/L, which can be specified exactly from the diffractometer geometry. H/L and S/L can be refined when diffraction data of sufficiently low 2θ are present. The Gaussian variance of the peak, σ^2 , varies with 2θ as

$$\sigma^2 = U \tan^2 \theta + V \tan \theta + W + \frac{P}{\cos^2 \theta} \quad (47)$$

where U, V and W are the coefficients described by Cagliotti *et al.*, 1958 and P is the Scherrer coefficient for Gaussian broadening. The coefficients U, V, W and P are within GSAS named GU, GV, GW and GP, respectively. Peak displacement errors are accounted for by varying the Lorentzian profile coefficients LX (particle size), LY (microstrain) and shft (sample displacement).

The coefficients from a CW powder profile function can also be interpreted to give both strain and particle size information. Line broadening due to microstrain is related in real space to 2θ broadening from

$$\frac{\Delta d}{d} = \Delta 2\theta \cot \theta = \text{constant} \quad (48) \quad \text{or} \quad \Delta 2\theta = \left(\frac{\Delta d}{d} \right) \tan \theta \quad (49)$$

In this expression $\Delta 2\theta$ is in radians. Examination of the expression for the Gaussian broadening (equation 47) indicates that the first term contains a strain-broadening component. This is a variance and the instrument contribution can be subtracted off. The variance is in centideg² and must be converted to radians to yield strain, thus

$$S = \frac{\pi}{18000} \sqrt{(8 \ln 2)(U - U_i)} 100\% \quad (50)$$

Alternatively, the Lorentzian component of a CW peak shape has the expression

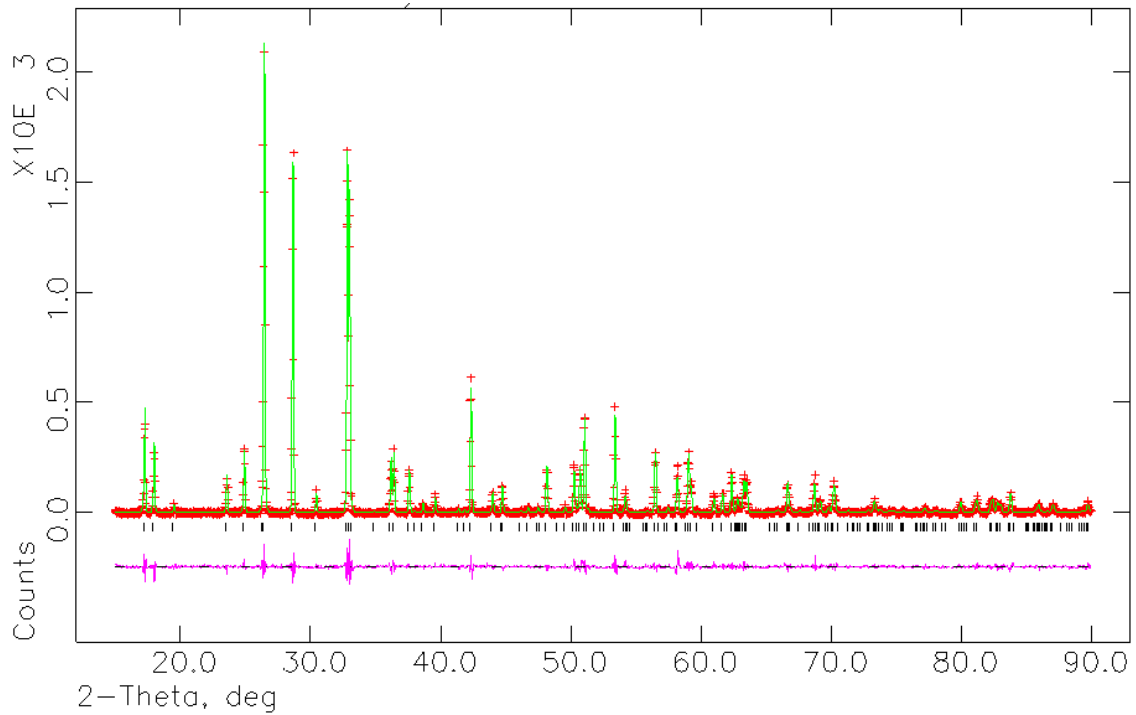
$$\gamma = \frac{X + X_s \cos \phi}{\cos \theta} + (Y + Y_e \cos \phi) \tan \theta \quad (51)$$

The strain term varies with $\tan \theta$. Any instrumental or spectral contribution can be subtracted to yield the strain component. This is in centidegree and is already a full width at half maximum so the strain is

$$S = \frac{\pi}{18000} (Y - Y_i) 100\% \quad (52)$$

Figure 1.8 displays the results of the refinement of the compounds $\text{Ca}(\text{Ti}_{10}\text{Zr}_{90})\text{OGeO}_4$ above the monoclinic – triclinic phase transition and $\text{Ca}(\text{Ti}_{10}\text{Zr}_{90})\text{OGeO}_4$ below T_c exhibiting the triclinic symmetry $\bar{A}1$.

(a)



(b)

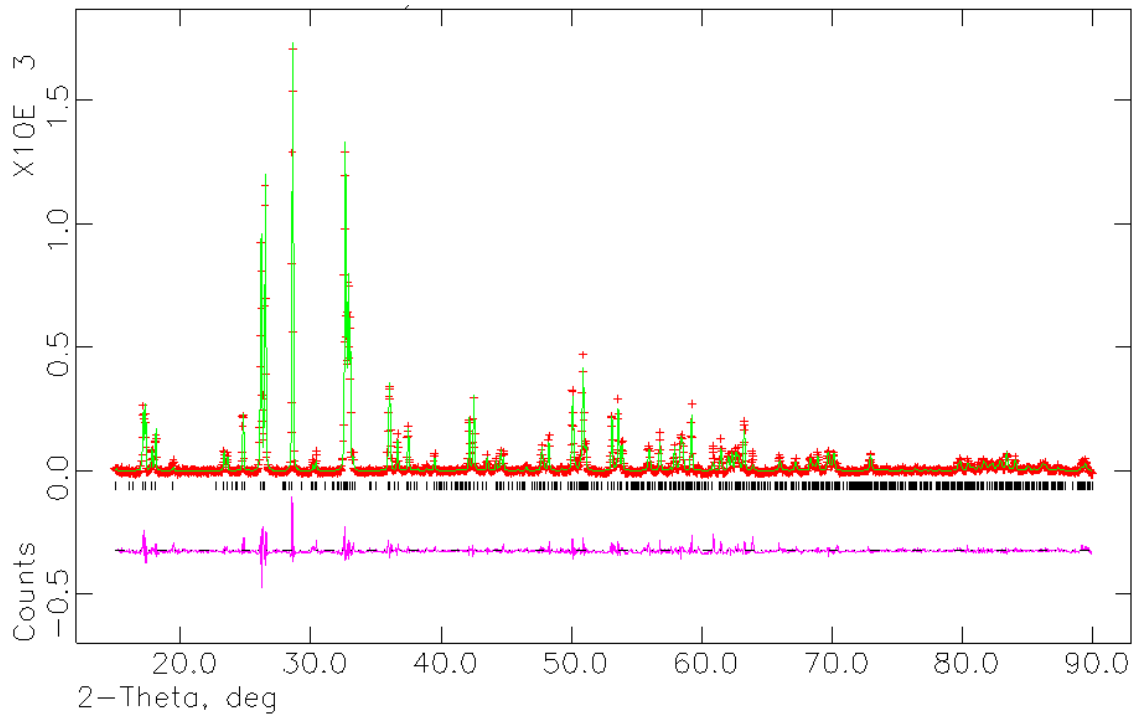


Fig. 1.8 The results of a refinement using the LeBail Method. (a) $\text{Ca}(\text{Ti}_{10}\text{Zr}_{90})\text{OGeO}_4$ at 598 K with SG symmetry $A2/a$ (b) $\text{Ca}(\text{Ti}_{10}\text{Zr}_{90})\text{OGeO}_4$ at 373 K with SG symmetry $A\bar{1}$. The observed profile is shown as red crosses and the calculated profile as a smooth green curve. Points appearing at the bottom show the differences between the observed and calculated intensities. Tick marks below the profile indicate the positions of the allowed peaks.

1.7 Transmission electron microscopy

Of the many techniques that have been applied to the study of crystal microstructures and defects, probably no single technique has contributed more to our understanding of their nature, properties and influence on the physical and chemical properties of crystalline materials than transmission electron microscopy (TEM).

Synthetic CaTiOGeO_4 single crystals were prepared for TEM to detect the behaviour of diffuse scattering with increasing temperature. Furthermore an examination of the antiphase domains in CaTiOGeO_4 was carried out.

The illuminating system of the TEM is based upon the use of electromagnetic lenses. Such lenses have the useful characteristic that their focal lengths and thus magnifications can be varied smoothly and almost continuously by altering the electric currents (McLaren, 1992).

Scattering of the incident electron beam by an object forms the TEM images (Fig. 1.9). The scattering radiation passes through the objective lens. This lens, immediately below the specimen, collects and focuses the diffraction pattern to form the primary image that is subsequently magnified by additional lenses to form a highly magnified final image. In the process of forming the primary image, the objective lens produces a diffraction pattern on the back focal plane of the objective lens. This diffraction pattern is the Fourier transform of the scattered electron wave. Apertures of various sizes inserted into the back focal plane control how much of the diffraction pattern passes on to contribute to the image. The widely diffracted beams carry the information about the fine detail of the scattering matter in the object, and hence must be collected to achieve a high resolution in the image. The projector lenses control the magnification of the image formed on the fluorescent viewing screen. Each lens successively magnifies the specimen until a highly magnified image results at the final image plane. The electrons generated in the heated filament are accelerated in our case at 300 kV and is focused by the condenser lenses into the specimen. By changing the strength of these lenses (altering the lens current) either the diffraction pattern or the image can be focused on the screen. Thus to view the diffraction pattern the imaging system lenses is adjusted so that the back focal plane of the objective lens acts as the object plane for the intermediate lens. To view the image the intermediate lens is readjusted so that its object plane is the image plane of

the objective lens. In each case therefore the intermediate lens selects the back focal plane of the objective lens as its object (Williams and Carter, 1996; McLaren, 1992).

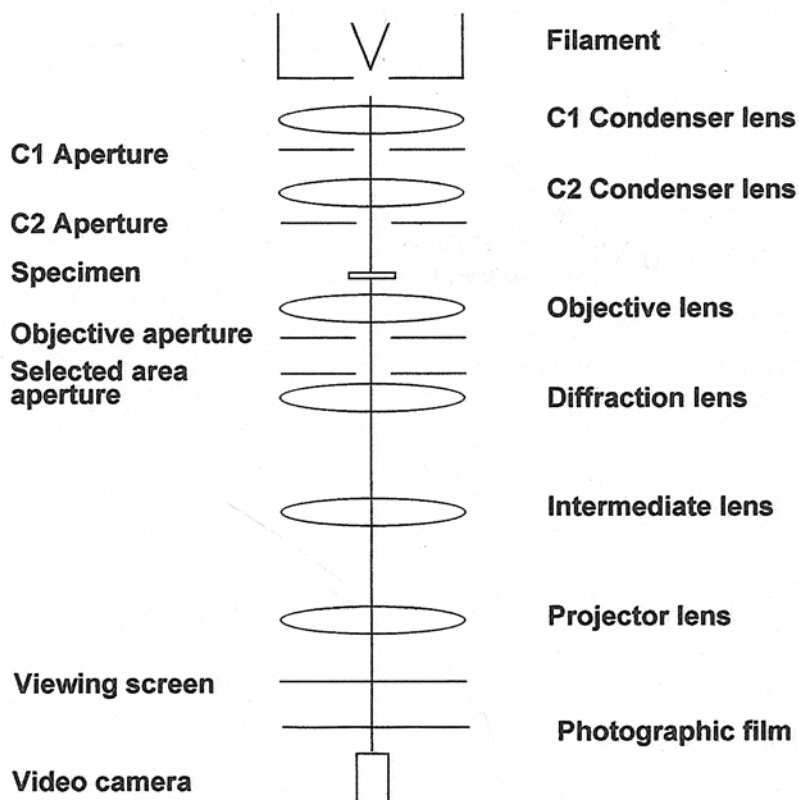


Fig. 1.9 Schematic representation of a transmission electron microscope (After McLaren, 1992).

Spherical aberration, chromatic aberration and astigmatism belong to the group of lens defects that limit the microscope performance in substantial ways. Spherical aberration is caused by the lens field acting inhomogeneously on the off-axis rays and is largely determined by the lens design. Spherical aberration degrades the image that is viewed in a TEM and as a result the magnification in the center of the lens differs from that at the edges. Chromatic aberration is related to variations of the magnification of the lens with the wavelength of the electrons in the beam. Producing thin samples can reduce chromatic aberration. Astigmatism is the most common defect in the TEM illumination system and arises when the electrons sense a non-uniform magnetic field as they spiral round the optic axis or because the final condenser limiting aperture is misaligned, thus deflecting the beam (Williams and Carter, 1996).

Although the principles of diffraction are identical in X-ray diffraction and electron diffraction, there are prominent differences arising from the contrasting character of X-radiation versus electron radiation (Buseck, 1992). The most prominent difference is that electrons can be focused, while X-rays except in very special cases, cannot. Also electrons can be focused into narrow, high intensity beams that permit measurements confined to small specimen volumes, *i.e.* at high spatial resolutions.

In addition the ease of obtaining diffraction patterns by the two methods differ greatly. X-rays interact with and are diffracted by orbital electrons, whereas electrons interact with and are diffracted by the electrostatic potential arising from both orbital electrons and the atomic nuclei. The result of this strong interaction is that electron scattering is far more efficient than for X-rays. Electrons have far shorter wavelengths than X-rays, and that difference greatly affects the diffraction conditions. It follows from the Bragg equation ($n\lambda = 2d \sin \theta$) that a decrease in λ results in a corresponding decrease in diffraction angles and so Bragg angles for diffraction are far smaller for electrons than for X-rays. A consequence of the difference in wavelength between X-rays and electrons is that the sphere of reflection (the Ewald sphere, relating real and reciprocal space) is far larger for electrons than for X-rays, and so diffraction patterns can be obtained much more simply with electrons than for X-rays. With the TEM the radius of the sphere is so large and the crystal so thin, that the image plane is essentially tangent over a large region of reciprocal space and many diffraction spots can normally be recorded without any detector motion. That in combination with the strong diffraction effects that occur with electrons means that planes through reciprocal space can be viewed almost instantaneously when operating in electron diffraction mode (Putnis, 1992; Williams and Carter, 1996).

The basic TEM operation, SAD (selected-area diffraction) has been applied extensively. SAD patterns are sharply focused spot patterns, which is used to obtain a diffraction pattern with a parallel beam of electrons. The aperture is inserted into the image plane of the objective lens. Therefore the aperture will only permit electrons that pass through it to hit the specimen. A SAD pattern forms the basis of bright-field (BF) and dark-field (DF) imaging.

In conventional electron microscopy amplitude contrast is produced by excluding significant fractions of electrons from reaching the image. Amplitude contrast results from a filtering process whereby some of the electrons from the incoming beam are unable to reach the image plane. These electrons that are extracted from the exiting beam decrease the image intensity,

and therefore the amplitude is reduced. In low-resolution (normal) bright-field electron microscopy, only the direct electron beam is allowed to reach the image plane. Insertion of an objective lens aperture excludes some of this scattered radiation, giving rise to strong amplitude contrast. In dark field electron microscopy (Fig. 1.11a), the direct electron beam is excluded from the image plane, and only one or more scattered beams are allowed to pass through the objective lens aperture (Buseck, 1992; Williams and Carter, 1996).

Previous work on titanite using TEM include: Van Heurck *et al.*, 1991; Higgins and Ribbe, 1976; Troitzsch *et al.*, 1999. Van Heurck *et al.*, 1991 investigated the paraelectric – antiferroelectric phase transition. They examined the disappearance of the $k + l = 2n + 1$ characterizing the $P2_1/a$ space group as a function of temperature as well as the dynamical behaviour of the antiphase domains. Troitzsch *et al.*, 1999 studied the crystal structural changes in titanite along the join TiO-AlF. They examined the change in space group from $P2_1/a$ to $A2/a$ with increasing Al and F in binary titanite solid solution. In all diffraction patterns reflections $k + l = 2n + 1$ are absent, indicating an A -centered symmetry. Troitzsch *et al.*, 1999 concluded that the change in space group in $\text{Ca}(\text{Ti,Al})(\text{O,F})\text{SiO}_4$ has to occur between $X_{\text{Al}} = 0$ and $X_{\text{Al}} = 0.18$. These observations are in agreement with previous studies based on natural titanite, containing substituents Fe and OH in addition to Al and F. Higgins and Ribbe, 1976 observed the disappearance of diffuse $k + l = 2n + 1$ reflections in natural titanite to be in the range of $X_{\text{Al+Fe}} = 0.08$ and $X_{\text{Al+Fe}} = 0.21$.

The behaviour of antiphase domains in CaTiOGeO_4 as a function of temperature has been examined. Titanite (Van Heurck *et al.*, 1991) and CaTiOGeO_4 here examined are both characterized by antiphase domains. Antiphase domain structures form whenever a phase transformation involves a loss of translational symmetry (Nord, 1992). This may be due to either displacive transitions or to cation ordering processes. The geometrical relationship of one domain to another is a function of the point symmetry (twin domains) or translation symmetry (antiphase domains) that are lost during the transformation. Figure 1.10 illustrates the formation of antiphase domains in titanite.

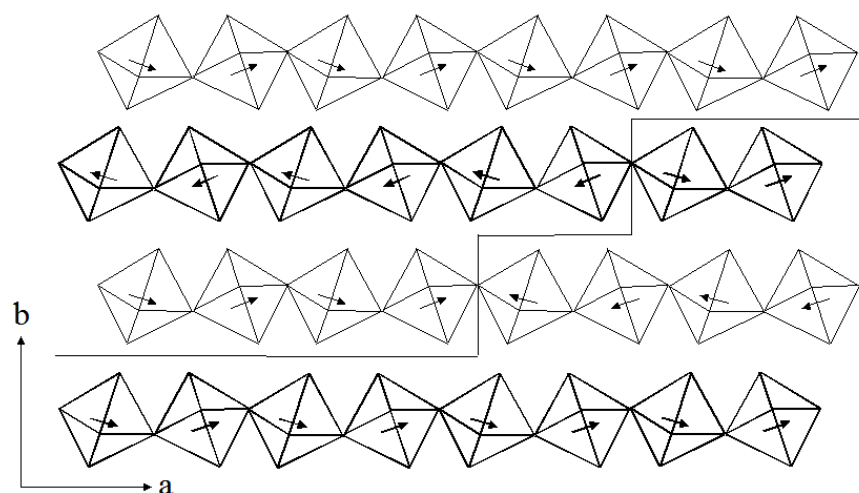


Fig. 1.10 Schematic diagram illustrating the formation of antiphase domains in titanite showing the chains of Ti-octahedra parallel to a . The dark and light chains represent those above and below the plane of the drawing, respectively. The arrows represent the direction of the Ti-displacement. Domains in opposite orientations are located on each side of the line through the figure (After Taylor and Brown, 1976).

The structure and orientation of antiphase domains (APD's) are identical; the only difference is a translation across the antiphase domain boundary (APB). When translation symmetry is lost extra spots are observed in the electron diffraction pattern that either occupy positions that are systematically absent in the disordered phase or as extra spots that change the volume of the unit cell. In the case of titanite the reflection $k + l = \text{odd}$ are absent in the high temperature phase (Van Heurck *et al.*, 1991). This is consistent with the A -centered cell. In the low temperature primitive cell all reflections must be present, so that reflections with $k + l = \text{odd}$ appear during the transition.

Antiphase domain boundaries are made visible in the transmission electron microscope because of a change in the phase of the electron beam as it crosses the boundary. Electron beams passing through adjacent domains will undergo an identical change in phase and amplitude. The diffraction contrast will be identical for each domain whether imaged in bright-field or dark-field conditions as in our case. However, at an inclined boundary between the domains, the beam is transmitted or diffracted first through one domain and then through the adjacent domain. Upon crossing the domain boundary the phase of the diffracted beam is shifted. Under two-beam conditions it is the presence of this phase shift that makes antiphase domain boundaries visible as a set of fringes parallel to the centre line of the thin specimen (McLaren, 1992 and Putnis, 1992).

In titanite and the compound CaTiOGeO_4 antiphase domains are made visible by the centered dark field method (CDF). In normal diffraction mode an appropriate superstructure reflection is selected and antiphase domains can now be viewed when shifting to dark field mode as described above. The antiphase domains are only visible in dark field using $k + l = \text{odd}$ as the operating vector (Van Heurck *et al.*, 1991). Electrons selected by the objective aperture travel off the optic axis (Fig. 1.11ab), since the aperture is displaced to select the scattered electrons. These off-axis electrons will suffer aberrations and astigmatism and the DF image is difficult to focus. As a consequence the objective lens strength has to be adjusted. This was done by adjusting the beam tilt potentiometers above the objective lens so that the incident beam hits the specimen at an angle equal and opposite to the scattering angle. The scattered electrons will as a result travel down the optic axis as shown in Figure 1.11c.

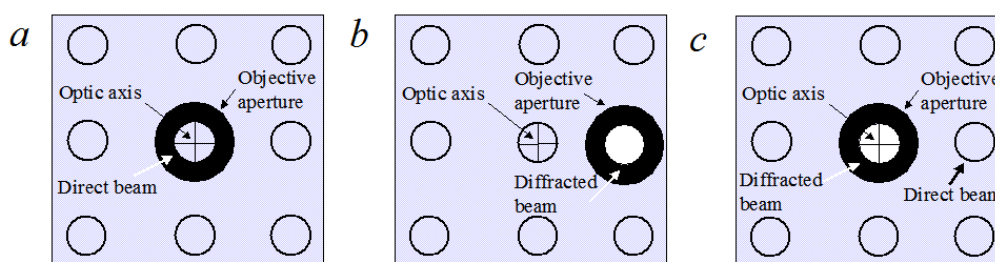


Fig. 1.11 Diagrams showing how the objective lens/aperture are used in combination to produce (a) a BF image formed from the direct beam (b) a displaced-aperture DF image formed with a specific off-axis scattered beam and (c) a CDF image where the incident beam is tilted so that the scattered beam remains on axis (After Williams and Carter, 1996).

Information with regard to domain microstructures will include the crystallographic relationship between adjacent domains and the mobility and geometric changes of domain boundaries or walls with respect to temperature.

Besides the information derived from studying the antiphase domains, we examined the behaviour of diffuse scattering in CaTiOGeO_4 . To detect the behaviour of diffuse scattering with increasing temperature samples of synthetic CaTiOGeO_4 single crystals were prepared. A double tilt heating-holder was used for the *in situ* heating electron diffraction experiments in a 300 kV Jeol, JEM-3010 electron microscope. No temperature calibration of the double tilt holder was carried out prior to the diffraction experiment as no calibration procedures had been established beforehand. According to Williams and Carter, 1996 heating and straining

holders, in particular, can produce effects in thin samples that are totally uncharacteristic of the bulk specimen and should therefore be used with care. Often surface reactions will dominate internal reactions when inducing phase transformations by heating. The surface may also prevent grain boundaries from migrating at temperatures where they would do so in the bulk material.

Electron diffraction patterns were obtained along a number of zones at microscope temperatures well below and above the transition and in the vicinity of the transition. The fundamental reflections are $k + l = \text{even}$. These are present in both the high symmetry and low symmetry phases. The $k + l = \text{odd}$ reflections are only present in the low temperature phase $P2_1/a$. Therefore the disappearance or strong streaking of the $k + l = \text{odd}$ reflections was used as an indication that the transition temperature had been reached. At all temperatures the sample was observed to be stable under the electron beam. The diffraction patterns show two families of spots: the sharp and intense spots with $k + l = \text{even}$ and the weak super-structure reflections with $k + l = \text{odd}$. As the temperature increases, the diffuse scattering becomes visible and finally at $T > T_c$ degenerates to almost continuous streaks elongated along the \mathbf{b}^* direction.

1.8 Single crystal diffraction measurement

Most of our detailed understanding of crystalline materials has resulted from single crystal X-ray and neutron diffraction experiments. The most common instrument for sampling the reciprocal lattice is a computer operated four-circle single crystal diffractometer. The essential geometry of a four-circle diffractometer is shown schematically in Fig 1.12.

The incident X-ray beam and the diffracted beam when oriented for measurement lie in the horizontal plane, which contains the crystal. The crystal can be rotated about three axes and the detector about a fourth axis. All four axes intersect at the crystal. The crystal is glued to a glass fibre, which is mounted on a goniometer head.

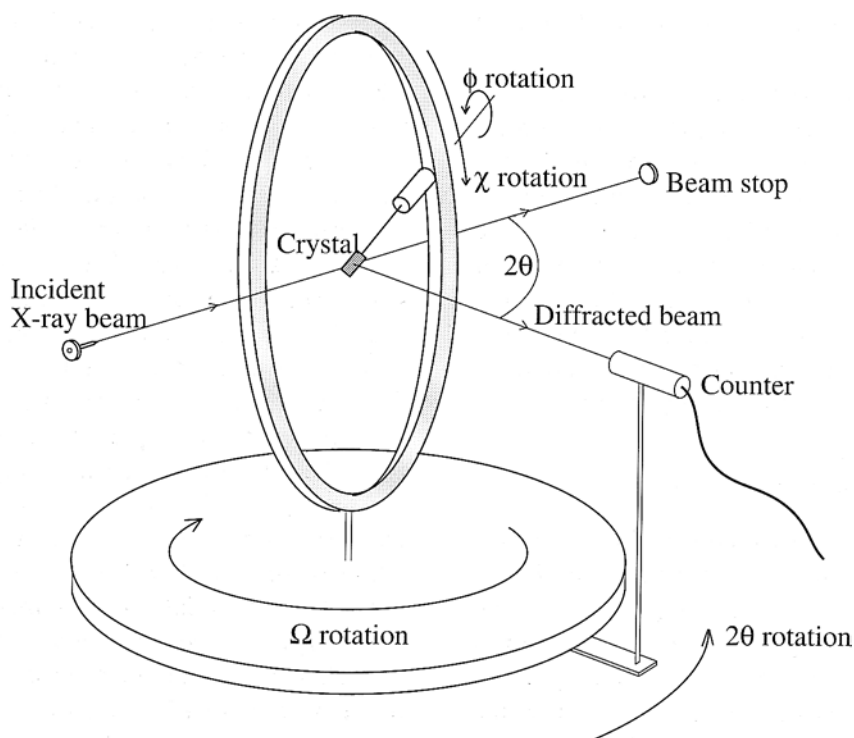


Fig. 1.12 The four-circle single crystal diffractometer. The crystal is centrally mounted in a circular ring that can be rotated around the three axes, Ω (ω), ϕ and χ (After Putnis, 1992).

The purpose of the three rotation axes: ϕ , χ and ω is to enable the normal to a selected reflection plane (hkl) to be brought into the horizontal plane defined by the axes of the collimator and the detector, so that it is inclined to the incident beam at an angle $90^\circ - \theta$. The detector (usually a scintillation counter) is mounted on an arm, which enables it to be rotated about a vertical axis, designated the 2θ axis, coincident with the ω axis and therefore inclined

in the horizontal plane at 2θ to the forward direction of the incident beam. The detector is then correctly positioned to measure the intensity of the X-ray beam reflected from the selected (hkl) plane. The instrument is programmed to rotate the crystal, while the detector scans the 2θ circle at twice the angular velocity of the crystal in order to keep the Bragg condition satisfied. That the crystal can be rotated about three axes leads to a degree of flexibility in the way in which it can be moved into the reflecting position for any given set of (hkl) planes. Once a few reflections have been located, a consistent unit cell can be identified and the instrument subsequently set to systematically collect a set of (hkl) reflections and measure their intensities. Typically several thousand reflections are collected and measured in this way (Monaco, 1992; Putnis, 1992).

The diffractometer used in this experiment is a CAD4, *i.e.*, it does not have a Eulerian cradle, but it uses the kappa-geometry, which is different from the standard Eulerian setting shown in Fig. 1.12. The heart of the CAD4 diffractometer is the kappa goniometer. It carries the goniometerhead, which keeps the crystal in the centre of the diffractometer. The kappa goniometer consists of a combination of three parts, bearing the three rotation axes. All axes intersect in the centre of the diffractometer. The goniometerhead is mounted on the ϕ -axis, which is supported by the kappa block. The kappa block can be rotated about the κ -axis being carried by the omega block. In turn, the omega block can be rotated about the ω -axis being carried by the base plate of the diffractometer. The angle included by the ω -axis and the κ -axis (α) is $\alpha = 50^\circ$. The angle between the κ -axis and the ϕ -axis is also 50° and the goniometer can therefore access all directions in χ within ca. 100° of the zero position. This geometry gives enhanced setting flexibility over the traditional Eulerian cradle while simultaneously the obscuration caused by the mount is drastically diminished. In addition to the goniometer the diffractometer contains a 2θ -axis, which supports the detector. The 2θ -axis coincides with the ω -axis. This enables the detector to describe an arc with radius R around the goniometer in the horizontal plane.

The data collection and reduction process related to a single crystal experiment is

1. Mounting and centring of the crystal
2. Collection of the initial reflections
3. Determination of the unit cell and orientation matrix

4. Selecting an appropriate portion of the limiting sphere to collection
5. Collection of data
6. Data reduction and absorption correction

Since crystals usually reflect over the finite width of the Bragg spots and since it is the total intensity reaching the detector from the given reflection that is required, the crystal is rotated through the reflecting position about the ω axis at constant speed. The reflection can be recorded using a pure ω scan *i.e.*, the detector position remains constant while the crystal rotates about the ω -axis, or the reflection can be recorded using a ω - 2θ scan as in this case. For accurate intensity measurements it is important both to set the limits of such a scan correctly for each reflection and to maintain the intensity of the incident beam at a constant magnitude. The background intensity is estimated from measurements at the limits of a chosen ω scan and subtracted from the peak measurement to yield the integrated intensity of the reflection.

As the crystal is mounted at random, it is initially necessary to determine the orientation of its reciprocal lattice relative to the fixed reference axes of the diffractometer. This is done by defining the orientation matrix and can be achieved by searching a predetermined θ range for reflections and then deducing the orientation of the conventional reciprocal unit-cell from the measured φ , χ and θ of the recorded reflections (McKie and McKie, 1986).

A prerequisite for determination of a crystal structure is the collection of a set of structure amplitudes $|F(hkl)|$ for as many independent reflections as possible together with an assessment of the accuracy of each measurement. The measured intensities (corrected for any background intensity) must be converted into a consistent set of structure factors. The process of obtaining structure factors from intensity data is called data reduction. During data reduction, all of the symmetry-equivalent intensity data are merged to form a single set of structure factor data using the following relationship

$$F^2 = \sum \omega_0 F_o^2 / \sum \omega_0 \quad (53)$$

where the summations are over the set of symmetry-equivalent data.

The structure factor depends on the kinds of atom in the unit cell and the position of the atoms within the unit cell. Since the space group symmetry gives information about the relative positions of the atoms, $F(hkl)$ will become dependent on the symmetry. This holds both for the phase and amplitude of $F(hkl)$. The intensity for a given (hkl) measured by rotating the crystal with a uniform angular velocity Ω through a reciprocal lattice position is given by

$$I = I^0 (\lambda^3 / \Omega) (V_x L p A / V^2) |F(hkl)|^2 \quad (54)$$

where, I^0 is the incident beam intensity, λ the wavelength of radiation, Ω the rotation velocity of the crystal, V_x the volume of the crystal, A the absorption factor, V the volume of the unit cell, $|F(hkl)|$ is the observed structure factor, L is the Lorentz factor, which depends on the relative amount of time the peak takes to pass through the Ewald sphere and p is the polarization factor (Monaco, 1992).

The Lorentz and polarisation factors are both dependent on the experimental conditions of the intensity measurement and on θ . The Lorentz factor is a geometrical factor concerned with the passage of the reciprocal lattice point through the reflecting sphere. The Lorentz factor affects the diffraction strength and describes different speeds with which reflections pass the Ewald sphere. Reflections that cut through the Ewald sphere will pass through quickly, whereas reflections that just touch the Ewald sphere will pass through slowly. This difference in time is corrected by a term called the Lorentz factor. For point detector systems performing either ω - 2θ or ω scan this correction is simply

$$L = 1/(\sin 2\theta) \quad (55)$$

The polarization factor arises because X-rays can be polarized. The crystal, however, does not reflect waves vibrating in all directions with equal efficiency so the reflected beam will be partially polarized. This is known to reduce the intensity of the diffracted beam by a factor of $(1+\cos^2 2\theta)/2$ and causes the greatest reduction for $2\theta = 90^\circ$, and the least for $2\theta = 0^\circ$ or 180° . The intensities therefore of the reflections at very low and very high Bragg angles are enhanced relative to those at intermediate values. When the incident beam has been monochromatized by reflection from a crystal, as in the case of a four-circle diffractometer, the polarization factor becomes

$$p = \frac{1 + \cos^2 2\theta_m \cos^2 2\theta}{1 + \cos^2 2\theta_m} \quad (56)$$

for the case in which the incident beam and the monochromatized beam lie in the horizontal plane. $2\theta_m$ is the angle between the incident beam and scattered beams in the monochromator.

Absorption by the crystal of the incident and diffracted X-ray beam affects the intensities and the directions of the scattered beams. The absorption effects that we have to take into account are attributable to the inelastic interaction of the X-rays with the atoms in the crystal. This absorption is related to the path length (τ) the X-rays travel through the material and the nature of the atoms in the crystal as expressed by the absorption coefficient μ . The linear absorption coefficient therefore depends on the composition of the crystal, its density and the wavelength of the radiation. Since μ depends on the density of the absorbing material, it is usually tabulated as the related function mass absorption coefficient $\mu_m = (\mu/\rho)$. The linear absorption coefficient is then calculated from the formula

$$\mu = \rho \sum (P_n / 100)(\mu / \rho) = \rho \sum (P_n / 100)\mu_m \quad (57)$$

where the summation is carried out over the n atom types in the cell, and P_n is the percent by mass of the given atom type in the cell.

Absorption of X-rays by the sample is often the most difficult correction to perform. The extent of absorption depends on the size and shape of the crystal as well as the types and relative amounts of different atoms in the sample, and the wavelength of radiation used in the experiment. Also absorption from the sample mount may need to be included in the correction.

The intensity I of an X-ray beam after it has travelled a distance x through a crystal is given by

$$I = I_0 \exp(-\mu x) \quad (58)$$

where I_0 is the intensity of the incident beam and μ is the linear absorption coefficient of the crystal and x is the distance through the absorbing medium.

Single-crystal X-ray diffraction (XRD) data of CaTiOGeO_4 were collected at 293 K using an Enraf-Nonius CAD4 automated four-circle diffractometer with radiation type $\text{MoK}\alpha$. A suitable crystal of CaTiOGeO_4 was selected and examined under a polarizing microscope for uniform and sharp extinction under crossed polarizers, regular shape and clarity. The quality of the crystals was checked by X-ray precession photographs prior to the measurement. The size of the crystal is $0.3 \times 0.2 \times 0.15$ mm. Figure 1.13 shows the shape and the faces bounding the chosen crystal.

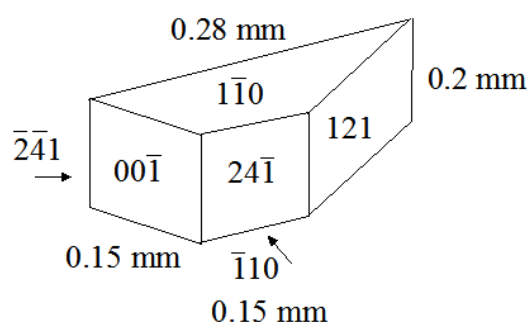


Fig. 1.13 The shape and faces bounding the measured crystal.

An automated search produced a list of centered reflections, *i.e.*, their setting angles. These reflections were automatically indexed using a set of shortest reciprocal lattice vectors leading to a first orientation matrix. By transforming the orientation matrix to an appropriate conventional cell, in this case monoclinic, the reflections were reindexed accordingly. Next the searched list of reflections was deleted and a set of 24 reflections equally distributed in reciprocal space was entered by hkl vectors. The new list of reflections was then centered and the orientation matrix was refined using the new centered setting angles. This procedure improved the lattice constants and the centering and refinement was repeated several times until no further decrease in the error of the lattice constants was observed. The final orientation matrix was used in the data collection to predict the location of the Bragg peaks. The range of h, k, l measured was $-11 \rightarrow 10$; $-14 \rightarrow 14$; $0 \rightarrow 10$ with $\theta_{\max} = 35^\circ$. The number of standard reflections was 3, while the number of measured, independent and observed reflections were 3648, 1704, 1470, respectively.

Intensity data for CaTiOGeO₄ were collected in the ω -2 θ scan mode. All unique reflections were classed as observed and Lorentz and polarization (Lp) corrections were carried out. Based on the observed crystal shape, given by the faces bounding the crystal at a certain distance to its center, the numerical absorption correction was carried out using the program X-RED (Stoe & Cie, 1996). The absorption coefficient μ was determined to 11.60mm⁻¹. After Lp factors and absorption corrections had been applied to the raw intensity data symmetry related reflections were merged to generate a set of $|F(hkl)|$ values for use in the determination of the crystal structure.

The structure was refined using *SHELXL97* in space group $P2_1/a$ (Sheldrick, 1997). *SHELXL97* uses a conventional structure factor summation and merges equivalents and eliminates systematic absences. To run SHELXL only two input files are required: atoms/instructions and reflection data files. The reflection data file (*.hkl) contains h, k, l, F_o^2 and $\sigma(F_o^2)$. The *.hkl file is read each time the program is run. Crystal data, refinement instructions and atom coordinates are all input in the file *.ins. After each refinement cycle a file *.res is (re)written. This file is similar to *.ins, but has updated values for all refined parameters. It must be copied or edited to *.ins for the next refinement run. Lorentz, polarization and absorption corrections are assumed to have been applied to the data in the *.hkl file. *SHELXL97* always refines against F_o^2 , even when F-values are input. The advantage is that more experimental information is incorporated (suitably weighted) and the possibility of receiving a local minimum is reduced.

Starting parameters were the known structural parameters of titanite (Ghose *et al.*, 1991). Full matrix least squares refinements were based on F^2 with weights

$$w = 1/[\sigma^2(F_o^2) + (WP)^2 + 0.01P] \quad (59)$$

where $P = (F_o^2 + F_c^2)/3$, $W = 0.0378$, $R[F^2 > 2\sigma(F^2)] = 0.0252$, $wR(F^2) = 0.0637$ and the goodness of fit, $S(\text{GooF}) = 1.131$.

The number reflections, restraints and parameters used in the refinement were 1704, 0, 74, respectively, while the extinction coefficient was 0.0018(5).

During refinement an R -factor was computed to give a measure of correctness between the observed and calculated intensities of a crystal structure. Ideally a good structure has an R -

value < 5%. The R -factor therefore gives an overall measure of how correct the structure is. A value of 0% means a perfect agreement between observed and calculated intensities, but this is never achieved due to random errors arising throughout experimental measurements. The internal R -value is given by

$$R_{\text{int}} = \frac{\sum |F_o^2 - F_o^2(\text{mean})|}{\sum (F_o^2)} \quad (60)$$

where the inner sums are over the symmetry-equivalent reflections and the outer sums are over the unique hkl data. The term n is the number of equivalent data for a given hkl being merged. The internal R -value is in this case, $R_{\text{int}} = 0.0214$.

2. Samples

The synthesis of the studied compounds forms an important part of the work. All experiments are performed on synthetic materials. This involves solid state synthesis of powder samples with several compositions along the studied joins.

The below listed table (Table 2.1) summarizes the composition of the samples prepared from solid state synthesis.

Table 2.1. Composition of the powder samples studied. The numbers refer to the x-value.

$\text{CaTiO}(\text{Ge}_x\text{Si}_{1-x})\text{O}_4$	$(\text{Ca}_x\text{Sr}_{1-x})\text{TiOGeO}_4$	$\text{Ca}(\text{Ti}_x\text{Zr}_{1-x})\text{OGeO}_4$
95	90	95
90	70	90
70	60	80
50	50	50
30	40	20
20	30	10
10	10	CaZrOGeO_4
	SrTiOGeO_4	

The stoichiometric starting mixtures were prepared from pure fine-grained powders of carbonates (CaCO_3 , SrCO_3) and oxides (TiO_2 , GeO_2 , SiO_2 and ZrO_2). Approximately 2.5 g starting oxides were used. Oxides and carbonates were mixed and carefully ground for several minutes, pressed into pellets and heated for 24 hours at 1173 K. The pellets were reground and again pressed into pellets and heated further for 24 hours at 1323 K. After the first short heating intervals the samples were kept in the furnace for 5 days intervals at a maximum temperature of 1323 K with intermittent grindings between. An open platinum crucible was used. Phase purity was first established by powder diffraction analysis after 3-6 heating intervals. In most cases the phase showed to be inhomogeneous and further heating intervals were applied. Between heating intervals phase purity was proved by powder diffraction analysis till the resulting phase showed to be homogeneous.

The last reactions at 1588 K of samples containing Zr were carried out in a welded platinum tube to avoid GeO_2 loss.

The synthesized powder samples were analysed by *in situ* heating X-ray powder diffraction using an Anton Paar HTK 1200 furnace mounted on a Philips Xpert diffractometer with

monochromatic $\text{CuK}\alpha_1$ -radiation. Diffraction patterns were recorded in the range $17\text{-}90^\circ 2\theta$ using a proportional counter with 4 s/step counting time and a step size of 0.02° .

Lattice parameters were determined using the LeBail or Rietveld method as implemented in the GSAS program (Larson and Von Dreele, 1994).

Table 2.2 summarizes the temperature range in which measurements were carried out and the number of refinements performed. Note that only the ratio between the substituting atoms is listed. Diffraction patterns were recorded in intervals of 20 – 50 K. For CaTiOGeO_4 diffraction patterns were recorded with intervals of 3-5 K in the vicinity of T_c . The endmember composition CaTiOGeO_4 is listed in Table 2.2 although the CaTiOGeO_4 powder specimen originates from single-crystals synthesized from the oxides GeO_2 and TiO_2 and the carbonate CaCO_3 following the method described by Robbins, 1968.

Table 2.2. Number of refinements performed and the temperature interval.

Compound	Number of refinements	Temperature interval (K)
CaTiOGeO_4	38	298-1123
$\text{Ge}_{95}\text{Si}_{05}$	19	298-773
$\text{Ge}_{90}\text{Si}_{10}$	19	298-773
$\text{Ge}_{70}\text{Si}_{30}$	19	298-773
$\text{Ge}_{50}\text{Si}_{50}$	25	298-1073
$\text{Ge}_{30}\text{Si}_{70}$	19	298-773
$\text{Ge}_{20}\text{Si}_{80}$	19	298-773
$\text{Ge}_{10}\text{Si}_{90}$	19	298-773
$\text{Ca}_{90}\text{Sr}_{10}$	19	298-773
$\text{Ca}_{70}\text{Sr}_{30}$	20	298-773
$\text{Ca}_{60}\text{Sr}_{40}$	19	298-773
$\text{Ca}_{50}\text{Sr}_{50}$	26	298-1073
$\text{Ca}_{40}\text{Sr}_{60}$	19	298-773
$\text{Ca}_{30}\text{Sr}_{70}$	20	298-773
$\text{Ca}_{10}\text{Sr}_{90}$	20	298-773
SrTiOGeO_4	25	298-1123
$\text{Ti}_{95}\text{Zr}_{05}$	19	298-773
$\text{Ti}_{90}\text{Zr}_{10}$	19	298-773
$\text{Ti}_{80}\text{Zr}_{20}$	19	298-773
$\text{Ti}_{50}\text{Zr}_{50}$	19	298-773
$\text{Ti}_{20}\text{Zr}_{80}$	19	298-773
$\text{Ti}_{10}\text{Zr}_{90}$	19	298-773
CaZrOGeO_4	29	298-1073

3. High temperature X-ray diffraction study of the solid solution $\text{CaTiO}(\text{Ge}_x\text{Si}_{1-x})\text{O}_4$

A scientific manuscript submitted to *American Mineralogist*
May 2004

Accepted
December 2004

Authors:

Rikke Ellemann-Olesen
Universität Heidelberg, Mineralogisches Institut, Im Neuenheimer Feld 236
69120 Heidelberg, Germany

Thomas Malcherek
Universität Heidelberg, Mineralogisches Institut, Im Neuenheimer Feld 236
69120 Heidelberg, Germany

Abstract

The structure of CaTiOGeO_4 (CTGO) has been refined using single crystal X-ray diffraction data. CTGO is isostructural with titanite, CaTiOSiO_4 . The displacive $P2_1/a - A2/a$ phase transition analogous to titanite has been studied by in-situ-heating X-ray powder diffraction and transmission electron microscopy. The transition is accompanied by the disappearance of superstructure reflections, $k + l = 2n + 1$, which are replaced by diffuse scattering for $T > T_c$. The diffuse scattering is seen as streaks along b^* in high temperature TEM SAD. Lattice parameters as a function of temperature and composition have been determined by X-ray powder diffraction between room temperature and a maximum of 1123 K. Strain analysis of CTGO indicates a transition temperature of $T_c = 588 \pm 4$ K and the additional occurrence of an isosymmetric anomaly at $T_i = 800 \pm 25$ K. There is complete solid-solution along the join $\text{CaTiO}(\text{Ge}_x\text{Si}_{1-x})\text{O}_4$. The lattice parameters across the solid solution vary continuously and the structural phase transitions are identified based on the determination of spontaneous strain associated with the transitions. The e_{11} and e_{13} components dominate the strain tensor. All compositions across the solid solution exhibit close to tricritical behaviour and nearly constant scalar strain.

1. Introduction

The titanite structure has attracted substantial interest because of its phase transitions, its occurrence as a metamict mineral (Hawthorne *et al.*, 1991) and its crystal chemical relation to the non-linear optical material KTiOPO_4 (KTP) (Kunz *et al.*, 2000). Titanite is a common accessory mineral in a variety of metamorphic and igneous rocks. Crystals with less than 3-4 mol% substitution of Fe and Al for Ti have the space group $P2_1/a$ whereas those with more than 4 mol% (Al + Fe) have diffuse reflections $k + l$ odd which become unobservable above 20 mol% substitution as the average structure approaches $A2/a$ symmetry (Higgins and Ribbe, 1976; Oberti *et al.*, 1991). The structural framework of titanite is formed by parallel chains of corner-sharing $[\text{TiO}_6]$ octahedra running along the a -direction. The parallel strings of 2 octahedra are connected by $[\text{GeO}_4]$ tetrahedra sharing corners with the $[\text{TiO}_6]$ octahedra and by Ca in [7]-coordination (Speer and Gibbs, 1976; Taylor and Brown, 1976). At about $T_c=487$ K, titanite

undergoes a phase transition associated with a displacement of Ti from the center of the $[\text{TiO}_6]$ octahedron (Ghose *et al.*, 1991; Bismayer *et al.*, 1992). Above the transition temperature the space group is $A2/a$ ($C2/c$) whereas below, the space group is $P2_1/a$ ($P2_1/c$) (Taylor and Brown, 1976; Ghose *et al.*, 1991). The ordered low-temperature phase is characterized by alternating short and long Ti-O bonds along $[100]$, with reversed sense of Ti displacement in adjacent octahedral chains. In the $A2/a$ -structure Ti is located at the centre of the $[\text{TiO}_6]$ octahedra. The transition is accompanied by the disappearance of superlattice diffraction maxima with $k + l = 2n + 1$. It is believed that the phase transition at 487 K involves merely a 2-dimensional loss of long-range coherence between the off-centre dipoles, while the structure remains ordered with respect to the (dynamic) Ti-displacement along individual octahedral chains (Malcherek *et al.*, 2000). True $A2/a$ symmetry is suggested to be attained at a second, isosymmetric phase transition around $T_i = 825$ K. First evidence of such a second anomaly had been obtained from excess birefringence (Bismayer *et al.*, 1992) and Raman spectroscopy (Salje *et al.*, 1993). Diffuse scattering intensity oriented in planes normal to $[100]$ disappears close to T_i (Kek *et al.*, 1997) and phonon bands associated with TiO_6 octahedral stretching modes exhibit strong softening at T_i (Zhang *et al.*, 1997). Changes in the average crystal structure at T_i amount to small variations in the interatomic distances and angles (mainly reorientation of the Ca displacement vector and slight tilting of the $[\text{TiO}_6]$ octahedra, Zhang *et al.*, 1997, Malcherek *et al.*, 1999). The occurrence of non-classical effective critical exponents has been reported by a number of authors. Values of β have been given with 0.32 (Ghose *et al.*, 1991) and close to 0.15 (*e.g.* Bismayer *et al.*, 1992; Salje *et al.*, 1993; Chrosch *et al.*, 1997). More recently Malcherek *et al.*, 2000 and Hayward *et al.*, 2000 both described the phase transition as tricritical, implying a classical value $\beta = 0.25$. Van Heurck *et al.*, 1991 observed antiphase domains in the low temperature phase, with broad and mobile interfaces at and above T_c . When the temperature is further increased these antiphase domains disappear. Groat *et al.*, 1996 found that similar behaviour does not occur in malayaite, CaSnOSiO_4 . Most probably, the transition in malayaite is similar to the isosymmetric transition at T_i in titanite. Robbins, 1968 was the first to synthesize CaTiOGeO_4 . X-ray precession photographs were indexed in $P2_1/n$ with $a = 6.65$, $b = 8.92$, $c = 7.49$ Å and $\beta = 119.45$. The present study reports displacive phase transitions in CaTiOGeO_4 and the solid solution it forms with titanite.

2. Experimental

Synthesis

Single-crystals of CaTiOGeO_4 were synthesized from the oxides following the method described by Robbins (1968). CO_2 was driven off at 1323 K from a mixture of bulk composition $\text{CaCO}_3 \cdot \text{TiO}_2 \cdot \text{GeO}_2$ prior to melting in a welded platinum tube at 1723 K. Crystals were obtained by slowly cooling the stoichiometric melt with 3 K/h. The crystals were then held at 1273 K for 1h and allowed to cool to room temperature. Colourless and transparent crystals were obtained. Wavelength-dispersive electron-microprobe analysis confirmed the stoichiometry. No impurities were observed in the electron-backscattering image.

Seven different samples at 5–20 mol% intervals across the solid solution $\text{CaTiO}(\text{Ge}_x\text{Si}_{1-x})\text{O}_4$ (CTGO_x) were synthesized by solid-state reaction. The stoichiometric starting mixtures were prepared from pure fine grained powders of CaCO_3 (Aldrich 20,293-2), TiO_2 (Rutile, Aldrich 20,475-7), SiO_2 (Aldrich 38,126-8) and GeO_2 (Aldrich 19,947-8) at a maximum temperature of 1323 K. Approximately 2.5 g starting oxides were ground, pressed into pellets, and heated for several intervals of 5 days with intermittent grindings. Phase purity was established by powder diffraction analysis. Minor amounts of CaTiO_3 (~ 0.5 wt %) and CaSiO_3 (~ 1.5 wt %) were observed in samples CTGO10, CTGO70 and CTGO90.

Single-crystal X-ray diffraction

Single-crystal X-ray diffraction (XRD) data were collected at 293 K using an Enraf-Nonius CAD-4 automated four-circle diffractometer. A suitable crystal of CaTiOGeO_4 was selected and the quality checked by X-ray precession photographs. The crystal was bounded by the forms $\{001\}$, $\{1\bar{1}0\}$ and $\{24\bar{1}\}$. A numerical absorption correction based on the observed crystal shape was applied to the data using the program X-RED (STOE & Cie GmbH 1996). Intensity data were collected in the ω -2 θ scan mode. The structure was refined using *SHELX97* (Sheldrick 1997). Crystal data and parameters of the data collections are listed in Table 1.

X-ray powder diffraction

In-situ X-ray powder diffraction measurements up to 1123 K were done using an Anton Paar HTK 1200 furnace mounted on a Philips Xpert diffractometer with monochromatic $\text{CuK}\alpha_1$ -radiation. Diffraction patterns were recorded in the range $17\text{-}90^\circ$ 2θ using a proportional counter with 4 s/step counting time and a step size of 0.02° . Lattice parameters were determined using the LeBail method as implemented in the GSAS program (Larson and Von Dreele, 1994) and the materials were refined with space group $A2/a$. The additional reflections with $k + l = 2n + 1$ that occur in the $P2_1/a$ phase are weak and mostly overlapping with the fundamental reflections. Additional Rietveld refinements were done at room temperature for all compounds across the solid solution. Starting fractional coordinates were taken from Ghose *et al.*, 1991. For CTGO50 and the endmember CTGO, the measurements were done up to 1073 K and 1123 K, respectively. For the remaining compositions, measurements were done up to 773 K. In order to take into account the structural anomaly at T_i , the linear reference functions of thermal expansion were obtained using the high-temperature data above T_i from CTGO50 and the endmember compositions CTGO and titanite (latter data from Malcherek, 2001). The slopes derived from extrapolation of the lattice constants were plotted against composition and fitted using a parabola. For the c lattice constant a straight line fit was sufficient. With these fixed line slopes, individual linear functions of thermal expansion were obtained from the data measured up to 773 K for the remaining compositions.

TEM

CaTiOGeO_4 samples for transmission electron microscopy were prepared by adding copper grids to 10-15 μm thin samples. These specimens were ion milled and carbon coated. A double-tilt heating-holder was used for the in-situ electron-diffraction experiments in a 300 kV Jeol, JEM-3010 electron microscope. Electron-diffraction patterns were obtained along a number of zones at microscope temperature as well as in the vicinity of the transition. The disappearance or strong streaking of the $k + l = \text{odd}$ reflections was used as an indication that the transition temperature had been reached. The sample was stable under the electron beam at all temperatures.

3. Results

Structure of CaTiOGeO₄

Robbins, 1968 first synthesized CaTiOGeO₄ and discussed its structure on the basis of X-ray precession films, which showed symmetry P2₁/n using the setting of Zachariasen, 1930 and suggested a structure similar to that of titanite. In order to compare the results of Robbins with our results it is necessary to transform the P2₁/n setting to the P2₁/a setting. Applying the transformation matrix (101, 010, $\bar{1}00$) to the lattice constants derived by Robbins, 1968 gives: $a = 7.13$, $b = 8.92$, $c = 6.65$ and $\beta = 114.28^\circ$. Considering the esd of the lattice parameters given by Robbins, 1968, this agrees with our results. The lattice parameters are also consistent with the data given in PDF entry #40-387. The structure of CTGO was refined in space group P2₁/a. CTGO is isostructural with titanite. Unit cell data, atom coordinates and interatomic distances for the single crystal structure refinement are given in Tables 1 - 3.

Structure refinement across CaTiO(Ge_xSi_{1-x})O₄

The refined structural parameters at room temperature are given in Table 4. The variation of the mean bond lengths is displayed in Table 5. For comparison of the corresponding lengths and angles for titanite see Kek *et al.*, 1997. The bond length of Ca-O is constant within the limits of the measurement accuracy, while, as expected, the mean bond length of Ge to the surrounding oxygen atoms increases with increasing Ge content. The composition dependence of the mean bond length of Ti is near symmetric with the endmembers exhibiting the shortest average bond lengths.

TEM

Electron diffraction patterns were obtained for a number of zones at temperatures spanning the transition. The diffraction patterns show two families of spots (Fig. 1a): sharp and intense spots

with $k + l = \text{even}$ and the weak super-structure reflections with $k + l = \text{odd}$ (marked by an arrow). As the temperature increases, the diffuse scattering becomes visible and finally at $T > T_c$ degenerates to almost continuous streaks elongated along \mathbf{b}^* . In analogy to titanite (Higgins and Ribbe, 1976), the streaks would result from planes of diffusely scattered intensity perpendicular to the octahedral chains. The spots with $k + l = \text{even}$ remain round and sharp and their intensities show no appreciable change on heating. The behaviour is shown in Fig. 1a-d, showing the zone [001] below and above T_c .

In the low temperature phase, antiphase boundaries can be observed using dark-field mode. A series of dark-field contrast images made with the (110) and $(2\bar{1}0)$ superstructure reflections is shown in Figures 2a-c. The geometrical features are consistent with the assumption that the antiphase domains have a cylindrical shape. Straight sections of the cylinder walls are oriented parallel to a *i.e.*, parallel to the chains of $[\text{TiO}_6]$ octahedra (Van Heurck *et al.*, 1991). During heating to above T_c , the domains are not mobile, but disappear somewhat above the phase transition. On renewed cooling below T_c the interfaces reappear at the same location as during heating. This memory effect may be due to pinning of the domain walls by defects or by the specimen boundaries. This is not in agreement with the behaviour observed in titanite. Van Heurck *et al.*, 1991 found that the antiphase domains become mobile until they disappear somewhat above the phase transition. Higgins and Ribbe, 1976 observed such antiphase domains in titanite at room temperature using the $k + l = \text{odd}$ reflections indicative of $\text{P2}_1/a$ symmetry. They concluded that the antiphase domains are linear and parallel to a . This behaviour is in agreement with our observations for CaTiOGeO_4 .

Lattice parameters

The $\text{A2}/a - \text{P2}_1/a$ structural phase transition in CaTiOGeO_4 has been observed using in situ heating X-ray powder diffraction methods. Diffraction patterns were recorded in the temperature range 298 – 1123 K. On the basis of the disappearance of $k + l = \text{odd}$ reflections the transition can be observed in the diffraction patterns. At low temperatures these clearly exhibit the $k + l = \text{odd}$ reflections indicative of $\text{P2}_1/a$ symmetry. The intensities of the $21\bar{2}$ and $22\bar{1}$ superlattice

reflections were extracted using the LeBail fit in space group $P2_1/a$. The superlattice reflections show a steady decrease with increasing temperature, but due to background noise and their relatively small intensity it is not possible to determine the exact critical temperature in this way. Within the temperature range 523 to 623 K the $P2_1/a$ reflections disappear, but below this temperature range they are clearly visible. By extrapolation of the lattice parameters measured for $T < 1123$ K towards lower temperatures, linear reference functions of thermal expansion are obtained for all lattice parameters. The complete set of lattice parameter data for CTGO is shown in Figures 3a-e. The transition is accompanied by a significant expansion of the a -axis. Another significant deviation from the extrapolated high temperature data is seen for the monoclinic angle, β . In the case of b only minor deviation from linear thermal expansion occurs over the entire temperature range. Likewise, only very small positive deviation occurs for the c lattice dimension. From the a lattice constant and the β -angle, there are clear indications in analogy to titanite for the additional occurrence of an isosymmetric anomaly at T_i in CaTiOGeO_4 (Figs. 3a and d). T_i for CTGO can be estimated to 800 ± 25 K, in accordance with the estimates for T_i in titanite (Malcherek 2001, Kek *et al.*, 1997, Zhang *et al.*, 1997). Measurement temperatures and lattice parameters are given in Table 6. Titanite and CTGO form a complete solid solution, with no evidence for phase-separation at any of the intermediate compositions. Lattice constants derived from Rietveld refinements for all intermediate compositions at room temperature are given in Table 7 and are displayed in Figure 4. Across the solid solution, replacement of Si by Ge leads to a gradual increase in cell volume by 4.5%. The a , b and c lattice parameters increase across the solid solution, while β shows a non-linear behaviour as the Ge-content increases. The endmember compositions have a larger β -angle than the intermediate compositions. The complete set of lattice parameter data is given in Table 8. Lattice parameters for each of the compositions, extracted from the LeBail analysis, show a very similar evolution with temperature as in CTGO and titanite.

Spontaneous strain in CaTiOGeO_4

One of the most significant physical effects that accompany a structural phase transition is lattice strain. Strain components were calculated according to the equations given by Carpenter *et al.*, 1998. The scalar spontaneous strain is defined as

$$e_s = (\sum e_{ij}^2)^{1/2}$$

In the case of a zone-boundary transition, this property is proportional to the square of the order parameter Q of the transition. The spontaneous strain associated with the $P2_1/a - A2/a$ phase transition in CTGO is relatively small (Fig. 5). By linear extrapolation of e_s^2 to zero, the transition temperature is estimated as $T_c = 588 \pm 4$ K, which coincides with the onset of volume strain (Fig. 3e). In agreement with previous work on synthetic titanite (Malcherek, 2001), the spontaneous strain due to the $P2_1/a - A2/a$ phase transition in CaTiOGeO_4 is dominated by the components e_{11} and e_{13} . The e_{22} and e_{33} components are nearly equal in magnitude and both are small and negative for $T < T_c$, e_{22} being the more negative. The e_{22} component differs from that in titanite, as its contribution to the strain cannot be completely neglected. The e_{11} component is significantly larger than the e_{22} and e_{33} components and it dominates the strain (along with e_{13}) as in titanite. The component e_{11} does not disappear at T_c but remains finite up to T_i (Fig. 5b) in CTGO. The scalar strain (Fig. 6) has been determined and the strain for titanite (Malcherek, 2001) is plotted for comparison. The square of the scalar strain (Fig. 7) is approximately linear with temperature above 400 K, which, as $e^2 \sim Q^4$, implies that the transition is close to tricritical.

Spontaneous strain in the solid-solution $\text{CaTiO}(\text{Ge}_x\text{Si}_{1-x})\text{O}_4$

The strain components (Figs. 8a-d) show a continuous, but non-linear, evolution from their room-temperature values to 773, 1073 for CTGO50 and 1123 K for CTGO. The component e_{22} (Fig. 8c) is in most cases very close to zero within the limits of accuracy. The component e_{33} is negative but near zero for $T < T_c$. The e_{11} component is positive below T_c whereas the e_{13} component is negative. The strain components show a similar evolution for all intermediate compositions across the solid solution, with the exception of e_{22} . A small volume strain is observed.

The magnitude of the strain component e_{11} decreases from titanite (data from Malcherek, 2001) to CTGO (Fig. 8a). In contrast, the e_{13} component shows a nearly symmetric variation with the endmembers having the most pronounced negative values and with intermediate compositions showing less shear strain (Fig. 8b). Overall, the scalar strain is constant across the solid solution (Fig. 8d). The compositions CTGO90 and CTGO95 deviate most by having a slightly smaller

scalar strain, 0.0014 and 0.0011, respectively, compared to 0.0016 in CaTiOGeO₄. From the e_{11} strain component of CTGO50 and CTGO (Fig. 8a) it is evident that the isosymmetric phase transition observed in titanite occurs across the entire solid solution. This has a significant influence on the evolution of e_{11} as it is finite at temperatures above T_c and vanishes only at $T_i \approx 800$ K. The square of the scalar strain, $\sum e_{ij}^2$, for the intermediate compositions (Fig. 9a-g) shows linear dependence on temperature over a wide range below the respective transition temperatures, T_c . Again this does hint towards tricritical character of the transition, just as in the endmembers. Based on the strain analysis, T_c for all compositions along the solid solution has been determined by extrapolation of e_s^2 to zero. T_c increases almost linearly from 487 K in titanite to 588 K in CTGO (Fig. 10). Determination of the isosymmetric transition temperature T_i is encumbered by large errors because of the way the extrapolation was done, but it appears to remain more or less constant at 800 ± 25 K.

4. Discussion

From Figure 10 it is clear that the substitution of Ge for Si has a marked influence on T_c . The evolution of T_c with composition is nearly linear and is marked by a gradual increase of nearly 100 K from the titanite endmember towards CTGO. Thus the substitution of Ge for Si stabilizes the ordered P2₁/a phase. On the other hand, the isostructural anomaly, T_i appears to be constant at 800 K. Zhang *et al.*, 1997 conclude that the high-temperature phase transition in titanite shows a completely different behaviour than the transition at $T_c = 487$ K. They observed that Fe and Al substituting for Ti have much less effect on the transition near 825 K than on that at 487 K, where substitution at the octahedral site has a large effect and the transition is eventually suppressed. The effect of Fe, Al substitution in titanite is to block the lower temperature transition, whereas substitution of Ge for Si has the opposite effect. On the other hand, T_i is neither sensitive to substitution on the octahedral site, nor do our results suggest that it is significantly altered by substitutions on the tetrahedral site. The e_{13} component is close to zero for most of the intermediate compositions (Fig. 11a). This implies that the shearing of the unit cell is lessened for intermediate compositions. At the same time, the magnitude of e_{11} decreases with increasing T_c

and Ge content. A possible explanation might involve the introduction of a minor strain along the b -axis as suggested by the e_{22} component. As the scalar strain is near constant across the solid solution, the decreasing strain due to expansion along the a -axis has to be compensated. A significant difference in strain behaviour between titanite (Malcherek, 2001) and CTGO is the presence of a minor negative strain along the b -axis expressed by the strain component e_{22} with a minimum of -0.00036. A similar trend is observed in CTGO20, CTGO30 and CTGO70 but with opposite sign. The component e_{11} for the endmember composition CaTiOGeO_4 does not disappear at T_c but remains finite up to T_i (Fig. 5b). This behaviour is different from that observed in titanite. In titanite, it is only the e_{13} component, which is finite above T_c and vanishes at T_i (Malcherek, 2001). The composition dependence of the mean Ti-O bond length does not correlate with the transition temperature, T_c , *i.e.*, the bond length does not increase with increasing T_c (Table 5 and Fig. 11). Instead it shows a similar evolution as the strain component e_{13} (Fig. 12). There is correlation between the shear strain and the Ti-O mean bond length (Fig. 12). Hammonds *et al.*, 1998 predicted that due to the absence of rigid unit modes in the titanite structure, polyhedral distortion is to be expected upon chemical substitution in titanite, rather than polyhedral tilting. Variation of the individual bond lengths is more pronounced for the intermediate compounds than for the endmember compositions and as a result the octahedra and tetrahedra are more distorted. Kunz *et al.*, 1997 observed increasing Ca-O bond lengths with increasing Sn content at the octahedral site of the titanite-malayaite join. In our case, near constant Ca-O bond lengths are observed with increasing substitution by Ge for Si on the tetrahedral site. A comparison of the single crystal data of CaTiOGeO_4 with the data of titanite (Kek *et al.*, 1997) shows that the most significant difference between the two isomorphs is the bond lengths Ti-O1 and Ti-O1'. For CaTiOGeO_4 these are 1.7615 Å and 2.0165 Å, respectively ($\Delta = 0.255$ Å). For titanite they are Ti-O1 = 1.754 Å and Ti-O1' = 1.989 Å ($\Delta = 0.235$ Å). The larger Ti displacement in CTGO compared to titanite is in accordance with the higher transition temperature observed in CTGO, if one assumes an Abrahams-Kurtz-Jamieson relation between T_c and cation displacement (Abrahams *et al.*, 1968). Tilting of the TiO_6 octahedra is slightly smaller in CTGO, with a Ti-O1-Ti angle of $\sim 143^\circ$, compared to 141° in titanite (Ghose *et al.*, 1991). This straightening of the octahedral chains can be attributed to the larger size of the GeO_4 tetrahedra. The bond valence sum (BVS, calculated according to Brese and O'Keefe, 1991) for the Ge site in CTGO has an

almost ideal value of 3.97, while the BVS for Si in titanite is less than ideal (3.73), hinting at tensile stress in the Si-coordination of titanite. As in titanite, Ti is slightly overbonded in CTGO, with a constant BVS close to 4.2 across the entire solid solution. Distortion of the TiO_6 octahedron is less in CTGO though.

5. Conclusion

Titanite and CaTiOGeO_4 form a complete solid solution with a near-linear increase of the critical temperature of the antiferrodistortive transition from 487 K to 588 K in CaTiOGeO_4 . As with titanite X-ray diffraction indicates the additional occurrence of an isosymmetric anomaly at $T_i = 800 \pm 25$ K that is constant across the solid solution. The lattice parameters change continuously across the solid solution and the transition appears to be close to tricritical for all compositions. Substitution of Ge for Si causes a drop in shear strain relative to the ordered endmember compositions CaTiOGeO_4 and titanite. This reduced shearing of the unit cell accompanying the $P2_1/a - A2/a$ transition correlates with a volume increase of the TiO_6 octahedra for intermediate compositions.

Acknowledgements

Financial support through the Deutsche Forschungs-Gemeinschaft (DFG) is gratefully acknowledged.

References

- Abrahams, S.C., Kurtz, S.K. and Jamieson, P.B., 1968. Atomic Displacement Relationship to Curie Temperature and Spontaneous Polarization in Displacive Ferroelectrics. *Physical Review* 172: 551-553.
- Bismayer, U., Schmahl, W., Schmidt, C. and Groat, L.A., 1992. Linear Birefringence and X-Ray Diffraction Studies of the Structural Phase Transition in Titanite, CaTiSiO_5 . *Physics and Chemistry of Minerals* 19: 260-266.

- Breese, N.E. and O'Keeffe, M., 1991. Bond-Valence Parameters for Solids. *Acta Crystallographica B* 47: 192-197.
- Carpenter, M.A., Salje, E.K.H. and Graeme-Barber, A., 1998. Spontaneous strain as a determinant of thermodynamic properties for phase transitions in minerals. *European Journal of Mineralogy* 10: 621-691.
- Chrosch, J., Bismayer, U. and Salje, E.K.H., 1997. Anti-phase boundaries and phase transitions in titanite: An X-ray diffraction study. *American Mineralogist* 82: 677-681.
- Ghose, S., Ito, Y. and Hatch, D.M., 1991. Paraelectric-Antiferroelectric Phase Transition in Titanite, CaTiSiO₅: I. A high temperature X-ray diffraction study of the order parameter and transition mechanism. *Physics and Chemistry of Minerals* 17: 591-603.
- Groat, L.A., Kek, S., Bismayer, U., Schmidt, C., Krane, H.G., Meyer, H., Nistor, L. and Van Tendeloo, G., 1996. A synchrotron radiation, HRTEM, X-ray powder diffraction, and Raman spectroscopy study of malayaite, CaSnSiO₅. *American Mineralogist* 81: 595-602.
- Hammonds, K.D., Bosenick, A., Dove, M.T. and Heine, V., 1998. Rigid unit modes in crystal structures with octahedrally coordinated atoms. *American Mineralogist* 83: 476-497.
- Hawthorne, F.C., Groat, L.A., Raudsepp, M., Ball, N.A., Kimata, M., Spike, F.D., Gaba, R., Halden, N.M., Lumpkin, G.R., Ewing, R.C., Gregor, R.B., Lytle, F.W., Ercit, T.S., Rossman, G.R., Wicks, F.J., Ramik, R.A., Sherriff, B.L., Fleet, M.E. and McCammon, C., 1991. Alpha-decay damage in titanite. *American Mineralogist* 76: 370-396.
- Hayward, S.A., del Cerro, J. and Salje, E.K.H., 2000. Antiferroelectric phase transition in titanite: Excess entropy and short range order. *American Mineralogist* 85: 557-562.
- Higgins, J.B. and Ribbe, P.H., 1976. The crystal chemistry and space groups of natural and synthetic titanites. *American Mineralogist* 61: 878-888.
- Kek, S., Aroyo, M., Bismayer, U., Schmidt, C., Eichhorn, K. and Krane, H.G., 1997. The two-step phase transition of titanite, CaTiSiO₅: a synchrotron radiation study. *Zeitschrift für Kristallographie* 212: 9-19.
- Kunz, M., Xirouchakis, D., Wang, Y., Parise, J.B. and Lindsley, D.H., 1997. Structural investigations along the join CaTiOSiO₄-CaSnOSiO₄. *Schweizerische Mineralogische und Petrographische Mitteilungen* 77: 1-11.
- Kunz, M., Arlt, T., and Stolz, J., 2000. In situ powder diffraction study of titanite (CaTiOSiO₄) at high pressure and high temperature. *American Mineralogist* 85: 1465-1473.

- Larson, A.C. and Von Dreele, R.B., 1994. General Structure Analysis System (GSAS). Los Alamos National Laboratory. Los Alamos, New Mexico.
- Malcherek, T., Domeneghetti, C.M., Tazzoli, V., Salje, E.K.H. and Bismayer, U., 1999. A high temperature study of synthetic titanite CaTiOSiO_4 . *Phase transitions* 69: 119-131.
- Malcherek, T., Paulmann, C., Domeneghetti, M.C. and Bismayer, U., 2000. Diffuse scattering anisotropy and the $P2_1/a - A2/a$ phase transition in titanite, CaTiOSiO_4 . *Journal of Applied Crystallography* 34: 108-113.
- Malcherek, T., 2001. Spontaneous strain in synthetic titanite, CaTiOSiO_4 . *Mineralogical Magazine* 65: 709- 715.
- Oberti, R., Smith, D.C., Rossi, G. and Caucia, F., 1991. The crystal-chemistry of high aluminium titanites. *European Journal of Mineralogy* 3: 777-792.
- Robbins, C.R., 1968. Synthetic CaTiSiO_5 and its germanium analogue. *Materials Research Bulletin* 3: 693-698.
- Salje, E., Schmidt, C. and Bismayer, U., 1993. Structural phase transition in titanite, CaTiSiO_5 : A Raman spectroscopic study. *Physics and Chemistry of Minerals* 19: 502-506.
- Sheldrick, G.M., 1997. *SHELX97*. University of Göttingen, Germany.
- Speer, J.A. and Gibbs, G.V., 1976. The crystal structure of synthetic titanite, CaTiOSiO_4 , and the domain textures of natural titanites. *American Mineralogist* 61: 238-247.
- Stoe & Cie GmbH, 1996. X-RED, Data Reduction. Darmstadt, Germany
- Taylor, M. and Brown, G.E., 1976. High-temperature structural study of the $P2_1/a - A2/a$ phase transition in synthetic titanite, CaTiSiO_5 . *American Mineralogist* 61: 435-447.
- Van Heurck, C., Van Tendeloo, G., Ghose, S. and Amelinckx, S., 1991. Paraelectric-Antiferroelectric Phase Transition in Titanite, CaTiSiO_5 . II. Electron Diffraction and Electron Microscopic Studies of the Transition Dynamics. *Physics and Chemistry of Minerals* 17: 604-610.
- Zachariasen, W.H., 1930. The crystal structure of titanite. *Zeitschrift für Kristallographie* 73: 7-16.
- Zhang, M., Salje, E.K.H., and Bismayer, U., 1997. Structural phase transition near 825 K in titanite: Evidence from infrared spectroscopic observations. *American Mineralogist* 82: 30-35.

Table 1: CaTiOGeO₄: Single crystal, experimental data.

Crystal data

Radiation type	Mo $K\alpha$
Z	4
Temperature (K)	293 K
Crystal system, space group	$P2_1/a$
a, b, c (Å)	7.158(1), 8.885(1), 6.649(1)
β (°)	113.834(1)
V (Å ³)	386.84(9)
Size (mm)	$0.3 \times 0.2 \times 0.15$
No. of reflections for cell parameters	24

Data collection

Diffractometer	Enraf-Nonius CAD-4
Data collection method	ω - 2θ
θ_{\max} (°)	35
Range of h, k, l	$-11 \rightarrow 10, -14 \rightarrow 14, 0 \rightarrow 10$
No. of standard reflections	3
No. of measured, independent and observed reflections	3648, 1704, 1470
R_{int}	0.0214
Absorption correction	Numerical

Refinement

Refinement	Full-matrix least squares on F^2
Weighing scheme	$w = 1/[\sigma^2(F_o^2) + (WP)^2 + 0.01P]$ where $P = (F_o^2 + 2 F_c^2)/3$
W	0.0378
$R[F^2 > 2\sigma(F^2)], wR(F^2), S(\text{GooF})$	0.0252, 0.0637, 1.131
No. of reflections, restraints and parameters used in refinement	1704, 0, 74
Extinction coefficient	0.0018(5)

Table 2. CaTiOGeO₄: Atomic positional parameters and anisotropic thermal vibration parameters ($\text{\AA}^2 \times 10^{-5}$) at room temperature.

	Ca	Ti	Ge	O1	O2A	O2B	O3A	O3B
<i>x</i>	0.2428(1)	0.5161(1)	0.7478(1)	0.7498(2)	0.9199(2)	0.0772(2)	0.3926(2)	0.6095(2)
<i>y</i>	0.4215(1)	0.2545(1)	0.4334(1)	0.3179(2)	0.3097(2)	0.1902(2)	0.4576(2)	0.0441(2)
<i>z</i>	0.2503(1)	0.7492(1)	0.2487(1)	0.7507(2)	0.4385(2)	0.0578(2)	0.6422(2)	0.8567(2)
U11	1574(3)	470(4)	485(4)	508(3)	1032(3)	943(3)	853(3)	836(2)
U22	704(3)	565(4)	551(5)	738(4)	946(5)	1001(3)	719(5)	720(3)
U33	663(4)	407(3)	394(2)	957(5)	571(3)	564(3)	815(3)	778(4)
U23	1(3)	-15(4)	-6(3)	-14(3)	181(3)	206(4)	72(4)	59(3)
U13	141(3)	209(3)	218(3)	353(3)	180(5)	237(3)	518(3)	503(3)
U12	52(3)	19(3)	-4(3)	47(4)	292(3)	284(4)	229(3)	212(3)

Table 3. CaTiOGeO₄: Interatomic distances (\AA) at room temperature and interatomic angles ($^\circ$) at room temperature.

Ti-O1	1.7615(1)	O1-Ti-O2A	91.56(1)
Ti-O1'	2.0155(1)	O1-Ti-O2B	95.95(1)
Ti-O2A	1.9795(2)	O1-Ti-O3A	89.76(1)
Ti-O2B	1.9792(2)	O1-Ti-O3B	96.68(1)
Ti-O3A	2.0088(2)	O1'-Ti-O2A	88.97(1)
Ti-O3B	2.0165(2)	O1'-Ti-O2B	83.53(1)
Mean	1.960	O1'-Ti-O3A	90.38(1)
Ca-O1	2.3155(2)	O1'-Ti-O3B	83.18(1)
Ca-O2A	2.4728(1)	O2A-Ti-O3A	88.97(1)
Ca-O2B	2.4588(3)	O2A-Ti-O3B	91.63(1)
Ca-O3A	2.4050(2)	O2B-Ti-O3A	91.45(1)
Ca-O3B	2.4153(2)	O2B-Ti-O3B	87.71(1)
Ca-O3A'	2.6394(2)	Ti-O1-Ti	142.74(1)
Ca-O3B'	2.5696(1)	O2A-Ge-O2B	102.18(2)
Mean	2.468	O2A-Ge-O3A	113.82(2)
Ge-O2A	1.7494(2)	O2A-Ge-O3B	106.66(2)
Ge-O2B	1.7483(1)	O2B-Ge-O3A	107.37(2)
Ge-O3A	1.7504(2)	O2B-Ge-O3B	114.23(1)
Ge-O3B	1.7552(2)	O3A-Ge-O3B	112.30(1)
Mean	1.751		

Table 4. Atomic positional parameters and isotropic thermal vibration parameters ($\text{\AA}^2 \times 10^{-5}$) at room temperature using SG $P2_1/a$ for $\text{CaTiO}(\text{Ge}_x\text{Si}_{1-x})\text{O}_4$.

Mol% Ge								
95	Ca	Ti	Ge,Si	O1	O2A	O2B	O3A	O3B
<i>x</i>	0.2368(5)	0.5035(4)	0.7450(3)	0.7342(5)	0.9300(1)	0.0955(5)	0.4058(2)	0.6179(2)
<i>y</i>	0.4201(1)	0.2378(4)	0.4324(6)	0.3203(9)	0.3003(9)	0.1923(5)	0.4539(1)	0.0357(3)
<i>z</i>	0.2419(9)	0.7480(6)	0.2560(9)	0.7473(3)	0.4558(6)	0.0838(3)	0.6402(8)	0.8670(7)
U_{iso}^*	1272(4)	1380(3)	1509(4)	660(3)	660(3)	660(3)	660(3)	660(3)
Occ	1.000	1.000	0.901(6) 0.098(4)	1.000	1.000	1.000	1.000	1.000
R_p	0.178							
$R(F^2)$	0.105							
90	Ca	Ti	Ge,Si	O1	O2A	O2B	O3A	O3B
<i>x</i>	0.2306(3)	0.5043(6)	0.7366(3)	0.7392(2)	0.9359(7)	0.0944(4)	0.4158(7)	0.6401(1)
<i>y</i>	0.4188(5)	0.2338(4)	0.4335(7)	0.3209(7)	0.3143(3)	0.2109(8)	0.4505(1)	0.0319(5)
<i>z</i>	0.2396(8)	0.7454(3)	0.2528(1)	0.7464(1)	0.4667(9)	0.0904(4)	0.6574(3)	0.8857(9)
U_{iso}^*	322(3)	1337(5)	830(4)	689(3)	689(3)	689(3)	689(3)	689(3)
Occ	1.000	1.000	0.871(4) 0.128(6)	1.000	1.000	1.000	1.000	1.000
R_p	0.203							
$R(F^2)$	0.129							
70	Ca	Ti	Ge,Si	O1	O2A	O2B	O3A	O3B
<i>x</i>	0.2479(3)	0.5078(1)	0.7491(8)	0.7399(6)	0.9252(2)	0.0927(7)	0.3920(7)	0.6140(4)
<i>y</i>	0.4193(2)	0.2433(9)	0.4331(5)	0.3257(8)	0.3083(5)	0.1942(6)	0.4616(2)	0.0378(8)
<i>z</i>	0.2424(5)	0.7420(1)	0.2557(7)	0.7611(9)	0.4453(3)	0.0741(9)	0.6538(3)	0.8689(8)
U_{iso}^*	1159(4)	2099(4)	1815(4)	985(3)	985(3)	985(3)	985(3)	985(3)
Occ	1.000	1.000	0.678(3) 0.321(7)	1.000	1.000	1.000	1.000	1.000
R_p	0.177							
$R(F^2)$	0.141							

50	Ca	Ti	Ge,Si	O1	O2A	O2B	O3A	O3B
<i>x</i>	0.2465(9)	0.5047(5)	0.7529(4)	0.7453(1)	0.9289(7)	0.1021(6)	0.4000(1)	0.6197(7)
<i>y</i>	0.4199(9)	0.2507(3)	0.4314(8)	0.3215(9)	0.3216(2)	0.2022(1)	0.4739(4)	0.0485(6)
<i>z</i>	0.2569(6)	0.7460(7)	0.2469(7)	0.7765(5)	0.4596(3)	0.0860(6)	0.6590(2)	0.8756(9)
U_{iso}^*	1865(4)	2468(4)	1907(3)	468(4)	468(4)	468(4)	468(4)	468(4)
Occ	1.000	1.000	0.490(0) 0.510(0)	1.000	1.000	1.000	1.000	1.000
R_P	0.178							
$R(F^2)$	0.120							

30	Ca	Ti	Ge,Si	O1	O2A	O2B	O3A	O3B
<i>x</i>	0.2474(1)	0.5023(6)	0.7558(6)	0.7504(1)	0.9108(6)	0.0901(8)	0.3869(2)	0.6252(1)
<i>y</i>	0.4203(4)	0.2488(9)	0.4308(7)	0.3200(2)	0.2943(9)	0.1687(9)	0.4543(5)	0.0270(5)
<i>z</i>	0.2524(6)	0.7527(6)	0.2589(8)	0.7777(9)	0.4363(1)	0.0635(3)	0.6343(2)	0.8388(1)
U_{iso}^*	2586(3)	2630(4)	552(4)	930(3)	930(3)	930(3)	930(3)	930(3)
Occ	1.000	1.000	0.336(3) 0.663(7)	1.000	1.000	1.000	1.000	1.000
R_P	0.169							
$R(F^2)$	0.124							

20	Ca	Ti	Ge,Si	O1	O2A	O2B	O3A	O3B
<i>x</i>	0.2315(1)	0.5062(2)	0.7460(1)	0.7490(6)	0.9007(9)	0.0840(9)	0.3824(1)	0.6381(7)
<i>y</i>	0.4175(2)	0.2530(1)	0.4316(4)	0.3174(2)	0.3160(6)	0.1929(6)	0.4736(6)	0.0462(6)
<i>z</i>	0.2476(6)	0.7404(4)	0.2577(6)	0.7673(8)	0.4501(8)	0.0714(9)	0.6462(2)	0.8449(3)
U_{iso}^*	2356(5)	2028(4)	1884(3)	922(4)	922(4)	922(4)	922(4)	922(4)
Occ	1.000	1.000	0.200(9) 0.799(1)	1.000	1.000	1.000	1.000	1.000
R_P	0.213							
$R(F^2)$	0.183							

10	Ca	Ti	Ge,Si	O1	O2A	O2B	O3A	03B
<i>x</i>	0.2311(1)	0.5061(7)	0.7350(9)	0.7503(9)	0.8786(5)	0.0714(9)	0.3680(8)	0.5993(3)
<i>y</i>	0.4186(9)	0.2510(4)	0.4318(9)	0.3214(5)	0.3219(2)	0.2034(1)	0.4772(4)	0.0461(4)
<i>z</i>	0.2519(1)	0.7354(8)	0.2468(1)	0.7826(1)	0.4454(1)	0.0670(1)	0.6593(1)	0.8530(2)
U_{iso}^*	2588(5)	2828(5)	1623(4)	541(4)	541(4)	541(4)	541(4)	541(4)
O_{cc}	1.000	1.000	0.096(7) 0.903(3)	1.000	1.000	1.000	1.000	1.000
R_p	0.201							
$R(F^2)$	0.187							

Table 5. Mean bond lengths (Å) at room temperature using SG P2₁/a.

Mol % Ge	Ge-O	Ti-O	Ca-O
CTGO	1.752	1.964	2.468
95	1.768	1.972	2.432
90	1.776	1.975	2.443
70	1.718	1.981	2.436
50	1.710	1.973	2.436
30	1.652	1.978	2.469
20	1.620	1.965	2.487
10	1.643	1.975	2.453
CTSO	1.651	1.957	2.432

Notes: bond lengths for titanite at $T = 298$ K is taken from Kek et al., 1997.

Table 6. CaTiOGeO₄. Lattice constants as a function of the temperature.

T (K)	a (Å)	b (Å)	c (Å)	β (°)
298	7.16144(6)	8.89229(2)	6.65311(4)	113.833(1)
348	7.16210(5)	8.89500(8)	6.65392(5)	113.828(1)
373	7.16264(7)	8.89658(6)	6.65428(6)	113.813(1)
398	7.16369(8)	8.89933(6)	6.65583(6)	113.806(1)
423	7.16373(6)	8.90061(7)	6.65640(8)	113.797(1)
448	7.16389(4)	8.90310(8)	6.65731(7)	113.787(1)
473	7.16336(7)	8.90510(5)	6.65812(8)	113.773(1)
498	7.16288(7)	8.90736(5)	6.65924(7)	113.758(1)
523	7.16210(6)	8.90963(6)	6.65999(5)	113.741(1)
548	7.16187(8)	8.91164(6)	6.66099(5)	113.729(1)
573	7.16135(5)	8.91345(7)	6.66185(8)	113.719(1)
593	7.16147(6)	8.91441(4)	6.66218(8)	113.711(1)
610	7.16198(6)	8.91560(6)	6.66303(7)	113.702(1)
613	7.16181(8)	8.91642(4)	6.66322(7)	113.701(1)
615	7.16197(7)	8.91662(5)	6.66319(5)	113.702(1)
618	7.16193(6)	8.91687(7)	6.66333(4)	113.699(1)
621	7.16194(7)	8.91732(9)	6.66382(6)	113.699(1)
623	7.16170(9)	8.91699(8)	6.66334(6)	113.700(2)
625	7.16202(6)	8.91760(7)	6.66384(6)	113.699(1)
628	7.16212(6)	8.91734(7)	6.66371(9)	113.695(1)
630	7.16209(8)	8.91754(8)	6.66398(6)	113.696(1)
633	7.16195(6)	8.91866(6)	6.66411(5)	113.697(1)
638	7.16211(7)	8.91843(6)	6.66405(8)	113.694(1)
643	7.16235(5)	8.91862(8)	6.66446(8)	113.693(2)
648	7.16201(5)	8.91959(9)	6.66490(7)	113.692(1)
653	7.16217(6)	8.91935(8)	6.66499(6)	113.692(1)
663	7.16273(6)	8.92046(7)	6.66530(6)	113.689(1)
673	7.16223(8)	8.92107(6)	6.66567(8)	113.686(1)
723	7.16361(7)	8.92515(6)	6.66807(7)	113.672(2)
748	7.16414(9)	8.92676(5)	6.66918(7)	113.665(1)
773	7.16433(6)	8.92847(7)	6.66989(6)	113.659(2)
823	7.16597(7)	8.93272(8)	6.67272(8)	113.653(1)
873	7.16718(7)	8.93646(7)	6.67470(4)	113.639(1)
923	7.16736(6)	8.93874(8)	6.67581(4)	113.631(1)
973	7.16906(8)	8.94262(9)	6.67852(5)	113.624(1)
1023	7.16993(8)	8.94597(7)	6.68077(6)	113.618(1)
1073	7.17204(7)	8.95028(5)	6.68332(7)	113.611(1)
1123	7.17332(8)	8.95395(6)	6.68559(6)	113.600(2)

Table 7. Lattice parameters for $\text{CaTi}(\text{Ge}_x\text{Si}_{1-x})\text{O}_4$ at room temperature.

Mol% Ge	a (Å)	b (Å)	c (Å)	β (°)	V (Å ³)
100	7.16144(6)	8.89229(2)	6.63921(4)	113.833(1)	387.633(5)
95	7.14287(6)	8.87820(6)	6.64268(3)	113.776(1)	385.500(5)
90	7.13460(4)	8.87346(4)	6.63886(9)	113.738(1)	384.738(7)
70	7.11815(6)	8.83215(7)	6.61777(5)	113.767(1)	380.765(6)
50	7.09534(4)	8.79173(3)	6.59620(8)	113.757(1)	376.606(6)
30	7.09137(7)	8.78567(7)	6.59344(5)	113.766(1)	375.952(6)
20	7.07182(5)	8.74371(5)	6.57304(7)	113.782(1)	371.925(4)
10	7.06582(8)	8.73056(7)	6.56626(5)	113.782(1)	370.668(5)

Table 8. CaTiO(Ge_xSi_{1-x})O₄. Lattice constants and volume for all intermediate samples as a function of temperature.

Mol% Ge						
95	<i>T</i> (K)	<i>a</i> (Å)	<i>b</i> (Å)	<i>c</i> (Å)	β (°)	<i>V</i> (Å ³)
	298	7.14287(6)	8.87820(6)	6.64268(3)	113.776(1)	385.499(5)
	348	7.14647(5)	8.88337(3)	6.64555(5)	113.760(1)	386.132(7)
	373	7.14706(2)	8.88464(4)	6.64592(5)	113.754(1)	386.258(7)
	398	7.14737(5)	8.88676(2)	6.64694(3)	113.742(1)	386.462(4)
	423	7.14756(4)	8.89055(5)	6.64837(9)	113.736(1)	386.738(5)
	448	7.14767(3)	8.89170(3)	6.64938(6)	113.725(1)	386.886(5)
	473	7.14734(8)	8.89396(2)	6.64978(2)	113.718(1)	387.010(5)
	498	7.14711(9)	8.89461(2)	6.65090(2)	113.712(1)	387.109(6)
	523	7.14712(6)	8.89802(5)	6.65209(3)	113.698(1)	387.369(5)
	538	7.14695(8)	8.89862(5)	6.65264(4)	113.696(1)	387.424(8)
	553	7.14680(9)	8.89817(5)	6.65189(9)	113.688(1)	387.376(8)
	573	7.14694(4)	8.90147(7)	6.65388(3)	113.674(1)	387.685(5)
	598	7.14705(3)	8.90228(2)	6.65382(4)	113.671(1)	387.731(4)
	623	7.14813(2)	8.90455(6)	6.65555(5)	113.666(1)	388.005(5)
	648	7.14846(8)	8.90608(4)	6.65623(2)	113.658(1)	388.153(7)
	673	7.14920(4)	8.90864(3)	6.65783(4)	113.657(1)	388.401(5)
	723	7.15006(7)	8.91079(6)	6.65960(8)	113.650(1)	388.665(7)
	748	7.15069(7)	8.91340(7)	6.66077(8)	113.634(1)	388.929(7)
	773	7.15125(4)	8.91418(7)	6.66133(5)	113.634(1)	389.026(6)
90	<i>T</i> (K)	<i>a</i> (Å)	<i>b</i> (Å)	<i>c</i> (Å)	β (°)	<i>V</i> (Å ³)
	298	7.13460(4)	8.87346(4)	6.63886(9)	113.738(1)	384.738(7)
	348	7.14113(8)	8.87499(4)	6.63976(5)	113.749(1)	385.176(8)
	373	7.14133(4)	8.87841(8)	6.64205(3)	113.748(1)	385.471(7)
	398	7.14119(3)	8.87860(5)	6.64165(5)	113.730(1)	385.502(5)
	423	7.14152(8)	8.88024(3)	6.64214(5)	113.734(1)	385.608(6)
	448	7.14142(7)	8.88428(2)	6.64445(2)	113.714(1)	385.971(5)
	473	7.14149(6)	8.88643(2)	6.64454(2)	113.695(1)	386.130(5)
	498	7.14142(4)	8.88907(3)	6.64646(4)	113.697(1)	386.346(5)
	523	7.14139(5)	8.89066(8)	6.64755(6)	113.679(1)	386.530(6)
	538	7.14130(4)	8.89045(9)	6.64718(3)	113.678(1)	386.498(8)
	553	7.14157(5)	8.89320(2)	6.64835(3)	113.670(1)	386.724(4)
	573	7.14144(5)	8.89336(6)	6.64824(4)	113.666(1)	386.729(5)
	598	7.14210(6)	8.89477(2)	6.65013(4)	113.675(1)	386.909(5)
	623	7.14228(6)	8.89792(3)	6.65069(4)	113.660(1)	387.133(5)
	648	7.14255(5)	8.89994(4)	6.65228(5)	113.657(1)	387.337(5)
	673	7.14297(5)	8.90114(8)	6.65305(6)	113.648(1)	387.484(6)
	723	7.14431(3)	8.90371(7)	6.65514(3)	113.638(1)	387.820(5)
	748	7.14506(8)	8.90570(3)	6.65582(6)	113.642(1)	387.975(6)
	773	7.14521(6)	8.90710(3)	6.65645(5)	113.631(1)	388.113(5)

70	T (K)	a (Å)	b (Å)	c (Å)	β (°)	V (Å ³)
	298	7.11815(6)	8.83215(7)	6.61777(5)	113.767(1)	380.765(6)
	348	7.12381(2)	8.83903(4)	6.62137(3)	113.763(1)	381.584(6)
	373	7.12413(2)	8.84111(3)	6.62210(7)	113.744(1)	381.789(7)
	398	7.12421(6)	8.84201(2)	6.62165(3)	113.739(1)	381.821(5)
	423	7.12425(6)	8.84669(5)	6.62504(3)	113.746(1)	382.200(5)
	448	7.12430(7)	8.84693(4)	6.62420(7)	113.730(1)	382.212(6)
	473	7.12433(4)	8.84845(3)	6.62605(2)	113.726(1)	382.397(4)
	498	7.12415(5)	8.85115(5)	6.62817(2)	113.726(1)	382.627(5)
	523	7.12325(3)	8.85297(6)	6.62804(6)	113.716(1)	382.679(5)
	538	7.12227(4)	8.85003(5)	6.62689(4)	113.701(1)	382.477(7)
	553	7.12302(7)	8.85325(5)	6.62790(3)	113.704(1)	382.706(6)
	573	7.12426(6)	8.85441(2)	6.62946(2)	113.697(1)	382.933(5)
	598	7.12469(8)	8.85736(3)	6.63095(5)	113.702(1)	383.155(6)
	623	7.12526(9)	8.85996(3)	6.63219(5)	113.692(1)	383.399(6)
	648	7.12559(5)	8.86257(4)	6.63300(6)	113.686(1)	383.595(6)
	673	7.12616(4)	8.86378(4)	6.63321(3)	113.668(1)	383.743(4)
	723	7.12667(5)	8.86568(4)	6.63530(5)	113.663(1)	383.988(5)
	748	7.12720(5)	8.86802(7)	6.63593(4)	113.653(1)	384.184(6)
	773	7.12749(5)	8.87007(9)	6.64071(9)	113.663(1)	384.536(8)

50	T (K)	a (Å)	b (Å)	c (Å)	β (°)	V (Å ³)
	298	7.09534(4)	8.79173(3)	6.59620(8)	113.757(1)	376.606(6)
	348	7.09631(4)	8.79439(5)	6.59834(6)	113.743(1)	376.934(7)
	373	7.09652(5)	8.79699(4)	6.59746(5)	113.719(1)	377.076(7)
	398	7.09696(3)	8.79826(4)	6.60112(3)	113.732(1)	377.325(4)
	423	7.09680(4)	8.79985(3)	6.60135(3)	113.726(1)	377.415(4)
	448	7.09668(4)	8.80112(5)	6.60297(3)	113.720(1)	377.573(5)
	473	7.09652(2)	8.80352(3)	6.60253(4)	113.708(1)	377.677(4)
	498	7.09626(6)	8.80481(2)	6.60435(5)	113.701(1)	377.843(5)
	523	7.09595(3)	8.80544(4)	6.60452(4)	113.694(1)	377.884(2)
	538	7.09600(5)	8.80625(5)	6.60514(5)	113.688(1)	377.974(4)
	553	7.09630(6)	8.80719(3)	6.60473(2)	113.685(1)	378.016(7)
	573	7.09680(5)	8.80912(3)	6.60629(3)	113.686(1)	378.212(5)
	598	7.09728(3)	8.81038(3)	6.60715(5)	113.684(1)	378.346(4)
	623	7.09783(3)	8.81203(4)	6.60890(5)	113.675(1)	378.573(5)
	648	7.09876(5)	8.81293(4)	6.60968(4)	113.680(1)	378.691(5)
	673	7.09929(8)	8.81510(5)	6.61082(4)	113.675(1)	378.893(5)
	723	7.10002(2)	8.81907(3)	6.61305(2)	113.659(1)	379.276(6)
	748	7.10035(8)	8.82034(2)	6.61341(4)	113.655(1)	379.381(4)
	773	7.10110(2)	8.82169(2)	6.61414(5)	113.648(1)	379.541(4)
	823	7.10233(4)	8.82624(5)	6.61724(2)	113.648(1)	379.981(4)
	873	7.10408(3)	8.83051(3)	6.61957(3)	113.628(1)	380.450(4)
	923	7.10587(3)	8.83419(4)	6.62194(7)	113.637(1)	380.815(5)
	973	7.10802(3)	8.83675(5)	6.62363(4)	113.630(1)	381.158(5)
	1023	7.11005(2)	8.83970(2)	6.62657(7)	113.624(1)	381.581(5)
	1073	7.11124(6)	8.84256(2)	6.62915(5)	113.634(1)	381.888(5)

30	T (K)	a (Å)	b (Å)	c (Å)	β (°)	V (Å ³)
	298	7.09137(7)	8.78567(7)	6.59344(5)	113.766(1)	375.952(6)
	348	7.09543(3)	8.78949(4)	6.59622(3)	113.761(1)	376.504(6)
	373	7.09579(3)	8.79050(4)	6.59741(2)	113.757(1)	376.646(6)
	398	7.09623(4)	8.79283(8)	6.59830(4)	113.743(1)	376.861(5)
	423	7.09585(4)	8.79614(5)	6.59990(4)	113.737(1)	377.091(5)
	448	7.09581(2)	8.79722(3)	6.60024(3)	113.728(1)	377.181(4)
	473	7.09562(6)	8.79879(5)	6.60066(3)	113.727(1)	377.265(5)
	498	7.09531(4)	8.80033(5)	6.60191(2)	113.720(1)	377.406(4)
	523	7.09484(3)	8.79958(6)	6.60096(5)	113.704(1)	377.341(5)
	538	7.09545(3)	8.80202(6)	6.60225(5)	113.708(1)	377.540(7)
	553	7.09609(5)	8.80377(6)	6.60352(3)	113.705(1)	377.731(5)
	573	7.09678(5)	8.80534(2)	6.60476(3)	113.699(1)	377.923(4)
	598	7.09714(4)	8.80647(6)	6.60513(2)	113.691(1)	378.035(5)
	623	7.09812(6)	8.80849(4)	6.60609(5)	113.692(1)	378.226(5)
	648	7.09888(6)	8.81083(7)	6.60826(8)	113.686(1)	378.509(7)
	673	7.09940(3)	8.81288(7)	6.60883(3)	113.682(1)	378.669(5)
	723	7.10052(3)	8.81609(5)	6.61132(2)	113.676(1)	379.027(4)
	748	7.10116(3)	8.81861(4)	6.61224(7)	113.667(1)	379.248(5)
	773	7.10242(6)	8.81878(4)	6.61352(9)	113.669(1)	379.390(7)

20	T (K)	a (Å)	b (Å)	c (Å)	β (°)	V (Å ³)
	298	7.07182(5)	8.74371(5)	6.57304(7)	113.782(1)	371.925(4)
	348	7.07100(2)	8.74596(3)	6.57382(4)	113.762(1)	372.079(6)
	373	7.07106(3)	8.74789(4)	6.57433(3)	113.754(1)	372.216(6)
	398	7.07110(3)	8.75089(5)	6.57609(5)	113.737(1)	372.494(5)
	423	7.07094(4)	8.75149(6)	6.57663(3)	113.732(1)	372.556(5)
	448	7.07037(2)	8.75287(6)	6.57822(4)	113.726(1)	372.692(5)
	473	7.06987(3)	8.75434(6)	6.57883(6)	113.728(1)	372.757(5)
	498	7.06898(4)	8.75630(4)	6.57948(5)	113.713(1)	372.873(5)
	523	7.07041(3)	8.75795(3)	6.58036(3)	113.702(1)	373.100(4)
	538	7.07034(5)	8.75784(2)	6.58134(2)	113.702(1)	373.147(6)
	553	7.07078(4)	8.75905(5)	6.58149(6)	113.703(1)	373.228(5)
	573	7.07088(6)	8.76108(3)	6.58317(2)	113.697(1)	373.432(5)
	598	7.07186(4)	8.76316(2)	6.58388(3)	113.689(1)	373.636(4)
	623	7.07194(5)	8.76498(2)	6.58532(4)	113.688(1)	373.802(5)
	648	7.07270(3)	8.76573(4)	6.58618(3)	113.685(1)	373.932(4)
	673	7.07365(3)	8.76844(5)	6.58708(3)	113.680(1)	374.163(4)
	723	7.07459(4)	8.77072(5)	6.58890(5)	113.668(1)	374.448(5)
	748	7.07520(3)	8.77232(6)	6.59070(4)	113.674(1)	374.634(5)
	773	7.07561(3)	8.77320(9)	6.59159(9)	113.666(1)	374.766(7)

10 T (K)	a (Å)	b (Å)	c (Å)	β (°)	V (Å ³)
298	7.06582(8)	8.73056(7)	6.56626(5)	113.782(1)	370.688(5)
348	7.06614(3)	8.73244(5)	6.56710(4)	113.785(1)	370.803(7)
373	7.06639(4)	8.73440(5)	6.56902(8)	113.773(1)	371.042(8)
398	7.06670(6)	8.73544(5)	6.56912(4)	113.762(1)	371.140(5)
423	7.06649(5)	8.73730(6)	6.57024(3)	113.756(1)	371.288(5)
448	7.06518(5)	8.73902(5)	6.57146(5)	113.736(1)	371.418(5)
473	7.06417(6)	8.74068(5)	6.57327(5)	113.735(1)	371.541(6)
498	7.06480(7)	8.74230(5)	6.57364(5)	113.726(1)	371.690(6)
523	7.06515(5)	8.74452(4)	6.57533(6)	113.722(1)	371.909(5)
538	7.06528(4)	8.74499(8)	6.57590(8)	113.720(1)	371.974(8)
553	7.06531(5)	8.74638(4)	6.57629(4)	113.714(1)	372.074(5)
573	7.06558(4)	8.74743(6)	6.57690(4)	113.711(1)	372.176(5)
598	7.06633(4)	8.74917(7)	6.57798(8)	113.702(1)	372.376(6)
623	7.06637(7)	8.75074(4)	6.57928(5)	113.698(1)	372.530(6)
648	7.06674(5)	8.75207(6)	6.58052(4)	113.704(1)	372.660(5)
673	7.06723(4)	8.75432(4)	6.58209(4)	113.701(1)	372.660(5)
723	7.06857(8)	8.75753(5)	6.58325(6)	113.681(1)	373.209(6)
748	7.06897(4)	8.75765(5)	6.58401(7)	113.683(1)	373.273(6)
773	7.07010(7)	8.75874(5)	6.58445(8)	113.671(2)	373.438(7)

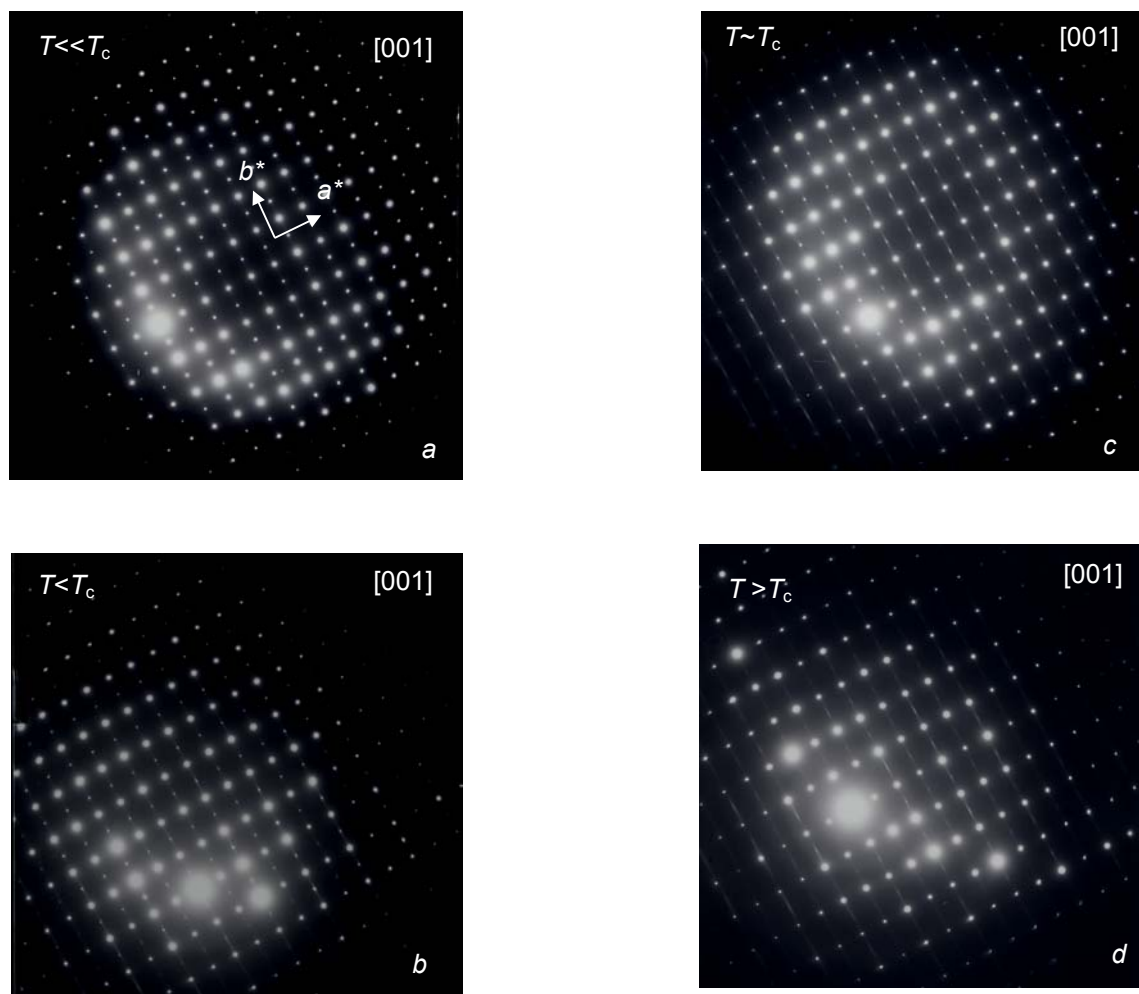


Fig. 1. Evolution of the electron diffraction patterns with temperature for the zone [001]. With increasing temperature the streaking along \mathbf{b}^* increases in the zone. At $T > T_c$ the spots with $k + l = \text{odd}$ have disappeared.

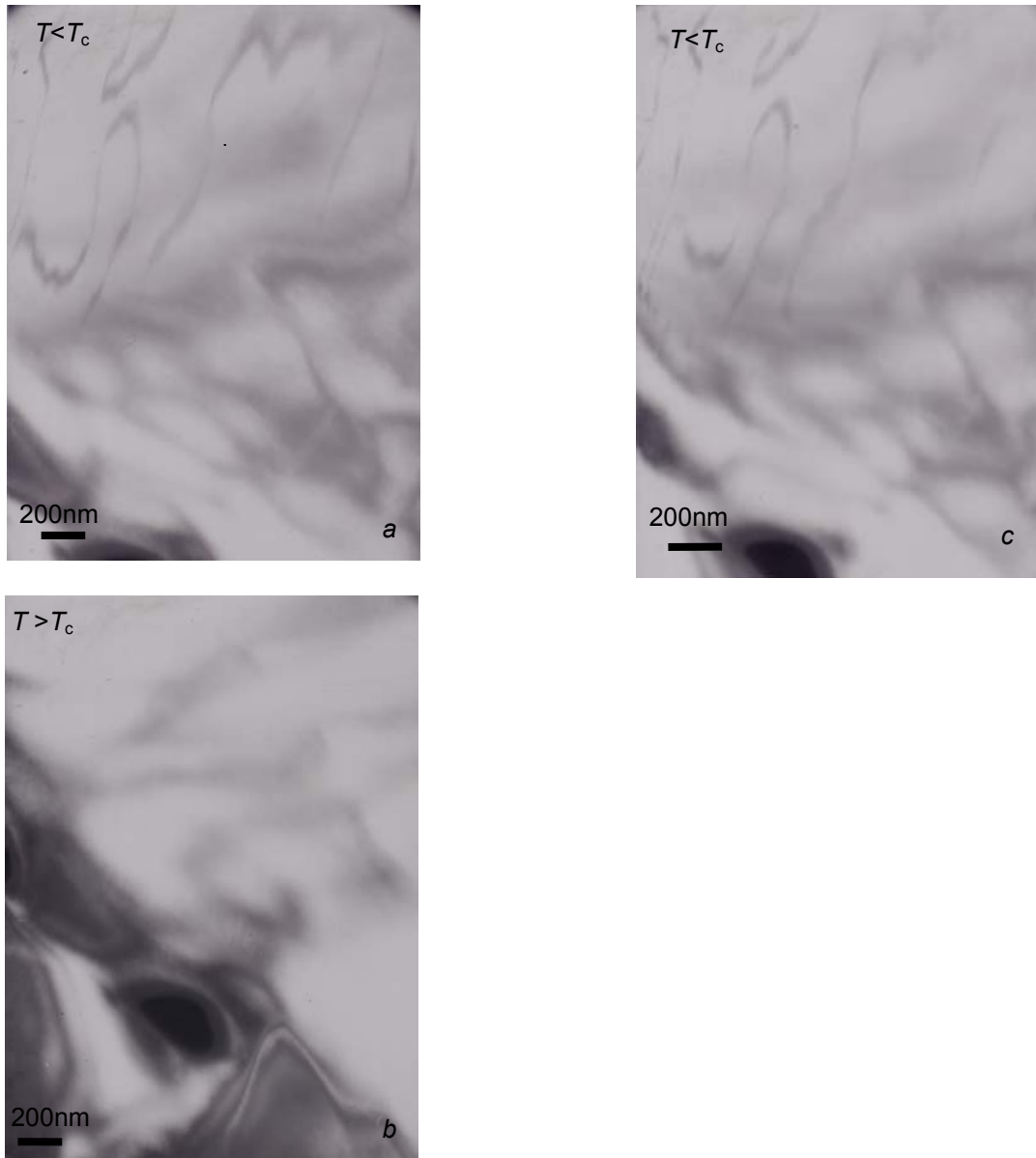


Fig. 2. Diffraction contrast images of domain boundaries as a function of temperature. The domain boundaries disappear at some temperature above T_c but appear at the same place when decreasing the temperature.

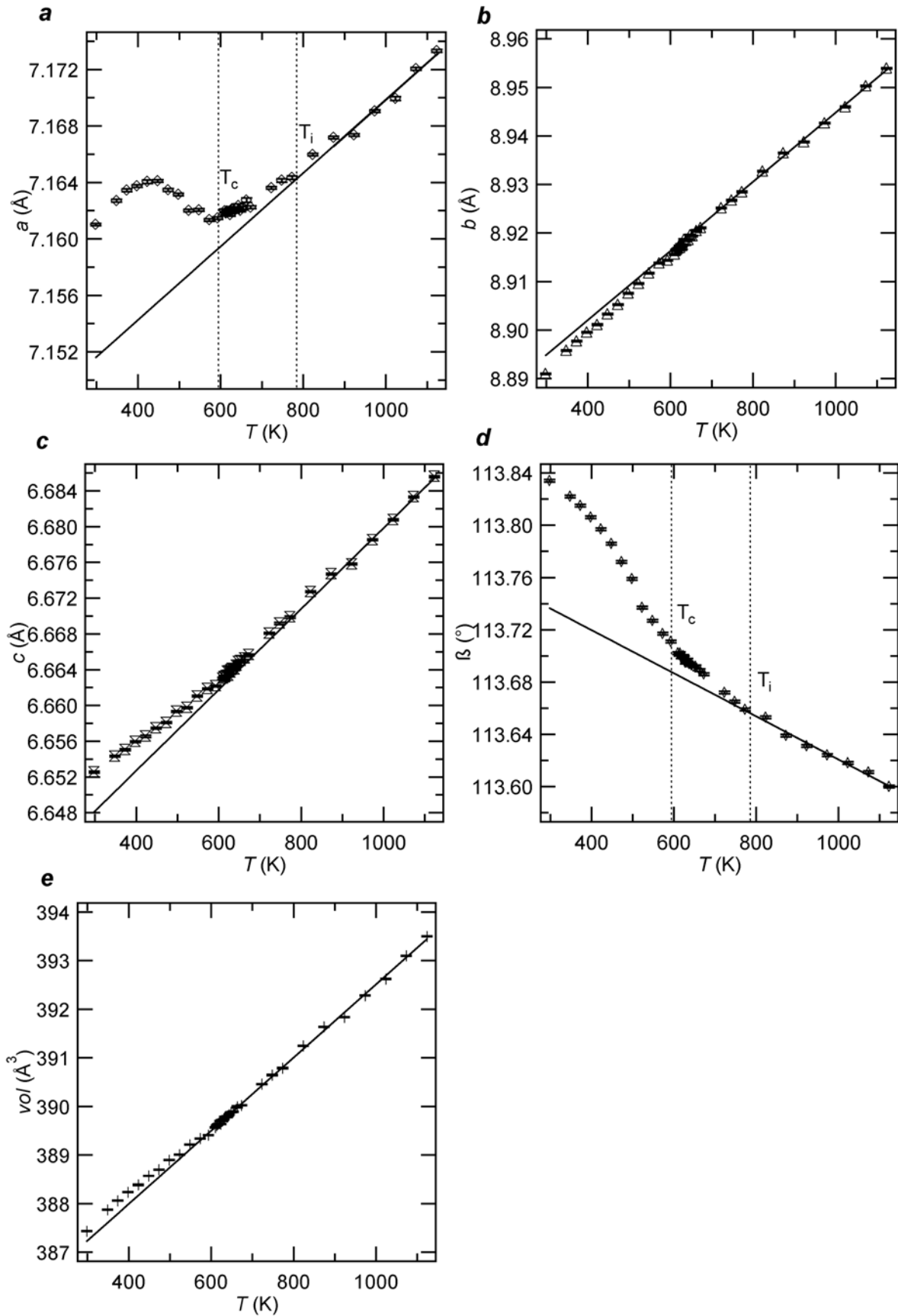


Fig. 3 Temperature plots of CaTiOGeO₄ lattice parameters. The straight lines have been obtained by fitting the data for $T < 1123$ K and extrapolating them towards lower temperatures. The perpendicular dashed lines in (a) and (d) indicate the position of the T_c (588 K) and the T_i (775 K) transition respectively.

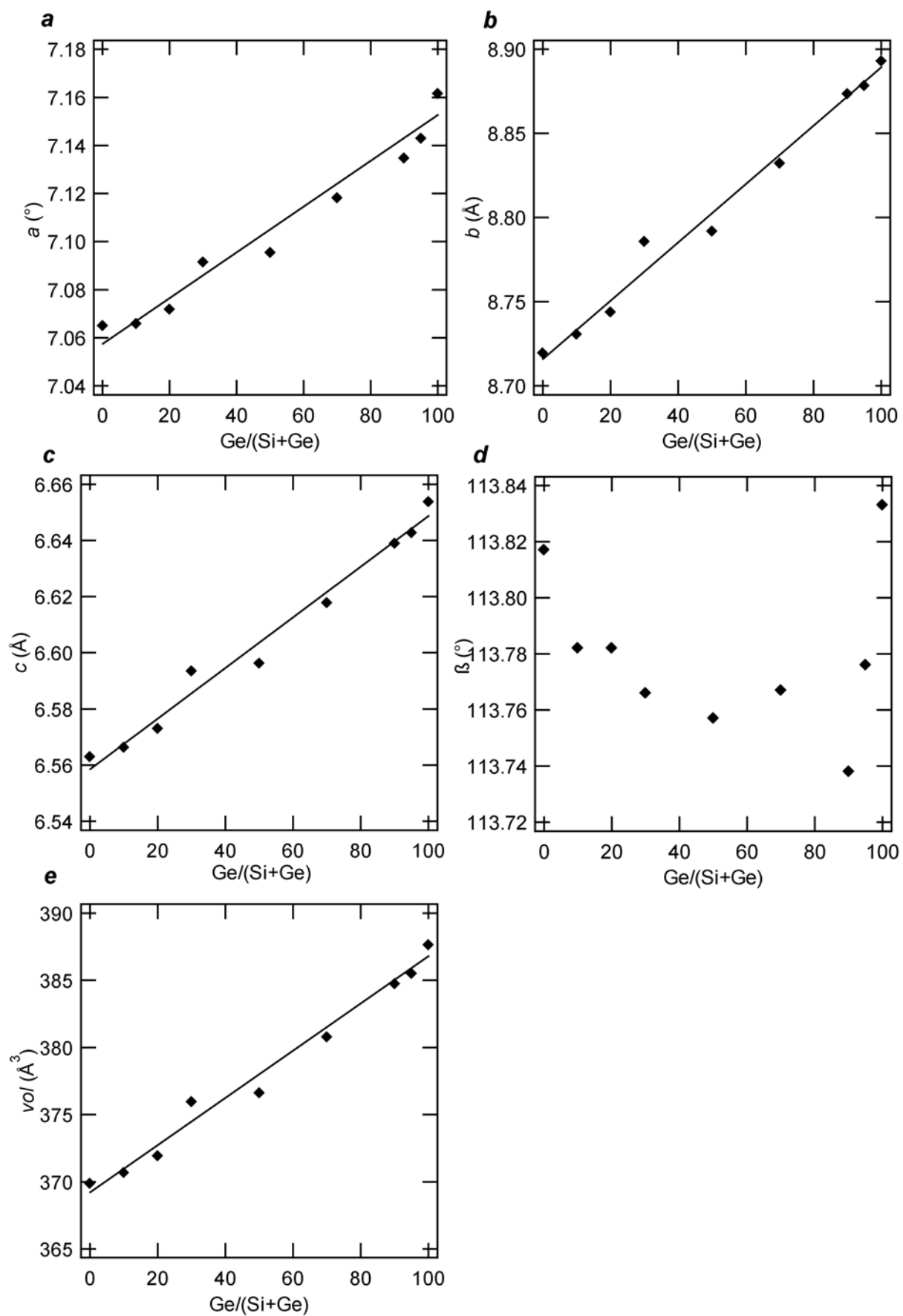


Fig. 4. The solid solution $\text{CaTiO}(\text{Ge}_x\text{Si}_{1-x})\text{O}_4$. Lattice constants as a function of Ge-content at room temperature.

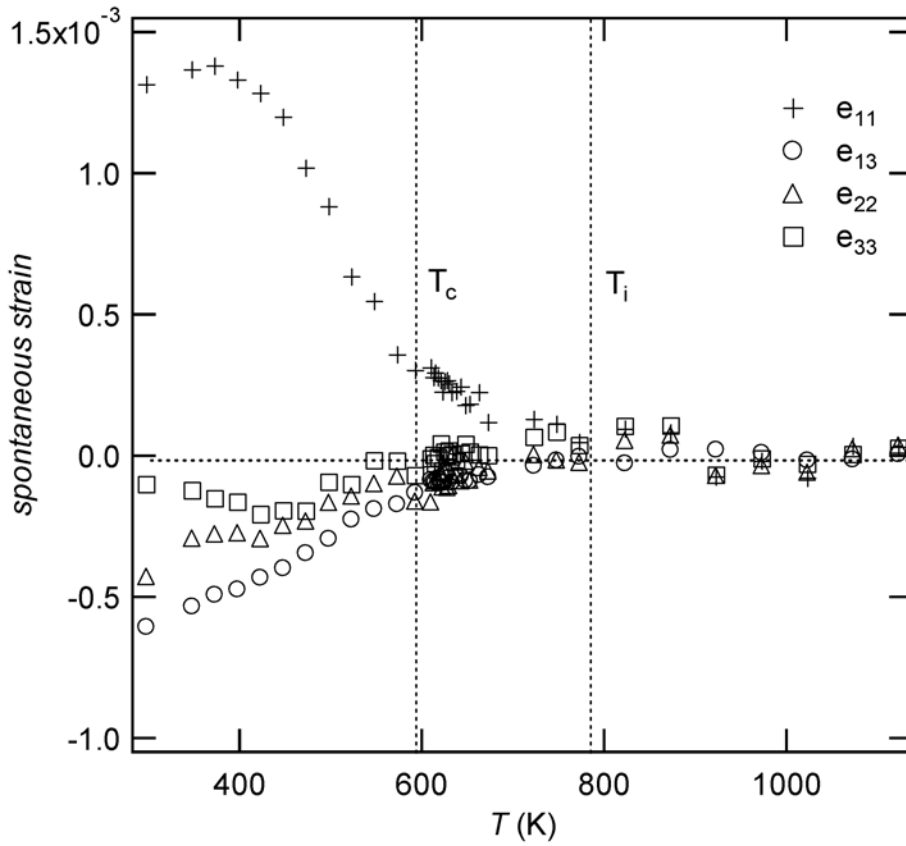


Fig. 5. Strain components for CaTiOGeO_4 as a function of temperature. Only the components e_{11} and e_{13} contribute significantly to the strain.

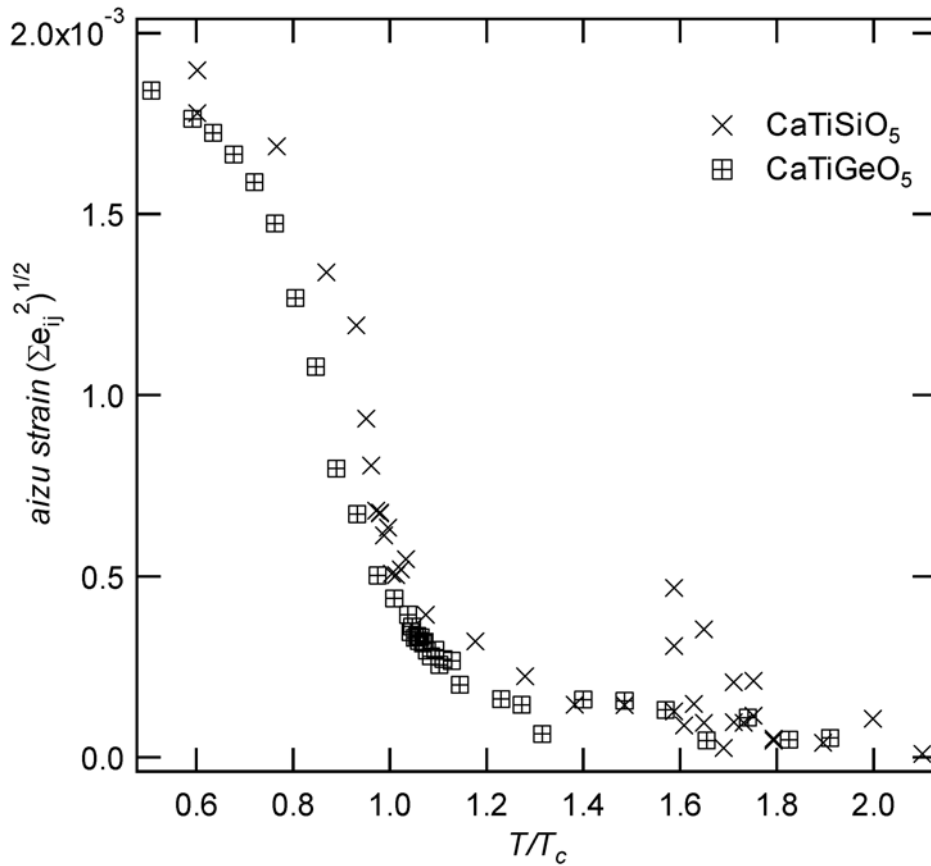


Fig. 6. The scalar strain (aizu strain) for CaTiOGeO_4 and titanite (data from Malcherek 2001) as a function of temperature.

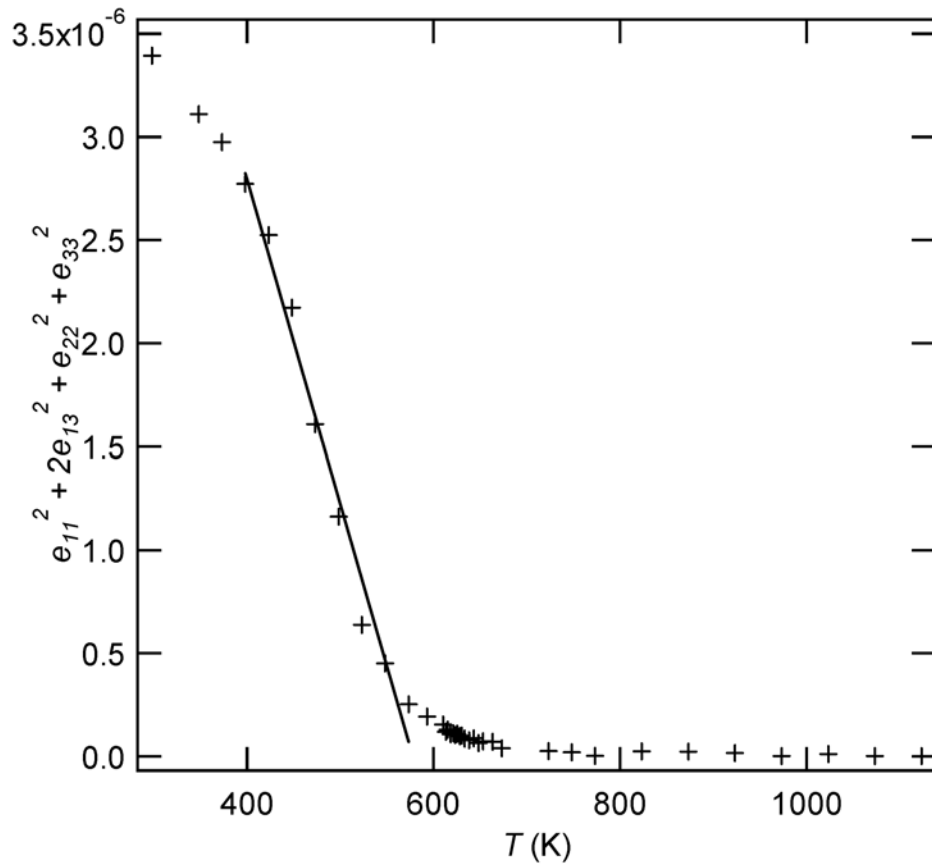


Fig. 7. The square of the scalar strain for CaTiOGeO_4 . The linearity at $T < T_c = 588$ K indicates the tricritical behaviour.

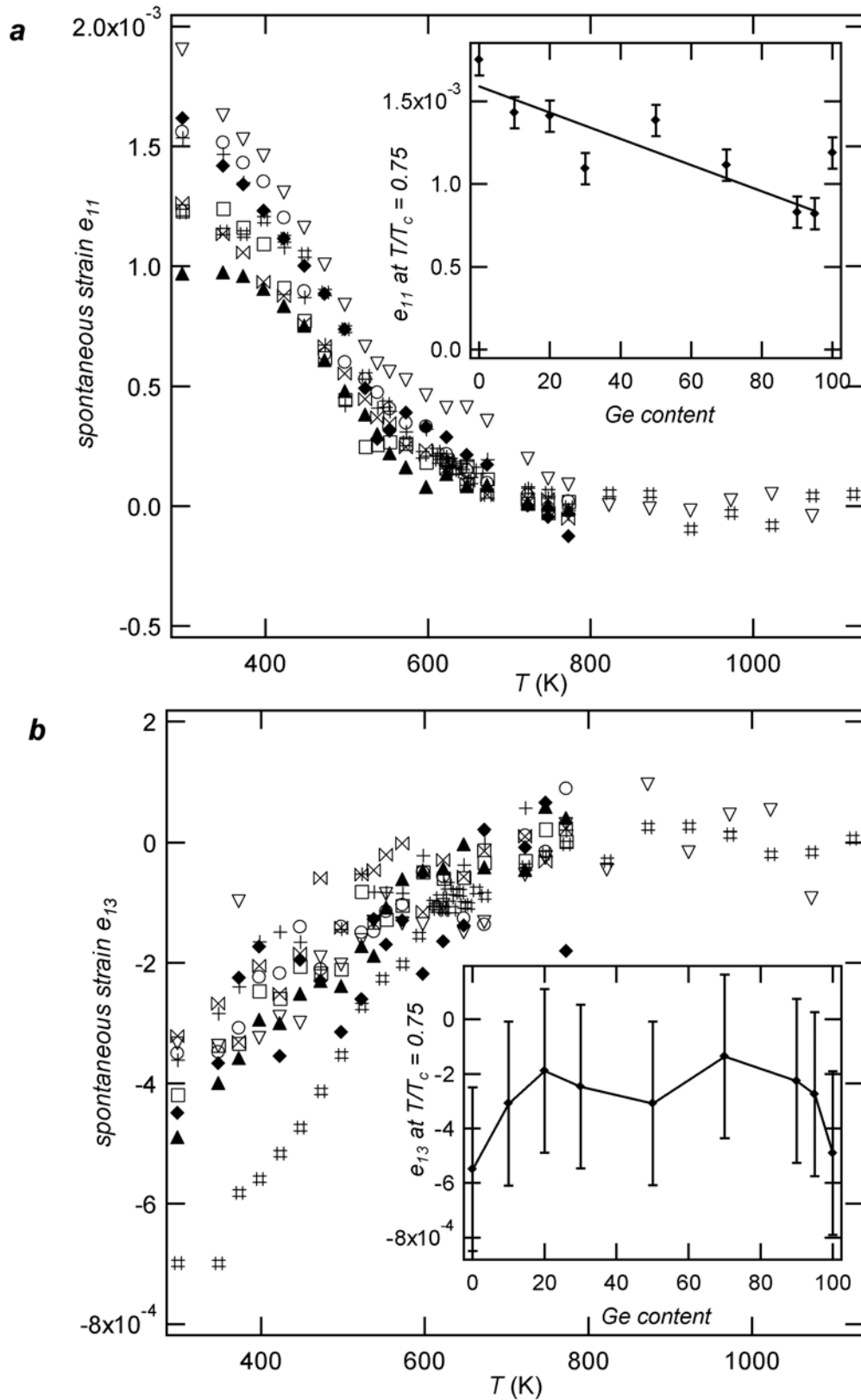


Fig. 8 Strain components e_{11} (a), e_{13} (b), e_{22} (c) and the scalar strain (d) for all intermediate compounds as a function of temperature. Inserted are the strain components at the reduced temperature $T/T_c = 0.75$ as a function of Ge content. The legend is:

- $\text{Ge}_{10}\text{Si}_{90}$ □ $\text{Ge}_{30}\text{Si}_{70}$ ▽ $\text{Ge}_{50}\text{Si}_{50}$ ◆ $\text{Ge}_{70}\text{Si}_{30}$ ⊠ $\text{Ge}_{90}\text{Si}_{10}$
- ▲ $\text{Ge}_{95}\text{Si}_{05}$ # CaTiGeO_5

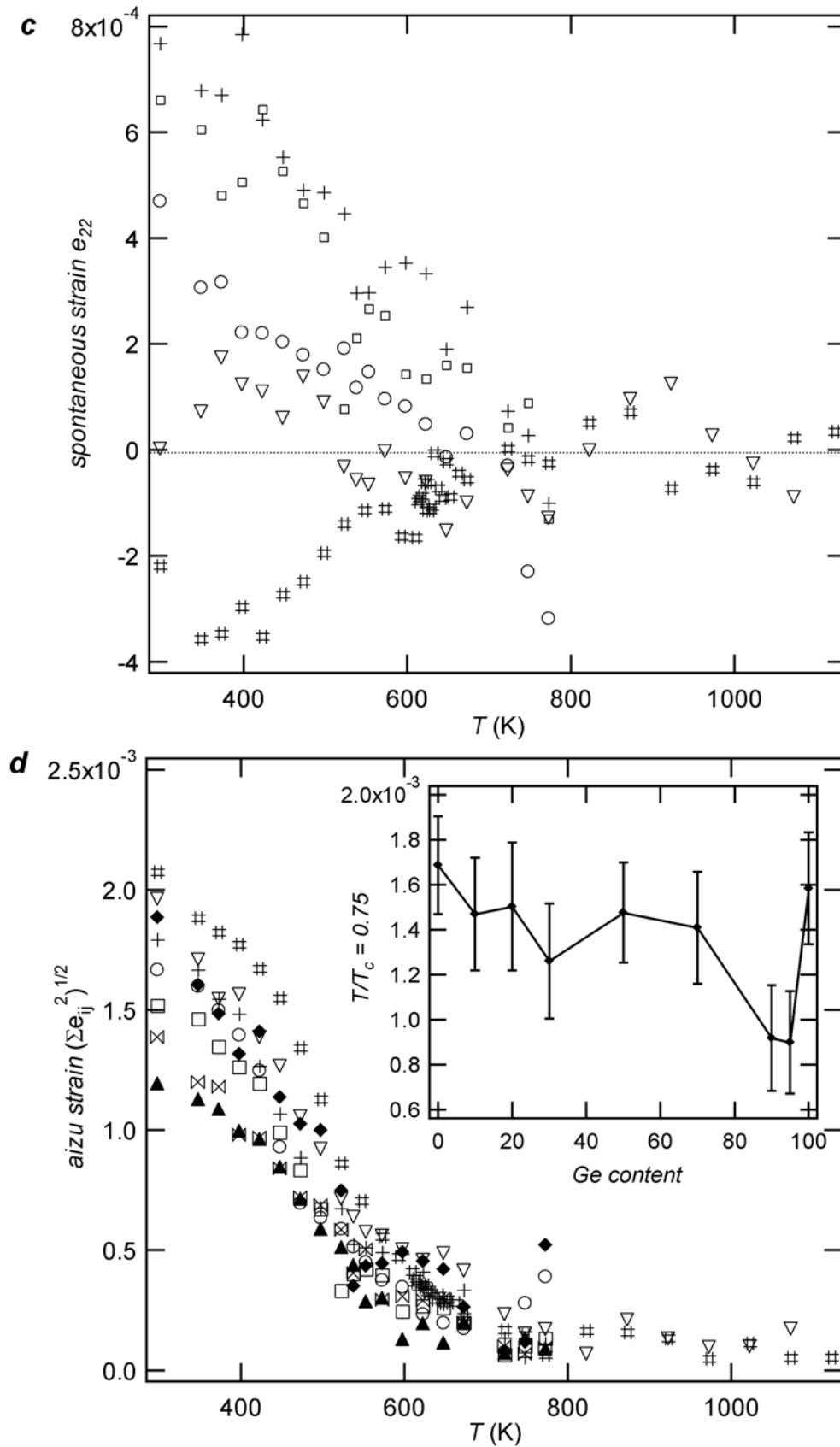


Fig. 8 Strain components e_{11} (a), e_{13} (b), e_{22} (c) and the scalar strain (d) for all intermediate compounds as a function of temperature. Inserted are the strain components at the reduced temperature $T/T_c = 0.75$ as a function of Ge content. The legend is:

- $\text{Ge}_{10}\text{Si}_{90}$ + $\text{Ge}_{20}\text{Si}_{80}$ □ $\text{Ge}_{30}\text{Si}_{70}$ ▽ $\text{Ge}_{50}\text{Si}_{50}$ ◆ $\text{Ge}_{70}\text{Si}_{30}$ ⋈ $\text{Ge}_{90}\text{Si}_{10}$
- ▲ $\text{Ge}_{95}\text{Si}_{05}$ # CaTiGeO_5

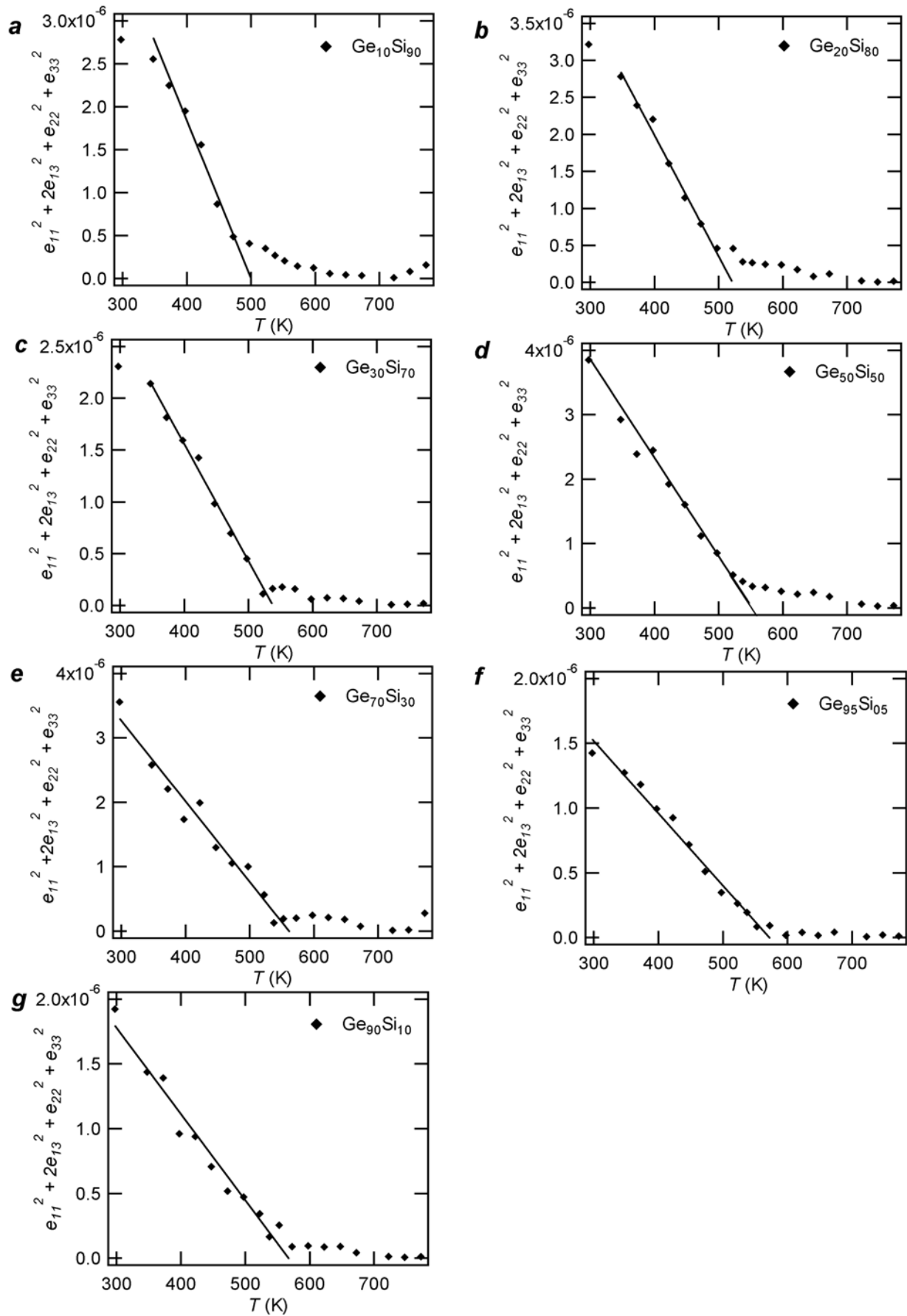


Fig. 9. The square of the scalar strain for all intermediate compositions. The relationship is linear with temperature and implies that the transition is tricritical in character.

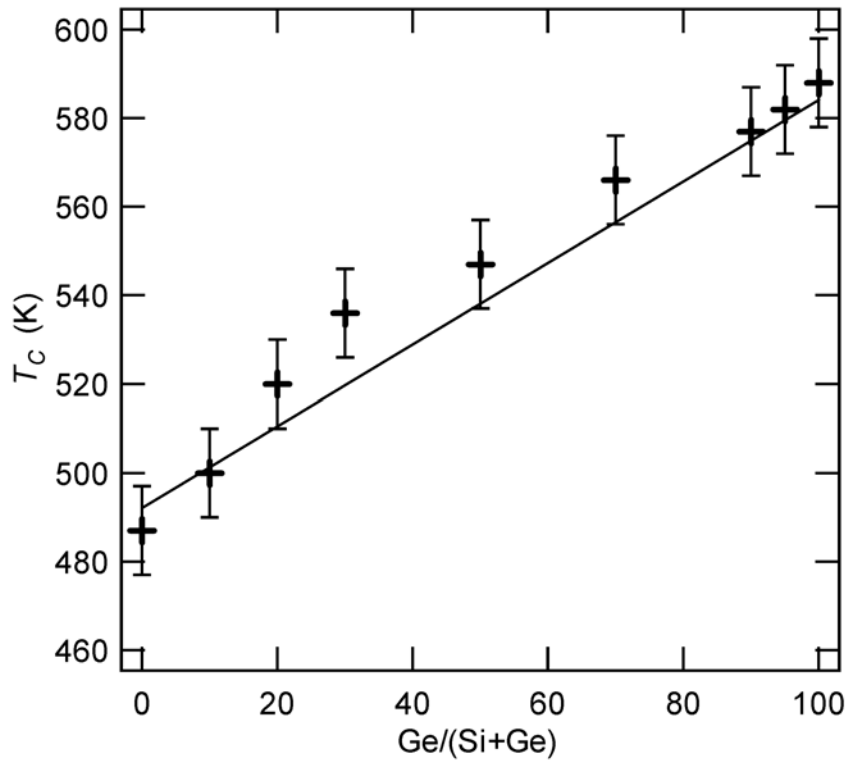


Fig. 10. Transition temperature, T_c across the solid solution, $\text{CaTiO}(\text{Ge}_x\text{Si}_{1-x})\text{O}_4$. $T_c = 588$ K for CaTiOGeO_4 and 487 K for titanite.

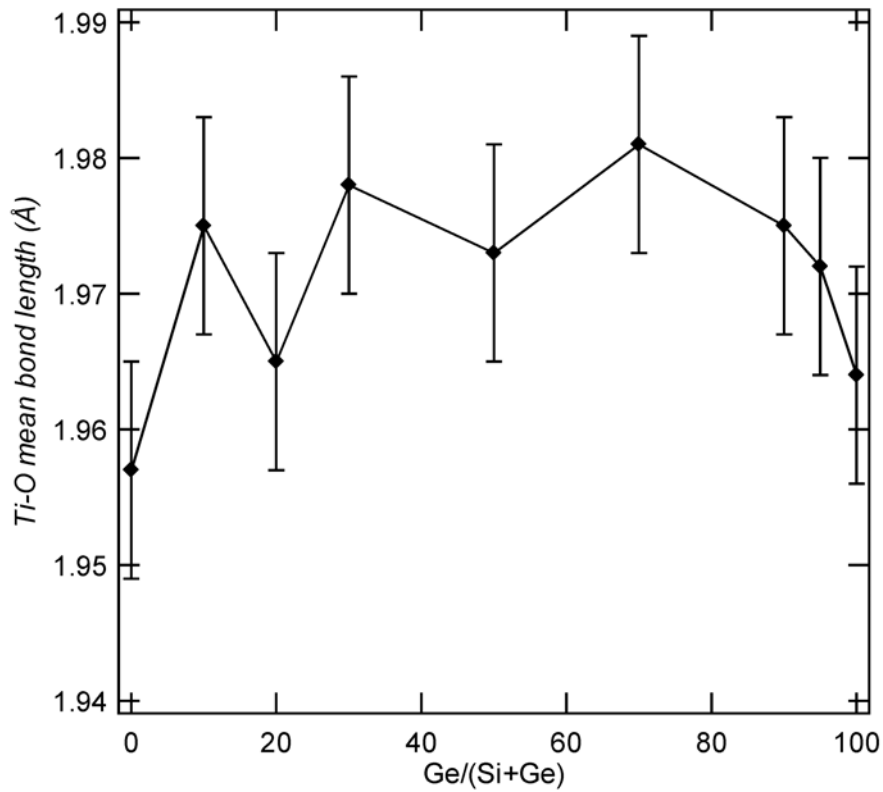


Fig. 11. The mean bond length Ti-O as a function of Ge content (*a*) and the strain component e_{13} at the reduced temperature $T_c/T=0.75$ as a function of Ge content (*b*).

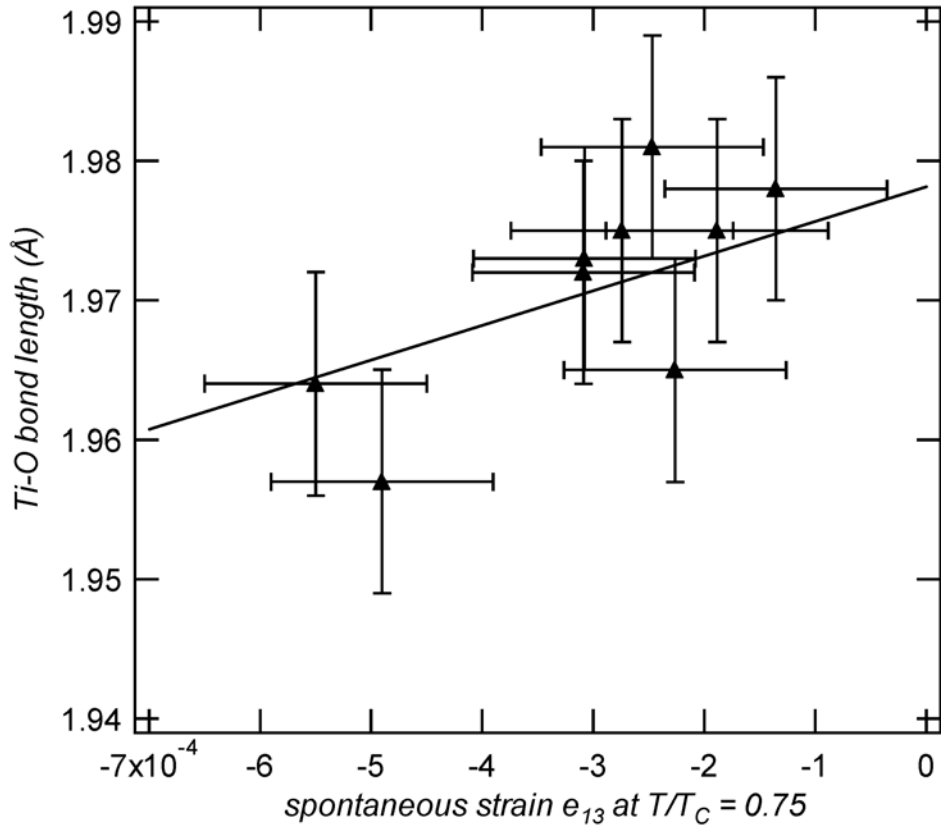


Fig. 12. Correlation between Ti-O and the shear strain e_{13} .

4. The structure of SrTiOGeO_4 and its solid solution with CaTiOGeO_4

A scientific manuscript submitted to *Physics and Chemistry of Minerals*

October 2004

Authors:

Rikke Ellemann-Olesen
Universität Heidelberg, Mineralogisches Institut, Im Neuenheimer Feld 236
69120 Heidelberg, Germany

Thomas Malcherek
Universität Heidelberg, Mineralogisches Institut, Im Neuenheimer Feld 236
69120 Heidelberg, Germany

Abstract

Solid solubility and structural phase transitions in $(\text{Ca}_x\text{Sr}_{1-x})\text{TiOGeO}_4$ have been studied by means of *in situ* high temperature X-ray powder diffraction. The displacive $\text{A}2/a - \text{P}2_1/a$ phase transition analogous to titanite has been followed across the solid solution. Strain analysis indicates a transition temperature of $T_c = 594 \pm 10$ K for SrTiOGeO_4 and the additional occurrence of an isosymmetric anomaly at $T_i = 800 \pm 25$ K, in analogy to the isomorphous compound CaTiOGeO_4 . Lattice parameters as a function of temperature and composition have been determined by X-ray powder diffraction between room temperature and a maximum of 1123 K. The e_{11} and e_{13} components dominate the strain tensor. All compositions across the solid solution exhibit close to tricritical phase transitions $\text{P}2_1/a - \text{A}2/a$. The critical temperature remains almost unaffected by substitution of Sr for Ca, but the magnitude of the spontaneous strain drops significantly with even small amounts of Sr present.

1. Introduction

Recent studies of solid solutions in the titanite structure field have shown that the stability of the ordered $\text{P}2_1/a$ phase of the titanite structure of generalized stoichiometry AMOXO_4 does depend not only on the nature of the octahedrally coordinated cation $\text{M} = \text{Ti}, \text{Al}, \text{Sn}, \text{Zr}$ (Oberti *et al.*, 1990; Groat *et al.*, 1996; Kunz *et al.*, 1997; Troitzsch *et al.*, 1999, Ellemann-Olesen and Malcherek, 2004b), but also on the tetrahedrally coordinated cation $\text{X} = \text{Si}, \text{Ge}$ (Ellemann-Olesen and Malcherek, 2004a). While these M and X cations are a part of the framework of parallel octahedral chains and laterally connecting isolated tetrahedra characteristic for titanite (Speer and Gibbs, 1976), the A cation represented by Ca in titanite, CaTiOSiO_4 , is needed to charge balance the residual charge of the framework. In the context of the $\text{P}2_1/a - \text{A}2/a$ phase transition observed in titanite (Speer and Gibbs, 1976; Taylor and Brown, 1976; Ghose *et al.*, 1991) the Ca cation appears to be disordered across a split position (Kek *et al.*, 1997) in the high temperature phase. Given the lack of known isovalent substitutions on the Ca-site, so far nothing is known about the effects of such substitutions towards the character and the critical temperature of the $\text{P}2_1/a - \text{A}2/a$ phase transition.

The displacive phase transition $\text{P}2_1/a - \text{A}2/a$ in CaTiOSiO_4 has been studied using a large number of methods (*e.g.* Ghose *et al.*, 1991; Bismayer *et al.*, 1992; Salje *et al.*, 1993, Zhang *et al.*, 1995). One experimental method that is very effective in locating the phase transition is the measurement of spontaneous strain by X-ray powder diffraction (Carpenter *et al.*, 1998). This has been applied to the structural phase transitions in titanite (Malcherek, 2001), which

showed that the strain tensor, when referred to the $A2/a$ space group setting of titanite, is rather simple, with only e_{11} and e_{13} significantly deviating from zero. The shear component e_{13} remains non-zero even above the transition to the nominally end-centered $A2/a$ phase and vanishes above 800 K. Similar studies have recently been conducted for $\text{CaTiO}(\text{Ge}_x\text{Si}_{1-x})\text{O}_4$ (Ellemann-Olesen and Malcherek, 2004a), where it was found that the strain evolution of these germanate-titanites is very similar to the silicate. Here we report on solid solution between CaTiOGeO_4 and SrTiOGeO_4 , tracking the occurring structural phase transitions by means of strain analysis.

2. Experimental

Sample synthesis

Eight samples selected at 10 – 20 mol % intervals across the solid solution $(\text{Ca}_x\text{Sr}_{1-x})\text{TiOGeO}_4$ (STGO $_x$) including the endmember composition SrTiOGeO_4 have been synthesized by solid state reaction. The stoichiometric starting mixtures were prepared from pure fine grained powders of CaCO_3 (Aldrich 20,293-2), TiO_2 (Rutile, Aldrich 20,475-7), SrCO_3 (Aldrich 47,201-8) and GeO_2 (Aldrich 19,947-8) at a maximum temperature of 1323 K. Approximately 2.5 g starting oxides were ground, pressed into pellets, and heated for several intervals of 5 days with intermittent grindings. Phase purity of the product was established by powder diffraction analysis. Minor amounts of $\text{Sr}_4\text{Ti}_3\text{O}_{10}$ (0.5 to 1.3 wt%) were observed in samples STGO90, STGO60 and STGO40.

Less than 1wt% TiO_2 and SrTiO_3 have been observed in samples STGO60 and STGO, respectively.

X-ray diffraction

In situ X-ray powder diffraction measurements up to 1123 K have been carried out using an Anton Paar HTK 1200 furnace mounted on a Philips Xpert diffractometer with monochromatic $\text{CuK}\alpha_1$ -radiation. Diffraction patterns were recorded in the range $17\text{-}90^\circ 2\theta$ using a proportional counter with 4 s/step counting time and a step size of 0.02° . Lattice parameters were determined using the LeBail method as implemented in the GSAS program (Larson and Von Dreele, 1994). Refinements were carried out using space group symmetry $A2/a$. Additional Rietveld refinements were carried out in the $P2_1/a$ setting at room temperature. Starting fractional coordinates were taken from CaTiOGeO_4 (Ellemann-Olesen

and Malcherek, 2004a). Significant sample displacement, caused by temperature expansion of the Al_2O_3 sample stage (Malcherek, 2001), has been refined as part of the profile function. The sample displacement exhibits a nearly linear behaviour as a function of temperature. Fig. 1 shows the powder diffraction pattern obtained for SrTiOGeO_4 at room temperature and the calculated pattern from Rietveld refinement.

3. Results

Lattice parameters and structure refinement

On the basis of the disappearance of $k + l = \text{odd}$ reflections the transition can be observed directly from the diffraction patterns but due to background noise and the small intensities of the superlattice reflections it is not possible to estimate the exact critical temperature in this way from the powder diffraction data. At low temperatures the diffraction patterns exhibit the $k + l = \text{odd}$ reflections indicative of $\text{P2}_1/a$ symmetry (Fig. 1). The intensities of the $2\bar{1}\bar{2}$ superlattice reflection were extracted using the LeBail fit in space group $\text{P2}_1/a$. The superlattice reflections show a steady decrease with increasing temperature. Beyond 523 K no clear indication of these reflections can be identified in the diffraction patterns.

By extrapolation of the lattice parameters measured for $T \leq 1123$ K towards lower temperatures, linear reference functions of thermal expansion have been obtained for all lattice parameters. The complete set of lattice parameter data for SrTiOGeO_4 is illustrated in Fig. 2 and given in Table 1. The pattern of their evolution with temperature is in perfect analogy to that observed for CaTiOGeO_4 (Ellemann-Olesen and Malcherek, 2004a). The transition is accompanied by a significant expansion of the a -axis. Also the monoclinic β -angle shows a significant deviation from the extrapolated high temperature behaviour. Both the a -lattice parameter and the monoclinic angle show clear indications for the additional occurrence of an isosymmetric anomaly at $T_i = 800 \pm 25$ K (Fig. 2a, d) in accordance with the estimates for T_i in titanite (Zhang *et al.*, 1997; Malcherek, 1999; Kek *et al.*, 1997) and CaTiOGeO_4 (Ellemann-Olesen and Malcherek, 2004a). Selected bond distances and interatomic angles for SrTiOGeO_4 are given in Tables 2 and 3.

No phase-separation is evident at any of the intermediate compositions, which we have synthesized. Across the solid solution the replacement of Ca by the larger Sr, as expected, leads to a gradual increase in unit cell volume by 5 %. A slight linear decrease of the β -angle is observed as the Sr-content increases. The a -, b - and c -lattice parameters increase linearly across the solid solution (Fig. 3).

Concerning the data measured at intermediate compositions across the solid solution, diffraction patterns have been recorded in the temperature range 298 – 773 K. An exception is STGO50 and STGO where the measurements have been carried out up to 1073 K and 1123 K, respectively. The complete set of lattice parameter data is given in Table 4. Irrespective of composition all intermediate compounds exhibit similar lattice parameter evolution as a function of temperature.

In order to take the possible occurrence of a structural anomaly at T_i above 773 K into account, the linear reference functions of thermal expansion were obtained by extrapolation of the lattice parameters measured for $T \geq 773$ K towards lower temperatures using STGO50 and the endmember compositions SrTiOSiO₄ and CaTiOGeO₄, respectively. The resulting individual line slopes were plotted against composition and fitted using a parabola. Only in the case of the c lattice parameter a straight line fit was sufficient to represent the composition dependence of its temperature coefficient of thermal expansion. With these fixed line slopes, individual linear functions of thermal expansion were obtained from the data measured up to 773 K. The same procedure has already been used when analyzing strain data across the CaTiO(Ge_xSi_{1-x})O₄ solid solution (Ellemann-Olesen and Malcherek, 2004a).

Rietveld refinements have been carried out for all room temperature data across the solid solution. Unit cell parameters and atomic coordinates for all intermediate compositions at room temperature are given in Table 5 and 6.

The variation of the mean bond lengths is displayed in Table 7. The mean bond distance Ge-O is constant within the limits of the measurement accuracy, while, as expected, the mean bond length of the A-cation to the surrounding oxygen atoms increases with increasing Sr content. The composition dependence of the mean Ti-O bond distance is nearly symmetric with the endmembers exhibiting the shortest bond lengths. Bond valence calculations were carried out in order to compare CaTiOGeO₄, SrTiOGeO₄ and the intermediate compounds (Table 8).

Spontaneous strain in SrTiOGeO₄

The components of the spontaneous strain tensor have been calculated according to the equations given by Carpenter *et al.*, 1998. In the following the scalar spontaneous strain is defined as

$$e_s = \left(\sum e_{ij}^2 \right)^{1/2}$$

In the case of a zone boundary transition this property is proportional to the square of the order parameter Q of the transition. The spontaneous strain associated with the $P2_1/a - A2/a$ phase transition in SrTiOGeO_4 is relatively small (Fig. 4). By extrapolation of e_s^2 to zero the transition temperature is estimated to $T_c = 624 \pm 7$ K. However, the evolution of e_s^2 with temperature is complicated by a marked bending at lower temperatures and a significant deviation from zero in the temperature range of 600 to 800 K (Fig 7). Similar behaviour is observed in CaTiOGeO_4 but to a much lesser extent. If e_s^2 is extrapolated to 0.2×10^{-6} in order to account for this effect, the estimated transition temperature is $T_c = 594 \pm 10$ K. At room temperature the observed volume strain amounts to +0.15% (Fig. 4b). The onset of this volume strain is located close to 800 K. The spontaneous strain components define rather well constrained trends which do to large extent agree with the results of previous investigations of titanite (Malcherek, 2001) and CaTiOGeO_4 (Ellemann-Olesen and Malcherek, submitted). The e_{11} component is significantly larger than the e_{22} and e_{33} components and it dominates the strain along with e_{13} in agreement with titanite and CaTiOGeO_4 . The e_{22} and e_{33} components are nearly equal in magnitude and very small. The component e_{22} is negative for $T < T_c$, while e_{33} is positive. In analogy to CaTiOGeO_4 , e_{11} does not disappear at T_c , but it remains finite up to the isosymmetric anomaly, T_i (Fig. 4a), giving rise to the significant scalar and volume strain in this temperature interval, as noted above. At room temperature the spontaneous strain component, e_{13} is approximately 55 % lower in STGO than in CaTiOGeO_4 . The scalar strain as a function of reduced temperature T/T_c is plotted in Fig. 5 in comparison with titanite (Malcherek, 2001) and CaTiOGeO_4 .

At room temperature the scalar strain for titanite and CaTiOGeO_4 is 36 % larger than in SrTiOGeO_4 . The square of the scalar strain is displayed in Fig. 7. This property shows a linear relationship with temperature. Given the zone boundary character of the symmetry change, $e^2 \sim Q^4$ is the expected relationship between strain and driving order parameter, so that the transition would be close to tricritical in character.

Spontaneous strain in the solid solution $(\text{Ca}_x\text{Sr}_{1-x})\text{TiOGeO}_4$

The temperature evolution of the spontaneous strain components for intermediate compositions is similar to that described for the end members (*cf.* above and Ellemann-Olesen and Malcherek, 2004a). A small volume strain is observed throughout. The scalar strain stays nearly constant across the solid solution and its temperature evolution and magnitude is similar to the endmember composition SrTiOGeO_4 (Fig. 5).

The strain components e_{11} and e_{13} at the reduced temperature $T/T_c = 0.75$ have been examined in order to evaluate a possible change in the strain behaviour as a function of composition (Fig. 6). The evolution of the spontaneous strain component e_{11} with increasing content of Ca is nearly linear across the solid solution. Only CaTiOGeO₄ differs. A significant drop in strain at this reduced temperature by nearly 45% takes place after addition of 10 mol% Sr to the structure. The component e_{13} is constant within the estimated error, while it is one order of magnitude smaller than e_{11} . The scalar strain is nearly constant across the solid solution except for CaTiOGeO₄ that exhibits a significantly larger scalar strain, due to the larger value of e_{11} .

The square of the scalar strain, Σe_j^2 for the intermediate compositions (Fig. 7) increases linearly below their respective transition temperatures, T_c , which indicates that the transition remains close to tricritical in character ($Q^4 \propto |T_c - T|$) irrespective of the nature of the A cation. The isostructural anomaly at T_i is best observed on the basis of the a -lattice parameter and the monoclinic angle, although to a lesser extent it can be observed for all compositions in Fig. 7.

Based on the strain analysis T_c for all compositions along the solid solution has been determined by extrapolation of e_s^2 to zero. Fig. 8 shows the behaviour of the transition temperature with composition. According to this analysis T_c remains almost constant with respect to the value of 588 K observed in CaTiOGeO₄. Determination of the isosymmetric transition temperature T_i is encumbered by large errors due to the way the extrapolation was done, but it appears to remain more or less constant at 800 ± 25 K in accordance with the value observed in titanite and in CaTiOGeO₄ (Malcherek, 2001; Ellemann-Olesen and Malcherek, 2004a).

4. Discussion

Structural parameters

Two parameters can be used to identify systematic changes of the titanite polyhedral framework in response to cation substitutions (Malcherek and Ellemann-Olesen, 2004): The *torsion angle* is defined as the angle between the chain direction, *i.e.* [100] in the present setting, and the direction of the tetrahedral edge that bridges two neighbouring MO₆ octahedra. It is controlled by the match between the length of the bridging tetrahedral edge and the M-M distance. The octahedral *tilt angle*, as measured by the angle M-O1-M, also

controls this M-M distance. The tilt angle Ti-O1-Ti is $\sim 148^\circ$ in STGO compared to $\sim 143^\circ$ in CaTiOGeO₄ (Ellemann-Olesen and Malcherek, 2004a) and 141.5° in titanite (Kek *et al.*, 1997). Hence the tilt angle in SrTiOGeO₄ is relatively large and the octahedral chains are stretched compared to CTGO and titanite, due to the larger size of the Sr-atom. A comparison of the individual torsion angles reveals a slightly smaller angle in STGO of about 20° contrary to a common value of 25° in titanite and CaTiOGeO₄. The torsion angle for the intermediate compounds is similar to CaTiOGeO₄. The Ti shift, *i.e.* the length of the displacement vector between the Ti position in P2_{1/a} and the special Ti position of the aristotype structure, is very similar in STGO and CTGO, with 0.129 Å and 0.123 Å respectively. For titanite the Ti shift amounts to only 0.115 Å, if based on the low temperature data of Kek *et al.*, 1997. The comparatively large and nearly identical Ti shifts in the two germanate compounds correspond to their elevated and nearly identical transition temperatures, as obtained from the strain analysis. In fact if we assume a common critical temperature of 594 K for both germanate compounds and an average Ti shift of 0.127 Å, the quotient of the square of these Ti-shifts in STGO-CTGO and titanite is identical with the ratio of the respective critical temperatures, *i.e.* 594 K/487 K. This confirms the validity of the Abrahams-Kurtz-Jamieson relation (Abrahams *et al.*, 1968) for the titanite structure.

Polyhedral distortion parameters such as the octahedral angle variance (Robinson *et al.*, 1971) suggest that the TiO₆ octahedron in the endmember compositions are closer to the geometry of an ideal octahedron than those at intermediate compositions, which are considerably distorted. The endmembers show similar angle variance at 14.4 and 16.8, respectively (Table 9). A similar trend is seen in the GeO₄ tetrahedra. The average Ge-O bond length is nearly constant across the solid solution, while an expected increase in the average size of the A-polyhedra is observed. The mean Ti-O bond distance shows a near symmetric behaviour with the endmembers having the lowest mean bond length (Fig. 9 and Table 5). The evolution of the mean bond distance is in close agreement with the evolution of the Ti-O mean bond distances across the solid solution CaTiO(Ge_xSi_{1-x})O₄ (Ellemann-Olesen and Malcherek, 2004a). Hammonds *et al.*, 1998 predicted that due to the absence of rigid unit modes in the titanite structure, polyhedral distortion is to be expected upon chemical substitution in titanite, rather than polyhedral tilting. The distortion of the octahedra is also apparent through the behaviour of the Ti-O bonds. The variation of the individual bond lengths is more pronounced for the intermediate compounds compared to the endmember compositions and as a result the octahedra and polyhedra are more distorted. This is in accordance with the observed

behaviour across the $\text{CaTiO}(\text{Ge}_x\text{Si}_{1-x})\text{O}_4$ solid solution (Ellemann-Olesen and Malcherek, submitted).

Calculated bond valence sums are close to the formal oxidation states (Table 8). The bond valence sums of STGO and CTGO indicate a nearly ideal valence for Ge (3.97 and 3.99, respectively), while the valence of the Ti cation is higher than ideal, but reasonable. The octahedra are as a result overbonded in this structure. This is the case for all investigated compositions. The bond valence sum stays constant with composition contrary to the variation of the bond valence sums along the titanite – malayaite join discussed by Kunz *et al.*, 1997. Along with the increasing overbonding on the octahedral site across the titanite-malayaite join a corresponding decrease in the Ca bond valence is seen. This shows an increasing coordination distortion of the CaO_7 polyhedron along the titanite-malayaite solid solution, induced by the sterically driven increase of the volume of the CaO_7 polyhedron. Across $(\text{Ca}_x\text{Sr}_{1-x})\text{TiOGeO}_4$ no such correlation is observed. In CaTiOGeO_4 an underbonding is observed in the polyhedron, while the bond valence sum of Sr in SrTiOGeO_4 is higher than ideal (Table 8).

Transition temperature and strain behaviour

One of our objectives was to determine how the transition temperature, T_c changes as a function of composition in the solid solution. Substitution of Ca by Sr leads within experimental uncertainty to hardly any compositional variation of the transition temperature (Fig. 8). In the titanite-structure the large A-polyhedron represents the most compressible structural unit along with the octahedral chain. Thus the structure can adjust better to substitution on the more flexible polyhedral site despite the larger size of the Sr-atom.

The observed behaviour in the $(\text{Ca}_x\text{Sr}_{1-x})\text{TiOGeO}_4$ solid solution contrasts with that of $\text{CaTiO}(\text{Ge}_x\text{Si}_{1-x})\text{O}_4$. Substitution of Ge for Si on the tetrahedral site has a rather significant effect as T_c increases linearly with increasing Ge-content (Ellemann-Olesen and Malcherek, 2004a). The solid solution titanite - malayaite (CaSnOSiO_4), studied by Kunz *et al.*, 1997, exemplifies how substitution of Ti by Sn on the octahedral site affects the structure. The refinements at room temperature reveal a high sensitivity of the crystal symmetry on the amount of octahedral Sn present. The series of experiments reveal that already at a Sn concentration of 10 % the ordered $\text{P2}_1/a$ phase is destabilized and the disordered monoclinic $\text{A2}/a$ structure is observed. In agreement with this behaviour substitution of Ti by Zr across the solid solution $\text{Ca}(\text{Ti}_x\text{Zr}_{1-x})\text{OGeO}_4$ is found to suppress T_c by 100 K already at 5 % Zr. By substitution of 20 % Zr the $\text{P2}_1/a$ – $\text{A2}/a$ transition is no longer observed at ambient

temperatures. Substitution of Zr for Ti however is further complicated by the fact that the endmember composition CaZrOGeO_4 exhibits a triclinically distorted structure in analogy with high-pressure malayaite (Malcherek and Ellemann-Olesen, 2004; Ellemann-Olesen and Malcherek, 2004b; Rath *et al.*, 2003).

In analogy to titanite (Zhang *et al.*, 1997) and $\text{CaTiO}(\text{Ge}_x\text{Si}_{1-x})\text{O}_4$ (Ellemann-Olesen and Malcherek, 2004a) the isostructural anomaly, T_i is found to remain rather constant at about 800 K. Zhang *et al.* (1997) conclude that the high-temperature phase transition in titanite shows a completely different behaviour contrary to the antiferroelectric phase transition at $T_c = 487$ K. They observed that impurities of Fe and Al substituted for Ti exhibit much less effect on the second phase transition near 825 K than on the first at 487 K, where substitution is having a large impact and the transition is suppressed. The effect of Fe, Al substitution is to block the lower temperature transition at T_c , while substitution of Sr for Ca does not seem to affect T_c .

Due to the structural changes that arise from substituting Sr for Ca significant differences appear in the behaviour of scalar strain between the two endmember compositions. Across most of the solid solution the scalar strain stays almost constant. But CaTiOGeO_4 differs with an increase of 36 % at room temperature. The temperature evolution of scalar strain in CaTiOGeO_4 is comparable to titanite (Malcherek, 2001). The smaller absolute strain in STGO can probably be related to the larger size of Sr and the resulting larger tilting of the octahedra. This will expand the axis parallel to the chain direction, so that the distortion generated by the shift of the Ti-cation is smaller.

The square of the scalar strain shows a noticeable deviation from zero in the temperature range of 600 – 800 K, in which a maximum value of $0.2 \cdot 10^{-6}$ is reached (Fig. 7). In the compound CTGO the square of the scalar strain remains finite up to 800 K, but to a much lesser extent and T_c is estimated by extrapolation to zero (Ellemann-Olesen and Malcherek, 2004a). Similar behaviour is not observed for titanite (Malcherek, 2001). A larger deformation of the unit cell is thus attributable to the isosymmetric anomaly in STGO.

The substitution of Ca by Sr leads to minor changes in the spontaneous strain component e_{11} related to the expansion along the a -axis. As observed (Fig. 6) the strain component e_{11} exhibits a minor gradual increase with increasing Sr-content. The observed strain of the endmember compositions, however, is near equal at room temperature (Fig. 6). The expansion along the a -axis indicates that substituting the larger Sr into the structure presumably affects

the Ti-octahedra, as the octahedral chain and the CaO_7 chain are mutually interconnected. The octahedral chains will adjust to yield space to the larger cation as discussed above, where the larger tilt angle of STGO is connected to changes of the titanite polyhedral framework in response to cation substitutions.

A significant difference in strain behaviour between SrTiOGeO_4 and the endmember composition CaTiOGeO_4 is the absence of strain parallel [010] in STGO, while in CTGO a small but non-zero value of e_{22} is observed (Ellemann-Olesen and Malcherek, 2004a). The strain in SrTiOGeO_4 is equally dominated by the spontaneous strain components e_{11} and e_{13} as in titanite (Malcherek, 2001). However, in analogy with CaTiOGeO_4 the strain component e_{11} does not disappear at T_c but it remains finite up to the isosymmetric anomaly, T_i (Fig. 3). This behaviour differs from that observed in titanite. In titanite it is only the e_{13} component, which is finite at temperatures above T_c and which vanishes at T_i (Malcherek, 2001). For $T > T_c$ the component e_{11} does not contribute to the strain in titanite.

5. Conclusions

The behaviour of SrTiOGeO_4 is similar to the well known behaviour of titanite characterized by the $\text{P}2_1/a - \text{A}2/a$ transition. SrTiOGeO_4 and CaTiOGeO_4 form a complete solid solution and they exhibit nearly identical properties with regard to the occurring structural phase transitions. The temperature of the $\text{P}2_1/a - \text{A}2/a$ transition is constant across the solid solution. In analogy with titanite X-ray powder diffraction indicates the additional occurrence of an isosymmetric anomaly at about 800 K, which is not altered by the Ca/Sr substitution either. The transition is close to tricritical in character for all compositions.

Acknowledgements

Financial support through the Deutsche Forschungs-Gemeinschaft (DFG) is gratefully acknowledged.

References

- Abrahams, S. C., Kurtz, S. K. and Jamieson, P. B., 1968. Atomic displacement relationship to Curie temperature and spontaneous polarization in displacive ferroelectrics. *Physics Reviews* 172: 551-553.
- Bismayer, U., Schmahl, W., Schmidt, C. and Groat, L.A., 1992. Linear Birefringence and X-Ray Diffraction Studies of the Structural Phase Transition in Titanite, CaTiSiO_5 . *Physics and Chemistry of Minerals* 19: 260-266.

- Breese, N.E. and O'Keeffe, M., 1991. Bond-Valence Parameters for Solids. *Acta Crystallographica B* 47, 192-197.
- Carpenter, M.A., Salje, E.K.H. and Graeme-Barber, A., 1998. Spontaneous strain as a determinant of thermodynamic properties for phase transitions in minerals. *European Journal of Mineralogy* 10: 621-691.
- Ellemann-Olesen, R. and Malcherek, T., 2004a. A high temperature diffraction study of the solid solution $\text{CaTiOSiO}_4 - \text{CaTiOGeO}_4$. *American Mineralogist*, *Submitted*
- Ellemann-Olesen, R. and Malcherek, T., 2004b. Temperature- and composition dependence of the phase transitions in $\text{Ca}(\text{Ti}_x\text{Zr}_{1-x})\text{OGeO}_4$. *American Mineralogist*, *in press*
- Ghose, S., Ito, Y. and Hatch, D.M., 1991. Paraelectric-Antiferroelectric Phase Transition in Titanite, CaTiSiO_5 : I. A high temperature X-ray diffraction study of the order parameter and transition mechanism. *Physics and Chemistry of Minerals* 17: 591-603.
- Groat, L.A., Kek, S., Bismayer, U., Schmidt, C., Krane, H.G., Meyer, H., Nistor, L. and Van Tendeloo, G., 1996. A synchrotron radiation, HRTEM, X-ray powder diffraction, and Raman spectroscopy study of malayaite, CaSnSiO_5 . *American Mineralogist* 81: 595-602.
- Hammonds, K.D., Bosenick, A., Dove, M.T. and Heine, V., 1998. Rigid unit modes in crystal structures with octahedrally coordinated atoms. *American Mineralogist* 83: 476-497.
- Kek, S., Aroyo, M., Bismayer, U., Schmidt, C., Eichhorn, K. and Krane, H.G., 1997. The two-step phase transition of titanite, CaTiSiO_5 : a synchrotron radiation study. *Zeitschrift für Kristallographie* 212: 9-19.
- Kunz, M., Xirouchakis, D., Wang, Yanbin, Parise, J.B. and Lindsley, D.H., 1997. Structural investigations along the join $\text{CaTiOSiO}_4 - \text{CaSnOSiO}_4$. *Schweizerisch Mineralogische Petrographische Mitteilung* 77: 1-11.
- Larson, A.C. and Von Dreele, R.B., 1994. General Structure Analysis System (GSAS). Los Alamos National Laboratory. Los Alamos, New Mexico.
- Malcherek, T., Domeneghetti, C.M., Tazzoli, V., Salje, E.K.H. and Bismayer, U., 1999. A high temperature diffraction study of synthetic titanite CaTiOSiO_4 . *Phase Transitions* 69: 119-131.
- Malcherek, T., 2001. Spontaneous strain in synthetic titanite, CaTiOSiO_4 . *Mineralogical Magazine* 65: 709- 715.
- Malcherek, T., and Ellemann-Olesen, R., 2004. CaZrGeO_5 and the triclinic instability of the titanite structure type. *Zeitschrift für Kristallographie*, *In press*
- Oberti, R., Smith, D.C., Rossi, G. and Caucia, F., 1991. The crystal-chemistry of high-aluminium titanites. *European Journal of Mineralogy* 3: 777-792.

- Rath, S., Kunz, M. and Miletich, R., 2003. Pressure-induced phase transition in malayaite, CaSnOSiO_4 . *American Mineralogist* 88: 293-300.
- Robinson, K., Gibbs, G.V. and Ribbe, P.H., 1971. Quadratic elongation: A quantitative measure of distortion in coordination polyhedra. *Science* 172: 567-570.
- Salje, E.K.H., Schmidt, C. and Bismayer, U., 1993. Structural phase transition in titanite, CaTiSiO_5 : A raman spectroscopic study. *Physics and Chemistry of Minerals* 19: 502-506.
- Speer, J.A. and Gibbs, G.V., 1976. The crystal structure of synthetic titanite, CaTiOSiO_4 , and the domain textures of natural titanites. *American Mineralogist* 61: 238-247.
- Taylor, M. and Brown, G.E., 1976. High-temperature structural study of the $P2_1/a - A2/a$ phase transition in synthetic titanite, CaTiSiO_5 . *American Mineralogist* 61: 435-447.
- Troitzsch, U., Ellis, D.J., Thompson, J. and Fitz-Gerald, J., 1999. Crystal structural changes in titanite along the join $\text{TiO}-\text{AlF}$. *European Journal of Mineralogy* 11: 955-965.
- Zhang, M., Salje, E.K.H., Bismayer, U., Unruh, H.G., Wruck, B. and Schmidt, C., 1995. An infrared spectroscopic, dielectric response and heat capacity study. *Physics and Chemistry of Minerals* 22: 41-49.
- Zhang, M., Salje, E.K.H., and Bismayer, U., 1997. Structural phase transition near 825 K in titanite: Evidence from infrared spectroscopic observations. *American Mineralogist* 82: 30-35.

Table 1. SrTiOGeO₄. Lattice parameters as a function of temperature.

T (K)	a (Å)	b (Å)	c (Å)	β (°)	V (Å ³)
298	7.22520(2)	9.07540(9)	6.78517(9)	113.510(1)	407.982(8)
348	7.22543(4)	9.07717(8)	6.78590(3)	113.499(1)	408.153(8)
373	7.22634(5)	9.07973(4)	6.78775(9)	113.493(1)	408.449(9)
398	7.22663(9)	9.08187(5)	6.78887(9)	113.487(1)	408.648(8)
423	7.22704(2)	9.08382(5)	6.78994(3)	113.481(1)	408.842(4)
448	7.22749(2)	9.08591(7)	6.79142(9)	113.472(1)	409.078(7)
473	7.22772(3)	9.08762(3)	6.79186(9)	113.467(1)	409.210(7)
498	7.22765(7)	9.08930(9)	6.79299(6)	113.460(1)	409.372(7)
523	7.22769(8)	9.09164(9)	6.79429(9)	113.452(1)	409.583(9)
538	7.22716(8)	9.09266(5)	6.79473(9)	113.444(1)	409.650(9)
553	7.22726(9)	9.09390(9)	6.79543(2)	113.440(1)	409.766(7)
573	7.22678(2)	9.09567(5)	6.79642(9)	113.435(1)	409.894(7)
598	7.22625(9)	9.09717(2)	6.79706(5)	113.427(1)	409.995(7)
623	7.22660(7)	9.09979(4)	6.79855(4)	113.415(1)	410.260(6)
648	7.22713(3)	9.10205(2)	6.80010(7)	113.409(1)	410.504(6)
673	7.22740(5)	9.10403(6)	6.80144(8)	113.404(1)	410.705(7)
723	7.22760(6)	9.10743(3)	6.80321(3)	113.391(1)	411.017(5)
748	7.22788(9)	9.10924(9)	6.80443(3)	113.384(1)	411.210(7)
773	7.22806(6)	9.11101(9)	6.80541(7)	113.379(1)	411.375(7)
873	7.22959(6)	9.11909(3)	6.81032(6)	113.357(1)	412.193(6)
923	7.23064(9)	9.12248(4)	6.81271(6)	113.350(1)	412.572(7)
973	7.23175(6)	9.12612(2)	6.81530(2)	113.342(1)	412.982(5)
1023	7.23294(8)	9.13018(3)	6.81806(5)	113.333(1)	413.429(6)
1073	7.23412(9)	9.13371(8)	6.82059(7)	113.325(1)	413.835(8)
1123	7.23553(8)	9.13782(4)	6.82332(7)	113.318(1)	414.289(7)

Table 2. SrTiOGeO₄: Interatomic distances (Å) at room temperature.

Ti-O1	1.787(1)
Ti-O1'	1.972(2)
Ti-O2A	1.959(2)
Ti-O2B	2.063(2)
Ti-O3A	2.114(3)
Ti-O3B	1.895(2)
Mean	1.965
Ca-O1	2.488(2)
Ca-O2A	2.475(2)
Ca-O2B	2.589(3)
Ca-O3A	2.516(2)
Ca-O3B	2.548(1)
Ca-O3A'	2.646(2)
Ca-O3B'	2.678(1)
Mean	2.563
Ge-O2A	1.783(2)
Ge-O2B	1.746(2)
Ge-O3A	1.688(1)
Ge-O3B	1.802(2)
Mean	1.755

Table 3. SrTiOGeO₄: Interatomic angles (°) at room temperature.

O1-Ti-O2A	92.06(1)
O1-Ti-O2B	97.40(1)
O1-Ti-O3A	91.20(1)
O1-Ti-O3B	93.65(1)
O1'-Ti-O2A	83.86(1)
O1'-Ti-O2B	86.60(1)
O1'-Ti-O3A	87.63(1)
O1'-Ti-O3B	87.77(1)
O2A-Ti-O3A	90.31(1)
O2A-Ti-O3B	92.76(1)
O2B-Ti-O3A	85.89(1)
O2B-Ti-O3B	90.27(1)
Ti-O1-Ti	147.94(1)
O2A-Ge-O2B	101.87(2)
O2A-Ge-O3A	109.65(2)
O2A-Ge-O3B	112.29(2)
O2B-Ge-O3A	105.28(2)
O2B-Ge-O3B	116.57(1)
O3A-Ge-O3B	110.60(1)

Table 4. $(\text{Ca}_x\text{Sr}_{1-x})\text{TiOGeO}_4$. Lattice constants and volume for all intermediate samples as a function of temperature.

Mol% Sr						
90	T (K)	a (Å)	b (Å)	c (Å)	β (°)	V (Å ³)
	298	7.21252(4)	9.05575(2)	6.76927(2)	113.520(1)	405.401(4)
	348	7.21313(7)	9.05921(2)	6.77096(3)	113.506(1)	405.735(5)
	373	7.21358(7)	9.05729(7)	6.76987(6)	113.518(1)	405.572(7)
	398	7.21323(5)	9.06185(5)	6.77196(5)	113.495(1)	405.953(6)
	423	7.21417(2)	9.06122(3)	6.77172(5)	113.502(1)	405.941(5)
	473	7.21450(9)	9.06510(4)	6.77397(3)	113.484(1)	406.324(6)
	498	7.21439(2)	9.06727(2)	6.77529(4)	113.471(1)	406.534(4)
	523	7.21423(9)	9.06932(3)	6.77633(3)	113.470(1)	406.683(6)
	548	7.21397(4)	9.07279(4)	6.77820(2)	113.460(1)	406.967(4)
	573	7.21379(6)	9.07483(5)	6.77928(2)	113.452(2)	407.138(7)
	623	7.21287(8)	9.07784(3)	6.78086(5)	113.433(2)	407.374(8)
	648	7.21380(5)	9.08007(2)	6.78252(6)	113.430(1)	407.636(6)
	673	7.21402(9)	9.08155(4)	6.78411(4)	113.425(2)	407.826(9)
	723	7.21520(7)	9.08654(5)	6.78667(3)	113.412(2)	408.311(8)
	748	7.21604(4)	9.08886(5)	6.78768(2)	113.406(1)	408.542(5)
	773	7.21665(3)	9.09017(3)	6.78931(2)	113.405(1)	408.737(4)
70	T (K)	a (Å)	b (Å)	c (Å)	β (°)	V (Å ³)
	298	7.19160(2)	9.01342(3)	6.73876(4)	113.593(1)	400.300(4)
	348	7.19505(4)	9.02119(4)	6.74248(3)	113.577(1)	401.108(5)
	373	7.19499(9)	9.02152(2)	6.74350(2)	113.583(2)	401.161(8)
	398	7.19531(2)	9.02342(6)	6.74460(8)	113.575(2)	401.353(8)
	423	7.19556(3)	9.02670(5)	6.74569(9)	113.557(1)	401.633(7)
	448	7.19541(2)	9.02789(9)	6.74609(4)	113.553(1)	401.714(6)
	473	7.19601(3)	9.02937(2)	6.74757(2)	113.553(1)	401.901(4)
	488	7.19594(6)	9.02950(3)	6.74688(9)	113.540(2)	401.902(9)
	508	7.19554(3)	9.03267(6)	6.74817(7)	113.529(1)	402.131(6)
	523	7.19617(9)	9.03370(2)	6.74939(9)	113.525(1)	402.297(8)
	538	7.19506(2)	9.03471(3)	6.74900(3)	113.524(1)	402.260(4)
	553	7.19511(2)	9.03731(5)	6.75160(9)	113.515(1)	402.561(7)
	573	7.19472(4)	9.03736(3)	6.75036(4)	113.504(1)	402.501(5)
	598	7.19476(4)	9.03911(3)	6.75125(3)	113.495(1)	402.662(4)
	623	7.19496(9)	9.03980(9)	6.75228(7)	113.507(1)	402.728(8)
	648	7.19556(2)	9.04205(2)	6.75366(7)	113.487(2)	403.006(8)
	673	7.19570(4)	9.04387(3)	6.75394(5)	113.474(1)	403.151(5)
	723	7.19706(3)	9.04688(4)	6.75654(9)	113.487(1)	403.477(7)
	748	7.19746(7)	9.04940(9)	6.75819(3)	113.468(1)	403.769(7)
	773	7.19825(2)	9.05293(4)	6.75990(2)	113.472(1)	404.060(4)

60	T (K)	a (Å)	b (Å)	c (Å)	β (°)	V (Å ³)
	298	7.19292(9)	8.99967(2)	6.72950(5)	113.647(2)	399.049(8)
	348	7.19220(8)	9.00046(2)	6.72795(4)	113.643(2)	398.964(8)
	373	7.19255(3)	9.00205(4)	6.72923(3)	113.629(1)	399.171(4)
	398	7.19240(3)	9.00395(5)	6.72971(7)	113.636(1)	399.255(6)
	423	7.19287(2)	9.00673(5)	6.73133(3)	113.627(1)	399.528(4)
	448	7.19281(5)	9.00822(8)	6.73251(5)	113.614(1)	399.701(6)
	473	7.19273(6)	9.00902(8)	6.73277(8)	113.606(1)	399.772(7)
	498	7.19284(6)	9.01101(9)	6.73442(8)	113.598(1)	399.988(8)
	523	7.19298(5)	9.01437(9)	6.73654(3)	113.590(2)	400.296(8)
	538	7.19311(3)	9.01599(3)	6.73671(4)	113.580(1)	400.415(4)
	553	7.19292(3)	9.01673(4)	6.73688(5)	113.582(1)	400.441(5)
	573	7.19313(9)	9.01778(2)	6.73699(6)	113.569(1)	400.522(7)
	598	7.19189(9)	9.01835(5)	6.73796(6)	113.560(1)	400.588(7)
	623	7.19287(3)	9.02084(6)	6.73924(3)	113.558(1)	400.835(5)
	648	7.19315(2)	9.02269(6)	6.74046(9)	113.556(1)	401.012(7)
	673	7.19398(3)	9.02379(4)	6.74084(5)	113.550(1)	401.147(5)
	723	7.19523(2)	9.02917(4)	6.74357(9)	113.542(1)	401.644(7)
	748	7.19599(9)	9.03019(8)	6.74476(4)	113.534(2)	401.826(9)
	773	7.19670(9)	9.03168(2)	6.74674(4)	113.526(1)	402.076(6)

50	T (K)	a (Å)	b (Å)	c (Å)	β (°)	V (Å ³)
	298	7.17794(9)	8.97526(2)	6.71050(2)	113.658(1)	395.983(6)
	348	7.18008(3)	8.97786(3)	6.71173(4)	113.658(2)	396.289(7)
	373	7.18080(5)	8.98129(5)	6.71318(3)	113.646(1)	396.602(5)
	398	7.18057(8)	8.98280(8)	6.71482(8)	113.645(1)	396.756(8)
	423	7.18183(9)	8.98651(2)	6.71617(5)	113.641(1)	397.081(7)
	448	7.18135(4)	8.99028(8)	6.71839(5)	113.630(1)	397.386(6)
	473	7.18202(2)	8.98988(3)	6.71830(8)	113.608(1)	397.467(6)
	488	7.18193(2)	8.99187(2)	6.71947(9)	113.607(2)	397.622(8)
	508	7.18198(3)	8.99228(8)	6.71963(7)	113.602(1)	397.668(6)
	523	7.18153(5)	8.99480(3)	6.72082(9)	113.600(1)	397.831(7)
	538	7.18204(8)	8.99505(3)	6.72119(3)	113.594(1)	397.910(6)
	553	7.18152(3)	8.99754(5)	6.72126(2)	113.584(1)	398.026(4)
	573	7.18182(2)	8.99824(2)	6.72199(5)	113.576(1)	398.141(4)
	598	7.18138(8)	9.00135(6)	6.72333(5)	113.572(1)	398.346(7)
	623	7.18185(3)	9.00128(3)	6.72414(4)	113.570(1)	398.423(4)
	648	7.18202(2)	9.00361(9)	6.72526(4)	113.565(1)	398.617(6)
	673	7.18318(2)	9.00638(9)	6.72721(8)	113.563(1)	398.926(7)
	723	7.18364(4)	9.00899(3)	6.72919(3)	113.547(2)	399.233(7)
	748	7.18430(5)	9.01179(7)	6.73034(2)	113.540(1)	399.483(5)
	773	7.18516(8)	9.01344(6)	6.73058(3)	113.533(1)	399.640(6)
	823	7.18566(3)	9.01461(2)	6.73209(9)	113.527(1)	399.827(6)
	873	7.18736(9)	9.01914(2)	6.73519(9)	113.518(1)	400.339(8)
	923	7.18852(3)	9.02281(5)	6.73745(2)	113.511(1)	400.717(4)
	973	7.18996(3)	9.02634(6)	6.73981(9)	113.508(1)	401.104(7)
	1023	7.19230(6)	9.02913(2)	6.74228(2)	113.499(1)	401.537(5)
	1073	7.19319(8)	9.03734(4)	6.74487(5)	113.491(1)	401.969(6)

40	T (K)	a (Å)	b (Å)	c (Å)	β (°)	V (Å ³)
	298	7.17573(9)	8.95649(3)	6.69879(2)	113.708(1)	394.157(6)
	348	7.17765(2)	8.96308(8)	6.70161(2)	113.686(1)	394.821(5)
	373	7.17832(7)	8.96210(5)	6.70222(5)	113.688(1)	394.844(6)
	398	7.17900(4)	8.96570(4)	6.70365(8)	113.674(1)	395.167(6)
	423	7.17865(5)	8.96726(3)	6.70455(5)	113.673(1)	395.272(5)
	448	7.17877(6)	8.96839(4)	6.70549(9)	113.670(1)	395.393(7)
	473	7.17900(8)	8.97031(8)	6.70593(4)	113.657(1)	395.556(7)
	498	7.17895(8)	8.97272(9)	6.70668(2)	113.650(1)	395.726(7)
	523	7.17897(3)	8.97496(2)	6.70856(4)	113.642(1)	395.960(4)
	538	7.17881(4)	8.97619(9)	6.70858(5)	113.631(1)	396.040(6)
	553	7.17881(5)	8.97703(9)	6.70972(5)	113.627(1)	396.157(6)
	573	7.17847(5)	8.97834(4)	6.70902(2)	113.624(1)	396.163(5)
	598	7.17835(5)	8.98057(3)	6.71106(7)	113.619(1)	396.390(6)
	623	7.17850(9)	8.98255(5)	6.71145(8)	113.611(1)	396.534(8)
	648	7.17900(9)	8.98351(7)	6.71268(2)	113.602(1)	396.704(7)
	673	7.17926(3)	8.98618(6)	6.71446(4)	113.599(1)	396.950(5)
	723	7.18059(4)	8.98991(6)	6.71675(6)	113.596(1)	397.334(6)
	748	7.18150(9)	8.99224(8)	6.71734(6)	113.583(1)	397.561(8)
	773	7.18197(8)	8.99347(8)	6.71839(3)	113.582(1)	397.706(7)

30	T (K)	a (Å)	b (Å)	c (Å)	β (°)	V (Å ³)
	298	7.16777(6)	8.94086(4)	6.68690(2)	113.724(1)	392.323(5)
	348	7.17064(6)	8.94437(8)	6.68902(3)	113.716(1)	392.783(6)
	373	7.17201(8)	8.94569(9)	6.68974(5)	113.727(1)	392.925(7)
	398	7.17219(2)	8.95084(4)	6.69183(5)	113.708(1)	393.341(5)
	423	7.17336(2)	8.95237(2)	6.69269(8)	113.694(1)	393.565(6)
	448	7.17316(4)	8.95576(2)	6.69463(5)	113.688(1)	393.836(5)
	473	7.17381(5)	8.95721(6)	6.69539(9)	113.677(1)	394.013(7)
	488	7.17344(5)	8.95875(4)	6.69637(2)	113.672(1)	394.133(5)
	508	7.17449(9)	8.96026(5)	6.69759(7)	113.671(1)	394.332(7)
	523	7.17421(9)	8.96115(7)	6.69765(8)	113.655(1)	394.408(8)
	538	7.17407(2)	8.96302(3)	6.69832(2)	113.657(1)	394.516(4)
	553	7.17366(2)	8.96443(2)	6.69856(3)	113.640(1)	394.621(4)
	573	7.17314(5)	8.96403(3)	6.69866(5)	113.640(1)	394.580(5)
	598	7.17304(3)	8.96556(8)	6.69969(9)	113.638(1)	394.709(7)
	623	7.17395(5)	8.97081(9)	6.70189(9)	113.610(1)	395.204(8)
	648	7.17444(8)	8.97097(9)	6.70231(5)	113.624(2)	395.221(9)
	673	7.17535(9)	8.97273(4)	6.70355(5)	113.606(2)	395.476(7)
	723	7.17659(3)	8.97699(9)	6.70528(8)	113.607(1)	395.831(7)
	748	7.17705(3)	8.97879(3)	6.70796(3)	113.614(1)	396.073(4)
	773	7.17747(4)	8.98155(2)	6.70845(7)	113.594(2)	396.307(8)

10	T (K)	a (Å)	b (Å)	c (Å)	β (°)	V (Å ³)
	298	7.15800(2)	8.90751(3)	6.66305(7)	113.766(1)	388.809(5)
	348	7.15990(4)	8.91229(4)	6.66440(4)	113.762(1)	389.212(5)
	373	7.16051(2)	8.91360(2)	6.66477(3)	113.739(1)	389.393(4)
	398	7.16113(4)	8.91640(9)	6.66724(3)	113.742(1)	389.684(6)
	423	7.16161(8)	8.91869(9)	6.66755(8)	113.727(1)	389.873(8)
	448	7.16172(2)	8.91998(5)	6.66822(7)	113.726(1)	389.978(6)
	473	7.16167(3)	8.92199(8)	6.66960(5)	113.714(1)	390.180(6)
	488	7.16167(7)	8.92422(9)	6.67042(5)	113.707(1)	390.346(7)
	508	7.16199(9)	8.92508(3)	6.67135(4)	113.701(1)	390.474(6)
	523	7.16238(7)	8.92588(5)	6.67163(8)	113.696(2)	390.561(9)
	538	7.16235(3)	8.92802(5)	6.67281(9)	113.689(2)	390.743(8)
	553	7.16234(2)	8.92858(4)	6.67254(9)	113.679(1)	390.781(6)
	573	7.16217(9)	8.93083(8)	6.67375(9)	113.677(2)	390.946(9)
	598	7.16203(5)	8.93217(8)	6.67428(4)	113.662(1)	391.074(6)
	623	7.16268(5)	8.93418(4)	6.67599(2)	113.662(1)	391.298(5)
	648	7.16325(6)	8.93689(2)	6.67639(2)	113.650(1)	391.507(5)
	673	7.16375(9)	8.93798(4)	6.67741(5)	113.647(1)	391.651(7)
	723	7.16447(8)	8.94164(2)	6.68000(2)	113.636(1)	392.036(6)
	748	7.16489(9)	8.94429(9)	6.68112(3)	113.634(1)	392.247(7)
	773	7.16638(3)	8.94561(5)	6.68240(8)	113.631(1)	392.470(6)

Table 5. Lattice parameters for $(\text{Ca}_x\text{Sr}_{1-x})\text{TiOGeO}_4$ at room temperature.

Mol % Sr	a (Å)	b (Å)	c (Å)	β (°)	V (Å ³)
100	7.22520(2)	9.07540(9)	6.78517(9)	113.510(1)	407.982(8)
90	7.21252(4)	9.05575(2)	6.76927(2)	113.520(1)	405.401(4)
70	7.19160(2)	9.01342(3)	6.73876(4)	113.593(1)	400.300(4)
60	7.19292(9)	8.99967(2)	6.72950(5)	113.647(2)	399.049(8)
50	7.17794(9)	8.97526(2)	6.71050(2)	113.658(1)	395.983(6)
40	7.17573(9)	8.95649(3)	6.69879(2)	113.708(1)	394.157(6)
30	7.16777(6)	8.94086(4)	6.68690(2)	113.724(1)	392.323(5)
10	7.15800(2)	8.90751(3)	6.66305(7)	113.766(1)	388.809(5)
0	7.15830(1)	8.88540(1)	6.64900(1)	113.834(1)	386.840(9)

Notes: Data for CaTiOGeO_4 see Ellemann-Olesen and Malcherek, 2004a.

Table 6. Atomic positional parameters and isotropic thermal vibration parameters ($\text{Å}^2 \times 10^{-5}$) at room temperature using SG $P2_1/a$ for $(\text{Ca}_x\text{Sr}_{1-x})\text{TiOGeO}_4$.

Mol% Sr					
100	x	y	z	U_{iso}	occ
Sr	0.2439(1)	0.4193(5)	0.2525(9)	2434(3)	1.000
Ti	0.5143(8)	0.2527(4)	0.7438(6)	1931(2)	1.000
Ge	0.7479(5)	0.4377(1)	0.2471(9)	2495(2)	1.000
O1	0.7478(1)	0.3067(7)	0.7327(3)	1446(3)	1.000
O2A	0.9031(2)	0.3097(1)	0.4425(6)	1446(3)	1.000
O2B	0.0789(7)	0.1791(7)	0.0545(1)	1446(3)	1.000
O3A	0.3936(7)	0.4661(3)	0.6510(1)	1446(3)	1.000
O3B	0.6069(9)	0.0605(4)	0.8444(2)	1446(3)	1.000

R_p 0.139

$R(F^2)$ 0.087

90	x	y	z	U_{iso}	occ
Ca	0.2444(7)	0.4195(8)	0.2533(1)	2524(5)	0.923(9)
Sr	0.2444(7)	0.4195(8)	0.2533(1)	2524(5)	0.076(1)
Ti	0.5122(9)	0.2595(1)	0.7483(6)	1545(4)	1.000
Ge	0.7457(3)	0.4365(7)	0.2468(9)	1300(6)	1.000
O1	0.7406(7)	0.3119(6)	0.7457(5)	1079(4)	1.000
O2A	0.9008(5)	0.3165(1)	0.4416(3)	1079(4)	1.000
O2B	0.0801(2)	0.1912(1)	0.0617(7)	1079(4)	1.000
O3A	0.4061(8)	0.4503(2)	0.6385(8)	1079(4)	1.000
O3B	0.6184(2)	0.0418(2)	0.8444(3)	1079(4)	1.000

R_p 0.183

$R(F^2)$ 0.129

70	<i>x</i>	<i>y</i>	<i>z</i>	U_{iso}	<i>occ</i>
Ca	0.2442(6)	0.4194(5)	0.2539(1)	2494(5)	0.699(7)
Sr	0.2442(6)	0.4194(5)	0.2539(1)	2494(5)	0.300(3)
Ti	0.5170(4)	0.2594(4)	0.7541(6)	1650(4)	1.000
Ge	0.7484(2)	0.4358(8)	0.2556(7)	1287(6)	1.000
O1	0.7565(7)	0.3075(6)	0.7682(1)	1116(4)	1.000
O2A	0.9041(7)	0.3217(6)	0.4482(1)	1116(4)	1.000
O2B	0.0771(2)	0.1986(8)	0.0693(5)	1116(4)	1.000
O3A	0.3867(1)	0.4594(9)	0.6410(9)	1116(4)	1.000
O3B	0.6049(2)	0.0447(6)	0.8477(8)	1116(4)	1.000

R_p 0.204

$R(F^2)$ 0.152

60	<i>x</i>	<i>y</i>	<i>z</i>	U_{iso}	<i>occ</i>
Ca	0.2452(7)	0.4207(6)	0.2499(6)	2720(4)	0.610(4)
Sr	0.2452(7)	0.4207(6)	0.2499(6)	2720(4)	0.389(6)
Ti	0.5116(2)	0.2511(9)	0.7446(1)	1322(5)	1.000
Ge	0.7499(8)	0.4341(9)	0.2472(8)	1577(3)	1.000
O1	0.7520(8)	0.3095(7)	0.7540(8)	762(4)	1.000
O2A	0.9108(3)	0.3046(8)	0.4187(9)	762(4)	1.000
O2B	0.0727(1)	0.1848(6)	0.0457(3)	762 (4)	1.000
O3A	0.3950(1)	0.4602(1)	0.6492(8)	762 (4)	1.000
O3B	0.6000(8)	0.0460(7)	0.8472(5)	762 (4)	1.000

R_p 0.096

$R(F^2)$ 0.040

50	<i>x</i>	<i>y</i>	<i>z</i>	U_{iso}	<i>occ</i>
Ca	0.2414(9)	0.4195(2)	0.2531(2)	2597(5)	0.492(6)
Sr	0.2414(9)	0.4195(2)	0.2531(2)	2597(5)	0.507(4)
Ti	0.5157(9)	0.2547(8)	0.7425(7)	1644(3)	1.000
Ge	0.7431(7)	0.4330(9)	0.2489(1)	1262(5)	1.000
O1	0.7506(6)	0.3192(2)	0.7410(9)	660(3)	1.000
O2A	0.9043(8)	0.3067(3)	0.4492(3)	660(3)	1.000
O2B	0.0670(6)	0.1856(1)	0.0846(6)	660(3)	1.000
O3A	0.3935(5)	0.4683(8)	0.6496(2)	660(3)	1.000
O3B	0.6125(2)	0.0554(4)	0.8544(1)	660(3)	1.000

R_p 0.204

$R(F^2)$ 0.164

40	<i>x</i>	<i>y</i>	<i>z</i>	U_{iso}	<i>occ</i>
Ca	0.2373(2)	0.4197(5)	0.2515(2)	2544(4)	0.406(7)
Sr	0.2373(2)	0.4197(5)	0.2515(2)	2544(4)	0.593(3)
Ti	0.5120(5)	0.2486(5)	0.7397(9)	1942(4)	1.000
Ge	0.7455(9)	0.4343(4)	0.2488(8)	1955(5)	1.000
O1	0.7433(6)	0.3152(1)	0.7511(7)	659(3)	1.000
O2A	0.8958(6)	0.3089(5)	0.4385(7)	659(3)	1.000
O2B	0.0676(5)	0.1973(1)	0.0777(8)	659(3)	1.000
O3A	0.4003(1)	0.4602(5)	0.6450(3)	659(3)	1.000
O3B	0.6091(3)	0.0399(6)	0.8513(7)	659(3)	1.000

R_p 0.144
 $R(F^2)$ 0.092

30	<i>x</i>	<i>y</i>	<i>z</i>	U_{iso}	<i>occ</i>
Ca	0.2444(5)	0.4202(9)	0.2550(3)	2071(5)	0.286(1)
Sr	0.2444(5)	0.4202(9)	0.2550(3)	2071(5)	0.713(9)
Ti	0.5114(6)	0.2553(3)	0.7421(1)	1362(4)	1.000
Ge	0.7446(2)	0.4343(6)	0.2483(6)	2339(5)	1.000
O1	0.7420(8)	0.3169(6)	0.7538(4)	1017(4)	1.000
O2A	0.9073(8)	0.3039(6)	0.4324(2)	1017(4)	1.000
O2B	0.0738(5)	0.1913(8)	0.0652(7)	1017(4)	1.000
O3A	0.3923(3)	0.4669(1)	0.6362(1)	1017(4)	1.000
O3B	0.6120(9)	0.0519(4)	0.8492(7)	1017(4)	1.000

R_p 0.215
 $R(F^2)$ 0.178

10	<i>x</i>	<i>y</i>	<i>z</i>	U_{iso}	<i>occ</i>
Ca	0.2391(6)	0.4206(9)	0.2506(5)	1289(5)	0.096(4)
Sr	0.2391(6)	0.4206(9)	0.2506(5)	1289(5)	0.903(6)
Ti	0.5148(1)	0.2580(1)	0.7497(2)	1483(4)	1.000
Ge	0.7499(1)	0.4340(2)	0.2462(9)	1938(4)	1.000
O1	0.7440(7)	0.3105(9)	0.7355(3)	1578(4)	1.000
O2A	0.9086(9)	0.3041(9)	0.4351(4)	1578(4)	1.000
O2B	0.0685(4)	0.1893(1)	0.0558(4)	1578(4)	1.000
O3A	0.3842(5)	0.4631(6)	0.6420(3)	1578(4)	1.000
O3B	0.6015(4)	0.0458(6)	0.8536(7)	1578(4)	1.000

R_p 0.210
 $R(F^2)$ 0.173

Notes: Data for CaTiOGeO₄ see Ellemann-Olesen and Malcherek, 2004a.

Table 7. Mean bond lengths (Å) at room temperature using SG P2₁/a.

Mol % Sr	Ge-O	Ti-O	Ca-O/Sr-O
STGO	1.755	1.965	2.563
90	1.758	1.978	2.526
70	1.743	1.981	2.521
60	1.758	1.985	2.510
50	1.737	1.996	2.498
40	1.745	1.995	2.470
30	1.747	1.972	2.474
10	1.750	1.964	2.479
CTGO	1.750	1.960	2.468

Table 8. Results of bond valence calculations performed on (Ca_xSr_{1-x})TiOGeO₄.

Mol % Sr	STGO	90	70	60	50	40	30	10	CTGO
Ge	3.99	3.98	4.02	4.04	3.96	3.93	4.02	3.99	3.97
Ti	4.17	4.17	4.17	4.18	4.18	4.18	4.18	4.18	4.18
Ca/Sr	2.08	2.06	2.02	2.00	1.98	1.96	1.94	1.90	1.88

Notes: bond valence sums were calculated according to Brese and O'Keefe (1991). Bond valence sums for mixed site occupancies have been calculated using weighted averages of the end member values. Data for CaTiOGeO₄ and CaZrOGeO₄ are taken from Ellemann-Olesen and Malcherek, 2004a and Malcherek and Ellemann-Olesen, 2004, respectively.

Table 9. Results of angle variance calculations performed on (Ca_xSr_{1-x})TiOGeO₄.

Mol % Sr	STGO	90	70	60	50	40	30	10	CTGO
Ge	27.0	28.4	27.3	37.9	60.4	68.1	44.4	38.5	23.0
Ti	14.4	21.7	33.1	14.6	30.7	34.5	18.9	26.4	16.6

Notes: the angle variance was calculated according to Robinson *et al.*, 1971. Data for CaTiOGeO₄ are taken from Ellemann-Olesen and Malcherek, 2004a and Malcherek and Ellemann-Olesen, 2004, respectively.

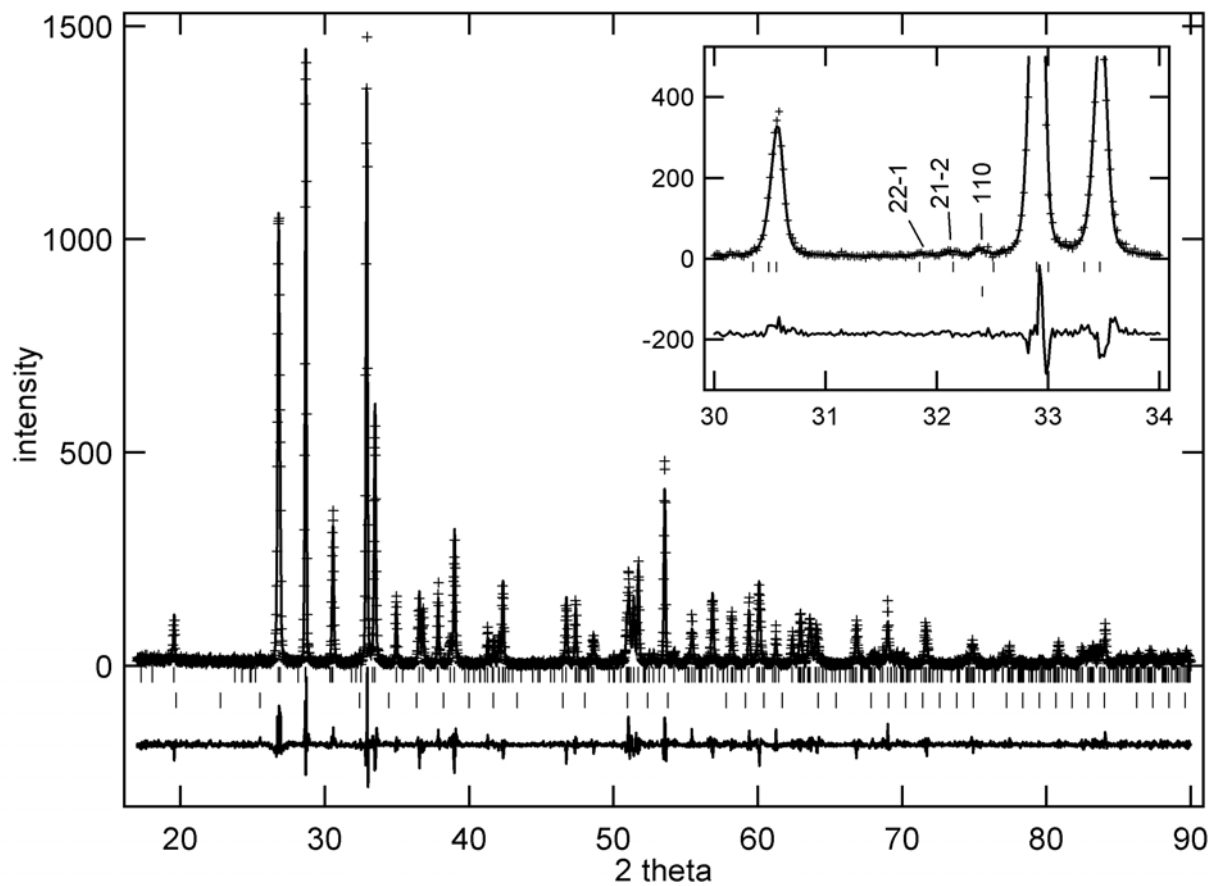


Fig. 1 Rietveld plot of SrTiOGeO_4 at room temperature in space group $P2_1/a$. The lower set of reflection markers indicates SrTiO_3 . The insert shows a magnified portion of the diagram around the 21-2 and 22-1 reflections. The 110 reflection belongs to SrTiO_3 .

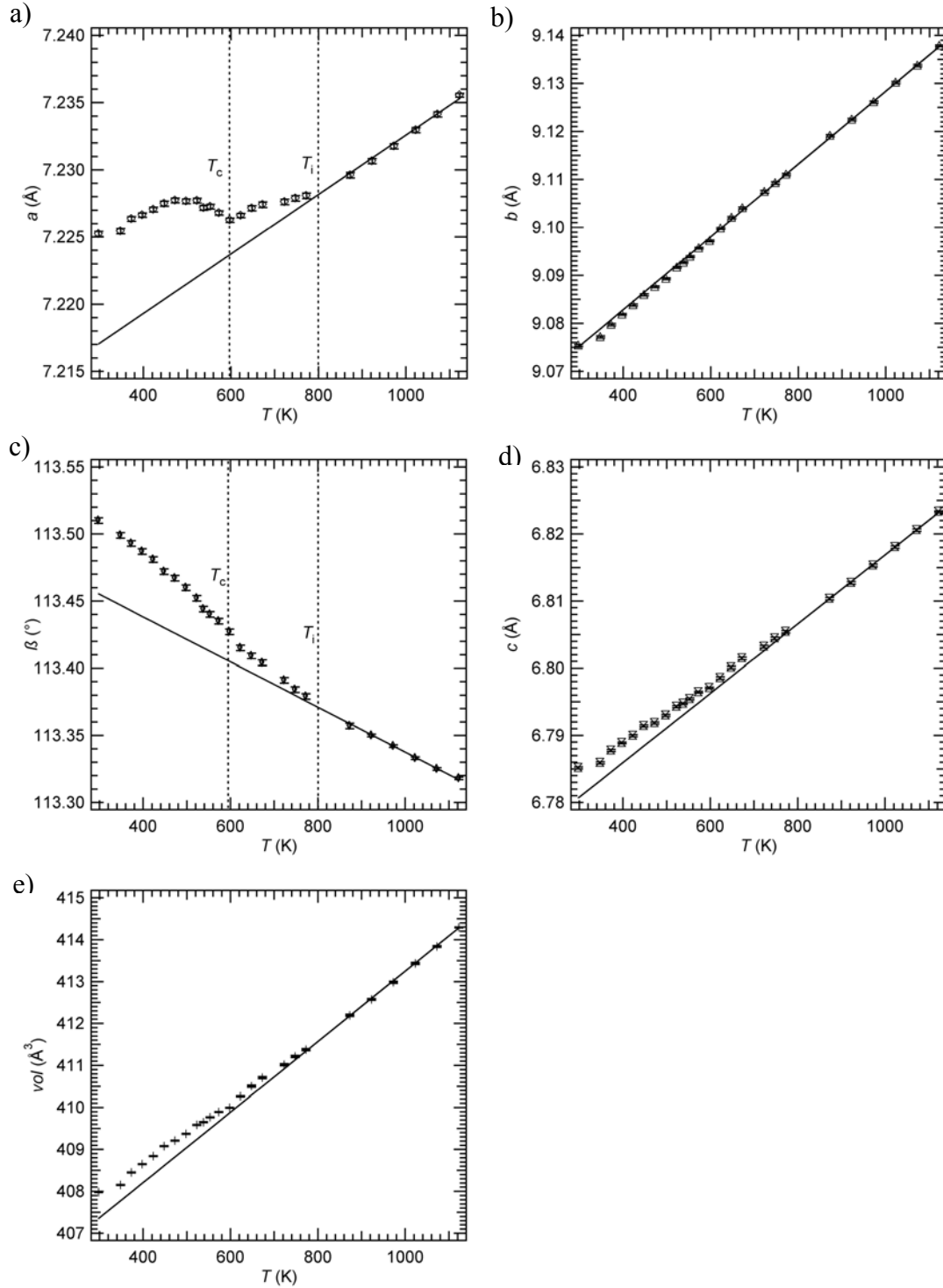


Fig. 2 Temperature plots of SrTiOGeO₄ lattice parameters. The straight lines are the extrapolated high temperature reference functions. The perpendicular dashed lines in (a) and (d) indicate the position of T_c (594 K) and T_i (800 K), respectively.

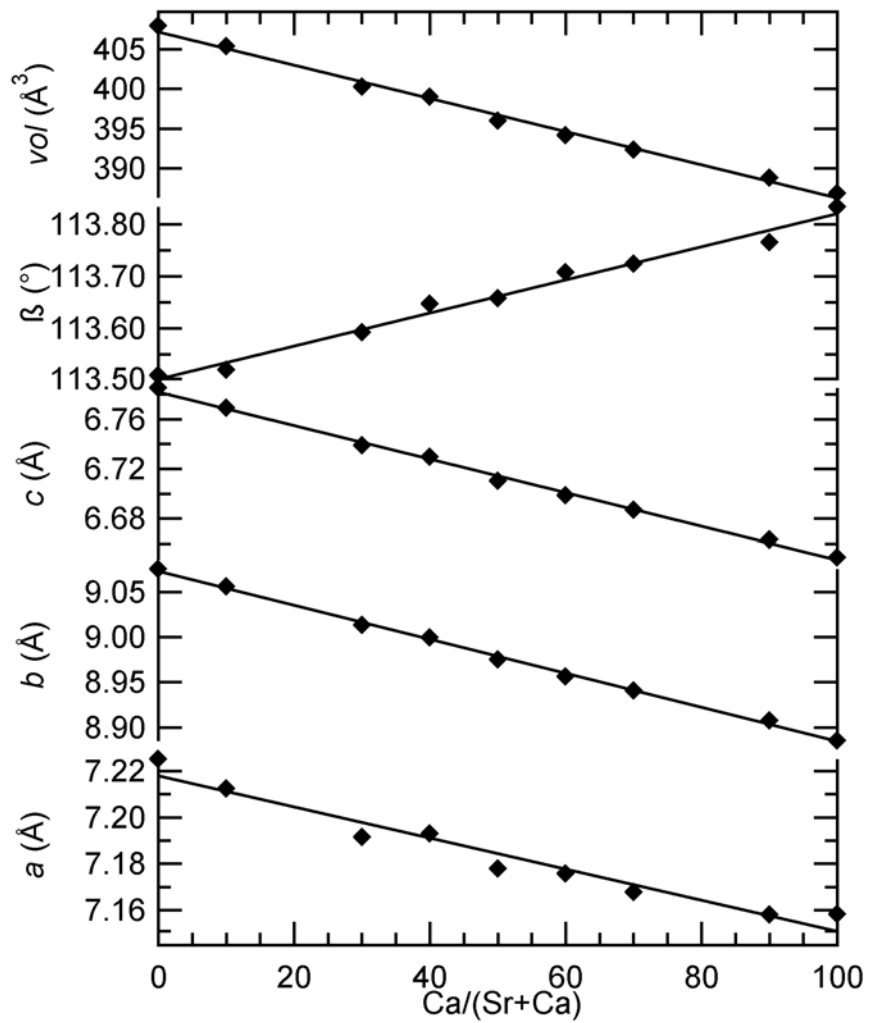


Fig. 3 $(\text{Ca}_x\text{Sr}_{1-x})\text{TiOGeO}_4$. Lattice constants at room temperature as a function of Ca content.

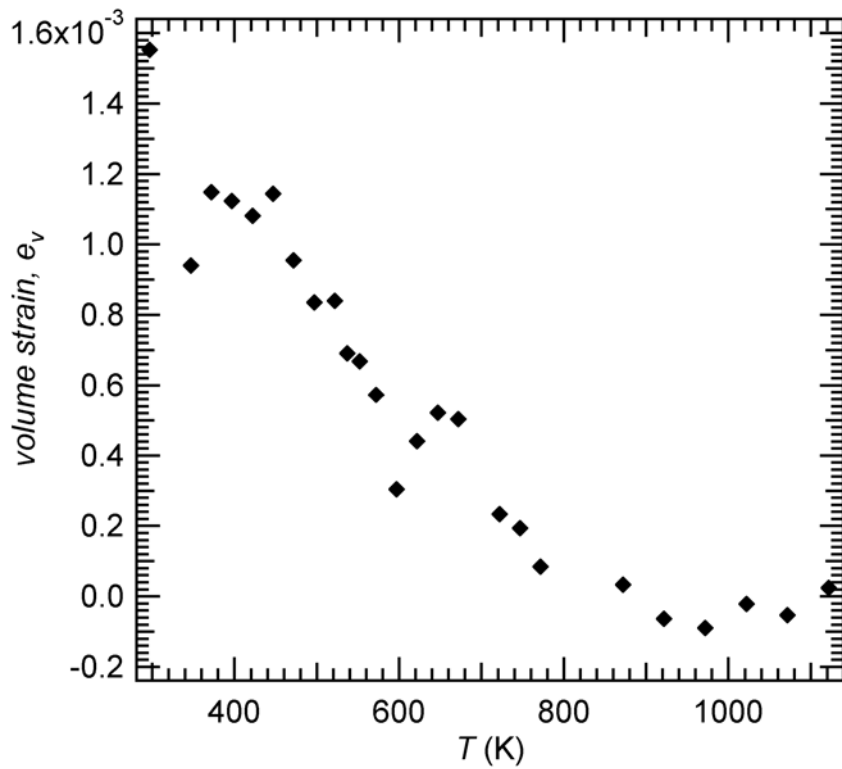
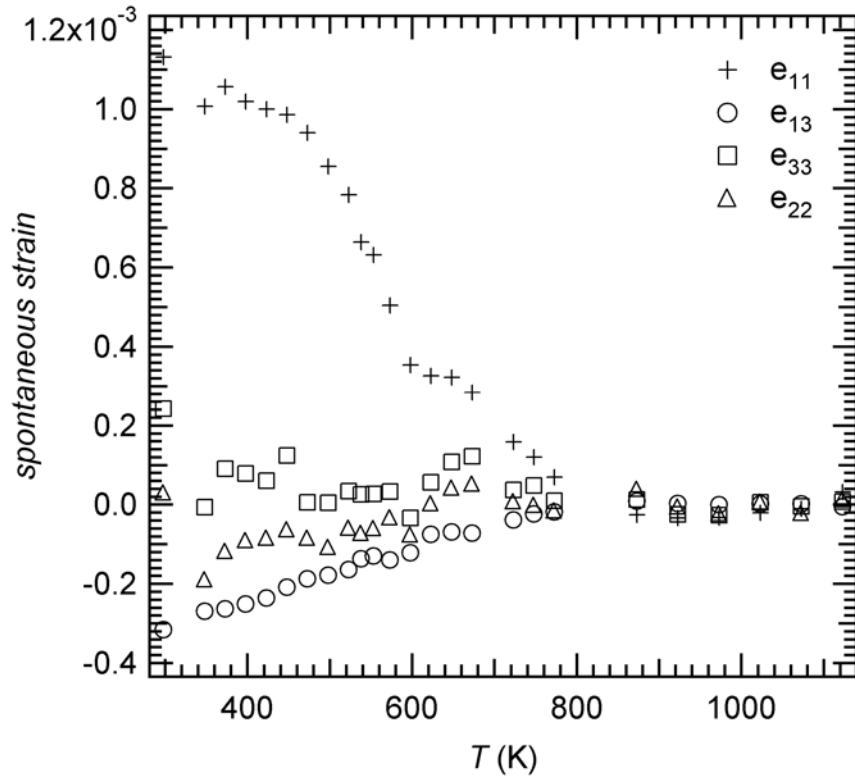


Fig. 4 Strain components (a) and volume strain, e_v (b) for SrTiOGeO₄ as a function of temperature.

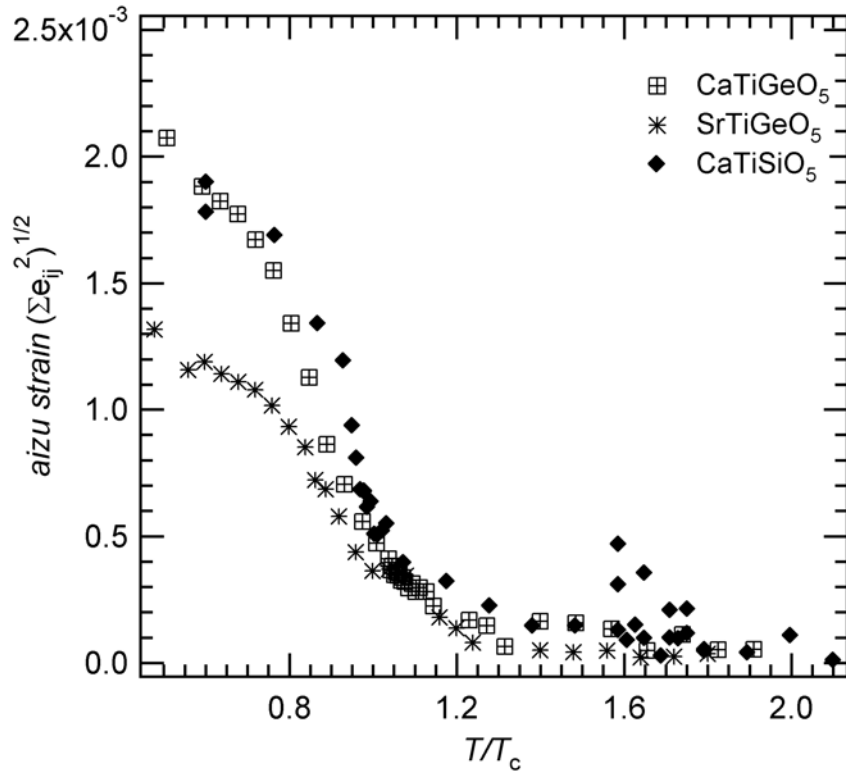


Fig. 5 The scalar strain as a function of reduced temperature for SrTiOGeO₄, CaTiOGeO₄ and titanite (data from Malcherek, 2001).

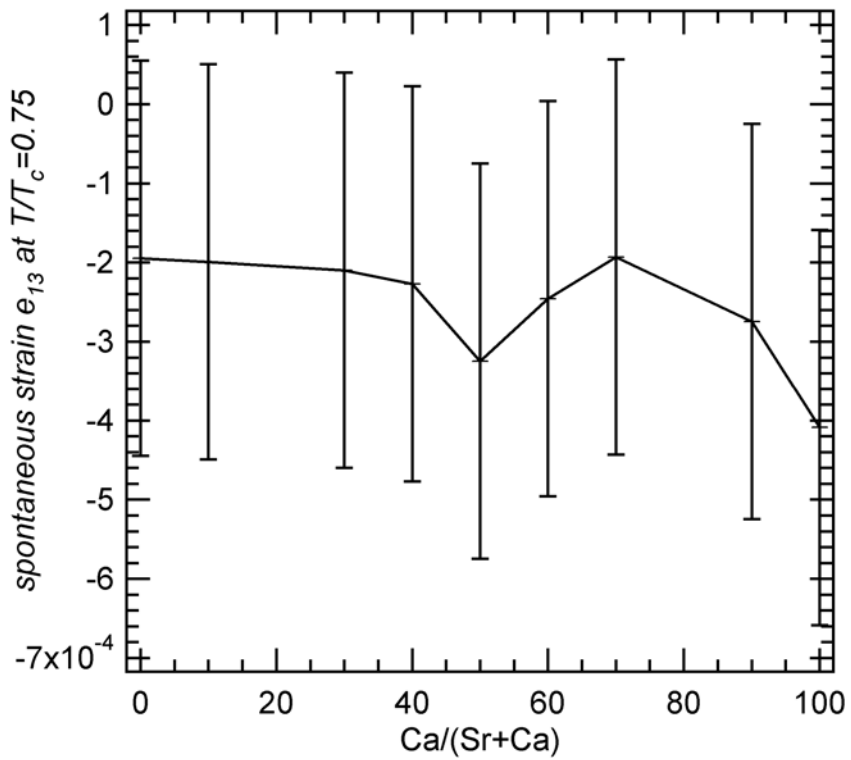
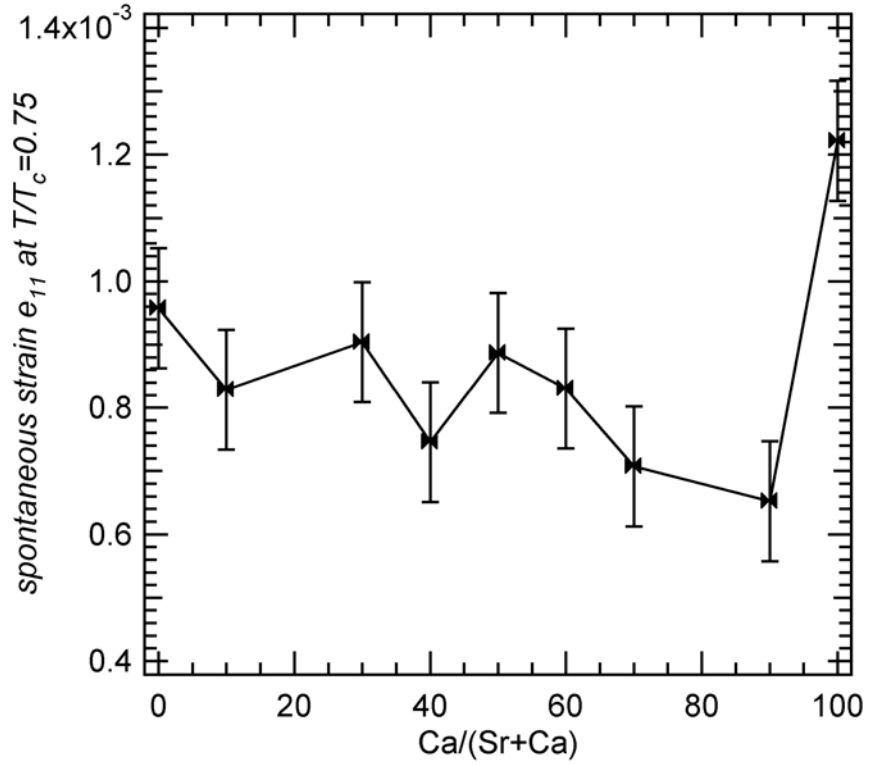


Fig. 6 Strain components e_{11} (a) and e_{13} (b) at $T/T_c = 0.75$ for $(\text{Ca}_x\text{Sr}_{1-x})\text{TiOGeO}_4$ as a function of Ca content.

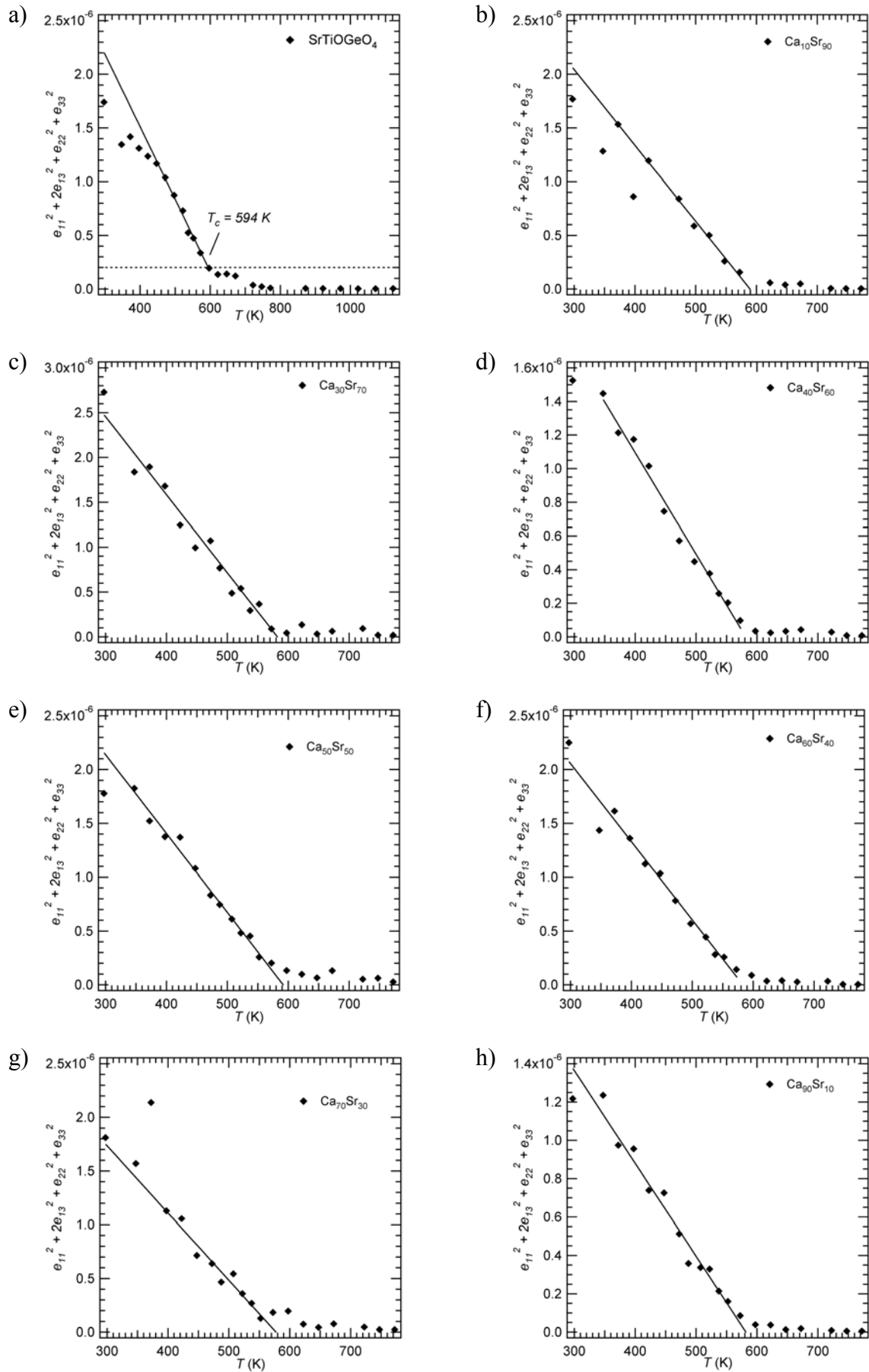


Fig. 7 The square of the scalar strain for all intermediate compositions. The relationship is linear with temperature and implies that the transition is tricritical in character.

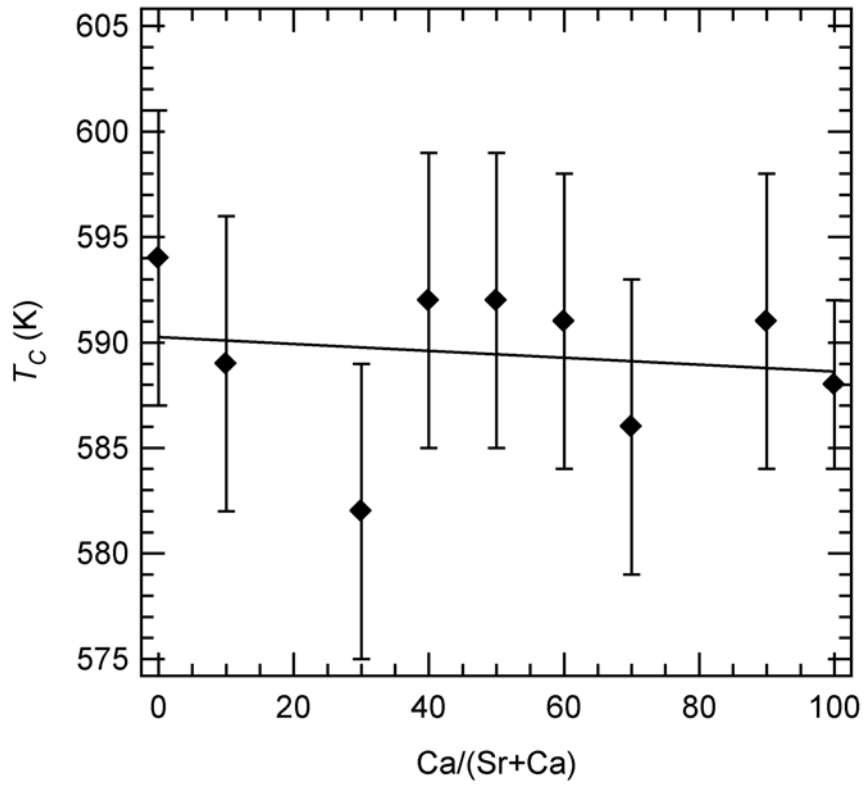


Fig. 8 The transition temperature, T_c across the solid solution $(\text{Ca}_x\text{Sr}_{1-x})\text{TiOGeO}_4$. $T_c = 594 \pm 10$ K for SrTiOGeO_4 and $T_c = 588 \pm 4$ K for CaTiOGeO_4 .

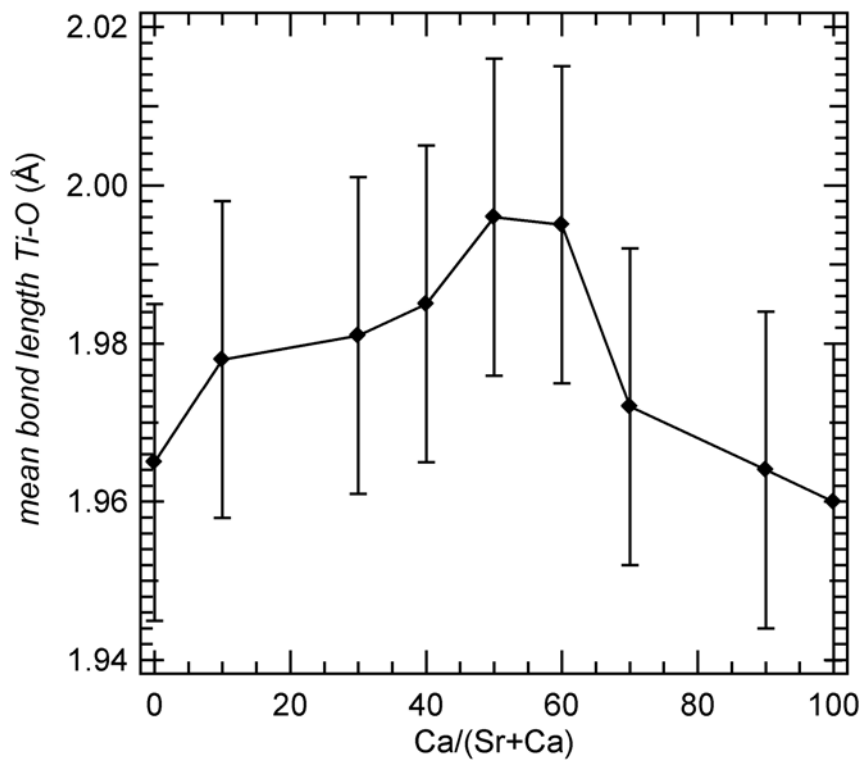


Fig. 9 The average Ti-O bond length at room temperature as a function of Ca content.

5. Temperature- and composition dependence of the phase transitions in $\text{Ca}(\text{Ti}_x\text{Zr}_{1-x})\text{OGeO}_4$

A scientific manuscript submitted to *American Mineralogist*
June 2004

Accepted
August 2004

Authors:

Rikke Ellemann-Olesen
Universität Heidelberg, Mineralogisches Institut, Im Neuenheimer Feld 236
69120 Heidelberg, Germany

Thomas Malcherek
Universität Heidelberg, Mineralogisches Institut, Im Neuenheimer Feld 236
69120 Heidelberg, Germany

Abstract

The solid solubility of CaTiOGeO_4 with CaZrOGeO_4 and the structural phase transitions occurring in this solid solution as a function of temperature and composition are examined using in situ high temperature X-ray powder diffraction. Structural phase transitions are identified based on the determination of spontaneous strain. The transition $\text{P}2_1/a - \text{A}2/a$ typical for titanite and CaTiOGeO_4 is observed in samples with Zr concentrations up to 10%. The addition of Zr destabilizes the ordered $\text{P}2_1/a$ phase and T_c decreases accordingly. The aristotype structure of titanite in space group symmetry $\text{A}2/a$ is observed for intermediate compounds. Compounds with high Zr content exhibit a triclinically distorted titanite structure. Their structure has been modelled in space group symmetry $\bar{A}1$. The triclinic structure appears at Zr contents of about 70% with T_c close to ambient temperature. Further increase of the Zr content stabilizes the triclinic structure and leads to an increase of T_c up to $T_c = 488$ K in CaZrOGeO_4 .

1. Introduction

The structure of CaZrOGeO_4 has recently been described as a triclinically distorted titanite structure, which transforms to the titanite aristotype structure near 488 K (Malcherek and Ellemann-Olesen, 2004). However, in terms of structural phase transitions the mineral titanite, CaTiOSiO_4 , is well known for its $\text{P}2_1/a - \text{A}2/a$ phase transition, related to off centering of the Ti cation within its octahedral oxygen coordination environment. Details of the titanite structure and its displacive phase transitions have been the subject of numerous articles (Speer and Gibbs, 1976; Taylor and Brown, 1976; Ghose *et al.*, 1991; Bismayer *et al.*, 1992; Salje *et al.*, 1993; Kek *et al.*, 1997; Kunz *et al.*, 2000; Malcherek 2001; Malcherek *et al.*, 2001). Very similar behaviour has been observed for the Ge-analogue, CaTiOGeO_4 (Ellemann-Olesen and Malcherek, 2004). In these materials the displacive phase transition is characterized by displacement of the titanium atom from the centre of the $[\text{TiO}_6]$ octahedron. The ordered low temperature phase exhibits alternating short and long Ti-O bonds along $[100]$, with reversed sense of Ti displacement among adjacent octahedral chains. In the macroscopically disordered form ($\text{A}2/a$), Ti is nominally found at the centre of the $[\text{TiO}_6]$ octahedra. In titanite true $\text{A}2/a$ symmetry is suggested to be attained only at a second phase transition at about $T_i = 825$ K, with correlated Ti and Ca displacements persisting in the intermediate regime (Zhang *et al.*, 1997; Kek *et al.*, 1997; Malcherek *et al.*, 1999; Malcherek, 2001). Similar behaviour is observed in isomorphous compounds and in solid solutions, with Sr substituting for Ca

(Ellemann-Olesen and Malcherek, in preparation) or with Ge substituting for Si (Ellemann-Olesen and Malcherek, 2004).

Furthermore it is known that the titanite topology may occur in a triclinically distorted form under certain conditions (Malcherek and Ellemann-Olesen, 2004). Examples include the montebrasite-amblygonite series $\text{Li}[\text{Al}(\text{PO}_4)\text{OH}]\text{-Li}[\text{Al}(\text{PO}_4)\text{F}]$ (Groat *et al.*, 1990), the structure of CaGe_2O_5 (Aust *et al.*, 1976) or the high-pressure form of malayaite (Rath *et al.*, 2003). The structure of CaZrOGeO_4 is topologically identical to the structure of the triclinic high-pressure form of malayaite (Malcherek and Ellemann-Olesen, 2004). Similar triclinic to monoclinic phase transitions may occur as a function of temperature, *e.g.* in CaGe_2O_5 at $T_c^* = 714 \pm 3$ K (Malcherek and Bosenick, 2004). The present study reports temperature- and composition dependent displacive phase transitions in the solid solution $\text{Ca}(\text{Ti}_x\text{Zr}_{1-x})\text{OGeO}_4$.

2. Experimental

A series of six samples has been synthesized by solid state reaction along the join $\text{Ca}(\text{Ti}_x\text{Zr}_{1-x})\text{OGeO}_4$ (CTGO_x) with $x = 0.95, 0.90, 0.80, 0.50, 0.20$ and 0.10 . The stoichiometric starting mixtures were prepared from pure fine grained powders of CaCO_3 , TiO_2 , ZrO_2 and GeO_2 in an open platinum crucible at a maximum temperature of 1323 K. Approximately 2.5 g starting oxides were ground, pressed into pellets and heated for several intervals of 5 days with intermittent grindings. The final reactions of the pressed oxide pellet at 1588 K were carried out in a welded Pt-tube in order to avoid GeO_2 loss. Phase purity of the resulting product has been established by powder diffraction analysis. The impurity phases ZrO_2 (baddeleyite, ca. 0.5 wt%) and CaGe_2O_5 (ca. 0.8 wt%) have been identified in CTGO10. No secondary phases have been observed for the remaining compositions.

In situ X-ray powder diffraction measurements up to 1073 K have been carried out using an Anton Paar HTK 1200 furnace mounted on a Philips Xpert diffractometer with monochromatic $\text{CuK}\alpha_1$ -radiation. Diffraction patterns were recorded in the range $17\text{-}90^\circ 2\theta$ using a proportional counter with 4 s/step counting time and a step size of 0.02° . Additional room temperature powder diffraction data in the range of $5 - 100^\circ 2\theta$ were obtained of CTGO10 and CTGO20 on a Philips Xpert diffractometer with $\text{CuK}\alpha$ -radiation and a secondary beam monochromator. Lattice parameters at elevated temperatures were determined using the LeBail method as implemented in the GSAS program (Larson and Von Dreele 1994). As far as the LeBail analysis is concerned, the compositions CTGO95, CTGO90, CTGO80 and CTGO50 have been refined using space group $A2/a$. The $A2/a$

setting was chosen as the superstructure reflections with $k + l = 2n + 1$ are weak and mostly overlapping with the fundamental reflections (Malcherek, 2001). For compositions CTGO20 and CTGO10 the $A\bar{1}$ space group setting was chosen. Rietveld refinements were carried out using the room temperature data only. For the Rietveld refinement the $P2_1/a$ setting was applied for the compositions CTGO95, CTGO90 and the $A2/a$ setting for CTGO80 and CTGO50. Triclinic compounds were refined using space group $A\bar{1}$ with the starting parameters of CaZrOGeO_4 (Malcherek and Ellemann-Olesen, 2004). The isotropic thermal parameters of the oxygen atoms had to be constrained to the same value in order to obtain positive definite thermal parameters for all atoms. Starting coordinates for monoclinic compounds were taken from the known structure of CaTiOGeO_4 .

The variation of the shape and size of the unit cell as a result of the phase transition is expressed in terms of the spontaneous strain. The components of the strain tensor have been calculated according to the equations given by Carpenter *et al.*, 1998. In the following we will distinguish symmetry breaking (sb) strain components, *i.e.* e_{12} and e_{23} , from non-symmetry breaking (nsb) components. The scalar spontaneous strain is defined as

$$e_s = \left(\sum e_{ij}^2 \right)^{1/2}$$

In the case of a zone centre transition, the sb-strain, which usually contributes most to the scalar strain defined above, should be proportional to the driving order parameter of the transition. If the critical point is located at the zone boundary of the first Brillouin zone of the high symmetry phase, the scalar strain should be proportional to the square of the order parameter, Q^2 , instead, as it is the case for the $P2_1/a - A2/a$ transition in titanite. Details regarding the coupling of order parameter and spontaneous strain can be found in Carpenter *et al.*, 1998 and Salje, 1990.

3. Results

The compounds CaZrOGeO_4 and CaTiOGeO_4 form a solid solution for all investigated compositions under the conditions of synthesis applied here. Rietveld refinements have been carried out for all room temperature data. The resulting ambient temperature lattice constants are given in Table 1. The refinements reveal a high sensitivity of the crystal symmetry on the amount of Zr present. Across the solid solution the replacement of Ti by the larger Zr leads to a gradual increase in cell volume by 9%. A decrease in the monoclinic angle β is observed as the Ti-content decreases. The a -, b - and c -lattice parameters increase across the solid solution towards the CaZrOGeO_4 endmember. The compositional variation of the a - and b -lattice

parameters is linear irrespective of the crystal symmetry at room temperature while the c -lattice parameter shows a minor change in slope depending on the actual structure. The deviation of the α - and γ -angles from 90° indicates the compositionally induced phase transition (Fig. 1). Lattice constants as a function of temperature for all intermediate compounds are listed in Table 2. By extrapolation of the lattice parameters measured for $T \geq 538$ K towards lower temperatures, linear reference functions of thermal expansion are obtained for all lattice parameters. These thermal expansion data are used to calculate the strain components.

The refined structural parameters at room temperature are given in Table 3. The variation of the mean bond lengths is displayed in Table 4. As expected the bond lengths of the octahedral cation to the surrounding oxygen atoms increase linearly with increasing Zr content. The mean Ge-O bond distance is constant within the limits of the measurement accuracy. The mean bond length of Ca to the surrounding oxygen atoms is constant but with a marked step between the monoclinic and triclinic compounds caused by the change in Ca-coordination. The mean $^{[8]}\text{Ca-O}$ bond length amounts to 2.55 \AA in the triclinic phases, whereas the $^{[7]}\text{Ca-O}$ bond length is 2.47 \AA in the Ti endmember (Fig. 2). Bond valence sums are given in Table 5.

The $P2_1/a - A2/a$ transition

The endmember composition CaTiOGeO_4 is isostructural to titanite and the displacive $A2/a - P2_1/a$ phase transition occurs at $T_c = 588 \pm 4 \text{ K}$ (Ellemann-Olesen and Malcherek, 2004). Judging by the strain analysis the $P2_1/a - A2/a$ phase transition is also observable in the compounds CTGO95 and CTGO90. The evolution of the lattice parameters is in agreement with CaTiOGeO_4 (Ellemann-Olesen and Malcherek, 2004). However deviation from the linear thermal expansion data is less significant for the a -lattice constant and the β -angle compared to titanite and CaTiOGeO_4 . Figure 3 displays the a -lattice parameter for CTGO80, CTGO90, CTGO95 and the endmember composition CTGO.

The X-ray diffraction data indicate the aristotype structure ($A2/a$) in the measured temperature range of CTGO50 and CTGO80. There is no discernable deviation from linear thermal expansion for all lattice constants. From this standpoint the compounds do not show evidence of a structural phase transition above ambient temperature. No measurements were carried out below room temperature.

In agreement with previous investigations of CaTiOGeO_4 (Ellemann-Olesen and Malcherek, 2004) and titanite (Malcherek, 2001), the spontaneous strain due to the $P2_1/a - A2/a$ phase

transition in CTGO95 is relatively small and dominated by the components e_{11} and e_{13} . The square of the scalar strain e_s^2 extrapolates linearly to zero at $T_c = 480 \pm 5$ K. In analogy with the endmember composition CaTiOGeO_4 the linear temperature dependence of e_s^2 below the phase transition indicates close to tricritical character of the transition ($Q^4 \propto T - T_c$).

The $A\bar{1}$ - $A2/a$ transition

In analogy to CaZrOGeO_4 the samples CTGO10 and CTGO20 exhibit the triclinic $A\bar{1}$ structure at low temperatures. The evolution of the lattice parameters agrees with that of the endmember composition CaZrOGeO_4 (Malcherek and Ellemann-Olesen, 2004) (Fig. 4). The triclinic distortion observed at room temperature, as indicated by the deviation of α and γ from 90° decreases with increasing Ti-content.

By linear extrapolation of e_s^2 to zero the transition temperature is estimated to $T_c = 429 \pm 5$ K and $T_c = 371 \pm 5$ K for CTGO10 and CTGO20, respectively.

The spontaneous strain associated with the triclinic to monoclinic phase transition in the titanite structure is relatively large and dominated by the symmetry breaking components e_{12} and e_{23} (Fig. 5). For CTGO20 ($T = 298$ K) the e_{23} and e_{12} components are -0.009 and 0.0045, respectively corresponding to a decrease of 33% and 45% from CaZrOGeO_4 . Therefore the triclinic distortion is lowered by the presence of Ti.

Figure 6 shows the evolution of the non-symmetry breaking strain as a function of reduced temperature. The components e_{13} and e_{33} dominate with symmetrical evolution about the temperature axis. The non-symmetry breaking strain components e_{13} and e_{33} describe a linear contraction of the unit cell approximately parallel to the c^* -direction and simultaneous shearing within the triclinic stability field. As a consequence the volume strain is negative and amounts to -0.19% and -0.27% in CTGO10 and CTGO20, comparable to -0.28% in CaZrOGeO_4 . The room temperature value of the e_{33} component falls to -0.001 for CTGO20, a decrease of nearly 62% from CaZrOGeO_4 . As the superposition of the nsb-strain components against reduced temperature demonstrates, the evolution of the nsb-strain is hardly affected by changes in the Ti content, which mainly alters T_c instead (Fig. 6).

A linear dependence is evident between temperature and the square of the scalar strain, e_s^2 (Fig. 7). As the triclinic to monoclinic change in symmetry implies the transition is of the zone centre type, it can be concluded that $Q^2 \propto T - T_c$ and the transition is continuous second-order in analogy to CaZrOGeO_4 (Malcherek and Ellemann-Olesen, 2004).

Figure 8 displays the evolution of the critical temperatures as observed by strain analysis across the solid solution.

4. Discussion

The temperature evolution of the $\text{Ca}(\text{Ti}_x\text{Zr}_{1-x})\text{OGeO}_4$ solid solution shows a more complicated behaviour than previously studied compositions in the titanite structure field (*e.g.* Kunz *et al.*, 1997; Angel *et al.*, 1999; Ellemann-Olesen and Malcherek, 2004). Whereas at high Ti-contents the commonly observed $A2/a - P2_1/a$ transition is found, a monoclinic to triclinic transition can be observed at high Zr-concentrations. The X-ray diffraction data indicate the aristotype structure ($A2/a$) in the measured temperature range for CTGO50 and CTGO80. The compositional range of the triclinic structure is broader than that of the $P2_1/a$ structure. The triclinic – monoclinic compositional phase transition is expected at $\text{Ca}(\text{Ti}_{32}\text{Zr}_{68})\text{OGeO}_4$, while the transition $P2_1/a - A2/a$ occurs at $\text{Ca}(\text{Ti}_{82}\text{Zr}_{18})\text{OGeO}_4$. These phase boundaries have been estimated from linear extrapolation of the known critical temperatures towards room temperature (Fig. 8).

As a result of the triclinic – monoclinic phase transition, the position of the Ca atom shifts away from the diad axis of the monoclinic phase. The direction of the displacement is approximately parallel to the a -axis. Figure 9 shows that the Ca displacement at room temperature is a linear function of the symmetry breaking strain components.

In agreement with CaZrOGeO_4 the triclinic compounds CTGO10 and CTGO20 show a 8-fold coordinated Ca atom when considering the bond distances to all nearest O atoms. The bond valence sums for Ca are 1.849 and 1.894, respectively. This change in coordination is also found in the high-pressure phase transition of malayaite (Rath *et al.*, 2003), in which the observed Ca displacement almost parallel to $[100]$ causes a change in coordination from the originally linear $[\text{CaO}_7]$ chains to sheets of $[\text{CaO}_8]$ parallel to $(\bar{1}11)$. This indicates that the chemically imposed structural strain across $\text{Ca}(\text{Ti}_x\text{Zr}_{1-x})\text{OGeO}_4$ has a similar effect on the structure as pressure induced strain in malayaite.

In the triclinic phase the Zr atom occupies two distinct sites. In the monoclinic $A2/a$ symmetry the $[\text{ZrO}_6]$ octahedra form linear chains parallel to $[100]$ analogous to the high temperature phase of CaTiOGeO_4 and titanite. In the triclinic form the distance between adjacent ZrO_6 chains is compressed more strongly parallel to $[011]$ than parallel to $[01\bar{1}]$, violating both the twofold screw axis and the glide plane in the $A2/a$ symmetry. As a

consequence, the Zr occupies symmetrically distinct positions along the octahedral chains. This asymmetric relative shift of the ZrO_6 chains is reflected directly by the distances between two ZrO_6 chains. In the monoclinic structure the distance is the same for all Zr-atoms while in the triclinic structure two distinct distances are observed.

Strain variations as a function of composition across the solid solution are expected to indicate in what way the substitution of the larger Zr atom influences the structure. Any structural or compositional change that changes the shape or volume of the octahedra must have a significant influence on any possible phase transition. The evolution of the non-symmetry breaking strain in CTGO10 and CTGO20 is, as in $CaZrOGeO_4$, in close agreement with the compound $CaTaOAlO_4$ studied by Malcherek *et al.*, 2004. The structure of $CaTaOAlO_4$ is topologically identical with the titanite structure and it displays several displacive phase transitions. The general contraction of the titanite-framework perpendicular to the octahedral chain direction is a common feature of the transitions in CZGO and CTAO. In CZGO this contraction is accompanied by additional triclinic distortion and ensuing alteration of the other nsb-strain components e_{11} and e_{22} . Furthermore the temperature evolution of the b -lattice parameter in $CaTaOAlO_4$ only reflects thermal expansion contrary to CTGO10 and CTGO20, which show a minor deviation in the b -lattice parameter and as a result an additional strain expressed by the e_{22} component contributes to the scalar stain. This is probably due to the additional triclinic distortion.

The temperature evolution of the symmetry breaking strain components can be modelled using a second-order Landau type free energy expansion. Malcherek and Bosenick, 2004 described the strain evolution of $CaGe_2O_5$ using such a model. In analogy to $CaGe_2O_5$ we therefore presume that the symmetry breaking strain components e_{23} and e_{12} behave in the same manner as the order parameter for the transition, giving $e_{23} \propto e_{12} \propto Q$ as the expected strain/order parameter relationship. The symmetry breaking strain $e_4 = 2e_{23}$ is taken to be the driving order parameter of the transition, with $e_6 = 2e_{12}$ being linearly coupled to it (Carpenter and Salje, 1998; Malcherek and Bosenick, 2004). The solid curves in Figure 5 indicate the

resulting temperature behaviour

$$e_4^2 = (e_4^0)^2 \left(1 - \frac{T}{T_c^*} \right)$$

Just as the temperature evolution of the symmetry breaking strain indicates a linear coupling to the order parameter of the phase transition (or its identity with the order parameter) the linear correlation between nsb-strain components and temperature indicates their coupling to the square of the order parameter (Carpenter *et al.*, 1998).

Across the measured temperature range Rietveld refinements reveal the disordered monoclinic structure ($A2/a$) for the intermediate compounds CTGO90, CTGO80 and CTGO50. Thus the transition $P2_1/a - A2/a$ typical for titanite and CaTiOGeO_4 is not observable above ambient temperature for Zr concentrations in excess of 10% in our experiments. However, from linear extrapolation of the obtained critical temperatures the phase boundary is expected at 81% Ti. The addition of Zr apparently destabilizes the ordered $P2_1/a$ phase. In the ordered $P2_1/a$ phase of titanite and its analogue CaTiOGeO_4 , the off-centre vectors are oriented parallel to each other within individual octahedral chains, but antiparallel with respect to neighbouring chains. In the $A2/a$ setting Ti is nominally found at the centre of the $[\text{TiO}_6]$ octahedra (Speer and Gibbs, 1976). The presented series of experiments reveals that replacing 10% of the octahedral Ti by Zr leads to a complete loss of the Ti out-off-centre coherence. This observation is in accordance with previous findings on natural titanites, where the presence of impurities on the octahedral site leads to a similar symmetry change. Oberti *et al.*, 1991 studied natural high-aluminium-titanites with $X_{\text{Al}} = \text{Al}/(\text{Ti} + \text{Al} + \text{Fe}) \geq 0.25$, using X-ray diffraction and electron microprobe analysis, and concluded that substitution of Al (X_{Al}) above 0.25 results in space group $A2/a$. Our observations are also in accordance with the behaviour of the solid solution titanite – malayaite studied by Kunz *et al.*, 1997. A series of experiments revealed that already at a Sn concentration of 10% no $k + l = \text{odd}$ reflections could be observed anymore, thus the addition of 10% Sn destabilizes the ordered $P2_1/a$ phase and the disordered $A2/a$ structure dominates. CTGO95 exhibits the displacive phase transition $P2_1/a - A2/a$ in analogy with titanite and CaTiOGeO_4 . However, even a small Zr concentration of 5% causes lowering of the critical temperature by nearly 100 K (Fig. 8).

Despite the similar electronic properties of Zr and Ti the $P2_1/a$ phase is suppressed in CaZrOGeO_4 , in analogy with the substitution of Ti by Sn across the titanite – malayaite join (Kunz *et al.*, 1997).

Given the d_0 -character of the Zr-cation a structural distortion similar to the Ti off centering in titanite might be expected in CZGO. The apparent absence of such an off centering, indicated by the suppression of the $P2_1/a$ -ordered phase may be caused by the larger size of the Zr cation. The common absence of such structural distortions in Zr- and Sc-oxide compounds has been discussed by Kunz and Brown, 1995.

In the solid solution $(\text{Ca}_x\text{Sr}_{1-x})\text{TiOGeO}_4$ substitution of the large Sr atom for Ca is not influencing the transition temperature (Ellemann-Olesen and Malcherek 2004, in preparation).

However, substitution of Ge for Si on the tetrahedral site has a marked influence on T_c . The evolution of T_c with composition is nearly linear and is marked by a gradual increase of nearly 100 K from the titanite endmember towards CaTiOGeO_4 . Therefore the substitution of Ge for Si stabilizes the ordered $\text{P2}_1/a$ phase (Ellemann-Olesen and Malcherek 2004, submitted).

Acknowledgements

Financial support through the Deutsche Forschungs-Gemeinschaft (DFG) is gratefully acknowledged. Helpful reviews of the original manuscript have been provided by M. Kunz and E. Salje.

References

- Angel, R.J., Kunz, M., Miletich, R., Woodland, A.B., Koch, M. and Knoche, R.L., 1999. Effect of isovalent Si,Ti substitution on the bulk moduli of $\text{Ca}(\text{Ti}_{1-x}\text{Si}_x)\text{SiO}_5$ titanites. *American Mineralogist* 84: 282-287.
- Aust, H., Völlenknecht, H. and Wittmann, A., 1976. Die Kristallstruktur der Hoch- und der Tieftemperaturform von CaGe_2O_5 . *Zeitschrift für Kristallographie* 144: 82-90.
- Breese, N.E. and O’Keeffe, M., 1991. Bond-Valence Parameters for Solids. *Acta Crystallographica B* 47: 192-197.
- Bismayer, U., Schmahl, W., Schmidt, C. and Groat, L.A., 1992. Linear Birefringence and X-Ray Diffraction Studies of the Structural Phase Transition in Titanite, CaTiSiO_5 . *Physics and Chemistry of Minerals* 19: 260-266.
- Carpenter, M.A. and Salje, E.K.H., 1998. Elastic anomalies in minerals due to structural phase transitions. *European Journal of Mineralogy* 10: 693-812.
- Carpenter, M.A., Salje, E.K.H. and Graeme-Barber, A., 1998. Spontaneous strain as a determinant of thermodynamic properties for phase transitions in minerals. *European Journal of Mineralogy* 10: 621-691.
- Ellemann-Olesen, R. and Malcherek, T., 2004. A high temperature diffraction study of the solid solution $\text{CaTiOSiO}_4 - \text{CaTiOGeO}_4$. *American Mineralogist*, *submitted*
- Ghose, S., Ito, Y. and Hatch, D.M., 1991. Paraelectric-Antiferroelectric Phase Transition in Titanite, CaTiSiO_5 : I. A high temperature X-ray diffraction study of the order parameter and transition mechanism. *Physics and Chemistry of Minerals* 17: 591-603.
- Groat, L.A., Raudsepp, M., Hawthorne, F.C., Ercit, T.S., Sherriff, B.L. and Hartman, J.S., 1990. The amblygonite-montebrazite series: Characterization by single-crystal structure refinement, infrared spectroscopy, and multinuclear MAS-NMR spectroscopy. *American Mineralogist* 75: 992-1008.

- Kek, S., Aroyo, M., Bismayer, U., Schmidt, C., Eichhorn, K. and Krane, H.G., 1997. The two-step phase transition of titanite, CaTiSiO_5 : a synchrotron radiation study. *Zeitschrift für Kristallographie* 212: 9-19.
- Kunz, M. and Brown, D.I., 1995. Out-of-center Distortions around Octahedrally Coordinated d^0 Transition Metals. *Journal of solid state chemistry* 115: 395-406.
- Kunz, M., Xirouchakis, D., Wang, Y., Parise, J.B. and Lindsley, D.H., 1997. Structural investigations along the join $\text{CaTiOSiO}_4 - \text{CaSnOSiO}_4$. *Schweizerisch Mineralogische Petrographische Mitteilung* 77: 1-11.
- Kunz, M., Arlt, T. and Stolz, J., 2000. In situ powder diffraction study of titanite (CaTiOSiO_4) at high pressure and high temperature. *American Mineralogist* 85: 1465-1473.
- Larson, A.C. and Von Dreele, R.B., 1994. General Structure Analysis System (GSAS). Los Alamos National Laboratory. Los Alamos, New Mexico.
- Malcherek, T., Domeneghetti, C.M., Tazzoli, V., Salje, E.K.H. and Bismayer, U., 1999. A high temperature diffraction study of synthetic titanite CaTiOSiO_4 . *Phase Transitions* 69: 119-131.
- Malcherek, T., 2001. Spontaneous strain in synthetic titanite, CaTiOSiO_4 . *Mineralogical Magazine* 65: 709- 715.
- Malcherek, T., Paulmann, C., Domeneghetti, M.C. and Bismayer, U., 2001. Diffuse scattering anisotropy and the $P2_1/a \leftrightarrow A2/a$ phase transition in titanite, CaTiOSiO_4 . *Journal of Applied Crystallography* 34: 108-113.
- Malcherek, T. and Bosenick, A., 2004. Structure and phase transition of CaGe_2O_5 revisited. *Physics and Chemistry of Minerals* 31: 224-231.
- Malcherek, T., Borowski, M. and Bosenick, A., 2004. Structure and phase transitions of CaTaOAlO_4 . *Journal of Applied Crystallography* 37: 117-122.
- Malcherek, T. and Ellemann-Olesen, R., 2004. CaZrGeO_5 and the triclinic instability of the titanite structure type. *Zeitschrift für Kristallographie*, submitted
- Oberti, R., Smith, D.C., Rossi, G. and Caucia, F., 1991. The crystal chemistry of high-aluminium titanites. *European Journal of Mineralogy* 3: 777-792.
- Rath, S., Kunz, M. and Miletich, R., 2003. Pressure-induced phase transition in malayaite, CaSnOSiO_4 . *American Mineralogist* 88: 293-300.
- Salje, E.K.H., 1990. Phase transitions in ferroelastic and co-elastic crystals. Cambridge University Press, Cambridge, UK.
- Salje, E.K.H., Schmidt, C. and Bismayer, U., 1993. Structural phase transition in titanite, CaTiSiO_5 : A raman spectroscopic study. *Physics and Chemistry of Minerals* 19: 502-506.

- Speer, J.A. and Gibbs, G.V., 1976. The crystal structure of synthetic titanite, CaTiOSiO_4 , and the domain textures of natural titanites. *American Mineralogist* 61: 238-247.
- Taylor, M. and Brown, G.E., 1976. High-temperature structural study of the $P2_1/a - A2/a$ phase transition in synthetic titanite, CaTiSiO_5 . *American Mineralogist* 61: 435-447.
- Zhang, M., Salje, E.K.H. and Bismayer, U., 1997. Structural phase transition near 825 K in titanite: Evidence from infrared spectroscopic observations. *American Mineralogist* 82: 30-35.

Table 1. Lattice parameters for $\text{Ca}(\text{Ti}_x\text{Zr}_{1-x})\text{OGeO}_4$ at room temperature.

Mol% Ti	a (Å)	b (Å)	c (Å)	α (°)	β (°)	γ (°)	V (Å ³)
100	7.16144(6)	8.89229(2)	6.65311(4)	90	113.833(1)	90	387.552(5)
95	7.15000(6)	8.89941(1)	6.65482(4)	90	113.730(1)	90	387.649(6)
90	7.15461(8)	8.90612(7)	6.65901(5)	90	113.701(1)	90	388.523(7)
80	7.17490(1)	8.93321(4)	6.67312(1)	90	113.600(1)	90	391.940(7)
50	7.25821(3)	9.01791(2)	6.72200(1)	90	113.351(1)	90	403.944(6)
20	7.35292(2)	9.10000(7)	6.75633(7)	89.085(1)	113.024(1)	91.001(1)	415.981(6)
10	7.38422(2)	9.12413(7)	6.76031(1)	88.765(1)	112.877(1)	91.297(1)	419.499(6)
0	7.4226(1)	9.1508(1)	6.7657(1)	88.482(1)	112.719(1)	91.502(1)	423.68(1)

Notes: Data for CaTiOGeO_4 and CaZrOGeO_4 are taken from Ellemann-Olesen and Malcherek, 2004a and Malcherek and Ellemann-Olesen, 2004, respectively.

Table 2. $\text{Ca}(\text{Ti}_x\text{Zr}_{1-x})\text{OGeO}_4$. Lattice constants and volume for all intermediate samples as a function of temperature.

Mol% Ti						
95	T (K)	a (Å)	b (Å)	c (Å)	β (°)	V (Å ³)
	298	7.15000(6)	8.89941(8)	6.65482(4)	113.730(1)	387.649(6)
	348	7.15000(6)	8.90215(9)	6.65564(3)	113.723(2)	387.859(8)
	373	7.15099(5)	8.90306(2)	6.65651(4)	113.707(2)	388.098(7)
	398	7.15147(5)	8.90598(2)	6.65732(2)	113.698(1)	388.340(4)
	423	7.15173(3)	8.90846(4)	6.65867(5)	113.688(1)	388.526(5)
	448	7.15202(5)	8.91033(9)	6.66001(8)	113.686(1)	388.669(7)
	473	7.15239(8)	8.91111(5)	6.66036(7)	113.680(1)	388.761(7)
	498	7.15261(9)	8.91365(5)	6.66124(4)	113.670(1)	388.965(7)
	523	7.15315(3)	8.91536(5)	6.66175(3)	113.659(1)	389.131(4)
	538	7.15353(6)	8.91659(2)	6.66263(7)	113.654(2)	389.272(8)
	553	7.15372(8)	8.91742(4)	6.66265(2)	113.655(1)	389.317(6)
	573	7.15424(4)	8.91947(6)	6.66449(7)	113.652(1)	389.551(6)
	598	7.15449(2)	8.92113(9)	6.66527(8)	113.647(1)	389.698(7)
	623	7.15546(4)	8.92320(8)	6.66648(7)	113.643(1)	389.924(7)
	648	7.15586(5)	8.92469(6)	6.66713(8)	113.637(1)	390.067(7)
	673	7.15651(7)	8.92677(7)	6.66864(5)	113.631(1)	390.299(6)
	723	7.15748(9)	8.92956(4)	6.66950(2)	113.616(1)	390.569(6)
	748	7.15796(9)	8.93160(8)	6.67063(5)	113.611(1)	390.766(7)
	773	7.15860(3)	8.93359(3)	6.67260(9)	113.618(1)	390.982(6)

90	T (K)	<i>a</i> (Å)	<i>b</i> (Å)	<i>c</i> (Å)	β (°)	V (Å ³)
	298	7.15461(8)	8.90612(7)	6.65901(5)	113.701(1)	388.523(7)
	348	7.15468(4)	8.90859(2)	6.65980(8)	113.687(1)	388.721(6)
	373	7.15497(8)	8.91073(3)	6.66000(9)	113.674(2)	388.880(8)
	398	7.15517(3)	8.91222(8)	6.66131(6)	113.665(2)	389.061(8)
	423	7.15569(2)	8.91458(8)	6.66279(3)	113.659(1)	389.296(7)
	448	7.15596(6)	8.91580(7)	6.66349(3)	113.655(1)	389.416(6)
	473	7.15639(5)	8.91762(3)	6.66375(4)	113.643(1)	389.569(5)
	498	7.15696(3)	8.92025(3)	6.66545(7)	113.638(1)	389.831(5)
	523	7.15754(2)	8.92136(7)	6.66590(3)	113.632(1)	389.955(6)
	538	7.15754(8)	8.92295(3)	6.66653(2)	113.632(2)	390.061(7)
	553	7.15784(5)	8.92414(4)	6.66793(2)	113.630(1)	390.217(6)
	573	7.15819(5)	8.92632(6)	6.66916(7)	113.622(1)	390.428(4)
	598	7.15826(2)	8.92795(5)	6.66880(2)	113.614(1)	390.505(5)
	623	7.15900(4)	8.92854(8)	6.66942(3)	113.611(1)	390.616(5)
	648	7.15936(2)	8.93094(5)	6.67102(4)	113.611(1)	390.835(6)
	673	7.16001(9)	8.93234(5)	6.67137(2)	113.603(1)	390.977(6)
	723	7.16057(2)	8.93457(2)	6.67244(3)	113.589(2)	391.209(6)
	748	7.16150(7)	8.93704(8)	6.67424(8)	113.588(1)	391.477(8)
	773	7.16176(2)	8.93881(2)	6.67512(4)	113.577(1)	391.653(4)

80	T (K)	<i>a</i> (Å)	<i>b</i> (Å)	<i>c</i> (Å)	β (°)	V (Å ³)
	298	7.17490(8)	8.93321(4)	6.67312(8)	113.600(1)	391.940(7)
	348	7.17427(6)	8.93700(8)	6.67498(5)	113.593(1)	392.202(6)
	373	7.17484(8)	8.93850(3)	6.67604(6)	113.590(2)	392.370(8)
	398	7.17592(3)	8.94170(5)	6.67675(2)	113.584(1)	392.630(4)
	423	7.17641(2)	8.94297(2)	6.67731(4)	113.567(1)	392.796(4)
	448	7.17686(5)	8.94496(3)	6.67833(9)	113.569(1)	392.962(7)
	473	7.17828(8)	8.94717(7)	6.68026(7)	113.563(2)	393.267(9)
	498	7.17918(2)	8.94796(8)	6.68084(4)	113.562(2)	393.389(7)
	523	7.17967(4)	8.95101(2)	6.68256(5)	113.549(1)	393.690(5)
	538	7.17942(8)	8.95152(8)	6.68232(6)	113.553(1)	393.673(7)
	553	7.18041(7)	8.95304(7)	6.68356(6)	113.556(1)	393.858(7)
	573	7.18086(5)	8.95419(3)	6.68400(2)	113.552(1)	393.971(4)
	598	7.18197(5)	8.95543(3)	6.68574(6)	113.546(1)	394.207(6)
	623	7.18290(4)	8.95786(6)	6.68670(2)	113.538(1)	394.446(5)
	648	7.18384(2)	8.96060(5)	6.68769(5)	113.530(1)	394.700(5)
	673	7.18347(4)	8.96246(3)	6.68927(3)	113.531(1)	394.852(4)
	723	7.18547(5)	8.96486(8)	6.69046(4)	113.528(1)	395.147(6)
	748	7.18564(7)	8.96677(3)	6.69148(3)	113.526(1)	395.308(5)
	773	7.18647(6)	8.96934(2)	6.69307(8)	113.523(1)	395.570(7)

50	T (K)	a (Å)	b (Å)	c (Å)	β (°)	V (Å ³)
298		7.25821(3)	9.01791(2)	6.72200(9)	113.351(1)	403.944(6)
348		7.25921(3)	9.02172(3)	6.72416(7)	113.338(1)	404.340(6)
373		7.26006(6)	9.02397(7)	6.72523(8)	113.338(1)	404.552(7)
398		7.26081(8)	9.02528(6)	6.72651(4)	113.335(1)	404.739(6)
423		7.26162(6)	9.02738(9)	6.72758(5)	113.334(1)	404.946(7)
448		7.26257(3)	9.02909(6)	6.72914(5)	113.332(1)	405.175(5)
473		7.26336(2)	9.03144(6)	6.72984(8)	113.329(1)	405.376(6)
498		7.26426(8)	9.03246(7)	6.73120(2)	113.324(1)	405.570(6)
523		7.26530(2)	9.03502(5)	6.73269(3)	113.321(1)	405.842(4)
548		7.26611(2)	9.03649(3)	6.73390(6)	113.321(1)	406.026(5)
573		7.26664(7)	9.03860(2)	6.73485(9)	113.314(1)	406.229(7)
598		7.26775(4)	9.04009(2)	6.73602(7)	113.314(1)	406.429(6)
623		7.26839(8)	9.04191(3)	6.73718(6)	113.308(1)	406.635(7)
648		7.26965(5)	9.04367(6)	6.73868(9)	113.308(1)	406.875(7)
673		7.27044(7)	9.04572(3)	6.73987(5)	113.304(1)	407.095(6)
723		7.27210(5)	9.04928(5)	6.74224(8)	113.300(1)	407.504(7)
748		7.27322(6)	9.05101(2)	6.74384(5)	113.301(1)	407.738(6)
773		7.27318(6)	9.05177(5)	6.74447(8)	113.297(1)	407.821(7)

20	T (K)	a (Å)	b (Å)	c (Å)	α (°)	β (°)	γ (°)	V (Å ³)
298		7.35292(2)	9.10000(7)	6.75633(7)	89.085(1)	113.024(1)	91.001(1)	415.981(6)
348		7.35513(5)	9.10561(6)	6.75543(8)	89.570(1)	113.069(1)	90.490(1)	416.848(7)
373		7.35499(6)	9.10184(6)	6.76906(5)	89.869(1)	113.063(1)	90.136(1)	416.928(6)
398		7.35792(2)	9.10477(4)	6.77186(3)	90	113.082(1)	90	417.344(4)
423		7.35814(3)	9.10576(8)	6.77342(4)	90	113.080(1)	90	417.504(6)
448		7.35896(3)	9.10781(8)	6.77459(2)	90	113.079(1)	90	417.720(5)
473		7.35960(6)	9.10947(2)	6.77616(8)	90	113.085(1)	90	417.910(7)
498		7.36089(8)	9.11109(3)	6.77763(7)	90	113.084(1)	90	418.152(7)
523		7.36146(6)	9.11231(3)	6.77875(3)	90	113.083(1)	90	418.312(6)
548		7.36266(9)	9.11502(3)	6.78092(7)	90	113.078(1)	90	418.654(8)
573		7.36371(4)	9.11662(6)	6.78218(8)	90	113.083(1)	90	418.850(7)
598		7.36381(8)	9.11850(2)	6.78375(2)	90	113.078(1)	90	419.054(6)
623		7.36537(7)	9.11952(5)	6.78468(6)	90	113.078(1)	90	419.248(7)
648		7.36578(5)	9.12148(8)	6.78634(6)	90	113.075(1)	90	419.473(7)
673		7.36700(5)	9.12322(3)	6.78777(7)	90	113.075(1)	90	419.711(6)
723		7.36833(2)	9.12593(8)	6.79074(8)	90	113.074(1)	90	420.098(7)
748		7.36904(3)	9.12776(8)	6.79188(7)	90	113.072(1)	90	420.300(7)
773		7.37016(5)	9.12940(6)	6.79355(8)	90	113.073(1)	90	420.539(7)

10	T (K)	<i>a</i> (Å)	<i>b</i> (Å)	<i>c</i> (Å)	α (°)	β (°)	γ (°)	<i>V</i> (Å ³)
	298	7.38422(2)	9.12413(7)	6.76031(1)	88.765(1)	112.877(1)	91.297(1)	419.499(6)
	348	7.38722(9)	9.12970(9)	6.77012(6)	89.009(1)	112.934(1)	91.070(1)	420.408(8)
	373	7.38826(2)	9.12980(9)	6.77625(9)	89.154(1)	112.952(1)	90.902(1)	420.824(8)
	398	7.38970(6)	9.13119(8)	6.78187(4)	89.407(1)	112.967(1)	90.637(1)	421.308(6)
	423	7.39068(8)	9.13331(4)	6.78783(6)	89.785(1)	113.005(1)	90.235(1)	421.744(7)
	448	7.39185(6)	9.13077(9)	6.78910(8)	90	112.993(1)	90	421.814(8)
	473	7.39254(3)	9.13241(5)	6.79062(8)	90	112.991(1)	90	422.030(7)
	498	7.39427(4)	9.13471(2)	6.79201(6)	90	112.996(1)	90	422.306(5)
	523	7.39379(3)	9.13582(7)	6.79356(2)	90	112.994(1)	90	422.433(5)
	548	7.39550(1)	9.13766(5)	6.79524(5)	90	112.995(1)	90	422.717(5)
	573	7.39596(9)	9.13953(2)	6.79671(1)	90	112.995(1)	90	422.921(6)
	598	7.39653(4)	9.14096(1)	6.79794(9)	90	112.988(1)	90	423.118(7)
	623	7.39771(9)	9.14270(9)	6.79952(1)	90	112.992(1)	90	423.352(7)
	648	7.39869(4)	9.14442(1)	6.80099(9)	90	112.992(1)	90	423.580(7)
	673	7.39896(8)	9.14604(1)	6.80220(7)	90	112.985(1)	90	423.767(7)
	723	7.40066(5)	9.14935(2)	6.80521(1)	90	112.990(1)	90	424.190(5)
	748	7.40174(1)	9.15031(1)	6.80653(3)	90	112.988(1)	90	424.385(5)
	773	7.40215(8)	9.15223(6)	6.80798(6)	90	112.987(1)	90	424.591(7)

Table 3. Atomic positional parameters and isotropic thermal vibration parameters (\AA^2) at room temperature across $\text{Ca}(\text{Ti}_x\text{Zr}_{1-x})\text{OGeO}_4$.

Mol% Ti					
95 ($\text{P2}_1/a$)	x	y	z	U_{iso}	occ
Ca	0.2413(4)	0.4219(4)	0.2503(2)	0.015(2)	1.000
Ti	0.5027(1)	0.2394(8)	0.7477(2)	0.012(3)	0.954(9)
Zr	0.5027(1)	0.2394(8)	0.7477(2)	0.012(3)	0.046(1)
Ge	0.7488(3)	0.4331(1)	0.2525(4)	0.021(1)	1.000
O1	0.7394(5)	0.3147(3)	0.7684(2)	0.009(4)	1.000
O2A	0.9225(3)	0.3123(8)	0.4287(5)	0.009(4)	1.000
O2B	0.0813(6)	0.1956(7)	0.0457(1)	0.009(4)	1.000
O3A	0.4005(1)	0.4694(3)	0.6430(5)	0.009(4)	1.000
O3B	0.6057(2)	0.0619(4)	0.8656(3)	0.009(4)	1.000

R_p 0.215
 $R(F^2)$ 0.175

90 ($\text{P2}_1/a$)	x	y	z	U_{iso}	occ
Ca	0.2502(7)	0.4223(5)	0.2530(1)	0.013(5)	1.000
Ti	0.5048(8)	0.2422(6)	0.7517(8)	0.019(7)	0.908(6)
Zr	0.5048(8)	0.2422(6)	0.7517(8)	0.019(7)	0.091(4)
Ge	0.7459(7)	0.4332(1)	0.2516(4)	0.025(1)	1.000
O1	0.7400(9)	0.3157(5)	0.7569(1)	0.003(5)	1.000
O2A	0.9261(1)	0.3248(3)	0.4445(1)	0.003(5)	1.000
O2B	0.0996(2)	0.2053(8)	0.0659(9)	0.003(5)	1.000
O3A	0.4146(5)	0.4605(3)	0.6749(9)	0.003(5)	1.000
O3B	0.6154(6)	0.0559(4)	0.8767(3)	0.003(5)	1.000

R_p 0.216
 $R(F^2)$ 0.183

80 ($\text{A2}/a$)	x	y	z	U_{iso}	occ
Ca	0.2500	0.6716(6)	0.5000	0.018(2)	1.000
Ti	0.5000	0.5000	0.0000	0.015(2)	0.807(1)
Zr	0.5000	0.5000	0.0000	0.015(2)	0.192(9)
Ge	0.7500	0.6820(4)	0.5000	0.014(2)	1.000
O1	0.7500	0.5653(9)	0.0000	0.005(3)	1.000
O2A	0.9162(9)	0.5559(6)	0.6887(7)	0.005(3)	1.000
O3A	0.3977(3)	0.7105(9)	0.8934(7)	0.005(3)	1.000

R_p 0.172
 $R(F^2)$ 0.112

50 (A2/a)	x	y	z	U _{iso}	occ
Ca	0.2500	0.6712(4)	0.5000	0.014(3)	1.000
Ti	0.5000	0.5000	0.0000	0.010(1)	0.507(7)
Zr	0.5000	0.5000	0.0000	0.010(1)	0.492(3)
Ge	0.7500	0.6816(2)	0.5000	0.013(2)	1.000
O1	0.7500	0.5695(6)	0.0000	0.009(5)	1.000
O2A	0.9194(8)	0.5539(1)	0.6795(1)	0.009(5)	1.000
O3A	0.3992(4)	0.7204(1)	0.8966(1)	0.009(5)	1.000

R_p 0.135
R(F²) 0.0883

20 (A1)	x	y	z	U _{iso}	occ
Ca	0.2329(8)	0.6674(2)	0.5044(8)	0.020(4)	1.000
Ge	0.7495(4)	0.6810(8)	0.4972(1)	0.018(1)	1.000
Ti(1)	0.5	0.5	0.0	0.009(8)	0.222(1)
Ti(2)	0.0	0.5	0.0	0.011(4)	0.222(1)
Zr(1)	0.5	0.5	0.0	0.009(8)	0.778(7)
Zr(2)	0.0	0.5	0.0	0.011(4)	0.778(7)
O1	0.7452(4)	0.5822(1)	0.9973(4)	0.008(2)	1.000
O2A	0.9216(2)	0.5617(8)	0.6757(7)	0.008(2)	1.000
O2B	0.5958(1)	0.5554(3)	0.3329(2)	0.008(2)	1.000
O3A	0.3879(5)	0.7142(7)	0.8923(3)	0.008(2)	1.000
O3B	0.1232(6)	0.7040(5)	0.1283(6)	0.008(2)	1.000

R_p 0.086
R(F²) 0.050

10 (A1)	x	y	z	U _{iso}	occ
Ca	0.2289(4)	0.6666(5)	0.5071(6)	0.025(4)	1.000
Ge	0.7481(3)	0.6811(6)	0.4959(6)	0.016(1)	1.000
Ti(1)	0.5	0.5	0.0	0.012(4)	0.114(3)
Ti(2)	0.0	0.5	0.0	0.013(5)	0.114(3)
Zr(1)	0.5	0.5	0.0	0.012(4)	0.885(7)
Zr(2)	0.0	0.5	0.0	0.013(5)	0.885(7)
O1	0.7492(7)	0.5831(7)	0.9941(3)	0.008(2)	1.000
O2A	0.9176(3)	0.5667(2)	0.6739(6)	0.008(2)	1.000
O2B	0.6083(5)	0.5515(3)	0.3273(2)	0.008(2)	1.000
O3A	0.3824(2)	0.7061(6)	0.8947(4)	0.008(2)	1.000
O3B	0.1111(7)	0.6982(5)	0.1128(4)	0.008(2)	1.000

R_p 0.094
R(F²) 0.061

Notes: Data for the endmember compositions CaTiOGeO₄ and CaZrOGeO₄ see Ellemann-Olesen and Malcherek, 2004 and Malcherek and Ellemann-Olesen, 2004.

Table 4. Mean bond lengths (Å) at room temperature.

Mol % Ti	Ge-O	Ti-O	Ca-O
CTGO	1.752	1.964	2.468 ^[7]
95	1.735	1.948	2.460 ^[7]
90	1.767	1.944	2.473 ^[7]
80	1.765	1.969	2.459 ^[7]
50	1.754	2.037	2.469 ^[7]
20	1.750	2.074/2.075	2.496 ^[7] , 2.568 ^[8]
10	1.753	2.057/2.045	2.516 ^[7] , 2.582 ^[8]
CZGO	1.75	2.11/2.12	2.505 ^[7] , 2.559 ^[8]

Notes: bond lengths for CaTiOGeO₄ and CaZrOGeO₄ at room temperature are taken from Ellemann-Olesen and Malcherek, 2004 and Malcherek and Ellemann-Olesen, 2004, respectively.

Table 5. Results of bond valence calculations performed with the room temperature data across the solid solution Ca(Ti_xZr_{1-x})OGeO₄. In the case of Ca values calculated for 7- and 8-fold coordination are given.

Mol%	CTGO	95	90	80	50	20	10	CZGO
Ge								
Ge	3.97	4.110	3.878	3.822	3.861	4.007	3.999	4.06
Ti,Zr	4.18	4.16	4.15	4.12	4.02	3.92	3.88	3.74/3.85
Ca ^[7]	1.88	1.877	1.920	1.887	1.841	1.795	1.844	1.865
Ca ^[8]	1.908	1.924	1.900	1.916	1.872	1.894	1.849	1.91

Notes: bond valence sums have been calculated according to Brese and O'Keefe (1991). Bond valence sums for mixed site occupancies have been calculated using weighted averages of the end member values. Data for CaTiOGeO₄ and CaZrOGeO₄ are taken from Ellemann-Olesen and Malcherek 2004 and Malcherek and Ellemann-Olesen 2004, respectively.

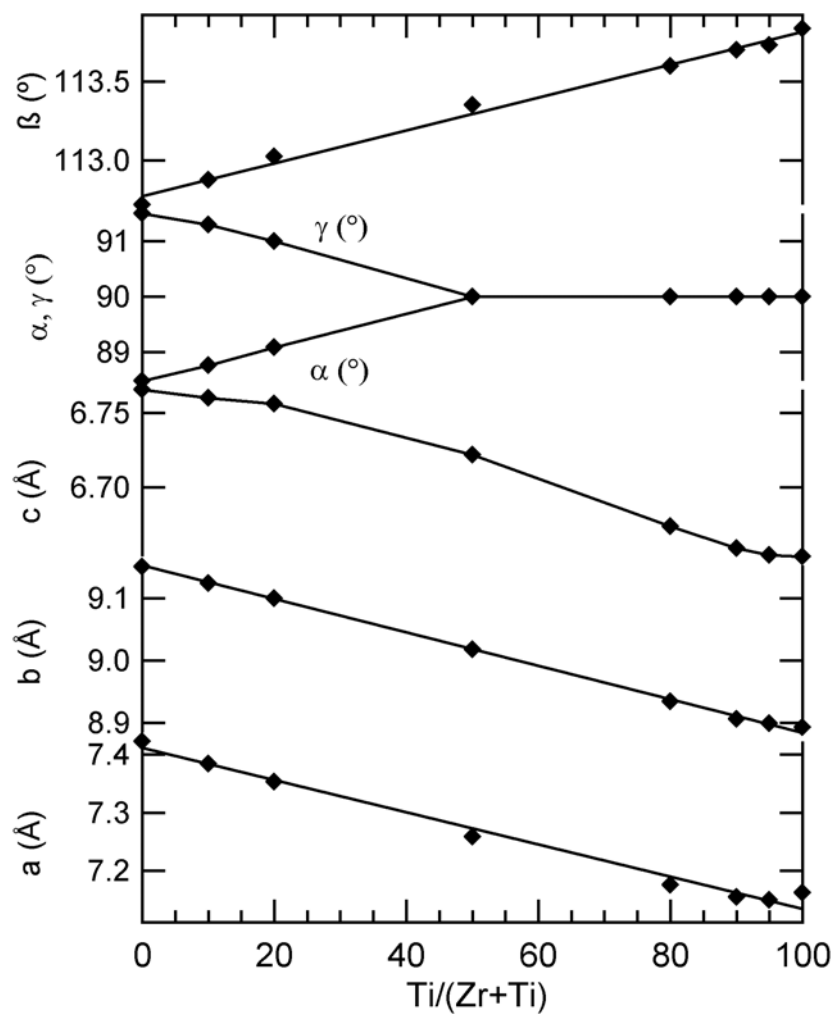


Fig. 1 $\text{Ca}(\text{Ti}_x\text{Zr}_{1-x})\text{OGeO}_4$. Lattice constants as a function of Ti-content at room temperature.

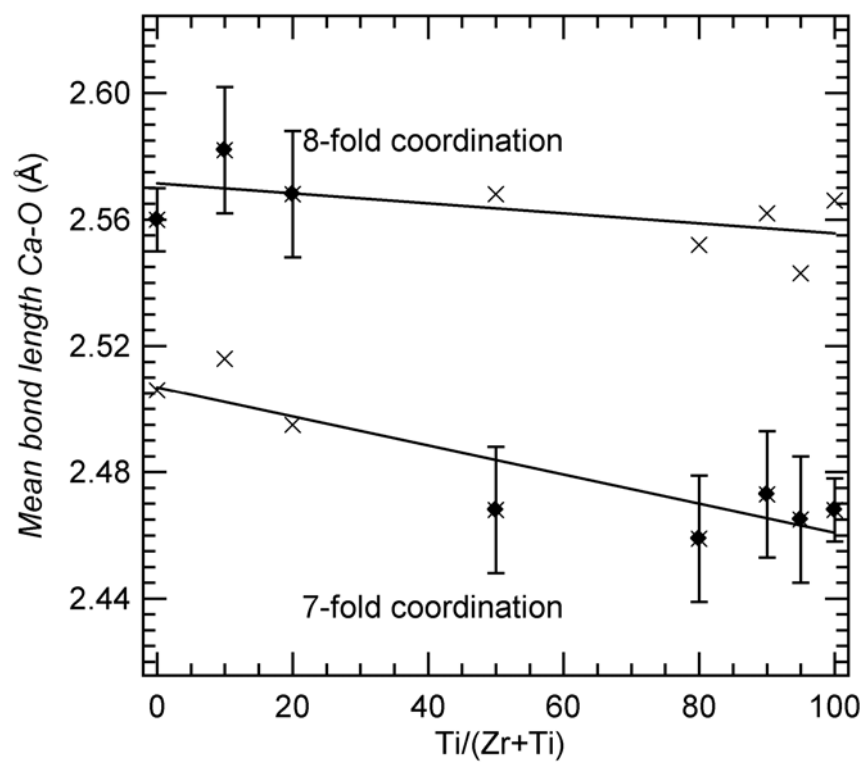


Fig. 2 The mean bond length Ca-O as a function of Ti-content. The dashed lines are calculated mean bond lengths for Ca in 7- and 8-fold coordination extended into the triclinic and monoclinic phases, respectively.

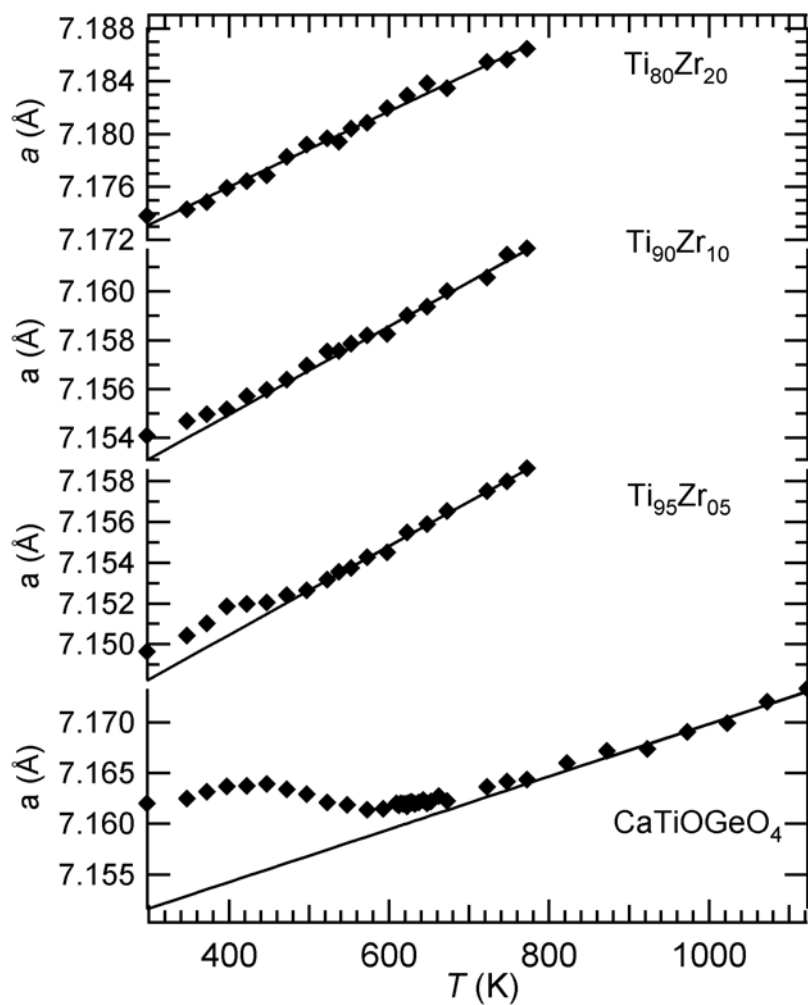


Fig. 3 The *a*-lattice constant for CTGO, CTGO95, CTGO90 and CTGO80 as a function of temperature.

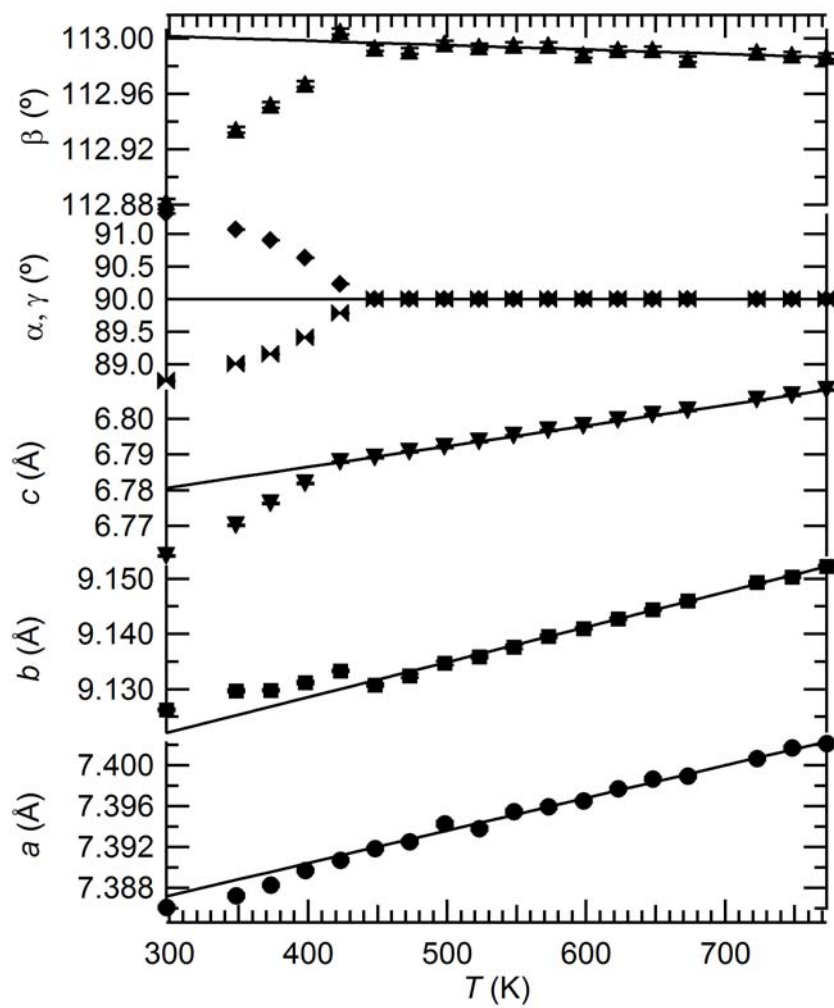


Fig. 4 Lattice parameters for the compound CTGO10 as a function of temperature. The lines have been fitted to the data for $T > 429$ K.

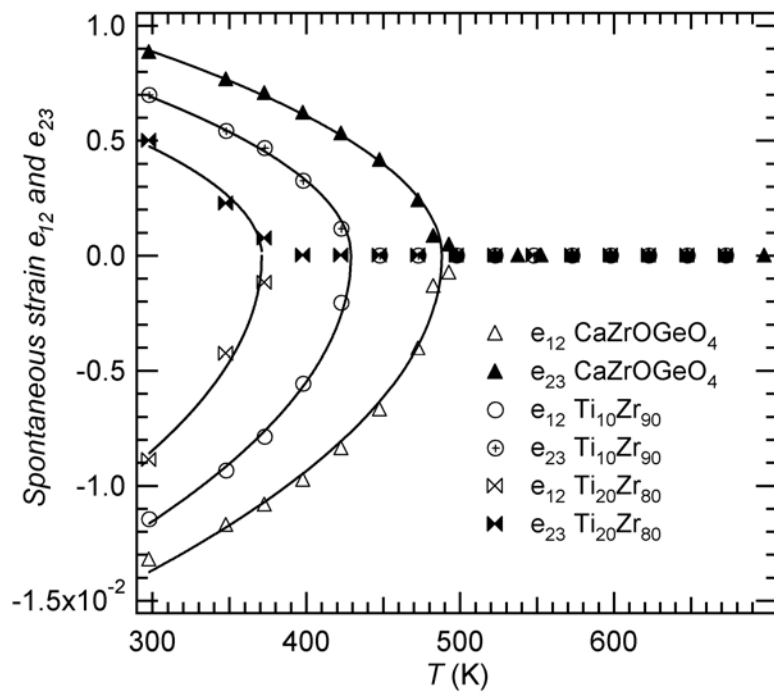


Fig. 5 Symmetry breaking strain e_{12} and e_{23} for CTGO10, CTGO20 and CaZrOGeO_4 . The solid curves indicate the temperature behaviour given by the Landau model.

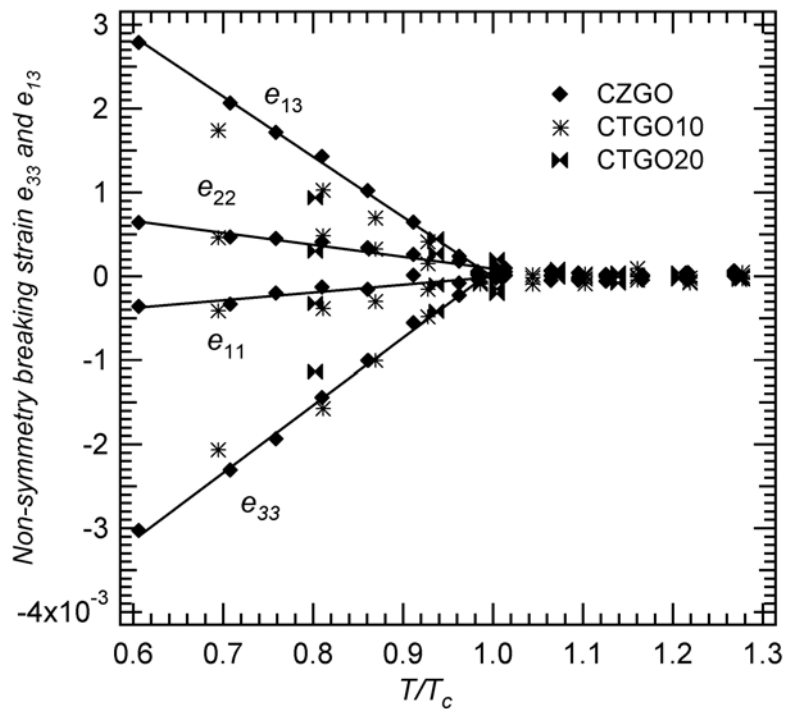


Fig. 6 The non-symmetry breaking strain components for the triclinic compounds as a function of reduced temperature.

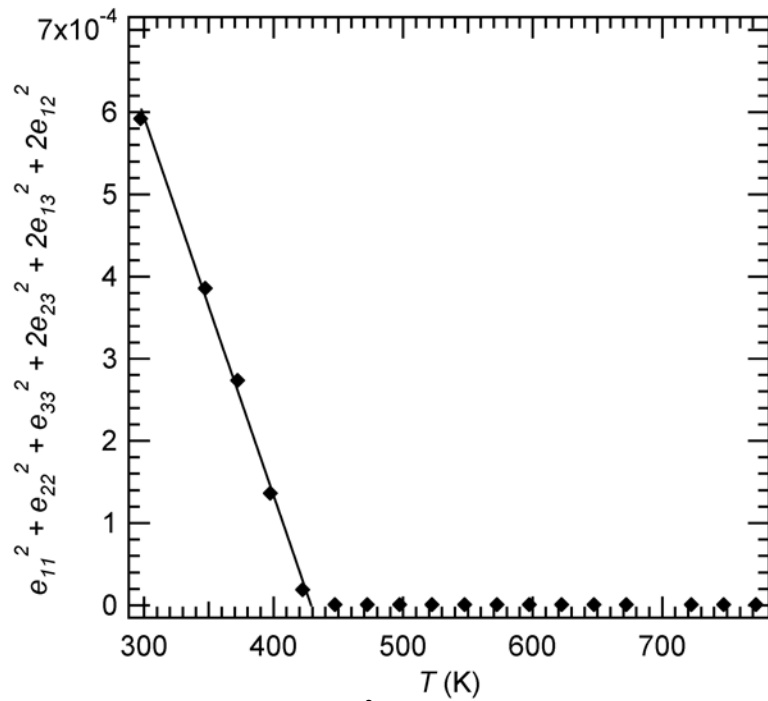


Fig. 7 CTGO10. The square of the scalar strain, e_s^2 , which linearly extrapolates to $T_c = 429$ K.

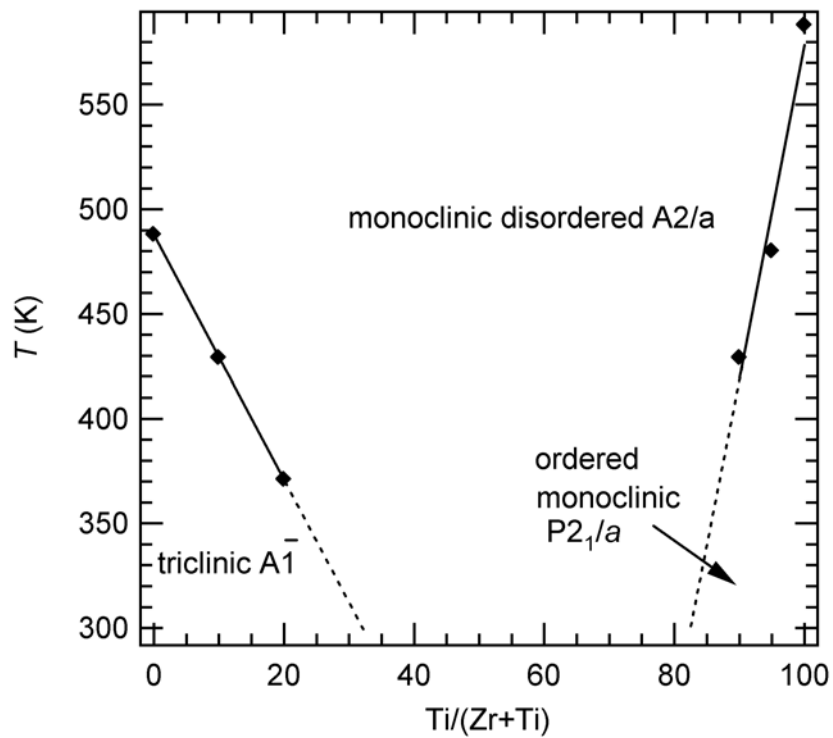


Fig. 8 The transition temperature as a function of increasing Ti-content. The different structure types are listed.

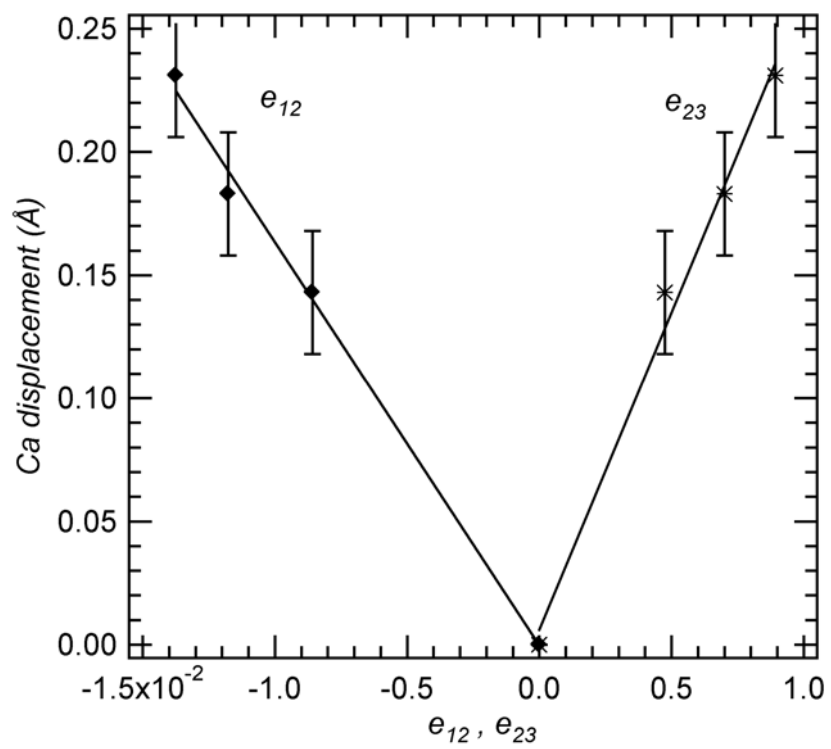


Fig. 9 Ca displacement as a function of the symmetry-breaking strain components e_{12} and e_{23} at room temperature.

6. Concluding remarks

The studied solid solutions reflect the ability of the titanite structural framework to accommodate and incorporate larger cations on the various crystallographic sites. An effect of the incorporation of larger cations is reflected in the behaviour of the transition temperature. The influence on the critical temperature by substitution on different crystallographic sites is significant and depends very much on the crystallographic site involved in substitution and the degree of substitution. The structural phase transitions have been identified based on the determination of spontaneous strain associated with the transitions. However variations in strain across the individual solid solutions are conspicuously absent. Apart from the Zr-Ti system there are only small strain variations.

The solid solution $\text{CaTiO}(\text{Ge}_x\text{Si}_{1-x})\text{O}_4$

Transition temperature and strain behaviour

The behaviour of CaTiOGeO_4 is in perfect analogy to the well known behaviour of titanite characterized by the $P2_1/a - A2/a$ transition. The behaviour of the critical temperature varies linearly with increasing substitution of Ge for Si on the tetrahedral site. Therefore the substitution of Ge for Si stabilizes the ordered $P2_1/a$ phase. The difference in transition temperature is near 100 K with $T_c = 588$ K for CaTiOGeO_4 and $T_c = 487$ K for titanite.

The evolution of strain in the solid solution $\text{CaTiO}(\text{Ge}_x\text{Si}_{1-x})\text{O}_4$ is analogous to titanite (Malcherek, 2001) and dominated by the spontaneous strain components e_{11} and e_{13} . The scalar strain is as a result composed of an expansion along the a -axis, *i.e.* along the octahedral chains and a shear strain involving the a - and c -axis and their angle, β . In analogy to titanite the compounds addressed exhibit tricritical phase transitions.

The substitution of Ge causes a drop in shear strain relative to the ordered endmember compositions CaTiOGeO_4 and titanite. This implies that the shearing of the unit cell is lessened for intermediate compositions. The reduced shearing of the unit cell accompanying the $P2_1/a - A2/a$ transition correlates with a volume increase of the TiO_6 octahedra for intermediate compositions.

In analogy with titanite X-ray diffraction indicates the additional occurrence of an isosymmetric anomaly at $T_i = 800 \pm 25$ K that contrary to T_c stays constant across the solid solution. Zhang *et al.*, 1995 concludes from observations of impurities of Fe and Al and substituting for Ti that the high-temperature phase transition in titanite shows a completely different behaviour compared to the antiferroelectric phase transition at $T_c = 487$ K. The effect of Fe, Al substitution is to block the lower temperature transition, T_c , while substitution of Ge for Si has rather the opposite effect on T_c . Therefore T_i is neither sensitive to substitution on the octahedral site (Zhang *et al.*, 1997), nor do our results suggest that it is significantly altered by substitutions on the tetrahedral site.

The solid solution $(\text{Ca}_x\text{Sr}_{1-x})\text{TiOGeO}_4$

Transition temperature and strain behaviour

SrTiOGeO_4 and CaTiOGeO_4 form a complete solid solution and they exhibit nearly identical properties with regard to the occurring structural phase transitions. Substitution of Ca by Sr leads to a constant transition temperature across the solid solution $(\text{Ca}_x\text{Sr}_{1-x})\text{TiOGeO}_4$ with $T_c = 590 \pm 10$ K. Variation of the size of the A-cation in titanites therefore does not appear to affect the critical temperature of the $P2_1/a - A2/a$ transition. In the titanite-structure the large A-polyhedron represents the most compressible structural unit along with the octahedral chain. Thus the structure can adjust better to substitution on the more flexible polyhedral site despite the larger size of the Sr-atom and the monoclinic ordered structure is preserved across the solid solution.

Due to the structural changes that arise from substituting Sr for Ca significant differences appear in the behaviour of scalar strain between the two endmember compositions. Across most of the solid solution the scalar strain stays almost constant. But CaTiOGeO_4 differs with an increase of 36% at room temperature. The temperature evolution of scalar strain in CaTiOGeO_4 is comparable to titanite (Malcherek, 2001). The smaller absolute strain in STGO can probably be related to the larger size of Sr and the resulting larger tilting of the octahedra. This will expand the axis parallel to the chain direction, so that the distortion generated by the shift of the Ti-cation is smaller.

Structural parameters

The Ti shift, *i.e.* the length of the displacement vector between the Ti position in $P2_1/a$ and the special Ti position of the aristotype structure, is very similar in SrTiOGeO_4 and CaOTiGeO_4 , with 0.129 Å and 0.123 Å respectively. For titanite the Ti shift amounts to only 0.115 Å. The comparatively large and nearly identical Ti shifts in the two germanate compounds correspond to their elevated and nearly identical transition temperatures, as obtained from the strain analysis. If we assume a common critical temperature of 594 K for both germanate compounds and an average Ti shift of 0.127 Å, the quotient of the square of these Ti-shifts in SrTiOGeO_4 - CaTiOGeO_4 and titanite is identical with the ratio of the respective critical temperatures, *i.e.* 594 K/487 K. This confirms the validity of the Abrahams-Kurtz-Jamieson relation (Abrahams *et al.*, 1968) for the titanite structure.

The solid solution $\text{Ca}(\text{Ti}_x\text{Zr}_{1-x})\text{OGeO}_4$

Transition temperature and strain behaviour

Contrary and in contrast to earlier studied solid solutions in the titanite structure field phase transitions appear to be both temperature and composition dependent across the solid solution $\text{Ca}(\text{Ti}_x\text{Zr}_{1-x})\text{OGeO}_4$. The endmember composition CaZrOGeO_4 and the samples $\text{Ca}(\text{Ti}_{10}\text{Zr}_{90})\text{OGeO}_4$ and $\text{Ca}(\text{Ti}_{20}\text{Zr}_{80})\text{OGeO}_4$ exhibit the triclinic $\bar{A}1$ ($P\bar{1}$) structure. A displacive structural phase transition from triclinic to the monoclinic structure of the titanite aristotype with space group symmetry $A2/a$ can be observed at high Zr-concentrations. The triclinic – monoclinic compositional phase transition is expected at $\text{Ca}(\text{Ti}_{32}\text{Zr}_{68})\text{OGeO}_4$, while the X-ray diffraction data indicate the aristotype structure ($A2/a$) in the measured temperature range for $\text{Ca}(\text{Ti}_{50}\text{Zr}_{50})\text{OGeO}_4$ and $\text{Ca}(\text{Ti}_{80}\text{Zr}_{20})\text{OGeO}_4$. The temperature dependent triclinic to monoclinic phase transition for the endmember composition CaZrOGeO_4 occurs at 488 ± 5 K and at $T_c = 429 \pm 5$ K and $T_c = 371 \pm 5$ K for $\text{Ca}(\text{Ti}_{10}\text{Zr}_{90})\text{OGeO}_4$ and $\text{Ca}(\text{Ti}_{20}\text{Zr}_{80})\text{OGeO}_4$, respectively. The compositional range of the triclinic structure is broader than that of the $P2_1/a$ structure. The antiferrodistortive phase transition observed in the titanite endmember composition appears to be present up to Zr-contents 18%, accompanied by a sharp drop of the critical

temperature. Already by 5% substitution of Zr for Ti a distinct drop in the critical temperature by 100 K is observed. This substitution therefore destabilizes the ordered $P2_1/a$ phase.

The spontaneous strain associated with the triclinic to monoclinic phase transition in the titanite structure is relatively large and dominated by the symmetry breaking components e_{12} and e_{23} in the low temperature phase. However it has been shown that the triclinic distortion is lowered by the presence of Ti.

The evolution of the symmetry breaking strains with temperature in the triclinic compounds allow a modelling using a simple second order Landau type free energy expansion. Therefore the temperature evolution of the symmetry breaking strain indicates a linear coupling to the order parameter of the triclinic to monoclinic phase transition.

The non-symmetry breaking (nsb) strain components e_{13} and e_{33} describe a linear contraction of the unit cell approximately parallel to the c^* -direction and simultaneous shearing within the triclinic stability field. The evolution of the nsb-strain is hardly affected by changes in the Ti content, which mainly alters T_c . Furthermore a linear correlation between the non-symmetry breaking strain components and temperature exists. This indicates their coupling to the square of the order parameter.

Structural parameters

The observed change in symmetry with increasing Zr-content implies that the monoclinic unit cell is only capable of incorporating a limited percentage of Zr into the octahedral site. The triclinic to monoclinic phase transition occurring as a function of temperature and composition is driven by a change in Ca-coordination from 7 to 8. The titanite framework contracts perpendicular to the direction of the octahedral chains bringing them closer together and reducing the available space for the Ca cations in between them. This behaviour contrasts the structural behaviour in other compounds of similar structural topology as CaTiOGeO_4 and SrTiOGeO_4 . In those compounds the $A2/a$ aristotype symmetry is lowered to $P2_1/a$ driven by the off centre displacement of the octahedral cations. Malcherek and Ellemann-Olesen, 2004 concluded that generally the triclinic distortion of the titanite type structure is likely to take place if a critical monoclinic distortion is overstepped. The monoclinic angle by which such a distortion is likely to set in is in the range $112.9 - 113^\circ$. However this is only true when the

cation occupying the large cavity in the titanite framework is Ca. The value of the critical monoclinic angle probably changes when going to other A-cations, but a triclinic instability might be nevertheless expected.

Despite the similar electronic properties of Zr and Ti the $P2_1/a$ phase is suppressed in CaZrOGeO_4 , in analogy with the substitution of Ti by Sn across the titanite – malayaite join (Kunz *et al.*, 1997). Given the d_0 -character of the Zr-cation a structural distortion similar to the Ti off centring in titanite might be expected in CaZrOGeO_4 . The apparent absence of such an off centring, indicated by the suppression of the $P2_1/a$ -ordered phase may be caused by the larger size of the Zr cation. Kunz and Brown, 1995, have discussed the common absence of such structural distortions in Zr- and Sc-oxide compounds. Consequently not only the size of the substituting cation plays an important role in relation to the stability of the structure.

The general contraction of the titanite-framework perpendicular to the octahedral chain direction is a common feature of the transitions in CaZrOGeO_4 and the compound CaTaOAlO_4 (Malcherek *et al.*, 2004). In CaZrOGeO_4 this contraction is accompanied by additional triclinic distortion and ensuing alteration of the other nsb-strain components e_{11} and e_{22} . Furthermore the temperature evolution of the b -lattice parameter in CaTaOAlO_4 only reflects thermal expansion contrary to $\text{Ca}(\text{Ti}_{10}\text{Zr}_{90})\text{OGeO}_4$ and $\text{Ca}(\text{Ti}_{20}\text{Zr}_{80})\text{OGeO}_4$, which show a minor deviation in the b -lattice parameter and as a result an additional strain expressed by the e_{22} component contributes to the scalar stain. This is probably due to the additional triclinic distortion.

7. References

- Abrahams, S.C., Kurtz, S.K. and Jamieson, P.B., 1968. Atomic Displacement Relationship to Curie Temperature and Spontaneous Polarization in Displacive Ferroelectrics. *Physical Review* 172: 551-553.
- Aizu, K., 1970. Determination of the state parameters and formulation of spontaneous strain for ferroelectrics. *Journal of the Physical Society of Japan* 28: 706-716.
- Angel, R.J., Kunz, M., Miletich, R., Woodland, A.B., Koch, M. and Xirouchakis, D., 1999a. High-pressure phase transition in CaTiOSiO_4 titanite. *Phase Transitions* 68: 533-543.
- Angel, R.J., Kunz, M., Miletich, R., Woodland, A.B., Koch, M. and Knoche, R.L., 1999b. Effect of isovalent Si,Ti substitution on the bulk moduli of $\text{Ca}(\text{Ti}_{1-x}\text{Si}_x)\text{SiO}_5$ titanites. *American Mineralogist* 84: 282-287.
- Angel, R.J. and Bismayer, U., 1999. Renormalization of the phase transition in lead phosphate, $\text{Pb}_3(\text{PO}_4)_2$, by high pressure: lattice parameters and spontaneous strain. *Acta Crystallographica B* 55: 896-901.
- Angel, R.J., 1997. Transformation of fivefold-coordinated silicon to octahedral silicon in calcium silicate, CaSi_2O_5 . *American Mineralogist* 82: 836-839.
- Angel, R.J., Ross, N.L., Seifert, F. and Fliervoet, T.F., 1996. Structural characterization of pentacoordinate silicon in a calcium silicate. *Nature* 384: 411-444.
- Arlt, T., Armbruster, T., Ulmer, P. and Peters, T., 1998. MnSi_2O_5 with the titanite structure: A new high-pressure phase in the MnO-SiO_2 binary. *American Mineralogist* 83: 657-660.
- Aust, H., Völlenke, H. and Wittmann, N., 1976. Die Kristallstruktur der Hoch- und der Tieftemperaturform von CaGe_2O_5 . *Zeitschrift für Kristallographie* 144: 82-90.
- Bismayer, U., Schmahl, W., Schmidt, C. and Groat, L.A., 1992. Linear Birefringence and X-Ray Diffraction Studies of the Structural Phase Transition in Titanite, CaTiSiO_5 . *Physics and Chemistry of Minerals* 19: 260-266.
- Bish, D.L. and Reynolds, R.C. Jr., 1989. Sample preparation for X-ray diffraction. *In* Bish, D.L. and Post, J.E., Ed. *Modern Powder Diffraction*, 369 p. *Reviews in mineralogy* 20, Mineralogical Society of America, Washington, D.C.
- Brese, N.E. and O'Keeffe, M., 1991. Bond-Valence Parameters for Solids. *Acta Crystallographica B* 47: 192-197.

- Buseck, P.R., 1992. Principles of Transmission Electron Microscopy. *In* Buseck, P. R. Ed. Minerals and Reactions at the Atomic Scale: Transmission Electron Microscopy, 516 p. Reviews in mineralogy 27, Mineralogical Society of America, Washington, D.C.
- Caglioti, G., Paoletti, A. and Ricci, F. P., 1958. Choice of Collimator for a Crystal Spectrometer for Neutron Diffraction. *Nuclear Instrumental Methods*. 3: 223-228.
- Carpenter, M.A., Meyer, H.-W., Sondergeld, P., Marion, S. and Knight, K.S., 2003. Spontaneous strain variations through the low temperature phase transitions of deuterated lawsonite. *American Mineralogist* 88: 534-546.
- Carpenter, M.A., Berceero, A. L. and Seifert, F., 2001. Strain analysis of phase transitions in (Ca,Sr)TiO₃ perovskites. *American Mineralogist* 86: 348-363.
- Carpenter, M.A., Salje, E.K.H. and Graeme-Barber, A., 1998. Spontaneous strain as a determinant of thermodynamic properties for phase transitions in minerals. *European Journal of Mineralogy* 10: 621-691.
- Carpenter, M.A., Salje, E.K.H., 1998. Elastic anomalies in minerals due to structural phase transitions. *European Journal of Mineralogy* 10: 693-812.
- Cheary, R.W., 1986. An analysis of the structural characteristics of hollandite compounds. *Acta Cryst.* B42, 229-236.
- Chrosch, J., Bismayer, U. and Salje, E.K.H., 1997. Anti-phase boundaries and phase transitions in titanite: An X-ray diffraction study. *American Mineralogist* 82: 677-681.
- De Vries, R.C., Ray, R. and Osborn, E.F., 1955. Phase equilibria in the system CaO-TiO₂-SiO₂. *Journal of American Ceramics Society* 28: 158.
- Ellemann-Olesen, R. and Malcherek, T., 2004a. A high temperature diffraction study of the solid solution CaTiOSiO₄ – CaTiOGeO₄. *American Mineralogist* *Accepted*
- Ellemann-Olesen, R. and Malcherek, T., 2004b. Temperature- and composition dependence of the phase transitions in Ca(Ti_xZr_{1-x})OGeO₄. *American Mineralogist* *In press*
- Finger, L.W., Cox, D.E. and Jephcoat, A.P., 1994. A correction for powder diffraction peak asymmetry due to axial divergence. *Journal of Applied Crystallography* 27: 892-900.
- Gascoyne, M., 1986. Evidence for the stability of the potential nuclear waste host sphene, over geological time, from uranium-lead ages and uranium-series measurements. *Applied Geochemistry* 1: 199-210.
- Genkina, E.A. and Mill, D.M., 1992. *Sov. Phys. Crystallogr.* 37: 769-772.

- Ghose, S., Ito, Y. and Hatch, D.M., 1991. Paraelectric-Antiferroelectric Phase Transition in Titanite, CaTiSiO_5 : I. A high temperature X-ray diffraction study of the order parameter and transition mechanism. *Physics and Chemistry of Minerals* 17: 591-603.
- Giacovazzo, C., 1992. Crystallographic computing. *In* Giacovazzo, C., Monaco, H.L., Viterbo, D., Scordari, F., Gilli, G., Zanotti, G. and Catti, M., *Fundamentals of Crystallography* (IUCr Texts on Crystallography No. 2) International Union of Crystallography. Oxford University Press.
- Gonzalez, C.R., 1987. General theory of the effect of granularity in powder X-ray diffraction, *Acta Crystallographica* A43: 769-774.
- Gottstein, G., 2001. *Physikalische Grundlagen der Materialkunde*, 2. Edition. Springer Verlag Berlin Heidelberg.
- Groat, L.A., Kek, S., Bismayer, U., Schmidt, C., Krane, H.G., Meyer, H., Nistor, L. and Van Trendeloo, G., 1996. A synchrotron radiation, HRTEM, X-ray powder diffraction, and Raman spectroscopy study of malayaite, CaSnSiO_5 . *American Mineralogist* 81: 595-602.
- Groat, L.A., Raudsepp, M., Hawthorne, F.C., Ercit, T.S., Sherriff, B.L. and Hartman, J.S., 1990. The amblygonite-montebasite series: Characterization by single-crystal structure refinement, infrared spectroscopy, and multinuclear MAS-NMR spectroscopy. *American Mineralogist* 75: 992-1008.
- Hammonds, K.D., Bosenick, A., Dove, M.T. and Heine, V., 1998. Rigid unit modes in crystal structures with octahedrally coordinated atoms. *American Mineralogist* 83: 476-497.
- Hatch, D.M. and Ghose, S. 1991. The $\alpha - \beta$ phase transition in cristobalite, SiO_2 . Symmetry analysis, domain structure, and the dynamical nature of the β -phase. *Physics and Chemistry of Minerals* 17: 554-562.
- Hayward, P. and Cechetto, E., 1982. Development of sphene-based glass ceramics tailored for Canadian waste disposal conditions. *In* Topp, S., Ed., *Scientific Basis for Nuclear Waste Management* 3: 91-98.
- Hayward, P.J., Doern, D.C. and George, I.M., 1990. Dissolution of a sphene glass-ceramic, and of its component sphene and glass phases in Ca-Na-Cl brines. *Journal of American Ceramics Society* 73: 544-511.
- Hawthorne, F.C., Groat, L.A., Raudsepp, M., Ball, N.A., Kimata, M., Spike, F.D., Gaba, R., Halden, N.M., Lumpkin, G.R., Ewing, R.C., Gregor, R.B., Lytle, F.W., Ercit, T.S., Rossman, G.R., Wicks, F.J., Ramik, R.A., Sherriff, B.L., Fleet, M.E. and McCammon, C., 1991. Alpha-decay damage in titanite. *American Mineralogist* 76: 370-396.

- Higgins, J.B. and Ribbe, P.H., 1976. The crystal chemistry and space groups of natural and . . synthetic titanites. *American Mineralogist* 61: 878-888.
- Hill, R.J. and Madsen, I.C., 1987. Data collection strategies for constant wavelength Rietveld analysis. *Powder Diffraction* 2: 146-162.
- Howard, S.A. and Preston, K.D., 1989. Profile fitting of powder diffraction patterns. *In* Bish, D.L. and Post, J.E., Ed. *Modern Powder Diffraction*, 369 p. *Reviews in mineralogy* 20, Mineralogical Society of America, Washington, D.C.
- Howard, C.J., 1982. The approximation of asymmetric neutron powder diffraction peaks by sums of Gaussians. *Journal of Applied Crystallography* 15: 615-620.
- Hunt, J.A. and Kerrick, D.M., 1977. The stability of sphene: experimental redetermination and geologic implications. *Geochimica et Cosmochimica Acta* 41: 279-288.
- Jenkins, R., 1989a. Instrumentation. *In* Bish, D.L. and Post, J.E., Ed. *Modern Powder Diffraction*, 369 p. *Reviews in mineralogy* 20, Mineralogical Society of America, Washington, D.C.
- Jenkins, R., 1989b. Experimental procedures. *In* Bish, D.L. and Post, J.E., Ed. *Modern Powder Diffraction*, 369 p. *Reviews in mineralogy* 20, Mineralogical Society of America, Washington, D.C.
- Kek, S., Aroyo, M., Bismayer, U., Schmidt, C., Eichhorn, K. and Krane, H.G., 1997. The two-step phase transition of titanite, CaTiSiO_5 : a synchrotron radiation study. *Zeitschrift für Kristallographie* 212: 9-19.
- Klug, H.P. and Alexander, L.E., 1974. *X-ray Diffraction Procedures for polycrystalline and Amorphous Materials*. John Wiley and Sons, New York.
- Knoche, R., Angel, R.J., Seifert, F. and Fliervoet, T.F., 1998. Complete substitution of Si for Ti in titanite $\text{Ca}(\text{Ti}_{1-x}\text{Si}_x)^{\text{VI}}\text{Si}^{\text{IV}}\text{O}_5$. *American Mineralogist* 83: 1168-1175.
- Kunz, M., Arlt, T. and Stolz, J., 2000. In situ powder diffraction study of titanite (CaTiOSiO_4) at high pressure and high temperature. *American Mineralogist* 85: 1465-1473.
- Kunz, M., Xirouchakis, D., Wang, Y., Parise, J.B. and Lindsley, D.H., 1997. Structural investigations along the join $\text{CaTiOSiO}_4 - \text{CaSnOSiO}_4$. *Schweizerische Mineralogische Petrographische Mitteilung* 77: 1-11.
- Kunz, M., Xirouchakis, D., Lindsley, D.H. and Hauserman, D., 1996. High-pressure phase transition in titanite (CaTiOSiO_4). *American Mineralogist* 81: 1527-1530.
- Kunz, M. and Brown, I.D., 1994. Out of center distortions around octahedrally coordinated d^0 -transition metals. *Journal of Solid State Chemistry* 115: 395-406.

- Ladd, M.F.C. and Palmer, R.A., 1978. Structure determination by X-ray Crystallography, 393 p. Plenum Press, New York and London.
- Langford, I.J. and Louër, D., 1996. Powder diffraction. Reports on Progress in Physics 59: 131-234.
- Larson, A.C. and Von Dreele, R.B. (1994) General Structure Analysis System (GSAS). Los Alamos National Laboratory. Los Alamos, New Mexico.
- LeBail, A. Duroy, H. and Fourguet, J.L., 1988. *Ab-initio* structure determination of LiSbWO₆ by X-ray powder diffraction. Materials Research Bulletin 23: 447-452.
- Malcherek, T. and Ellemann-Olesen, R. 2004. CaZrGeO₅ and the triclinic instability of the titanite structure type. Zeitschrift für Kristallographie. *In press*.
- Malcherek, T., Borowski, M. and Bosenick, A., 2004. Structure and phase transitions of CaTaOAlO₄. Journal of Applied Crystallography 37: 117-122.
- Malcherek, T. and Bosenick, A., 2004. Structure and phase transition of CaGe₂O₅ revisited. Physics and Chemistry of Minerals 31: 224-231.
- Malcherek, T., 2002. Structure and phase transitions of LiTaOGeO₄. Acta Crystallographica B 58: 607-612.
- Malcherek, T., 2001. Spontaneous strain in synthetic titanite, CaTiOSiO₄. Mineralogical Magazine 65: 709-715.
- Malcherek, T., Paulmann, C., Domeneghetti, M.C. and Bismayer, U., 2001. Diffuse scattering anisotropy and the P2_{1/a} ↔ A2/a phase transition in titanite, CaTiOSiO₄. Journal of Applied Crystallography 34: 108-113.
- Malcherek, T., Domeneghetti, M., Tazzoli, V., Salje, E.K.H. and Bismayer, U., 1999. A high temperature X-ray diffraction study of synthetic titanite, CaTiOSiO₄. Phase transitions 69: 119-131.
- Masuda, K., Erskine, D. and Anderson, O.L., 2000. Differential laser-interferometer for thermal expansion measurements. American Mineralogist 85: 279-287.
- McKie, D. and McKie, C., 1986. Essentials of Crystallography, 437 p. Blackwell Scientific Publications, Oxford.
- McLaren, A.C., 1992. Transmission electron microscopy of minerals and rocks. Putnis, A. and Liebermann, R.C., Ed. Cambridge topics in mineral physics and chemistry 2. Cambridge University Press.

- Meyer, H.W., Zhang, M., Bismayer, U., Salje, E.K.H., Schmidt, C., Kek, S., Morgenroth, W. and Bleser, T., 1996. Phase transformation behaviour of natural titanite: An infra-red, Raman, birefringence and X-ray diffraction study. *Phase Transitions* 59: 39-60.
- Mill, B, Belokoneva, E. and Butashin, A., 1990. *Sov. Phys. Crystallogr.* 35: 176-180.
- Monaco, H.L, 1992. Experimental methods in X-ray crystallography. *In* Giacovazzo, C., Monaco, H.L., Viterbo, D., Scordari, F., Gilli, G., Zanotti, G. and Catti, M., *Fundamentals of Crystallography (IUCr Texts on Crystallography No. 2)* International Union of Crystallography. Oxford University Press.
- Mongiorgi, R. and Di Sanserverino, L.R., 1968. A reconsideration of the structure of titanite. *Mineral. Petrogr. Acta* 14: 123-141.
- Muscat, A.J., 2000. A practical guide to the propagation and analysis of experimental error, 39 p. Department of Chemical and Environmental Engineering, University of Arizona, Tucson.
- Newnham, R.E., 1974. Domains in minerals. *American Mineralogist* 59: 906-918.
- Nord, G.L., Jr., 1992. Imaging Transformation-induced Microstructures. *In* Buseck, P. R. Ed. *Minerals and Reactions at the Atomic Scale: Transmission Electron Microscopy*, 516 p. *Reviews in mineralogy* 27, Mineralogical Society of America, Washington, D.C.
- Nye, J.F., 1985. *Physical properties of crystals*, 329 p. Oxford University Press, Oxford.
- Oberti, R., Smith, D.C., Rossi, G. and Caucia, F., 1991. The crystal-chemistry of high-aluminium titanites. *European Journal of Mineralogy* 3: 777-792.
- Pitschke, W., Mattern, N. and Hermann, H., 1993a. Incorporation of microabsorption corrections into Rietveld analysis, *Powder Diffraction* 8: 223-228.
- Pitschke, W., Hermann, H. and Mattern, N., 1993. The influence of surface roughness on diffracted X-ray intensities in Bragg-Brentano geometry and its effect on the structure determination by means of Rietveld analysis, *Powder Diffraction* 8: 74-83.
- Putnis, A., 1992. *Introduction to material sciences*, 457 p. Cambridge University Press.
- Rath, S., Kunz, M. and Miletich, R., 2003. Pressure-induced phase transition in malayaite, CaSnOSiO_4 . *American Mineralogist* 88: 293-300.
- Redfern, S.A.T., Graeme-Barber, A. and Salje, E. K. H., 1988. Thermodynamics of plagioclase III: Temperature evolution of the spontaneous strain at the $I\bar{1} \Rightarrow C\bar{1}$ phase transition in Ca-rich plagioclase. *Physics and Chemistry of Minerals* 16: 157-163.

- Redfern, S.A.T. and Salje, E. K. H., 1987. Thermodynamics of plagioclase II: Temperature evolution of the spontaneous strain at the $I\bar{1} \Rightarrow C\bar{1}$ transition in anorthite. *Physics and Chemistry of Minerals* 14: 189-195.
- Reynolds, R.C., Jr., 1989. Principles of powder diffraction. *In* Bish, D.L. and Post, J.E., Ed. *Modern Powder Diffraction*, 369 p. Reviews in mineralogy 20, Mineralogical Society of America, Washington, D.C.
- Ribbe, P.H., 1982. Titanite. *In* Ribbe, P.H., Ed. *Orthosilicates*, 450 p. Reviews in Mineralogy 5.
- Rietveld, H.M., 1969. A profile refinement method for nuclear and magnetic structures. *Journal of Applied Crystallography* 2: 65-71.
- Rietveld, H.M., 1967. Line profiles of neutron powder-diffraction peaks for structure refinement. *Acta Crystallographica* 22: 151-152.
- Robbins, C.R., 1968. Synthetic CaTiSiO_5 and its germanium analogue. *Materials Research Bulletin* 3: 693-698.
- Sales, M., Eguia, G., Quintana, P., Torres-Martinez, L. and West, A., 1999. Crystal structures of $\text{Ca}_2\text{AlTaO}_6$ and CaAlTaO_5 . *Journal of solid state chemistry* 143: 62-68.
- Salje, E.K.H., 1995. Chemical mixing and structural phase transitions: the plateau effect and oscillatory zoning near surfaces and interfaces. *European Journal of Mineralogy* 7: 791-806.
- Salje, E.K.H., 1993. Phase transitions in ferroelastic and co-elastic crystals (student edition), 229 p. Cambridge University Press, Cambridge.
- Salje, E.K.H., Schmidt, C. and Bismayer, U., 1993a. Structural phase transition in titanite, CaTiSiO_5 : A raman spectroscopic study. *Physics and Chemistry of Minerals* 19: 502-506.
- Salje, E.K.H., Graeme-Barber, A. and Carpenter, M.A., 1993b. Lattice parameters, Spontaneous strain and Phase Transitions in $\text{Pb}_3(\text{PO}_4)_2$. *Acta Crystallographica* B49: 387-392.
- Salje, E.K.H., 1990. Phase transitions in ferroelastic and co-elastic crystals. Cambridge University Press, Cambridge, UK.
- Salje, E.K.H., 1989. Characteristics of Perovskite-Related Materials. *Philosophical Transactions of the Royal Society of London. Series A, Mathematical and Physical Sciences* 328 (issue 1599) 409-415.
- Schofield, P.F. and Redfern, S.A.T., 1993. Temperature- and composition-dependence of the ferroelastic phase transition in $(\text{Cu}_x\text{Zn}_{1-x})\text{WO}_4$. *Journal of Physics and Chemistry of Solids* 54: 161-170.

- Shannon, R.D., 1976. Revised effective ionic radii and systematic studies of interatomic distances in halides and chalcogenides. *Acta Crystallographica* A32: 751 – 767.
- Sheldrick, G.M., 1997 *SHELX97*. Programme for the refinement of crystal structures. University of Göttingen, Germany.
- Speer, J.A. and Gibbs, G.V., 1976. The crystal structure of synthetic titanite, CaTiOSiO_4 , and the domain textures of natural titanites. *American Mineralogist* 61: 238-247.
- Stoe & Cie GmbH, 1996. X-RED, Data Reduction Program. Darmstadt, Germany
- Taylor, M. and Brown, G.E., 1976. High-temperature structural study of the $\text{P2}_1/\text{a} \rightleftharpoons \text{A2}/\text{a}$ phase transition in synthetic titanite, CaTiSiO_5 . *American Mineralogist* 61: 435-447.
- Thompson, P., Cox, D.E. and Hastings, J.B., 1987. Rietveld refinement of Debye-Scherrer synchrotron X-ray data from Al_2O_3 . *Journal of Applied Crystallography* 20: 79-83.
- Toby, B.H., 2001. EXPGUI, a graphical user interface for GSAS. *Journal of Applied Crystallography* 34: 210-213
- Toraya, H., 1986. Whole-pattern fitting without reference to a structural model: Application to X-ray powder diffractometer data. *Journal of Applied Crystallography* 19: 440-447.
- Troitzsch, U. and Ellis, D.J., 1999. The synthesis and crystal structure of CaAlFSiO_4 , the Al-F analog of titanite. *American Mineralogist* 84: 1162-1169.
- Troitzsch, U., Ellis, D.J., Thompson, J. and Fitz-Gerald, J., 1999. Crystal structural changes in titanite along the join TiO-AlF. *European Journal of Mineralogy* 11: 955-965.
- Van Heurck, C., Van Tendeloo, G., Ghose, S. and Amelinckx, S., 1991. Paraelectric-Antiferroelectric Phase Transition in Titanite, CaTiSiO_5 . II. Electron Diffraction and Electron Microscopic Studies of the Transition Dynamics. *Physics and Chemistry of Minerals* 17: 604-610.
- Van Laar, B. and Yelon, W.B., 1984. The peak in neutron powder diffraction. *Journal of Applied Crystallography* 17: 47-54.
- Will, G., Parrish, W. and Huang, T.C., 1983. Crystal structure refinement by profile fitting and least-squares analysis of powder diffraction data. *Journal of Applied Crystallography* 16: 611-622.
- Williams, D.B. and Carter, B.C., 1996. *Transmission electron microscopy*, 729 p. Plenum Press, . New York.

- Xirouchakis, D., D. H. Lindsley, and D. J. Andersen, 2001, Assemblages with titanite (CaTiOSiO₄), Ca-Fe-Mg olivine and pyroxenes, Fe-Mg-Ti oxides, and quartz: Part I. Theory: *American Mineralogist*, v. 86, p. 247-253.
- Xirouchakis, D., D. H. Lindsley, and B. R. Frost, 2001, Assemblages with titanite (CaTiOSiO₄), Ca-Fe-Mg olivine and pyroxenes, Fe-Mg-Ti oxides, and quartz: Part II. Application: *American Mineralogist*, v. 86, p. 254-264.
- Xirouchakis, D. and Lindsley, D.H., 1998. Equilibria among titanite, hedenbergite, fayalite, ilmenite, and magnetite: experiments and internally consistent thermodynamic data for titanite. *American Mineralogist* 83: 712-725.
- Young, R.A., ed. 1993. *The Rietveld Method*. IUCr Monographs on Crystallography 5. International Union of Crystallography, 298 p. Oxford Science Publications, Oxford University Press.
- Young, R.A. and Wiles, D.B., 1982. Profile shape functions in Rietveld refinements. *Journal of Applied Crystallography* 15: 430-438.
- Zachariasen, W.H., 1930. The crystal structure of titanite. *Zeitschrift für Kristallographie* 73: 7-16.
- Zhang, M., Salje, E.K.H., and Bismayer, U., 1997. Structural phase transition near 825 K in titanite: Evidence from infrared spectroscopic observations. *American Mineralogist* 82: 30-35.
- Zhang, M., Salje, E.K.H., Bismayer, U., Unruh, H.G., Wruck, B. and Schmidt, C., 1995. Phase transition(s) in titanite CaTiSiO₅. *Physics and Chemistry of Minerals* 22: 41-49.

8. Erklärung

Ich erkläre hiermit, dass ich die vorgelegte Dissertation selbst verfasst und mich dabei keiner anderen als den von mir ausdrücklich bezeichneten Quellen und Hilfen bedient habe.

Heidelberg den 13/12-04